A DESCRIPTION AND DISCUSSION OF THE APPARATUS AND DATA ACQUISITION IN THE CERN WA7-EXPERIMENT

(With particular emphasis on the hadron calorimeter as a trigger rejection device and on the fast on-line filtering electronics).

Kim Kirsebom

Thesis submitted to the degree cand. real. at the University of Oslo, Institute of Physics, 1981.

PREFACE

As a member of the group for high energy physics at the University of Oslo, I have participated in the CERN WA7 experiment. The purpose of this experiment has been and still is the study of elastic scattering processes between hadrons. The WA7 collobration consists of the following groups: Annecy (LAPP) - CERN - Copenhagen (Niels Bohr Institute) - Genova - University College London - University of Oslo.

Due to the very low cross sections, the detection of elastic scattering processes necessitates intense beams and therefore also efficient data-acquisition/filtering-systems.

This thesis is concerned with the accumulation of data; starting with the incident beam and ending up with triggers written onto magnetic tape. The physics of the very rare elastic processes is not studied, nor the off-line analysis which is based on the magnetic tape data. Two main topics are treated: The calorimeter (chapter 4) which the Oslo group has constructed. This device is used in the filtering process at an early stage to exclude some of the inelastic triggers. The second topic is concerned with the decision making logics (chapter 5). Here, by means of fast electronics, the actual filtering is performed. For both topics a description is given, the performances are discussed and possible improvements are also considered.

Since, in chapter 5, all the detectors are involved, a brief description is also given of the other detectors. Therefore, the overall experimental setup of WA7 plus the physics aspects are treated in chapter 1. Chapter 2 treats the scintillation hodoscopes (including some theory on scintillation and photomultipliers). Multi wire proportional chambers is the topic of chapter 3, and finally are the cerenkovs treated in chapter 6. To understand the performances of a fast decision making logic, I have found it necessary to do the small developments of appendices 1 - 3; about the Poisson-probability in relation with randomly distributed pulses,

about deadtimes in different connections and finally about accidental coincidences. In appendices 4 and 5, details about the calibration work of chapter 4 are presented.

I am grateful to many people for helping me realize this thesis. To Arne Lundby and Bernard Mouellic for initiating me into this kind of detector physics; to the off-line people, Kjell Brobakken, Lars Bugge, Per Helgaker, Jan Myrheim and Geir Skjevling for helping me in extracting all the interesting rates from the data; to Torleiv Buran, Ivar Gjerpe and Sven O. Sørensen for their help and encouragement in the implementation of the calorimeter and to Eliane Lauper and Rosemarie Audria for their typing and editing aid. Naturally the list of those who have contributed ideas and offered help and assistance, is far from complete. I hope I will be excused for not mentioning everybody.

Oslo 27.4.81

Kim Kirsebom

C O N T E N T S

PAGE

D. Use of the detector in the present setup; how a 5-plane and 14-plane calorimeter would affect the trigger rates. 4 - 32

The interest of a 2-plane calorimeter, e-hadron separation - reconstructed forward arm momentum spectra are used to analyse the effect of the cerenkovs and the expected effect from a fully equipped calorimeter on the trigger rate, effect of a reduced 5-plane calorimeter (both based on appendix 4) - possible bias since reconstructed sample only is 25% of all triggers? - comparison 5-plane versus 8-plane - physics motivation for detecting muon pairs, definition of the trigger.

E. Installation and calibration of counters. 4 - 49

Definition of a q-distribution and a q-measurement, use of the L3001 (4-49 to 4-55) - installation of planes L3, R1 and R2, use of the FWHM to determine counter quality (4-55 to 4-58) - installation of calorimeter counters, discussion of common setting, linearity considerations (4-58 to 4-66) - results; photoelectron yield distribution for the 64 counters (4-66 to 4-69) - counting rates (all 5 planes) normalized to to the beam intensity (+20 GeV/c incident) (4-69 to 4-73) - fanning in of calorimeter signals, definition of Cal.yes - signal (4-73 to 4-75) - counting rates (all planes, -92 GeV/c) (4-75 to 4-82) - multiplicities in the calorimeter based on the rates, how they should be measured (4-82 to 4-87) - pulseheight versus charge, timing, comparison between a charge and a threshold cut on the total signal (rejection of bad events and loss of good events?) (4-87 to 4-95) - the muon pair logic, rate considerations, timing, the μ-matrix (4-95 to 4-101).

PAGE

CHAPTER 1

OUTLINE OF THE WA7 EXPERIMENT

A. Physics

The purpose of the WA7 experiment is the study of elastic scattering processes between hadrons, such as

$$\pi^+p \rightarrow \pi^+p$$
$$K^+p \rightarrow K^+p$$
$$pp \rightarrow pp$$
$$(12 \rightarrow 12)$$

Also the processes in which the incoming hadron is negatively charged, have been measured. The first particle (π^+, π^-, K^+, K^-, p or p^-) will be called the beam particle and after the collision, the scattered (beam) particle. The second particle is at rest in the laboratory system before the collision; since we used a liquid hydrogen target (H_2), this was always a proton. After collision it recoils. The more violent the scattering the more energy is transferred to the scattered proton. We were interested in collisions where the energy transfer exceeded the proton rest energy by more than a factor 3. To produce these collisions we used an unseparated hadron beam incident on the liquid H_2-target.

What is measured is the elastic cross section. In general the cross section for a certain process is related to the probability of observing the same process in the following way,

> The cross section $\sigma \equiv$
> (the statistical probability of observing the process if exactly one beamparticle is incident anywhere on an area A (say 1 cm^2) where somewhere there is one target particle) multiplied by (the area A).

This area is specific for the process (or the type of reaction) in question and is called its cross section, σ. At least in some circumstances is σ actually reflecting a measured cross section. For example the hadronic total cross section for proton-proton → anything (excluding the electromagnetic interaction), should be interpreted as the extension of the strong forces in a projection 'around the proton'.

The only means of studying experimentally elastic scattering is by measuring the elastic cross section, σ_{el}, and in particular how σ_{el} is distributed in ϑ_{CM} or $|t|$ (see Fig. 1.1). Most interes-

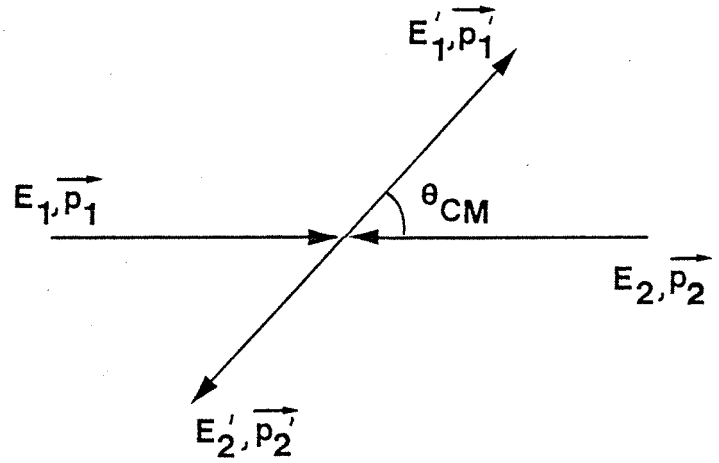

Fig. 1.1

The center of mass system (the CM-system), by definition is such that $\vec{p_1} = -\vec{p_2}$. If the collision is elastic, we see that $\vec{p_2} = -\vec{p_2}'$ and that $|\vec{p_1}| = |\vec{p_2}| = |\vec{p_1}'| = |\vec{p_2}'|$, hence $E_1 = E_1'$ and $E_2 = E_2'$. t, is defined as the four momentum transfer squared. For an elastic interaction we find,

$$t = [(E_1', \vec{p_1}') - (E_1, \vec{p_1})]^2 = -(\vec{p_1}' - \vec{p_1})^2 = -2p^2(1 - \cos \vartheta_{CM})$$

s, is defined as the sum of the four momenta p_1 and p_2 squared.

$$s = (p_1 + p_2)^2 = [(E_1, \vec{p_1}) + (E_2, \vec{p_2})]^2 = (E_1 + E_2)^2 = (E_1' + E_2')^2 = s'$$

---

ting is perhaps $|t|$ since it is a Lorentz invariant and directly reflects the violence of the collision. This differential cross section is denoted, $\frac{d\sigma}{dt}$ in general and, $\frac{d\sigma_{el}}{dt}$ when only elastic scattering is considered. Notice that to obtain the actual cross section for producing an elastic event so that, $t_o - \Delta t_o < t < t_o + \Delta t_o$, one has to calculate $d\sigma_{el}/dt|_{t=t_o} \cdot \Delta t_o$. We also studied the elastic differential cross section at fixed CM scattering angle ϑ_{CM} as a function of the CM-energy squared, i.e., the behaviour of,

$$\frac{d\sigma}{dt}(s, \vartheta_{CM} = \text{constant})$$

In WA7 we have taken data in two |t|-ranges. 1), The high-t range corresponding to roughly $55^o < \vartheta_{CM} < 90^o$. This translates into $7 < |t| < 17$ $(GeV/c)^2$ with a beam momentum of 20 GeV/c and into $10 < |t| < 25$ $(GeV/c)^2$ with a 30 GeV/c beam. 2), The medium-t range, corresponding roughly to $15^o < \vartheta_{CM} < 60^o$ or $0.6 < |t| < 8$ $(GeV/c)^2$ with 20 GeV/c incident, and to $9^o < \vartheta_{CM} < 40^o$ or $0.6 < |t| < 10$ $(GeV/c)^2$ with 50 GeV/c incident. In this thesis will be discussed only the setup for the high-t measurement. The medium-t data were taken more recently (1979-80), and hence could not be the subject of this thesis. Other students are working on this, Tom Fearnley and Tore Sørsdal (Univ. of Oslo) and Zidan Asad and Martin Phillips (University College of London).

Notice the very high values of |t|, in particular for |t|-range 1). Remember that to break up atoms some eV's are needed while MeV's will break up atomic nuclei. In the |t|-range we were measuring, $\sqrt{|t|}$ were up to many times the restmasses involved. Actually with these very high |t|'s it is surprising that elastic reactions may still occur. As we shall see, they are very rare.

The reason for measuring these special reactions is their comparatively simple theoretical treatment. One disregards the binding between the hadron constituents (quarks), and the hadron-hadron collisions are only considered by means of quark-quark interactions. For example the CIM (the Constituent Interchange Model) gives predictions for $d\sigma_{el}/dt$, no absolute normalization is given, but both the t-dependence and the s-dependence at constant ϑ_{CM}, are predicted. The dimensional counting rule is another model which also gives the s-dependence of $d\sigma_{el}/dt$ at fixed ϑ_{CM}. These theories are based on rather detailed assumptions on the structure of the hadrons and also on the forces acting between the quarks at close distance. Therefore measuring the elastic cross sections will indicate the best model and hence the best way to understand the hadrons. For references and a thorough treatment, see thesis[1] by Lars Bugge, Univ. of Oslo. It is important that the probing should be done with hadrons. This is the only way to gather information about the nature of the strong forces between the hadron constituents.

From refs. 2,3 and 4 have been collected some central figures from the three high-t data taking periods, see table 1.1.

Charge & momentum of incident beam particle GeV/c	Incident particle type	Nr of incident beam particles $\times 10^{12}$ (N_{inc})	Nr[1] of target interactions $\times 10^{11}$ (N_{int}) & nr[2] of days of data taking	Nr of triggers onto tape $\times 10^{6}$ (N_{trig})	Nr of elastic events (N_e)	t_{min}/t_{max} in $-(GeV/c)^2$	Mean acceptance in t-range % (A)	Integrated cross section in t-range 10^{-34} cm^2 (σ_{el})
-20	π^-	1.81	1.53	5.56	38	6.8/22	6.4	5.19
	K^-	0.051		1.26	4	6.8/18	8.1	15.50
	p^-	0.049	7.4 days	2.17	0	6.8/18	8.1	0
+20	π^+	2.63	2.45	6.98	66	6.2/18	4.9	5.33
	K^+	0.101		2.60	2	6.2/16	5.6	2.86
	p^+	0.332	11.8 days	2.28	16	6.2/12	4.7	14.30
-30	π^-	7.53	6.43	14.16	26	8.0/28	7.9	0.66
	K^-	0.296		2.29	1	8.0/28	7.9	0.38
	p^-	0.208	31.0 days	0.52	0	8.0/22	8.4	0

Table 1.1

Central results and conditions from the high-t data taking. 1), only ≈ 8% of the beam particles actually interact in the target, 2), assuming an intensity of $3 \cdot 10^7$ beamparticles per burst (which lasts ≈ 1 second every 10 second).

Already before setting out to measure the cross sections it was clear that they would be very small. The apparatus was optimized for these measurements. Here is the relationship between the important parameters which fixes the number of observed elastic events,

$$N_e = \sigma_{el} \cdot N_{inc} \cdot N_{tar} \cdot A \cdot E_f \qquad (1.1)$$

where N_e is the number of elastic events, σ_{el} the integrated elastic cross section in a certain t-range $[t_{min}, t_{max}]$, A is the mean geometrical acceptance of the apparatus for elastic events in the same

t-range, N_{inc} is the number of incoming beam particles, N_{tar}, the number of target protons per cm^2 which the incoming beam sees and finally is E_f the detection efficiency given that an elastic event has occured inside our geometrical acceptance. The main criterion when fixing these parameters, was a reasonable event rate, dN_e/dt. Physics considerations set the t-range we wanted to cover with the apparatus. A, which is a function of the four momentum transfer, was maximized inside this range, essentially by means of large surface detectors covering a non-negligible fraction of the solid angle corresponding to $t_{min} < |t| < t_{max}$. At the same time both the apparatus and the data acquisition electronics had to be designed to handle the highest possible interaction rate ($dN_{int}/dt = \sigma_T \cdot N_{tar} \cdot dN_{inc}/dt$, where σ_T is the total cross section). In WA7 the electronics set the upper limit for dN_{int}/dt at roughly $4.8 \cdot 10^6$ s^{-1} corresponding to $dN_{inc}/dt = 7 \cdot 10^7$ s^{-1}. Above this intensity the overall efficiency - including the apparatus efficiency, the efficiency of the on-line filtering plus the data acquisition deadtime (when data are transferred to the computer, the on-line filtering electronics is inhibited) - which is intensity dependent, drops faster than dN_e/dt increases. This will be discussed in chapter 5.

Charge and momentum of incident beam particle	N_{int}/N_{trig}	N_{trig}/N_e	$E_f(\pi)$
-20 GeV/c	17,000	214,000	15%
+20 GeV/c	20,700	141,000	23%
-30 GeV/c	37,900	629.000	16%

Table 1.2

Column 2 and 3 give numbers which show the effect of the on-line and off-line filtering respectively. E_f is the detector efficiency for elastic events produced inside the acceptance.

Notice from table 1.1 that the filtering is a two step procedure, one done by the apparatus/electronics which accepts only a small fraction of the target interactions (N_{int}), this is also called on-line

filtering; the second step is performed off-line (by computer analysis). Table 1.2 gives the number of target interactions which will produce one trigger (written onto tape), and in the same way the number of triggers which in the mean will produce one elastic event. Setting $N_{tar} = 4.265 \cdot 10^{24}$ protons/cm^2, equation (1.1) with the figures given in table 1.1 may be used to calculate E_f. The values given in table 1.2 are pion detection efficiencies. Naturally this efficiency logically preceedes the cross section. E_f is established independently and is actually used to calculate the cross section (σ_{el}) through relation (1.1). A substantial amount of work went into determining all the inefficiencies both on the detector side and in the data acquisition logic which all combined yielded the overall inefficincy, $= 1 - E_f$.

For general information about the physics results and the data taking, the reader is also referred to refs. 5, 6 and 7.

B. The experimental setup, some details.

The setup is shown in Figs. 1.2.a and b, showing respectively the incident beam apparatus (upstream of the target) and the downstream part which defines the geometrical acceptance, A. In Fig. 1.3 is

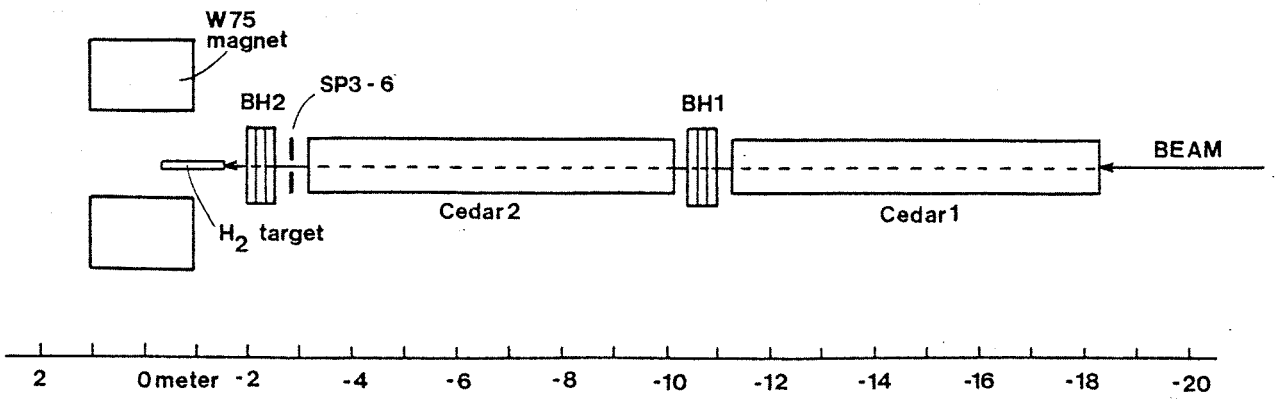

Fig. 1.2.a

Experimental setup upstream of the target. The Cedars are cerenkov counters for identifying the incoming beam particle. Two are necessary to flag either a pion, a kaon or a proton. The BH's are beam-hodoscopes used to monitor intensities and incoming particle directions. The four veto counters SP3 - 6 which sit around the beam are also indicated.

shown the definition of our right handed coordinate system which also will be used in the following description of the apparatus. 'z' is parallel with the (undeviated) beam, 'y' is vertical pointing up and 'x' is horizontal pointing to the left when looking downstream.

A general description of the apparatus shown in Figs. 1.2.a and b follows. The upstream part shown in Fig. 1.2.a consists of 2 beam-hodoscopes modules (BH1 and BH2 in the figure). In addition, there are two cerenkov counters, Cedar 1 and Cedar 2. Also in between Cedar 2 and BH2 are shown the veto counters SP3 - 6, see Fig. 5.5.a. The ionization chamber (used to check the beam intensity) was located well upstream of Cedar 1. Merely the use of these detectors will be explained here.

By means of the two Cedars we could positively identify two of the incoming particles, in our case we flagged kaons and protons. The third

particle (i.e., pions) is identified indirectly by a non-firing of both Cedars. These detectors are sophisticated differential pressure cerenkov counters, see chapter 6. They were used both in the fast trigger (that is, in the fast electronics which selects elastic event candidates) and in the off-line normalization work (the scalers counting the Cedars gave the integrated number of incoming kaons and protons, N_{inc} for π's and K's in (1.1); in addition the Cedar information was used to reject background events in the off-line analysis).

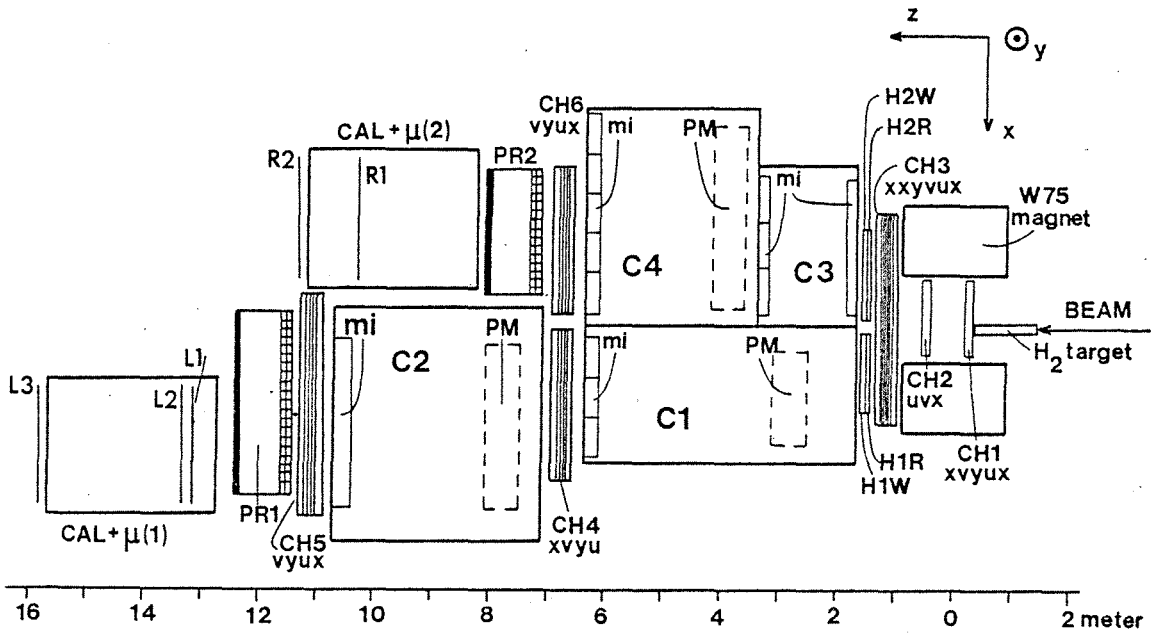

Fig. 1.2.b

Experimental setup downstream of the target, topview. CH's are multi wire proportional chambers, the sequence of the inside wire planes are given, see Fig. 1.3. CAL + μ 's are calorimeter/muon-detectors (consisting of iron/scintillator sandwiches), see Fig. 4.1 etc. The positions of the scintillator planes are shown; L1, L2 and L3 in the left arm, R1 and R2 in the right. C's are cerenkovs (used for particle identification and finally, H1R, H1W, H2R, H2W, PR1 and PR2 are six scintillation hodoscopes. For the prompt-hodoscopes (PR1 and PR2) and the cerenkovs, some details about the detectors are indicated. For the prompts the particle sensitive volume is 4 cm thick (checkered and the most upstream part of the detectors), the readout electronics is located most downstream (thickly drawn lines). For the cerenkovs the light reflecting mirrors are indicated. Also, for C1, C2 and C4, is shown the position of the readout (Winston cones/photomultiplier - ensembles). In C3 the light is reflected twice and the readout (not shown), is located roughly above the wall separating C3 and C4.

The beamhodoscopes are systems of scintillation counters allowing fast ($\sigma_t \approx \pm 3$ ns) and precise ($\sigma_x = \sigma_y \approx \pm 1$ mm, $\sigma_z = \pm 20$ cm) detection of the beamparticle[8,9]. More will be said about scintillation counters in chapter 2. Both BH1 and BH2 consist of 3 planes, each plane being a system of parallel elements (dimensions, $2.2 \times 5 \times 100$ mm^3, where 2.2×100 mm^2 is the sensitive area which the beam particle will see and 5 mm is the thickness along z). The elements are inclined 0^o, 45^o or 135^o in the xy-plane, relative to the x-axis. Due to the different inclinations, BH1 and BH2 data allow reconstruction off-line of two points on the beam particle trajectory, hence also the direction of the incident particle may be found. This information is used in conjunction with that coming from the downstream detectors to reconstruct the complete event (i.e., $\vec{p}_{inc}$, $\vec{p}_{1,out}$ and $\vec{p}_{2,out}$).

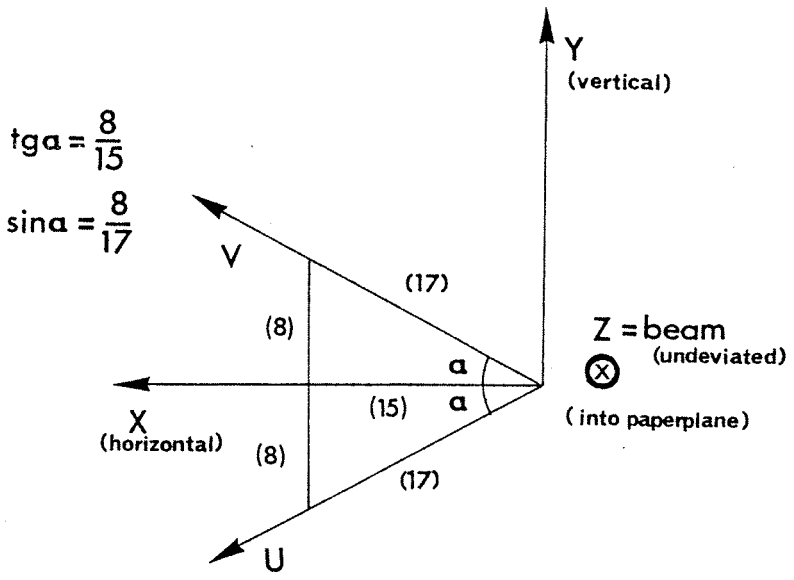

Fig. 1.3

Definition of the coordinate axes in WA7. In the multi wire proportional chambers, all the wire planes are orthogonal to the z-axis. By definition the x-wires in such a sense wire plane are orthogonal to the x-axis, the y-wires to the y-axis etc.

Another important use of the beamhodoscopes is the monitoring of the beam intensity. The total number of particles which have been incident on the target is found by adding all 40 scalers which count the individual elements of one plane, N_{inc} in table 1.1.

Lastly the data acquisition deadtime is measured by means of two BH2 planes. While 40 scalers sitting on one plane are gated by the burst (thereby giving the total incoming flux, N_{inc} in table 1.1), another 40 scalers counting the 40 elements of a second plane, are livetime-gated. The livetime is the time during which our data acquisition

system was not busy. Therefore the sum of the counts of this second set of scalers will yield directly the integrated flux for which we are sensitive. In formula (1.1),
hence a deadtime correction has to be applied. This is done through the efficiency E_f where one of the factors is the relative livetime (≡ the ratio between livetimegated and burstgated beamhodoscope scalers).

The veto counters SP3 - 6, are only used in the fast decision making logic. They are scintillation counters and surround the beam. A firing in one of these counters in principle is incompatible with an elastic event in the hydrogen target. Hence such a firing is taken as a signature of an inelastic event which should be vetoed. More details about this in chapter 5.

The target as already mentioned, is fluid hydrogen, the only material exempted for neutrons. Its dimensions are $r \equiv \sqrt{x^2 + y^2} = 4$ cm and $z = 100$ cm. The location is inside the magnet aperture, see Figs. 1.2.a and b.

For the momentum determination of the outgoing reaction products, we used an Oerlikon W75 magnet. The setting of the beam line magnets defines p_{inc}, while BH1 and BH2 gives the direction $\vec{p}_{inc}/p_{inc}$. Downstream detectors are used to determine $\vec{p}_{1,out}$ and $\vec{p}_{2,out}$. This will be explained in the following.

Scintillation hodoscopes, in all 6, are used in the very fast selection of elastic event candidates. The hodoscopes are denoted H1R, H1W, H2R, H2W, PR1 and PR2 in Fig. 1.2.b. 'R' is short for ring and 'W' for wedge, both refer to the shape of the sensitive area of the individual elements (in xy-planes), see chapter 2. Electronics sitting on all individual hodoscope elements (H1R: 28 elements, H1W: 10 elements, H2R: 26, H2W: 10, PR1: 92 and PR2: 82) responds positively if 1), there are at least 6 coincident firings, at least one from each hodoscope and 2), the pattern of the fired elements is not incompatible with the kinematics of elastic events, (1), coplanarity of the three vectors, $\vec{p}_{inc}$, $\vec{p}_{1,out}$ and $\vec{p}_{2,out}$ and 2), correct opening angle, i.e., if one scattering angle is given, for instance between $\vec{p}_{inc}$ and $\vec{p}_{1,out}$, then the other, between $\vec{p}_{inc}$ and $\vec{p}_{2,out}$, is fixed). If an elastic event candidate is present, high spatial

resolution data from all the multi wire proportional chambers (MWPC's, CH1-CH6 in Fig. 1.2.b) will be recorded by the data acquisition system. For MWPC's, see chapt.3. Before the MWPC data are actually transferred to magnetic tape, the event is checked against the information from other detectors and additional constraints. These detectors are the cerenkovs, the calorimeter (both downstream of the target) and the beam line Cedar counters. The cerenkovs check that the particle identification does not disagree with an elastic event hypothesis. For example a coicident firing of C3 and C4 (see Fig. 1.2.b) would mean that the right arm contained a particle which could not have been an elastically recoiling proton. The cerenkov thresholds for protons were well above the maximum recoil momentum, $p_{2,out}$. Since we insisted on having the recoil particle in the right arm and the forward particle (the scattered beam particle), in the left arm (imposed by means of cerenkovs C1 and C2), a coincident C3 - C4 firing could be used to veto fake elastic events candidates. Cedars and cerenkovs will be discussed to some extent in chapter 6. The calorimeter checks the kinetic energy of the forward particle. Additional constraints were mentioned above. They consist of more sophisticated coplanarity checks based on the PR1 and PR2 firings and also of a multiplicity limitation. This last constraint is justified by the fact that in elastic scattering the number of outgoing particles is two, hence ideally the number of hodoscope elements that fire should be exactly 6 (3 in each arm). More about this in chapter 5.

I have explained the use of the downstream detectors in the on-line event selection electronics. As for the upstream detectors, the information from all downstream detectors: hodoscopes, MWPC's, cerenkovs and calorimeters, would be recorded on magnetic tape in case the on-line filtering responded positively. The recorded data were used off-line, those from the MWPC's to reconstruct the outgoing tracks, the other data to check the elastic event hypothesis. $\vec{p}_{1,out}$ and $\vec{p}_{2,out}$ were found using the geometry of the reconstructed event; the directions of the momenta are given by angles at the vertex (≡ best meeting point of the two or three tracts in the target), the absolute values for the momenta are proportional with the magnetic field strength B, and the track curvature ρ ($p = q \cdot \rho \cdot B$, where q is the charge).

C. References

1. High energy hadronic reactions at large transverse momenta and the CERN SPS experiment WA7.
Lars Bugge (Thesis, Institute of Physics, Univ. of Oslo, 1979).

2. Results from -20 GeV/c high-t analysis.
K. Brobakken et al. (ELAS 134, internal WA7-report, CERN 1980).

3. Results from +20 GeV/c high-t analysis.
K. Brobakken et al. (ELAS 135, internal WA7-report, CERN 1980).

4. Results from -30 GeV/c high-t analysis.
K. Brobakken et al. (ELAS 136, intetnal WA7-report, CERN 1980).

5. A large acceptance experiment at the CERN super proton synchrotron to study elastic and other 2-body hadronic interactions up to 100 GeV/c.
L. Bugge and T. Buran (Report 80 - 07, Institute of Physics, Univ. of Oslo).

6. Meson-proton large-angle elastic scattering at 20 and 30 GeV/c.
R. Almås et al. (Submitted to the EPS international conference on high-energy physics, Genova 27. June - 4. July 1979).

7. Large-angle elastic scattering of charged pions on protons at 20 and 30 GeV/c incident momenta.
R. Almås et al. (Physics Letters 93B (1980) 199).

8. Thesis by J. Tavernier, Annecy (LAPP), 1979.

9. The beam hodoscope (first aid guide).
M. Yvert (ELAS 100, internal WA7-report, CERN 1977).

CHAPTER 2

SCINTILLATION COUNTERS IN GENERAL AND IN WA7

A. Fundamentals of scintillation materials.

The subject of this chapter and related topics are discussed at lenght in refs. 1, 2 and 3. For what concerns section A, ref. 1 is particularly complete.

Many materials scintillate, which means that atoms and molecules in the material emit light upon deexcitation of excited electrons. This supposes excited electrons, often the deposition of external energy among the atoms and molecules may trigger excitations. In the following will be explained the source of this deposited energy in high energy physics, i.e., the electromagnetic interaction between a charged (elementary) particle and the medium it traverses. Scintillation detectors (or counters) are devices which are sensitive to the emitted light; hence they may be used to flag the passage of charged particles.

Only the electromagnetic energy loss is relevant for scintillation counters; the strong-interaction energy loss is disregarded. A charged particle traversing whatever material will loose energy through electromagnetic interactions. Several physical processes contribute, cerenkov radiation, bremsstrahlung and collisions with atomic nuclei and electrons. The loss to the atomic electrons (which are either excited or knocked free, ionization) is by far the most important process for all particles except electrons. Due to their very small mass, electrons with some energy will experience big energy losses through bremsstrahlung. For lead more than 50% is lost in such processes when $E_{electron}$ is greater than 7 MeV, the same figure is 340 MeV for hydrogen. The energy loss of electrons in matter won't be discussed here, see for example 'High Energy Particles' by B. Rossi, ref. 4.

For all other particles, the mean differential ionization energy loss (= the mean differential electromagnetic energy loss) per length, x, and per density, ρ, is given by,

$$-\frac{dE}{d(x\rho)} = 0.6\,\frac{Zz^2}{A}\,\frac{m_e c^2}{\beta^2}\left(\ln\frac{2m_e c^2\beta^2}{(1-\beta^2)\,I(Z)} - \beta^2 - \delta - U\right) \qquad (2.1)$$

where 0.6 is a constant with dimension $cm^2\ g^{-1}$; ρ, Z, A and I(Z) are respectively the density (in $g\ cm^{-3}$), the charge number, the mass number and the average ionization potential for the stopping material; z and β, the charge (in units of e, the elementary charge) and the relativistic velocity (= v/c) of the incoming particle, m_e, the electron mass and finally, δ and U, correction terms which are effective for the very low and high values of β. Notice that $dE/(x\rho)$

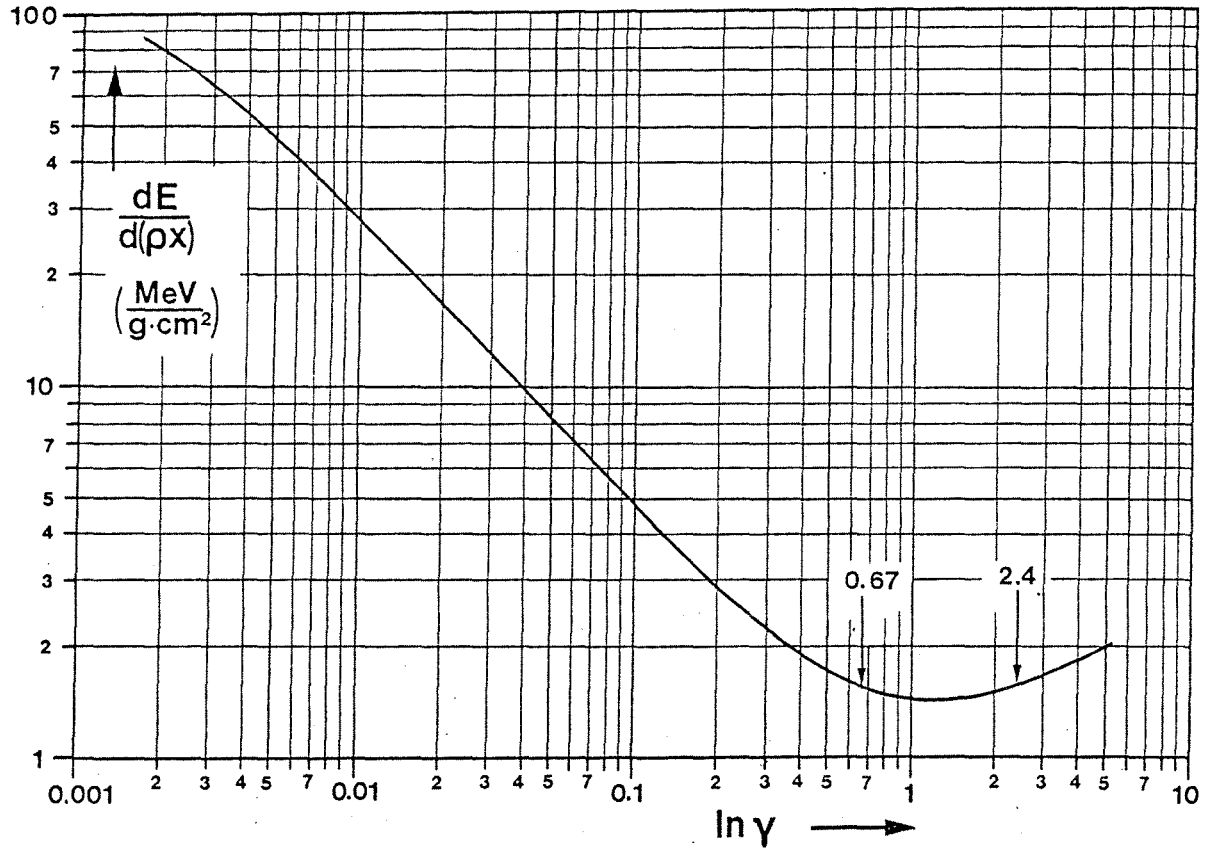

Fig. 2.1

The differential electromagnetic energy loss for unit charged particles as a function of $\ln\gamma$, where $\gamma = (1 - \beta^2)^{-\frac{1}{2}}$. Stopping material, Cu.

only depends on β, z^2 and the material. For unit charged particles traversing the same material $dE/(x\rho)$ only depends on β. In Fig. 2.1 is shown the behaviour of this function when the stopping material is copper. Along the abscissa is $\ln\gamma$ where $\gamma = (1 - \beta^2)^{-\frac{1}{2}}$. Remember that $E_{total} = m\gamma$, so that the energy loss can easily be had for all

unit charge particles from Fig. 2.1. For, for instance protons with $m_p = 0.938$ Gev/c^2, the range covered corresponds to a kinetic energy of the proton between 2 MeV and 100 GeV ($E_{kin} = E_{tot} - m_p$). Also indicated is the region of minimum energy loss; for $0.67 < \ln\gamma < 2.4$, $dE/(x\rho)$ varies les than ±5%. For protons this corresponds to $0.9 < E_{kin} < 9$ GeV. Particles with β in the vicinity of β_{min} (≈ 0.97), are called minimum ionizing. The $-\beta^2$ term in (2.1) is responsible for the fast decrease in $dE/(x\rho)$ while the logarithmic term brings about the small increase above $\ln = 1.22$, called the relativistic rise since it is an relativistic effect.

Another important quantity when working with scintillation counters, is the fluctuations in the energy loss. Since the loss is due to collisions between the incident particle and the atomic electrons, it is a statistical process. The exact loss will depend on the number of collisions and also on the loss in each collision, the more violent the collision the more energy is transferred. The relative fluctuations, $\delta\Delta E/\Delta E_p$ ($\delta\Delta E$ is the full width at half maximum of the distribution of the energy loss, ΔE; ΔE_p is the most probably energy loss, see Fig. 2.2.a), naturally will decrease with an increasing mean number of collisions. Therefore $\delta\Delta E/\Delta E_p$ depends on β, on the density ρ, and the thickness x, of the stopping material. Fig. 2.2.a and b show respectively a calculated energy loss spectrum[2] and measured fluctuations as a function of the reduced thickness ρx, and the velocity β, for organic scintillator materials[3].

Now the mechanism of scintillation will be briefly reviewed. Many materials scintillate; examples of scintillation crystals are NaI and CsI, some crystalline hydrocarbons (e.g., anthracene and stilbene) as well as some special plastic materials also scintillate. Terphenyl and diphenyloxazole are examples of scintillating plastics, they are made up of complex molecules, the main atomic constituents being carbon and hydrogen.

The light emission comes from the deexcitation of these complex molecules which have been excited during the passage of the charged particle with its accompanying shower of δ-electrons. The crucial point in applications is then to be able to transport the light with acceptable losses to a photomultiplier, PM, which can

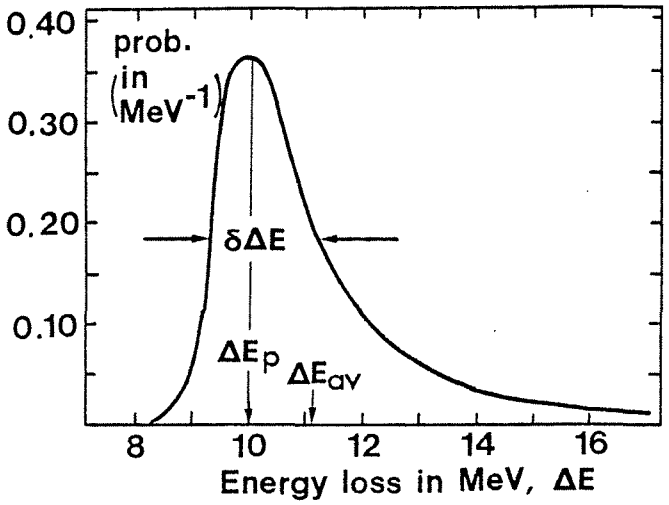

Fig. 2.2.a

Spectrum of a calculated energy loss from ref. 2. The incident particles are 3 GeV's protons. The stopping material is 6.97 g/cm^2 of Be. The most probable energy loss is ΔE_p, the mean energy loss, ΔE_{av}, and the full width at half maximum, $\delta\Delta E$.

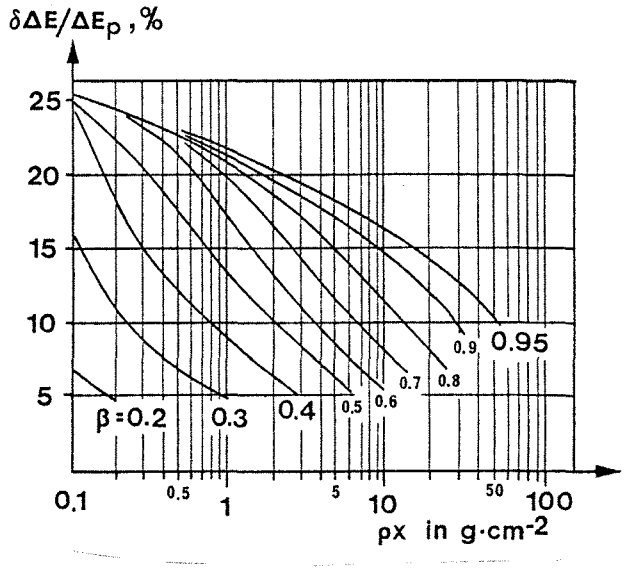

Fig. 2.2.b

Relative fluctuations in the energy loss for organic scintillator materials as a function of the reduced thickness ρx. $\delta\Delta E/\Delta E_p$ is given for several values of β. Results from ref. 3.

convert the light pulse into an electric pulse. Equally very important, the time resolution of the scintillation-, or more correctly, the fluorescence-process; one should be able to determine the time of an event as precisely as possible. Flourescence refers to the complete process of excitation with the resulting light emittance; scintillation, only to the last part of the process. Practical considerations (cost, handling and machining difficulties, etc.) together with transportability and time resolution requirements, prohibit using 'pure scintillation' materials as the stopping material in big counter setups (like for ex. the H12-hodoscopes in WA7 (H12 = H1R + H2R + H1W + H2W, see Fig. 1.2.b)). Often the problem of big and cheap scintillators which also are pure, is the high self absorption of the fluorescence light. Since the absorption increases a lot with the dimensions of the sensitive area of detection, the use of such scintillators is not very interesting. On the other hand, the pure,

but expensive scintillators, mostly are excellent light transporters. Apart from the cost, many of these scintillators have the disadvantage of a slow fluorescence response which again means bad time resolution. The problem of an adequate scintillator material has been solved by doping a solvent with a solute; the first acting as an absorber of most of the primary energy loss left by the incident particle, the second acting as the real scintillator. Roughly this happens, the solvent molecules are excited and deexcite, some of the resulting freed energy is transferred to the solute molecules both by radiative and non-radiative processes. The transferred energy will trigger a fluorescence process among the solute molecules, the wavelengths of this light spectrum naturally is red-shifted relative to the light emitted by the solvent (red-shifted means longer wavelengths, hence lower energy for the light quanta). The red shifting reduces very much the probability of the solute fluorescence light being absorbed by the solvent, in other words the solvent is transparent to this light. Typically the solute concentration is some percent, and therefore the self absorption in this medium will be small. The technique of doping has made possible to increase drastically the transportability of scintillation light. For the Nuclear Enterprise 110 material (NE 110), used in the WA7 H12 and PR1/PR2-hodoscopes, the attenuation length (≡ the distance the light has to go before its intensity is reduced to 1/e) is 2 - 3 meter (somewhat dependent on the wavelenght). In some of the newer calorimeter planes (see chapter 4F), another material was used, so-called plexipop (attenuation length, 1.5 to 2 m). The light yields differ by a factor ≈3, NE 110 emitting the most, while the decay constant (≡ time before the intensity of the emitted light drops to 1/e) is roughly 4 ns for both materials. One may describe the emitted light intensity by an exponential fuction of t. The onset of the emission is very fast (< 1 ns) after which it falls off exponentially. There is also a slow fluorescence component which falls off over a period of several microseconds. This component will not be considered here.

Scintillation counters are very convenient, they can be machined to many shapes and may cover large surfaces. One talks about the active or sensitive area of a counter, this is where scintillation

may be produced. Often the geometry is such that complicated light guide systems has to be used so that the light can be transported to the PM. The PM is crucial for the efficiency of the scintillation counter, it will be studied in some detail in the next section.

B. Fundamentals of the PM and its power supply.

Both for details and general aspects about designs, performances and operation specifications, the reader is referred to excellent PM-producers handbooks (see for instance the documentation from EMI, Philips or RCA).

The photomultiplier (PM) converts the light pulse into an electric signal. The basic conversion takes place at the photocathode; through the photoelectric effect the incident photons produce photoelectrons. The rest of the PM amplifies the small electric pulse produced at the cathode.

I shall go through the main considerations for the design of a photomultipier. This should bear out that the PM is a complex eye capable of seeing very small light glimpses.

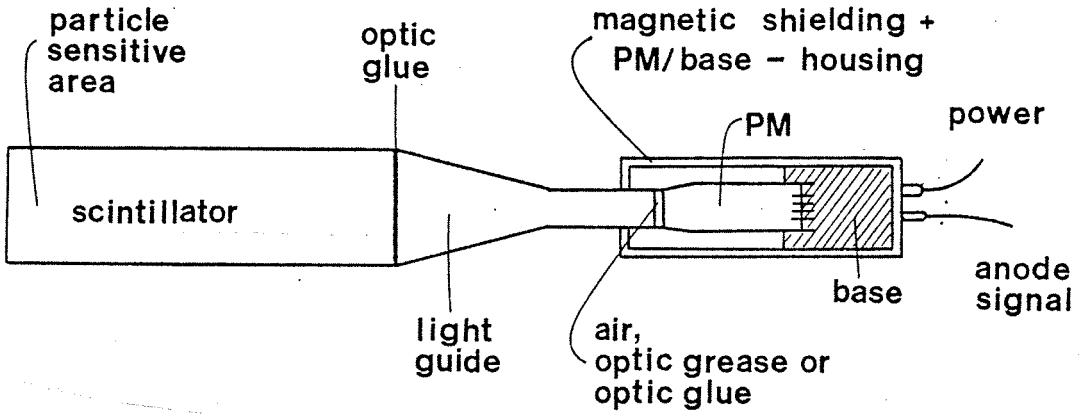

Fig. 2.3.a

Principles of a scintillation counter assembly. The sensitive area often is rectangular. Both the scintillator and the light guide surfaces should be reflecting, most currently used are aluminum foils. The complete ensemble must be light tight, therefore the aluminum foils commonly are kept in place by black adhesive tape.

The conversion and multiplication process should take place in vacuum. Hence the necessity of a photocathode window. This should have optimal transparancy for the scintillation light.

Having traversed the window, the photons strike the photocathode. This is the most difficult part of the PM to optimize. In Fig. 2.3.b have been shown a semi-transparant cathode, this means that the elec-

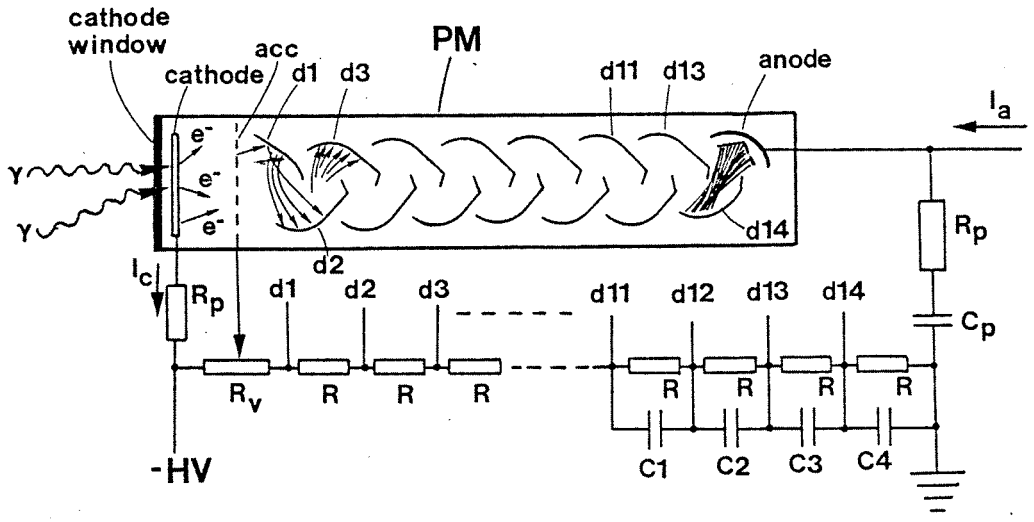

Fig. 2.3.b

PM and base ensemble. 'acc' is short for accelrating grid and 'd' for dynode. I_c and I_a are respectively the cathode and anode current. The R_p's and C_p are protective components. R_V allows varying the inter cathode/d1 voltage drop. The C1 - C4 capacitors serve as electron reservoirs in case of high peak currents through the PM-tube.

trons are emitted from the opposite side of where the photons are incident. The optimization concerns the quantum efficiency ($\varepsilon_q(\lambda) \equiv$ the probability that a photon of wavelength λ, triggers the emittance of an electron) in the first place. The quantum efficiency naturally should be matched as much as possible to the wavelenght spectrum of the scintillation photons. ε_q depends on the converter material, and for semi-transparant cathodes, also on the thickness of the converting material.

Several materials are used, for example, what is called the bi-alkali (made up of K, Cs and Sb); also cesium-antimony (Cs Sb) is a satisfactory converter, and recently rubidium-cesium-antimony (Rb Cs Sb) cathodes have been developed.

Two other interdependent parameters have to be optimized for the cathode, the noise level and the linerarity of the cathode current, I_c, see Fig. 2.3.b. In general when the dc cathode current is too big, I_c (which is an ac-current) will no more be proportional with the incident light flux. This is due to inefficiency in the transmission of photoelectrons to the first dynode (see again Fig. 2.3.b). For full

linearity the PM should be operated in a saturated mode, that is, 100% collection efficiency at the first dynode should be ensured. This may be obtained by good focussing and sufficient field gradients (through an adequate voltage drop) between the cathode and the first dynode. However, this influences negatively the second important parameter which is the cathode noise level.

PM's may be made sensitive enough to detect single photoelectrons. In this case, to keep the noise/signal ratio down, the spontanuous emission of one photoeletron from the photocathode (which is the most important contribution to the noise), must be kept as low as possible. Apart from the mentioned cathode/first dynode voltage drop, also the photocathode material and the operating temperature play important roles for the noise level.

Here it is natural to introduce some ideas of the power supply for the PM, i.e., the base. Normally the cathode is at negative high voltage as shown in Fig. 2.3.b, typically this high voltage ranges from -1.2 to -2.5 kV. Except for the inter cathode/first dynode and sometimes last dynode/anode voltage drops, all voltage drops in the dynode chain are the same. Between the cathode and the first dynode there are focussing electrodes which guide the electrons, in addition the gradient may be controlled by an accelerating grid, see Fig. 2.3.b. For the same reason of maintaining the linearity, the inter last dynode/anode voltage drop often may also be controlled. Notice that the anode is at ground, the load which the anode pulse see, very often is a 50 Ω coaxial cable.

The multiplication process takes place in the dynode chain, the principle being that one electron incident on a dynode will trigger the release of more than one electron which, due to the repelling negative electrostatic forces, are accelerated to the next dynode in the chain, etc.

For the dynodes as well, several considerations influence the optimization. The design should be for the best focussing of the emitted electrons onto the next dynode in the chain. The dynode yield, δ, (= the mean number of electrons emitted per incident electron) depends on the voltage applied to the dynodes. For the PM to have high sensitivity, the dynode material should be chosen for maximal

δ (at fixed voltage). Often, however, at the same time one wants linearity for the highest possible pulses going through the chain (that is, all the incident electrons N_i, should each, in the mean, trigger δ electrons out, even for high values of N_i). Also for the dynodes should noise be considered (although of smaller importance than for the cathodé), the spontanuous release of dynode electrons should be kept low. Again the optimization is necessarily a compromise; a material which give little noise (e.g. the bialkalis) and which have a high δ, cannot be operated linearly when the incident current is too high (i.e., N_i above, RCA gives a maximum value of 100 μA per cm^2 for the bialkali dynodes); on the contrary, dynodes made of Cu Be O will support high rates, but has a higher spontanuous emission of electrons.

Actually for Cu Be O - dynodes the linearity will not be limited by the material. In this case what is called space charge effects, between the dynodes will be decisive. To some extent this effect may be compensated for; 1), by the insertion of electron reservoirs between the last dynode stages and 2), by simply increasing the interstage voltage drops. See fig. 2.3.b, the capacitors C1 - C4 will maintain the nominal voltage between successive dynodes even when space charges build up. The capacitors have a second function which is independent of the space charge effects. Generally it is interesting to keep the current through the resistor chain as low as possible, however, this is incompatible with the same chain operating linearly even for the highest pulses. The capacitors solve the problem, acting as electron rservoirs so that also the biggest pulses are amplified linearly.

Two more considerations should be mentioned. The linearity of the PM is not only related to the peak currents, but also to the average dc-current. With an optimized base, our PM's in the calorimeter, the Philips XP 2232B tubes, can produce linearly peak anode currents of 250 mA. However, the maximum anode current to be drawn continuously without degrading the linearity, is only 0.2 mA. The value of δ increases with the applied high voltage. For a given cathode incident light flux, both the ac and dc current will therefore only depend on the voltage. Given a scintillation counter, the

particle flux it sees will define an upper limit for the high voltage, HV_{max}, above which all signals will be amplified nonlinearly. HV_{max} in turn defines a maximum signal I_{max} which the PM can produce at the anode. Ideally $I_{max} > I_{all\ signals}$, however, for high particle fluxes through a counter this very often is not the situation and some nonlinearity for the highest pulses has to be accepted.

The last important point is concerned with timing. The time resolution of the scintillator counter depends on the rise time of the anode signal, defined as the time it takes for the pulse to increase from 10% to 90% of its peak amplitude. The resolution worsens with longer rise times, this is a consequence of using a voltage threshold to define the time; since the rise time is amplitude independent, small pulses will trigger later than the bigger pulses. There is also a pure PM contribution to the resolution, namely the jitter in transit time. Typical anode rise times may range from 2 to 20 ns, and the transit times from 20 to 100 ns. The PM time characteristics are mainly determined by the dynode configuration and the applied high voltage.

Still other considerations have to be made before choosing a PM. For example, the environment (temperature and magnetic fields) will influence the PM performances, also the lifetime should be thought of, and finally, the geometry of the PM and the light guide should be matched. These topics will not be treated here.

From what has been said it should be clear that the choice of PM will depend entirely on the applications,

1) How small signals does one want to detect, the ones corresponding to 1 photoelectron or 100?

2) What linear range is needed. None? 5 - 500 photoelectrons out from the cathode? etc.

3) What will be the maximum expected anodic dc-current? This depends on 1) and 2) (through the HV-settings).

4) What time resolution is needed? What is the upper limit for the an acceptable transit time?

5) Enviromental considerations, temperature, magnetic fields, electronic noise; lifetime; geometry.

C. Fluctuations in the response from the scintillation counter.

From section A and B one will understand that before a signal is output at the anode, it has developed through several statistical processes.

1) The ionization loss in the scintillator fluctuates. See Fig. 2.2.a.

2) For a given energy loss there will be fluctuations in the number of fluorescence photons. This most often is very small. To see this let us calculate the mean number of photons, N_p, produced by a relativistic particle (= a minimum ionizing particle, see Fig. 2.1), traversing 1 cm of scintillator. Using (2.1) one finds the mean enrgy loss to be ≈ 2 MeV. Typically 2.5% (NE 110) of this energy is actually dissipated as light (the major fraction of the kinetic energy of the δ-electrons is deposited as heat in the scintillator). The wavelength of the emitted light ≈ 400 nm which corresponds to an energy of 3 eV. Hence N_p and the relative fluctuations in N_p may easily be found,

$$N_p = 0.025 \times (2\,\text{MeV}/3\,\text{eV}) = 1.6 \times 10^4 \quad \text{and}$$
$$\sigma_{N_p,R} = \sqrt{N_p}/N_p = 0.08\%$$

3) For a given number of fluorescence photons there are fluctuations in the number of photons which reach the photocathode. This is due to:

   a) The statistical nature of the process of absorption when the light travels through the scintillator.

   b) The dimensions of the scintillator plus the spread in space of the incident particles imply varying pathlengths for the light to the photocathode. Whence fluctuations in the amount of absorbed light.

4) For a given number of photons incident on the photocathode, the number of emitted photoelectrons fluctuates according to poisson statistics.

5) For a given number of photoelectrons from the cathode, the number of electrons produced by the first dynode also fluctuates according to poisson statistics.

6) Idem for the all the successive dynode-stages.

Notice that all processes except 3b) is of a statistical nature. The '1)-fluctuations' may be reduced by increasing the scintillator thickness. This quantity will have to be a compromise between the amount of light wanted at the photocathode and the probability of loosing the traversing particle due to an inelastic collision with a scintillator nucleus (the probability of an interaction $\approx$1.5% per cm of scintillator material).

2) fluctuations will depend on the scintillator material, some materials convert a larger fraction of the deposited energy into light than others.

3a) depends on the transparancy of the scintillator, the lightguide, the joints between scintillator and lightguide and between lightguide and the PM and finally on the transparancy of the cathode window, see Fig. 2.3.a. Also 3a) depends on the inner reflectivity of the scintillator and light guide surfaces. These are most often covered by aluminum foils which again is kept tight to the surfaces by black adhesive tape (to ensure lightproof counters). It should be noted that also the design of the lightguides plays an important role in minimizing the losses due to reflections.

3b) will depend both on the dimensions of the scintillator and on the dispersion of the incident particles. Obviously if the geometry is given, point 3) fluctuations can be reduced only by acting on all factors which contribute in the attenuation of the light.

The photocathode quantum efficiency determines the statistical fluctuations on the cathode (remember that the incident light flux, in watt, is assumed constant). Often this is the most important contribution to the overall fluctuation.

4), 5), and 6) will depend on the choice of PM while 5) and 6) also depend on how it is operated (in particular, the applied high voltage).

The combined effect of all the fluctuations may be measured as the width of the q_a-distribution, q_a being the measured charge of the anode pulse. An example of this is shown in Figs. 4.20 and 4.21. Here the relative width of the distribution will be a measure for how good the counter is (consisting of scintillator, lightguide, PM and line from anode to receiver module in control room, 25 meter of coaxial signal cable for H12 counters in the WA7 experiment).

D. Description of the WA7 scintillation hodoscopes (H1R, H1W, H2R, H2W, PR1 and PR2, or H12 and PR12).

The 6 different hodoscopes are shown in Figs. 2.4 - 5. Their location in the general setup is shown in Fig. 1.2.b. The dimensions

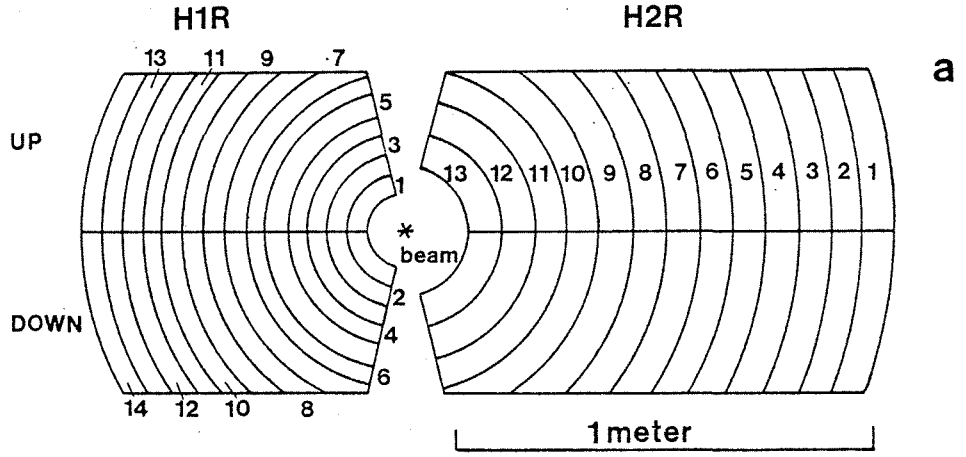

Fig. 2.4.a

The ring shaped H1R and H2R hodoscopes viewed from the target. The ring elements in both hodoscopes are split in one UP and one Down element. The readout sits respectively on the top and the bottom side of the scintillators. Along x the widths are 5 and 8 cm respectively, for H1R and H2R.

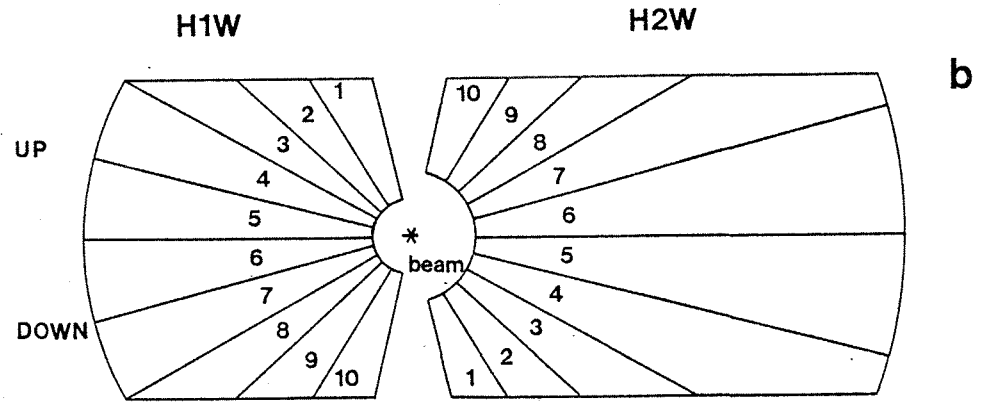

Fig. 2.4.b

The wedge shaped H1W and H2W hodoscopes viewed from the target. Each wedge element covers 15° in φ, the azimuth angle in the xy-plane.

of the elements may be read from Figs. 2.4 - 5; each element in H1W and H2W covers 15° in φ, the widths of the ring shaped elements are

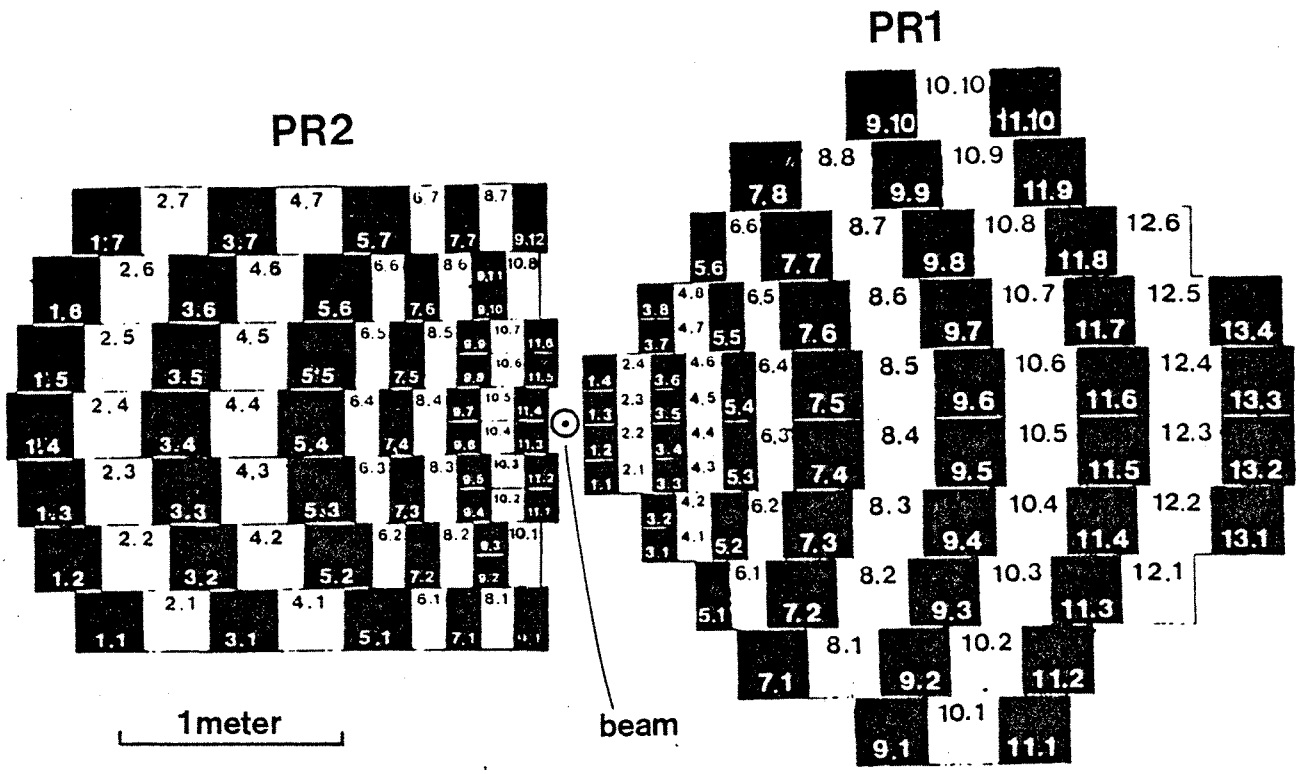

Fig. 2.5

The PR1 and PR2 hodoscopes viewed towards the target. Notice that the square and rectangular elements are arranged in rings, the first digit in the element refers to the ring number (e.g., PR1R7 contains 8 elements).

respectively 5 and 8 cm for H1R and H2R. PR12 elements are either 30 × 30, 15 × 30 or 15 × 15 cm^2. The scintillator thicknesses are 1 cm for H12 and 4 cm for PR12, and both are equipped with the Nuclear Enterprise material, NE 110.

The 4 cm thickness of PR12 elements is necessary due to the rather inefficient light collection system. The poor light collection was the price one had to pay for a good time resolution. For details see ref. 4. The basic idea was that one PM sees the whole sensitive area at an angle of roughly 90^{o} from the downstream side of the scintillator, hence the jitter arising from varying pathlengths to the cathode will be very small.

The readout of the scintillators are performed by Philips PM's, mostly 56 AVP's, in addition, some Philips XP 2020's are used on PR12,

on those counters which see the highest particle fluxes (i.e., those closest to the beam). The power supplies (bases for the PM's plus the base drivers) won't be described here. The high voltages were set manually, the voltage delivered to the base resistor chain could be monitored precisely. In chapter 4A is described the power supply for the calorimeter planes, this is identical with the H12 power supply, but not the same as the one used for PR12.

E. Incorporation and use of H12 and PR12 in the data acquisition system.

All 6 hodoscopes participate in the generation of a fast strobe, see Fig. 5.3. The shapes of the elements were designed so that the kinematics constraints of elastic events could easily be implemented. The H1W and H2W naturally are used to impose coplanarity of the two outgoing tracks with the incident beam track. H1R and H2R are correlated with each other in such a way that if one ring fires in H1R (the logic OR, see chapter 5A, of one element UP and one DOWN, see Figs. 2.4.a and 2.7), then at least one among some consecutive rings in H2R should fire in coincidence (at the same time). Otherwise the event cannot be elastic. The rings in H2R which are correlated with one certain ring in H1R, are again defined by the kinematics of elastic events in our setup. Naturally also the geometrical acceptance of the apparatus, set by the physical size of the apparatus and the bending of the magnetic field, have to be taken into account when determining the correlations. In the same way half rings in PR1 are

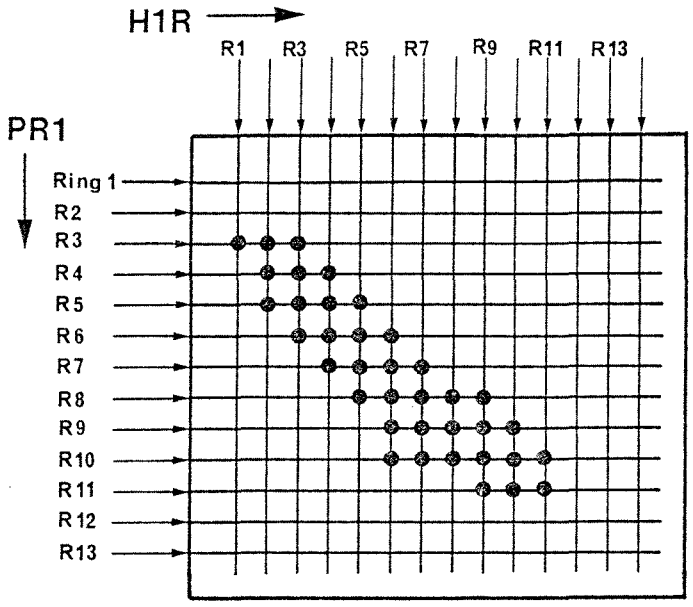

Fig. 2.6.a

Layout of the fast matrix between H1R and PR1 which defines straight lines from the target through the two hodoscopes in the left arm. Intersections covered with •, correspond to enabled nodes, see Fig. b. The enabled pattern is the actual setting which was used when running elastic scattering at -30 GeV/c.

Fig. 2.6.b

Buildup of one node and the matrix output, see Fig. 2.6.a. There are 14×13 inputs to the general OR, the output of which is the matrix response. The enabling/disabling is done by computer.

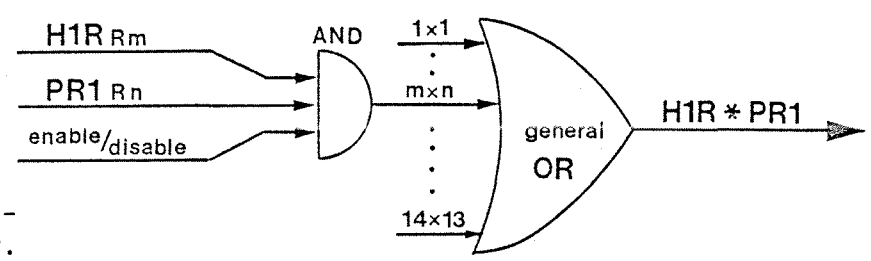

correlated with half rings in PR2 (a half ring in PR12 is an OR between several elements, see Figs. 2.5 and 2.7). This is both an opening angle and a coplanarity constraint. H1R is also correlated with PR1; a coincidence between one ring in H1R and some rings in PR1 is demanded, see Fig. 2.6.a. The same applies to the recoil arm. Both hodoscopes in each arm should fire elements on roughly straight lines through the target, the bending of elastically scattered particles is small. These two matrices are the H1R * PR1 and the H2R * PR2.

In Fig. 2.6 is shown the principles of a fast matrix, in this case the H1R * PR1. For details about the functioning and drawing conventions for logic modules see chapter 5A. Except PR1 * PR2, all the matrices are identical with the H1R * PR1-matrix. But naturally they are programmed differently. In spite of its different design, the PR1 * PR2-matrix logically is identical with the other matrices. In Fig. 2.7 is shown the logic which defines all the inputs to the matrices. The fast matrix outputs are used in the fast decision making logic as shown in Fig. 5.3.

The hodoscopes are also used in the decision making at a later stage, i.e., in the event logic. H12 and PR12 are used to check the multiplicity of an reaction, that is, by simply counting the number of elements that have fired (in coincidence), one will find a number which is related to the number of outgoing particles. A maximum number of allowed firings is therefore imposed above which the event is vetoed. To operate this veto is tricky, as we shall see in chapter 5B. PR12 is used for an additional purpose. By correlating single elements in the two hodoscopes (instead of half rings) stricter kinematical constraints (on opening angle and coplanarity) are imposed. These correlation matrices are called the slow matrices.

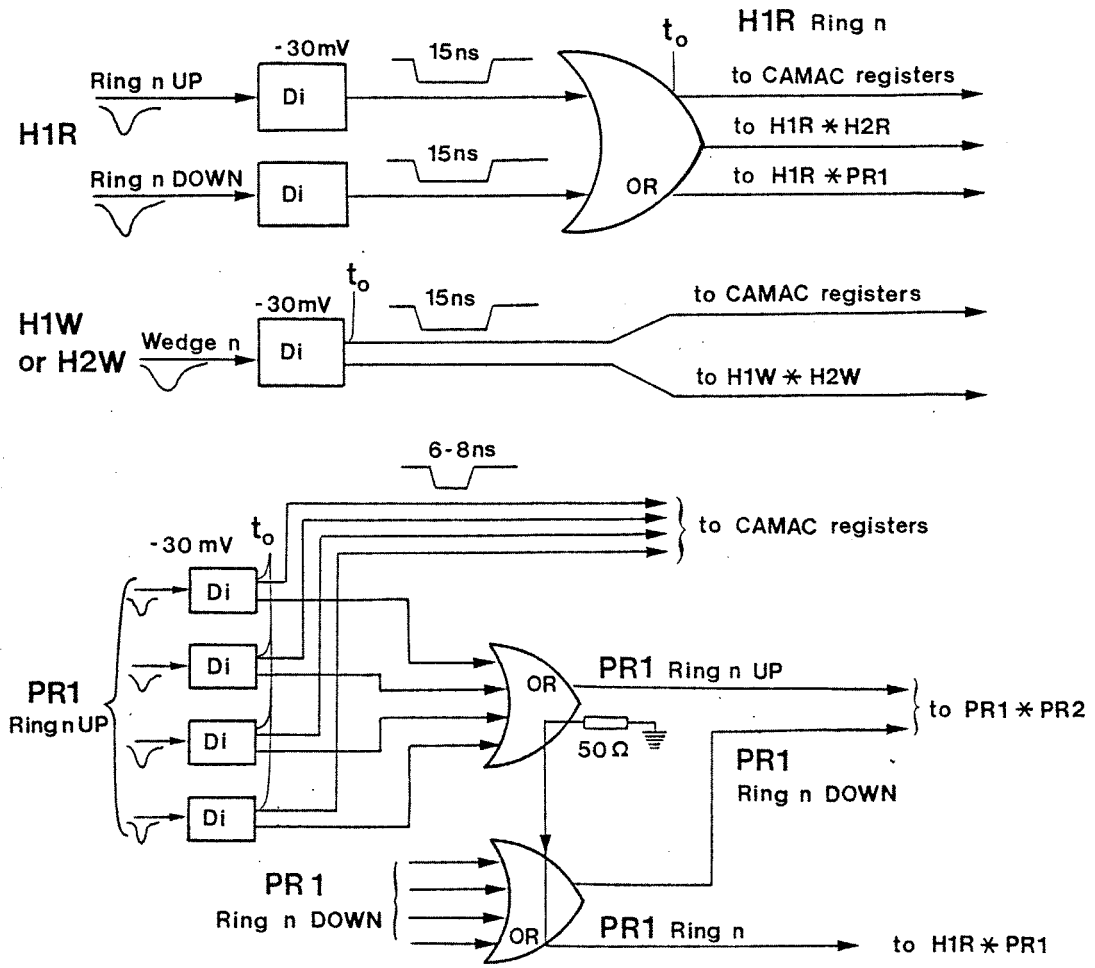

Fig. 2.7

Logic producing the matrix inputs starting with the analog signals from the PM's. The logic for H2R is equivalent to the one for H1R except that one of the OR-outputs go to the H2R * PR2-matrix (instead of to H1R * PR1). H2W-signals are treated in the same way as the H1W-signals. For PR2 the setup is equivalent with the PR1-setup; PR2 ring (number) m Down and Up separately go to PR1 * PR2 while PR2 Ring m goes to H2R * PR2. The widths of the discriminated pulses and the typical voltage threshold which the analog signals see, are given. On each line to CAMAC bit registers there is a 100 ns delay.

F. Setting up the counters, high voltage settings and timing.

All counters in H12 and PR12 were used to flag the passage of relativistic particles; that is, only a yes/no answer was demanded. As we shall see in chapter 4E, this is much simpler than when one wants to make use of the analog information conveyed by the signal.

The settings of the high voltages therefore should be for maximum efficiency (practically 100%) and minimum noise. Both increase with the voltage. Fig. 4.20 bears out the important points. The second peak corresponds to the true particle signals. Those should all be well above the discriminator imposed threshold (seen in Fig. 4.20 as the sharp cutoff to the left). The more the right peak is shifted to the right (by increasing the PM high voltage), the more the noise moves above the discriminator threshold and will be accepted in the logic of Fig. 2.7.

At least three methods may be used to set high voltages.

1) By an oscilloscope. The PM pulses are simply looked at on the screen of this instrument. It should be triggered properly, i.e., by a signal which, if coincident with the signal under consideration, will be a signature of a relativistic particle having traversed our counter. Knowing the voltage calibration of the oscilloscope, one should then adjust the PM high voltages so that all the relativistic particle signals will lie well above the known discriminator threshold. This method was first used when setting the voltages of our 6 hodoscopes.

2) By measurement of the rate of a coincidence relative to the rate of a reference counter as a function of the voltage, see Fig. 2.8. The efficiency of a counter will increase with the voltage as long as some of particle signals produced at the anode have amplitudes below the voltage threshold defined by a discriminator. Let '1' be the reference counter (for ex. a counter in PR1) and '2', the counter to be adjusted (say a counter in H1). For a given configuration of the apparatus and with the whole beam incident on the target (so that all the outgoing particles come from the target), a constant beam intensity independent

fraction of the particles which traverse one counter, will also traverse the other counter. Hence by measuring the ratio between the rates, R(1 * 2) and R(1), as a function of the high voltage on counter 2, one will observe a curve like the one shown in Fig. 2.8. At the plateau the counter 2 efficiency is ≈ 100%.

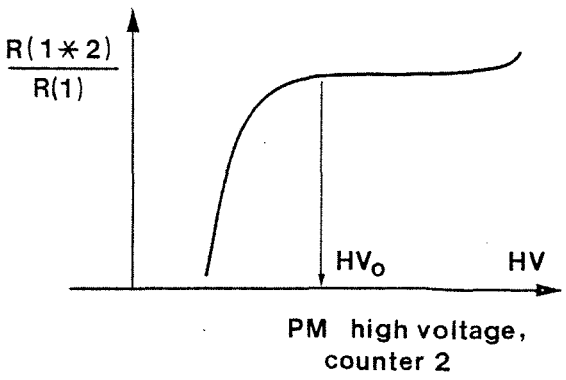

Fig. 2.8

Efficiency curve for counter 2 as a function of the high voltage (HV) applied to its PM. R(1 * 2)/R(1) is proportional with the efficiency, at the plateau (HV > HV$_o$), eff ≈ 100%.

Notice that this measurement does not depend on the effiency of counter 1. However, it is time consuming and was not used to set our voltages. One reason that the adjustments take long come from the fact that the timing of the coincidence between '1' and '2' changes with the voltage on '2', the higher the voltage, the earlier will the PM2-pulses arrive. Hence the timing between '1' and '2' should be checked at each voltage.

3) This method makes use of the charge spectrum of the PM anode pulses. A description of how such a spectrum is obtained, may be found in chapter 4E. The idea is that the anode pulses which the minimum ionizing particles produce, should be fully distributed above the voltage threshold. In Fig. 4.20 is clearly shown the cutoff corresponding to -50 mV. This method also have the problem of triggering, i.e., selecting for analysis (namely the integration of I_a, see Fig. 2.3.b) as efficiently as possible the pulses corresponding to minimum ionizing particles. Confer again Fig. 4.20, notice that it is actually an advantage with some noise. This helps define the threshold cut precisely. In Fig. 4.20 the whole minimum ionizing spectrum is well above the -50 mV threshold. To see this observe that the events in a bin in the dip are equally shared between noise and true signals, hence the spectrum for the latter extrapolates (with decreasing charge) to zero events per bin clearly above the threshold cut. This was the method employed for both H12 and PR12 high voltage settings.

The settings for H12 ranged from -1.3 to -1.8 kV, and the most probbable pulse amplitude (q_{max} in Fig. 4.21) varied between -100 and -500 mV with a 50 Ω load. The discriminator thresholds for most counters were -30 mV.

For PR12, adjusting was more difficult. This was due to the low light yield of these counters. An example of the worst minimum ionizing spectrum observed from one such element, is shown in Fig. 2.9. The problem was the bad noise/signal separation. Since the noise is a parameter only for the counter readout (PM + coaxial signal cable), the lower the light yield, the more the amplitudes of true signals approach the amplitudes of the noise signals. Hence a much larger fraction of the noise signals will be above the threshold, and judging whether the PM high voltage is sufficient to make all the true signals be above the threshold may be delicate, as in Fig. 2.9. The noise nearly completely hides the true signals. The high voltages on the PR12 elements ranged from -2.0 to -2.8 kV .

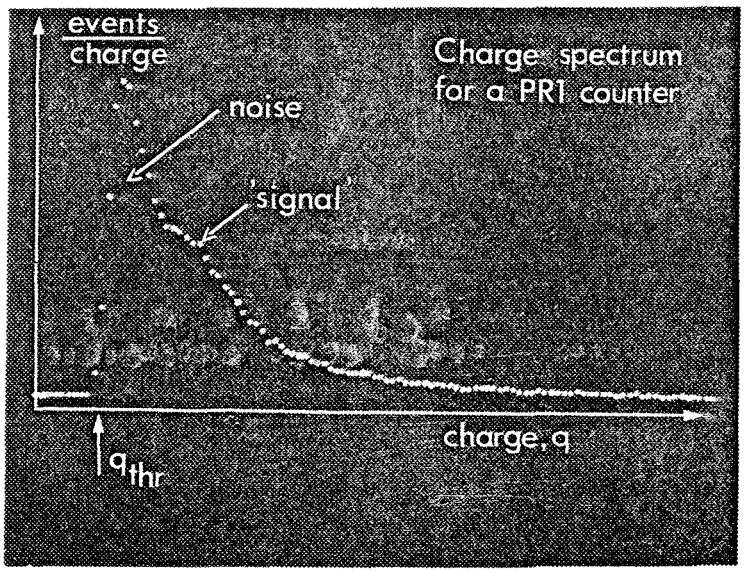

Fig. 2.9

Example of the worst charge spectrum from a PR1-counter. The sharp cutoff at q_{thr} corresponds to a discriminator threshold which imposes a lower limit on the amplitude of the pulses to be analysed. The true signals from minimum ionizing particles are seen as the small bump, the 'signal', on the approximately exponential noise fall-off.

Some words will be said about the timing of the signals in Fig. 2.7. When the incident momentum is as high as 20 or 30 GeV/c, a considerable fraction of the particles produced in the target are relativistic, $\beta \approx 1$. This is particularly true for the particles incident on the hodoscopes; a lot of the low momentum reaction products are swept outside the hodo-

scope acceptance by the magnetic field. The counter firings which result from the passage of a shower of relativistic particles all coming from the same vertex in the target, will be very well correlated timewise. The time delay between the primary interaction, at the vertex, and the arrival of the counter signal at the discriminator in the electronics control room, will only depend on the counter (its position relative to the vertex, its PM (transit time and high voltage) and the delay of the signal cable; and not on the momenta as long as $\beta \approx 1$). Hence the time delay between the arrival times in the control room of various physically correlated signals, is an apparatus constant which may be adjusted (through the addition/subtraction of cable delay).

Notice that when the PM high voltages were adjusted prior to the timing, this was because the timing depends on the high voltage.

I shall quickly go through the timing of the 'very fast elastic logic'. First all the t_o's in Fig. 2.7 were made to coincide. This was done by measuring the time delays of all individual counters relative to one reference counter (an element in PR1). The correct timing was then obtained by adjusting the cable lenghts according to the measured delays. Cable lengths in the logic of Fig. 2.7 were arranged for optimal timing at the matrix inputs (= maximum overlap between the input signals to the coincidence unit in Fig. 2.6.b, in particular was it important that the short PR12 signals (6 - 8 ns) should always be well inside (timewise) the longer H12 signals (15 ns) at the inputs of the H1R * PR1 and H2R * PR2 matrices). Also, with the timing adjusted as explained, the delay lines to the registers ensured that all H12-signals would be coincident there. This obviously was done so that the registers could be gated by one common gate for all the H12-counters. The same naturally applies to the PR12-elements although their register timing was slightly shifted relative to that of H12.

The second step in the timing was to center the PR1 * PR2, H1R * PR1 and H2R * PR2-matrices on the two other matrices (H1R * H2R and H1W * H2W) at the inputs of CU1, see Fig. 5.3. This ensures that the time of the fast strobe is defined by the PR12 hodoscope.

Essential when timing signals, is the actual measurement of time delays, how much one signal arrives before or after another. Some words

will be said about that.

Timing may also be done in at least three ways.

1) By use of an oscilloscope. One looks at the two pulses at the same time, the oscilloscope should be triggered by one of the two pulses or by an external pulse. This may be an ok and fast method when there are many coincidences and the signals don't jitter (timewise) too much relative to one another.

2) By making a delay curve. Maybe this is the best method. One counts two rates, R(1 * 2) and R(1), where '1' and '2' refer to two counters. The relative delay between the two counters is varied and the rates measured for each value of the delay. The ratio between R(1 * 2) and R(1) typically behaves like in Fig. 2.10. To get the highest coincidence rate (= the best timing) obviously, $t = t_o$. For the significance of the delay curve, see chapter 5B. As when going through the examples for how to set high voltages, also in this case should fluctuations in the particle fluxes affect the two counters likewise so that the ratio f, will be stable.

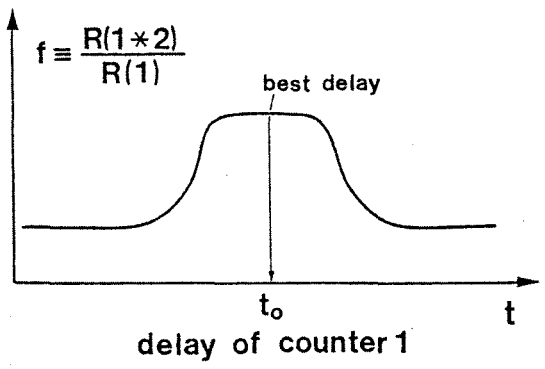

Fig. 2.10

Delay curve between counters 1 and 2. 'f' is the ratio of the coincidence rate (1 * 2) over the rate of either 1 or 2.

3) By use of the LeCroy L3001 multichannel analycer. When this TDC-device (Time to Digital Converter) is properly calibrated, the jitter-distribution between two signals (see for ex. Fig.5.6) may be obtained very quickly (> 10,000 conversions per second). If the two signals under consideration are of equal width, the peak of the jitter-distribution should be adjusted (by insertion of delay) on the time scale so that t_{peak} coincides with the

t-bin that is filled when two coincident signals are applied to the L3001 analycer. On the contrary, if the two signals are of unequal widths, one should compensate for the fact that this device establishes the jitter-distribution between the falling edges of the signals and not between the signal centers, see Fig. 2.11. The L3001 allows to measure either a Δt ($\equiv t_{stop} - t_{start}$) so that $0 < \Delta t < 1000$ ns with 1 ns resolution, or a Δt so that $0 < \Delta t < 100$ ns with 0.1 ns resolution, or finally, $0 < \Delta t < 250$ ns, resolution 0.25 ns. The L3001 was used for all final timings of hodoscope signals.

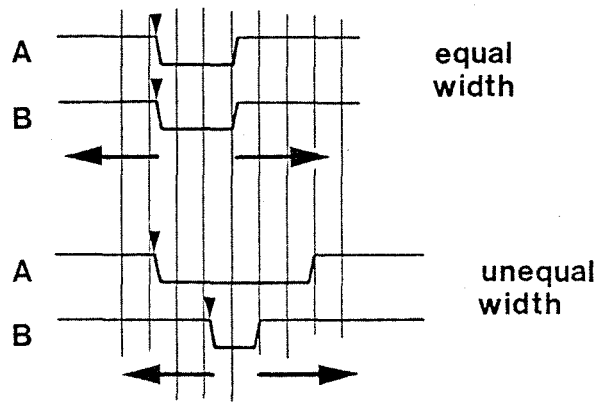

Fig. 2.11

Optimal timing when maximal overlap is wanted. Signal A is considered fixed while B fluctuates (jitters) according to the arrows to the left and the right relative to its mean positon. The L3001 triggers on the falling edges, marked with vertical arrows.

G. References

1. The theory and practice of Scintillation counting.
J.B. Birks (Pergamon Press, 1964).

2. Methods in experimental physics, Vol. 5, Part A, chapter 1.1.
R.M. Sternheimer.

3. Scintillation counters in high energy physics.
Yu. K. Akimov (Academic Press, New York and London 1965).

4. An air light-guide, plastic scintillator counter.
M. Poulet and A. Santroni (Nuclear Instruments and Methods 148 page 359, 1978).

CHAPTER 3

MULTIWIRE PROPORTIONAL CHAMBERS (MWPC) IN GENERAL AND IN WA7

A. General outline.

MWPC's are used to detect charged particles with good spacial resolution and time resolution (typically $\sigma_r = \pm 1$ mm and $\sigma_t = \pm 30$ ns). In addition, they may be operated at high incident fluxes. Less than 5% inefficiency have been measured for rates up to 10^5 s^{-1} mm^{-2} (1).

Like for scintillation counters, the output signal is based on the primary energy loss of the charged particle traversing the detector medium, in this case a gas mixture. The ionized electrons will,

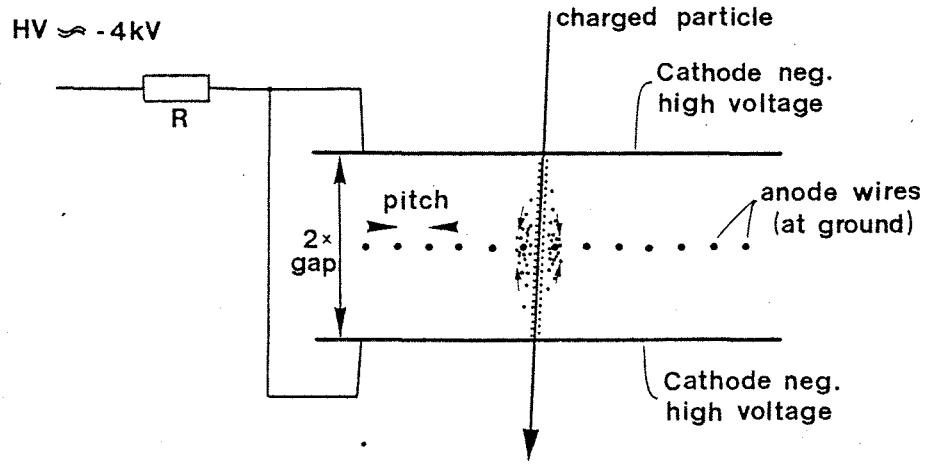

Fig. 3.1

Principles of detection in a MWPC. The electrons liberated along the particle trajectory are pushed by the electrostatic fields towards the anode wires. Very close to the sense wire(s) concerned, the drifting electrons experience a field gradient which is sufficient for producing an electron avalanche. The multiplication makes possible the detection of very small ionization losses.

due to the electric fields, drift towards the nearest collection point, namely one or more of the anode wires, see the figure. With the shown structure one can arrange the fields so that the electrons drift without causing any avalanche effects until they are very close to the anode (< 0.1 mm). Here, due to the very small anode wire diameter, a strong field builds up (≈ 50 kV/cm) which ensures the necessary multiplication of the electrons (avalanche effects), so that the collected charge on the anode wire will be sufficient for external detection.

Notice that the final shower is well localized. With our chamber parameters, which also are typical (2 mm pitch and 6 mm gap), for less than 10% of the events would the situation of Fig. 3.1 happen, i.e., that two neighbouring wires fire.

Although the principles for detection are simple, making a MWPC work is far from trivial. As for scintillation counters, the point is to get out as big a signal as possible without perturbing the operation of the detector. For example will the incident particle flux and the size of the output signal, be compromise parameters. Increasing the multiplication, that is, increasing the collected charge for a given primary ionization, will lower the flux at which the detector reaches for example 5% inefficiency. At the same time the multiplication must be sufficient so that the true signals will be well above the noise signals.

The multiplication factor can be acted upon by several means.

1) Decreasing the anode wire diameter. This leads to higher field gradients in the space just around the wire, hence stronger multiplication. The lower limit for the diameter is set by mechanics considerations. In the WA7 chambers, most wires were 20 µm. When such wires get long (in WA7 for chambers CH4, CH5 and CH6, > 2 m), simply handling them becomes very tricky. They are in general made of tungsten coated with gold, to reduce oxydizing and maintain high conductivity).

2) Acting on the cathode high voltage. Increasing it can be done as long as there is no danger of sparks. A true spark between the cathode and the anode will surely burn the anode wire concerned. If this happens, due to the resulting short circuit, the whole chamber is disabled until the broken wire is replaced. The cathodes should be considered as huge capacitors. With the dimensions of the anode wires it is clear that if the infinite resistance between the cathodes and the anode becomes finite through a spark, even for a very short time, then there is no chance of the anode performing such an energy transfer without melting. This possibility of sparks come from imperfections in the system, non-uniformity of the cathode surfaces as well as

in the mechanical stretches applied to the individual wires and in their positioning (both will contribute to the non-uniformities in the plane defined by the anode wires). Also dust and impurities in the chamber may cause spark breakdown.

3) A third way of influencing the multiplication is through the choice of the gas mixture. Optimizing this parameter is far from simple. As always the point is to minimize the noise/signal-ratio. For example should the emittance of electrons from the cathodes be kept as low as possible. One important contribution to this process is the photoelectric effect, photons produced by the drifting electrons strike the cathodes and sometimes electrons are released. Hence the gas mixture should be γ-quenching.

   Another important consideration is related to the lifetime of the chamber. As a result of the ionization, ions will be deposited on the electrodes, however, the amount and where, strongly depends on the gas type. For example will some gases produce a layer on the anodes, this leads to increased wire diameters and consequently the field gradients in the critical zone of avalanching will be reduced. Therefore, to maintain the same multiplication factor, the high voltage on the cathodes must be increased. This naturally is a disadvantage since the higher the voltage, the more one approaches the threshold for spark breakdown in the chamber.

An important part of an MWPC is the readout. Unlike for the PM's, the pulses which are collected at the anode wires are most often not suffiently amplified so that they may be transferred directly onto the delaylines (which lead to the electronics control room). Chamber pulses therefore are amplified at the end of the anode wires (physically, outside the chamber). The electronic amplification have two advantages, first, the multiplication in the chamber may be kept down (means that one can handle higher incident rates) and second, by use of the amplified signal and its inverted counterpart, one can reduce the noise pickup on the delay lines drastically. This is done at the receiver end (in the control room) by reinverting the inverted signal, and then adding it to the non-inverted signal. Since noise is picked up with

the same polarity on both lines (the one carrying the non-inverted plus the one carrying the inverted signal), when the linear adding is performed, only the noise contributions cancel.

I shall list the important parameters to be measured when putting an MWPC into operation.

1) The efficiency. The dependence on several variables should be determined: The applied high voltage, the voltage threshold which the analog signals see before they may be registered in the control room and the register gate width. This last pulse should be produced by an external trigger, for instance by a coincidence-signal from scintillator counters upstream and downstream of the chamber.

   In general the chamber high voltage should be set as low as possible compatible with ≈ zero inefficiency. This, at the same time, will set the upper limit for the incident particle intensity at which the chamber may be operated with near 100% efficiency. The effect of the high voltage setting on the behaviour of the efficiency versus the incident intensity, is discussed below under point 2).

   Having set the high voltage, the signal thresholds should be set at the maximum value for which the efficiency is near 100%. In this way the noise/signal - ratio will be the smallest possible.

   Also to reduce the noise; when the efficiency as a function of the gatewidth is known, the minimum allowed gatewidth may be determined. The width of the jitter distribution between the chamber signals and the gate (see for ex. Fig. 5.11.a), fixes the time resolution of the chamber, or simply the minimum gate width that may be used without loosing in efficiency. The jitter comes mainly from the varying time of drift, depending on where exactly relative to an anode wire that the particle passed.

2) The occupation time of the affected wire. This parameter is related to the deadtime and the efficiency of the chamber. Two effects enter.

   First, the internal blackout of the region where the multiplication takes place (intrinsic deadtime). This effect is localized

to some tenths of a millimeter along the anode wire concerned. Its duration may be some multiples of 10 μs. Both the duration and the extension (along the anode wire) depend on the mode of operation of the chamber, that is, on the avalanche multiplication factor which is imposed through the high voltage setting. Therefore the maximum rate with 90% efficiency, to be calculated below, depends on the high voltage. Using a blackout time of 20 μs and 0.2 mm for the extension of the hot spot along the wire, the rate per cm of wire, at which the efficiency drops to 90%, is calculated in chapter 4A. This rate is found to be $2.6 \times 10^5\ cm^{-1}s^{-1}$. With a 2 mm pitch, this corresponds to $1.3 \times 10^6\ cm^{-2}s^{-1}$. For some chambers in WA7 the sense wires were 2 m long, for these the 90% efficiency rate corresponds to $5.2 \times 10^7\ s^{-1}(2m)^{-1}$.

Evidently the electronics has to be fast to keep up with such a rate. In WA7, typical pulse durations (above threshold at the receiver end for the CH4, CH5 and CH6-chambers) were 200 - 400 ns. The occupation time increases quickly with the applied high voltage. Clearly the electronics deadtime was our rate limitation; with 400 ns deadtime per wire, the efficiency drops below 90% for rates exceeding $3.5 \times 10^5\ s^{-1}wire^{-1}$ (for the method of calculation, see again chapter 4A). Comparing this rate with the maximum rate set by the intrinsic deadtime ($= 5.2 \times 10^7\ s^{-1}wire^{-1}$), it is evident that the overwhelming contribution to the overall deadtime comes from the long occupation times. Hence the importance of measuring this parameter. Reducing the deadtime is equivalent to increasing the efficiency, therefore it is interesting to lower the high voltage the most possible so that the occupation time will be minimal. Apart from the high voltage, the occupation time is also a function of the signal threshold and to some extent also dependent on the gas mixture.

3) The cluster size. That is, the number of consecutive wires that fire as a result of the passage of one single particle. The cluster size is also a function of high voltage, threshold and gas mixture. Also it depends on the gate width and the inclination of the incident particle. A clustersize close to 1 with near 100% efficiency is desirable, such a result would indicate a well optimized chamber.

In connection with the rate limitations should also be mentioned the possible lowering of the effective chamber high voltage. Some ohmic resistance always has to sit on the line from the high voltage supply to the high voltage cathodes of the chamber. If the particle flux is high, the dc-current drawn through the resistor (to restore full negative potential at the cathodes) may cause a voltage drop over the resistor which again lowers the effective cathode voltage. One should take care so that the voltage drop isn't sufficient to bring the chamber voltage below the voltage plateau of full efficiency.

B. The MWPC's in WA7.

An attached publication[2] give details about the large $2 \times 2\ m^2$ MWPC's constructed by the Genova group. These are CH4, CH5 and CH6 in Fig. 1.2.b.

The other three chambers, CH1, CH2 and CH3, were constructed by the group from University College of London. By means of the firings in these chambers the off-line analysis program tries to extend the already reconstructed lines (between CH3, CH4 and CH5 in the forward arm and between CH3 and CH6 in the recoil arm) through the magnetic field to a common vertex in the target.

The essentials of the English chambers are listed in the table below. Notice that the 'projection' refers to the coordinate which is measured with one particular plane of anode wires, see Fig. 1.3.

Chamber	Plane number	Projection	Pitch (mm)	Nr of wires
CH1	1	x	1	960
	2	u	2	384
	3	y	2	128
	4	v	2	384
	5	x	1	960
CH2	1	x	1	1088
	2	v	2	448
	3	u	2	448
CH3	1	x	2	1024
	2	u	2	768
	3	v	2	768
	4	y	2	288
	5	x	2	1024
	6	x	2	1024

Table 3.1. Essential parameters for the English MWPC's. The plane number increases with the z-coordinate.

C. References

1. Principles of operation of multiwire proportional and drift chambers.
F. Sauli (Yellow report 77 - 09, CERN).

2. Development of large planar proportional chambers.
M. Bozzo et al. (Nuclear Instruments and Methods 178 page 77, 1980).

EUROPEAN ORGANIZATION FOR NUCLEAR RESEARCH

CERN-EP/80-57
29 April 1980

DEVELOPMENT OF LARGE PLANAR PROPORTIONAL CHAMBERS

S. Ferroni, V. Gracco, A. Santroni

Istituto Nazionale di Fisica Nucleare, Sezione di Genova

and

Università di Genova, Italy

R. Kiesler, K. Kirsebom, M. Macri*), B. Mouellic

CERN, Geneva, Switzerland

ABSTRACT

We describe a set of large multiwire proportional chambers used in an experiment at the CERN Super Proton Synchrotron. The sensitive area is 2320 × 2320 mm^2, and four detecting planes, each with different orientation, are grouped together within the same mechanical frame. The number of wires for each module is 5000.

Very uniform efficiency over the whole area is achieved by means of a simple mechanical construction.

The chambers were operated for a long time without any damage under high particle flux.

(Submitted to Nuclear Instruments and Methods)

---

*) Present address: Istituto Nazionale di Fisica Nucleare, Sezione di Genova, Italy.

1. INTRODUCTION

A set of large multiwire proportional chambers (MWPCs) has been designed and built for use in an experiment at the CERN Super Proton Synchrotron (SPS). The experiment[1] (CERN/SPS/WA7) was intended to measure exclusive processes (mainly elastic) at large p_T. The large acceptance required by the low magnitude of the cross-sections, necessitated using detectors with a large sensitive area (typically 2.5×2.5 m^2). The use of proportional chambers with good spatial resolution ($\sim$ 1 mm) allowed acceptance of high incident particle fluxes, minimizing dead-time losses.

In this paper we describe the design characteristics and the behaviour of the chambers.

2. DESIGN SPECIFICATION

The useful detector size was determined by the aperture of the analysing magnet to be 2320×2320 mm^2. In order to minimize the amount of material along the particle trajectories, the required detecting surface was provided by proportional planes covering the entire area.

The spacing between the signal wires was chosen to be 2 mm for all planes in order to provide adequate resolution. To speed up data processing, we introduced planes with rotated coordinates, thereby reducing the number of ambiguities caused by the presence of multiple hits in the chambers.

The detector length was kept as short as possible by grouping together in a "module", within the same mechanical frame, four sensitive planes [working in fact as four independent chambers sharing common gas circulation]. A metal frame provided rigidity, acted as a support for the whole module, and made it gas-tight.

The design parameters for the four planes of each module are summarized in Table 1.

The reason for choosing the unconventional value of 28.7° for the angles in the u and v planes is due to the fact that for such an angle both the "sin" and "cos" functions can be expressed as rational numbers; this simplifies the on-line data filtering (by means of dedicated hardwired processors)[2], thus avoiding floating-point calculations.

Since the MWPCs had to withstand high particle fluxes, particular care was taken to avoid performance deterioration with ageing due, for example, to deposits on signal and HV electrodes, observed and reported by many users[3].

Tests have been performed on the MWPCs using wire cathode planes and cathode planes made of graphite-coated stretched Mylar foils (which were the only mechanically feasible solutions over such large dimensions). The properties of the so-called "magic gas" and various $Ar + CO_2$ mixtures have been investigated.

After an integrated number of particles ($\sim 3 \times 10^{13}$ part./cm^2) traversed a chamber with wire cathode planes, we definitely observed (as expected) a deposit on both the signal and the HV wires when operating with the "magic mixture"; some deposit was also suspected to be present with the $Ar + CO_2$ mixture. When the graphite-coated cathode planes were used, we observed no deposit on the HV planes, neither with the "magic mixture" nor with $AR + CO_2$. However, a suspect deposit was present on the signal wires after using the "magic mixture", whilst the wires remained clean with $Ar + CO_2$.

The low cost and the absence of safety problems was an additional advantage which finally led us to choose the $Ar + CO_2$ gas mixture, which has proved to be very stable.

3. CHAMBER CONSTRUCTION

Figures 1 and 2 show respectively a cross-sectional and an exploded view of an MWPC module. Figure 3 gives an over-all view of the module. Each module is made of 4 signal planes and 8 high-voltage planes; the frames are made of Vetronite*), a fibre-glass reinforced epoxy resin.

*) Stesalit No. 4411.

The HV planes are prepared by epoxying directly to a fibre-glass frame a Mylar foil (67 μm thick) stretched under a linear tension of ∿ 50 kg/m. After the epoxy has hardened, the Mylar foil is stretched still further by heating it uniformly. The surface is then sprayed with several layers of graphite paint*) and carefully polished to produce a shiny, smooth electrode surface.

This construction satisfies both economy and simplicity. Another advantage is that it facilitates the carrying out of minor repairs to the electrodes.

The signal sense wires were made of 20 μm gold-plated tungsten wires spaced by 2 mm, stretched with a tension of 50 ± 5 g, and soldered to the pads of a printed-circuit board glued to the fibre-glass frame. A precision of ±0.1 mm was achieved on the position of the soldered wires over all the plane length.

For the x and y planes, the last three wires on both sides were replaced by guard wires having larger diameters (40, 70, 150 μm). No such guard wires have been used on the u and v planes.

All the mechanical stresses from the signal and HV planes are supported by two identical Al frames, carrying a precision-placed dowel system by means of which the individual planes are assembled. This construction ensures automatic positioning of all planes with an accuracy of ±0.05 mm. After the module is assembled, the relative coordinates of each plane are completely determined by the construction only. Absolute coordinates are obtained from an external survey of only the four corner dowels.

The Al frames provide rigidity and also form the main body of the gas-tight enclosure. The two external windows, glued directly to the Al frames, are made of Mylar-Aclar**) foils 50 μm thick. The sides of the module are made of Plexiglas windows through which the connections to the PC boards protrude. Gas-tightness along the PC boards is provided by soft rubber-cord "O" rings (see Fig. 1).

---

*) Graphite-loaded paint, type Acheson 502, diluted with 50% methy-butyl ketone.

**) Mylar-Aclar 33 type Kel-ef.

4. WIRE STABILITY AND ELECTROSTATIC FORCES

The signal wires are exposed to electrostatic forces. In our case the maximum free wire length compatible with sufficient stability is around 70 cm [4]. Since this is much less than the actual wire lengths (cf. Table 1), some mechanical support had to be devised.

Moreover, the electrostatic attraction of the HV electrodes towards the anode plane tends to reduce the gap width, mainly in the centre of the chamber. As a result, the efficiency is not uniform across the sensitive area, and electrical breakdown could occur.

The maximum inwards sagitta Δy for a plane (assuming, for simplicity, a squared shape) of surface H^2, stretched with a linear tension T and subject to a pressure P (due to electrostatic attraction) is[5]

$$\Delta y = \frac{P}{T}\frac{H^2}{8} , \quad P = \frac{C^2V^2}{8\varepsilon_0 s^2} ; \quad s = \text{wire spacing} , \quad C = \text{chamber capacity} .$$

For the present chambers typically $V \sim 4$ kV and $P \sim 0.8$ N/m^2; hence to keep $\Delta y < 0.1$ mm, the tension T should be $> 4 \times 10^3$ N/m.

Stretching the Mylar foil with such a tension would pose complicated constructional problems. In an attempt to solve the two above-mentioned problems simultaneously, we placed suitably spaced-out corrugated Kapton strips on both sides of the signal wires (Fig. 4) [6]. With regularly alternated strips spaced by about 27 cm, it is easy to counteract the forces trying to pull together the anode and cathode planes, as well as to prevent wire displacement and the resulting instabilities. The corrugation allows the strip to remain vertical when laid on a plane. A nylon wire (diameter = 0.3 mm) is stretched tightly parallel to the longitudinal direction of the Kapton strip half-way between the sense wire and high-voltage planes. This wire traverses the Kapton strip through appropriate holes, once for each lateral deflection of the strip. Hence the lateral rigidity of the entire garland structure is ensured (especially important for x, u, and v-planes, where the garlands are horizontal). Also, by the use of

this wire, one obtains an even spacing of the lateral deflections along the garlands (important for the vertical garlands in the y-planes). The electric field modification around the strip, because of its dielectric rigidity, would result in a rather wide inefficient region ($\sim$ 2 cm) (Fig. 4). To correct for this unwanted effect, we stretched a PVC-insulated copper wire (0.9 mm external diameter) along the Kapton strip: the signal wires therefore are orthogonal to the PVC wires in the x and y-planes and make a 61.3° angle with the PVC wires in the u and v-planes. By applying a negative voltage to the wire, one can compensate for the field distortion and restore good efficiency nearly everywhere around the strip (Fig. 4).

5. PERFORMANCE OF THE CHAMBERS

As already mentioned in Section 2, the gas mixture used consisted of $Ar + CO_2 +$ freon. Compared to the standard one, the use of this mixture introduced a small reduction in the gas amplification under normal operating conditions, and a shortening of the plateau length[7].

With an electronic threshold level of 2 mV on the signal wires, a mixture containing 25.0% CO_2 + 74.25% Ar + 0.75% freon gives a plateau (Fig. 5) extending over $\sim$ 300 V, somewhat shorter than what is obtained with the "magic mixture" (Fig. 6), but quite sufficient for correct operation. We stress that all the MWPCs exhibited exactly the same behaviour: the start of the plateau region for different gaps or chambers never departed from the average value by more than 50 V. Even more important, a careful scanning over the whole area of each plane showed a remarkably uniform efficiency at each voltage. No spurious sparking or discharge -- which could eventually lead to a wire breakdown -- has been observed during about two years of operation.

The dark current in the chamber has been observed to decrease in time, and after a few days of operation the current had a typical value of $\sim$ 0.5 μA, i.e. about 0.1 $\mu A/m^2$ at 4.0 kV; this behaviour was consistent in all planes. When the field-correcting wires along the strips are brought to a negative potential

of 2.0 kV, the dark current is seen to increase from 0.5 to about 4 or 5 μA, probably because of the high field gradients created. However, after a few days the current falls again to much lower values (about 1 μA). It should be remarked that no particular care was taken during the assembly (such as operating in a dust-free room), as this would have been impractical for a chamber of such large dimensions.

The chamber efficiency has been measured in detail in the region around the strips. Without applying any voltage to the correction wire, the efficiency drops drastically (as would be expected) over a rather wide (∿ 2 cm) region on both sides of the strips. The inefficient region is, however, reduced when the wire is brought to a negative potential (Fig. 7).

The transverse size of the corrugation must be chosen carefully.

If the strip extends transversely more than ∿ 10 mm, a satisfactory recovery in the efficiency cannot be obtained. For narrower strips, on the contrary, the efficiency is almost entirely recovered (Fig. 8).

6. THE ELECTRONICS AND THE SAFETY SYSTEM

The read-out electronics used for the chambers has been described in detail elsewhere[8]. Because of the high rates expected, this read-out system had to be fast (which it also is) so as to minimize dead-time losses[9]. The solution adopted consisted in storing the signals from the sense wires into twisted-pair delay lines (one line per wire). A delay of 450 ns was long enough to allow the trigger electronics to decide whether the event was a possible good candidate and to generate a strobe signal which latched the signals from the chamber into memory registers.

The amplitude attenuation after 85 m of cable was 30%, with negligible time slewing.

On the chamber side there is only a preamplifier, which acts as a line driver; its input impedance was chosen to be rather low (400 Ω) in order to minimize the time duration of the pulse*) over threshold. The latter can be adjusted at the receiver end to between 1.2 and 5 mV, typical values being about 2 mV.

The amplitude variation between the ends of the long sense wires is negligible.

Because of the large number of wires involved (∿ 5000 in each module and a total of about 20 000 wires) it was important to provide a testing facility simulating the behaviour of the chamber. To this end, on each signal plane an Al strip, 1 cm wide, was laid across the pads of the PC boards, separated by a 100 μm thick Mylar insulator. By injecting a suitable pulse along the strip, the signals induced through capacitive coupling to the wires could simulate real pulses from ionizing particles.

For such large chambers it is also extremely important to ensure that the wires do not break during the course of operation, as this would result in unacceptable loss of experimental time because of the long period needed for disassembly and repair.

The usual dark-current monitoring and disconnection of the chamber HT in case of excessive current was not quite efficient, probably because of the long delay between detection and switch-off (by relay contact).

Using a small test chamber, we got some indication of how one could possibly protect the chamber. It was seen that, whilst normal current pulses (due to traversing particles) were of short duration and were irregularly spaced in time, bursts of current pulses with very regular pulse spacing and high rate occasionally occurred; in some cases the dark current increased by several orders of magnitude after particularly long bursts of this type. This was interpreted as a pre-warning of a larger discharge, and we decided to base a prototype protection system on this observation.

---

*) A typical time over threshold at full efficiency is ∿ 240 ns.

We designed a current transformer to be inserted into the HV line, and a Crytron*) switch was connected, in parallel, to the chamber. The transformer had to integrate the current pulse burst with a time constant of $\sim$ 0.25 μs, and the resulting pulse fired the Crytron switch via a current comparator and amplifier. With this system the HV across the chamber could be lowered to less than 10% of the operating voltage within 0.5 μs after the detection of one of the current pulse bursts. A full-scale chamber equipped with the system and exposed to a test beam proved capable of providing full protection against wire breaks over a long period of time.

During this test run we were able to prove that even with high-intensity beams traversing the chamber a clear distinction could be made between current pulses due to normal proportional operation and the occasional regularly spaced current pulse bursts considered as a "warning" of possible discharges.

In addition to the current pulse burst detection, the final system (shown in Fig. 9) also housed a d.c. current monitor which acted upon the Crytron switch when the current was considered as dangerous for the chamber. Remote control of comparator bias and some timing circuitry for automatic slow recovery of chamber voltage after switch-off was added, as well as a status output for use in the on-line experimental data acquisition system.

During two years of uninterrupted operation of the 12 gaps we had only one wire break, which must, however, be attributed to an error in the gas filling of that chamber, as pure argon was erroneously used. In this case the spark formation time was much too rapid for the protection system to react.

7. CONCLUDING REMARKS

The operation and results described above demonstrate the feasibility of constructing proportional detectors with a very large sensitive area working

---

*) Crytron type KN6, manufactured by EG & G.

reliably, with good and uniform efficiency and low dead-time, in the presence of high particle fluxes.

Our experience has shown that these goals can be obtained at a reasonable price using a simple construction and operating the chamber with a safe and inexpensive $Ar + CO_2$ + freon mixture.

Acknowledgements

We thank all the technical staff of the INFN Section in Genova, and in particular G.C. Barisone, S. Bianconi, F. Conforti, G. Massari, A. Morelli, P. Poggi and L. Traspedini, as well as D. Ploujoux and P. Anzoli from CERN.

We are particularly indebted to G. Trucco for her enthusiastic help during the construction of the detectors and to M. Bozzo and A. Buzzo for their help in the early stage of the work.

We also acknowledge useful conversations with A. Michelini and R. Lorenzi.

REFERENCES

1) R. Almas, C. Baglin, R. Böck, E.T.C. Borggaard, K. Brobakken, L. Bugge, T. Buran, A. Buzzo, P. Carlson, L. Causton, C. Caverzasio, M. Coupland, D.G. Davis, J.D. Hansen, B.G. Duff, A. Eide, S. Ferroni, I. Gjerpe, V. Gracco, K. Guettler, J.P. Guillaud, J. Haldorsen, P. Helgaker, F.F. Heymann, D.C. Imrie, T. Jacobsen, K.E. Johansson, K. Kirsebom, S. Kooijman, R. Lowndes, A. Lundby, G.J. Lush, M. Macri, R. Møllerud, J. Myrheim, M. Poulet, L. Rossi, A. Santroni, B. Schistad, H. Schwartz, G. Skjevling, S.O. Sørensen, J. Tavernier and M. Yvert, Large-angle elastic scattering of charged pions on protons at 20 and 30 GeV/c incident momenta, Submitted to Physics Letters B.

2) M. Letheren, B. Martin, J. Joosten and I. Gjerpe, A specification of the hard-wired processor for experiment WA7 (Version 2), Internal note, SP section DD, 26.11.1976.

3) G. Charpak, H.G. Fisher, C.R. Gruhn, A. Minten, F. Sauli, G. Plch and G. Flügge, Submitted to Nucl. Instrum. Methods 99 (1972) 279-284.
P. Le Dû, P. Borgeaud, G. Burgun, R. Hammarström, R. Lorenzi and A. Michelini, CERN EP Internal Report 77-11 (1977).

4) T. Trippe, CERN NP Internal Report 69-18 (1969).

5) A. Michelini and K. Zankel, CERN Internal Report OM/SPS/75-5 (1975).

6) S. Majewsky and F. Sauli, CERN NP Internal Report 75-14 (1975).
A. Michelini: private communication.

7) F. Sauli, CERN NP Internal Report 77-09 (1977).

8) J.B. Lindsay, C. Millerin, J.C. Tarlé, H. Verweij and H. Wendler, Nucl. Instrum. Methods 156 (1978) 329.

9) B. Sadoulet and B. Makowski, CERN Internal Report DPH/11/PHYS 73-3 (1973).

Table 1

Chamber parameters

	Plane type			
	x	v	y	u
Angle with vertical direction (degrees)	0	-28.7	90	28.7
Wire spacing (mm)	2	2	2	2
Wire diameter (μm)	20	20	20	20
Longest signal wire (mm)	2320	3000	2320	3000
Gap thickness (mm)	6	6	6	6

Figure captions

Fig. 1 : Cross-sectional view of a module:

(1) Plexiglas side windows

(2) Printed-circuit boards

Vetronite frame and spacers (hatched).

(S) Sense wires

(HV) High-voltage electrodes

(M) Mylar-Aclar window.

Fig. 2 : Exploded view:

(1) Al main frame and Mylar-Aclar gas window

(2) Vetronite spacers

(3) HV plane with supporting garlands

(4) Sense plane.

Fig. 3 : Over-all view of a chamber module.

Fig. 4 : Garland details:

(1) Corrugated Kapton strip

(2) PVC-insulated copper wire

(3) Sense wires

(4) HT electrodes.

Fig. 5 : Efficiency and dark current versus HV for Ar + CO_2 + freon mixture.

Fig. 6 : Efficiency and dark current for Ar + isobutane + freon mixture.

Fig. 7 : Efficiency along an axis (x) orthogonal to the corrugated Kapton strip. x = 0 corresponds to the PVC-insulated copper wire position.

V_{ch} : chamber high voltage

V_{thr}: electronic read-out threshold

V_G : correcting voltage applied to PVC insulated wire.

Fig. 8 : Efficiency versus correcting-wire voltage at the wire position (x = 0).

Fig. 9 : Electronic diagram of the safety system.

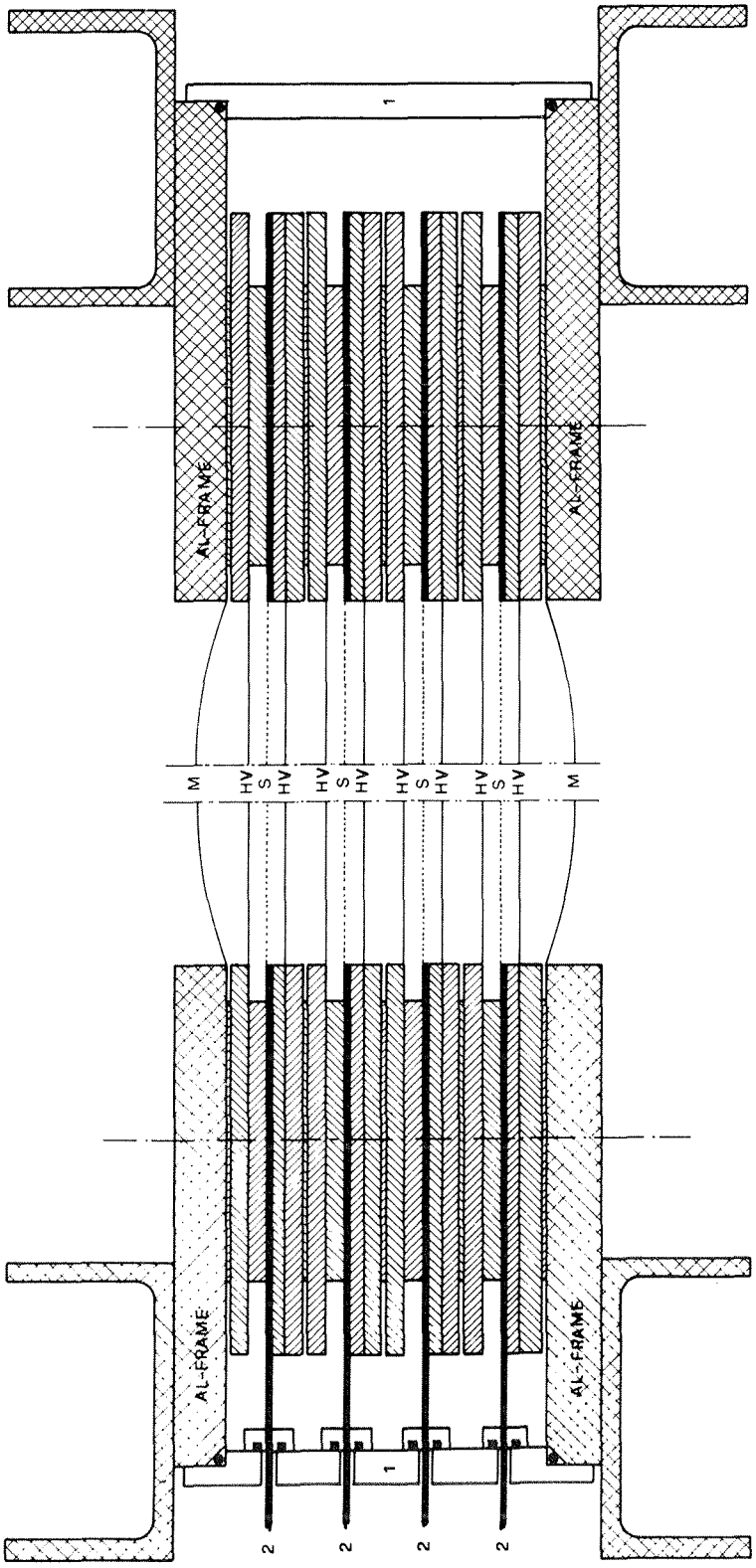
1
AL-FRAME
AL-FRAME
M
HV
S
HV
HV
S
HV
HV
S
HV
HV
S
HV
M
AL-FRAME
AL-FRAME
1
2
2
2
2

Fig. 1

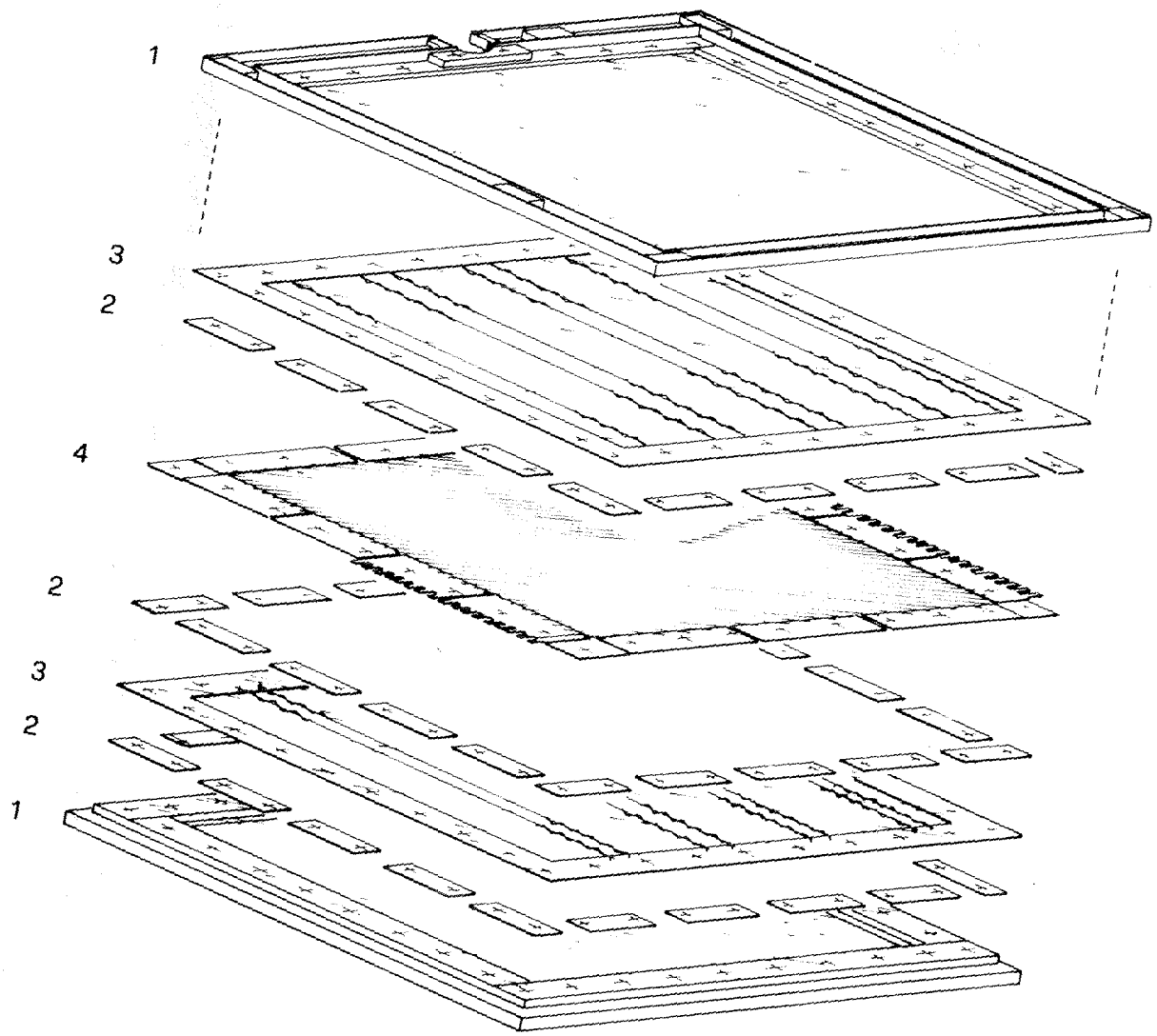

Fig. 2

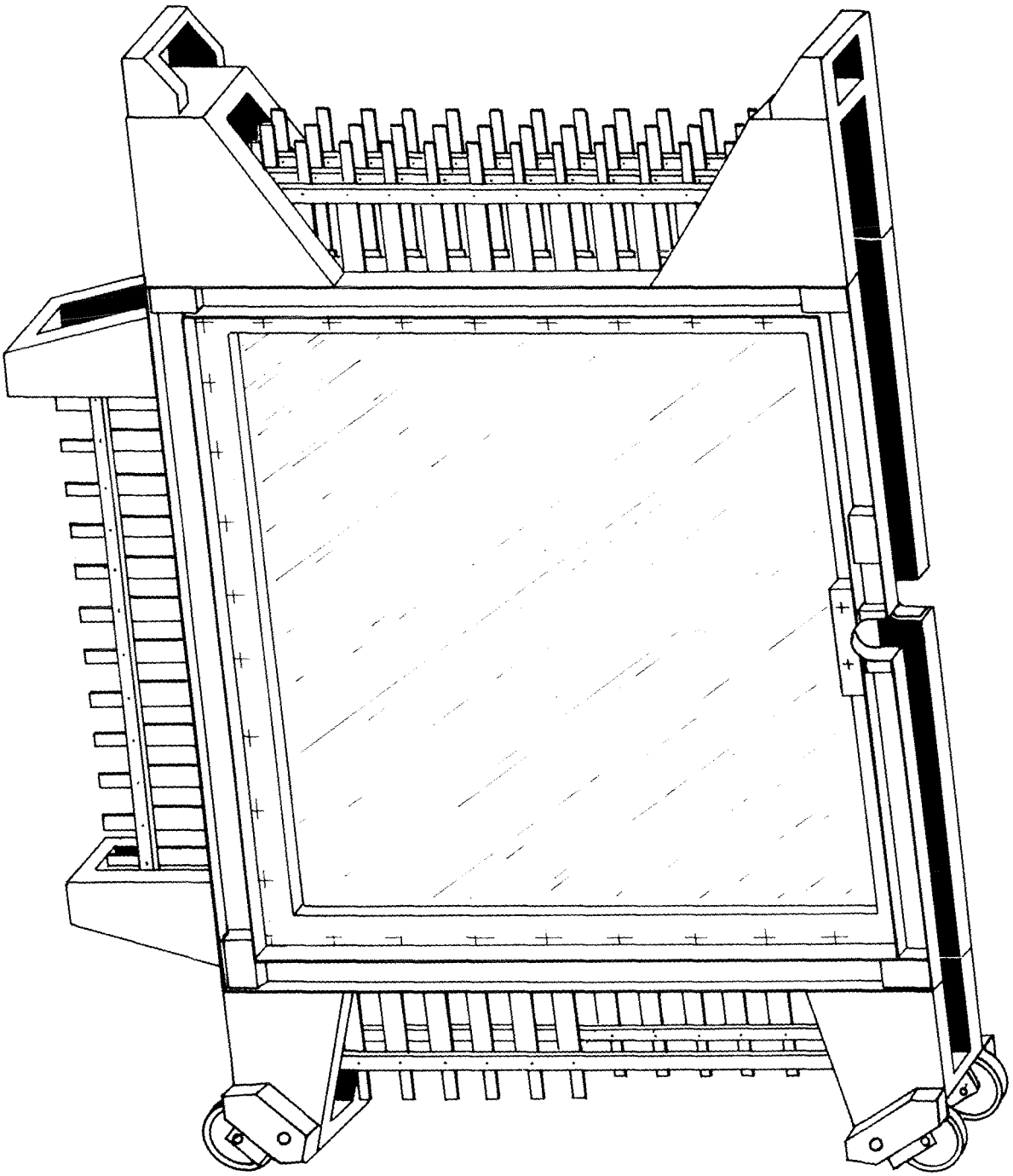

Fig. 3

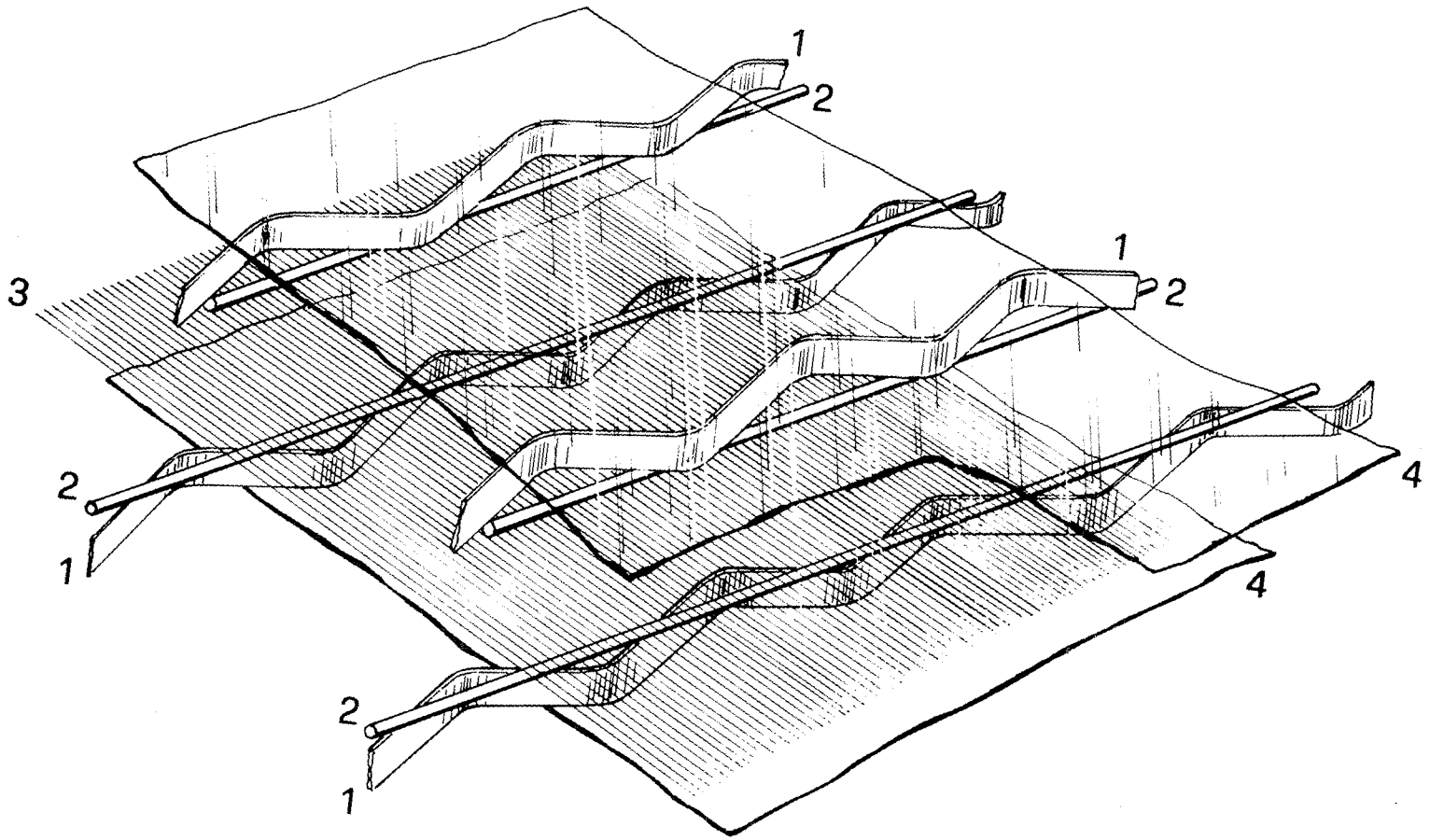

Fig. 4

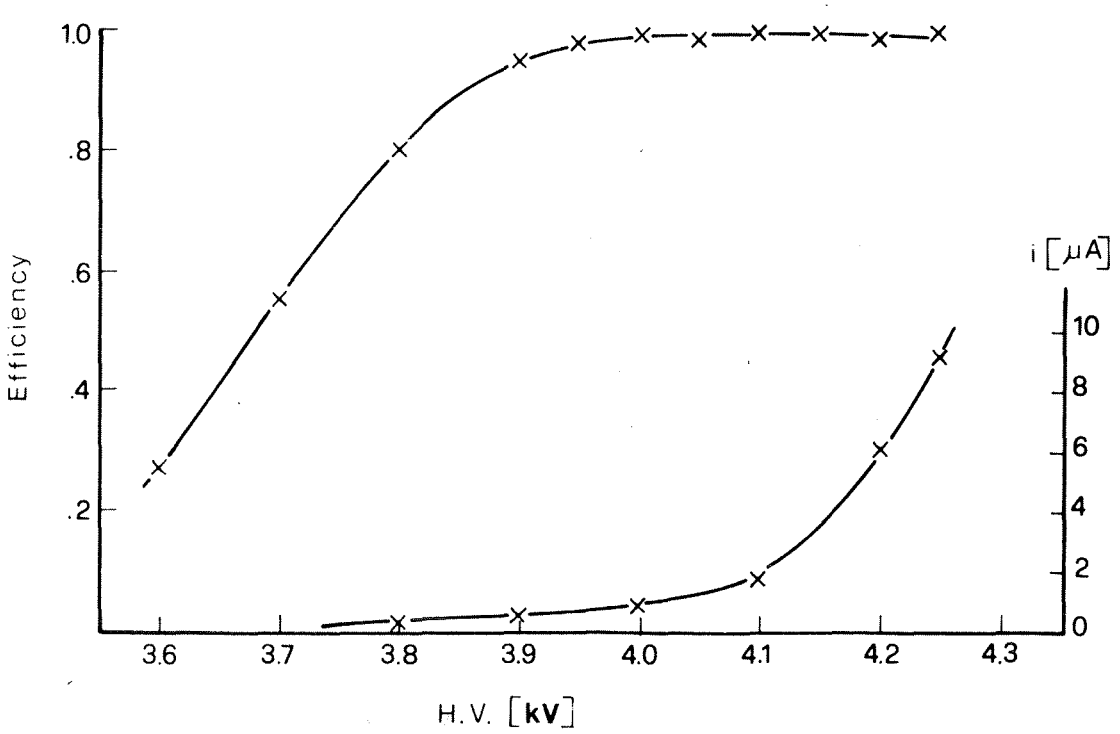

Gas Mixture	**Ar**	74.25%	V_{thr} = 2 mV
	Freon	0.75%	
	CO_2	25.0 %	

Fig. 5

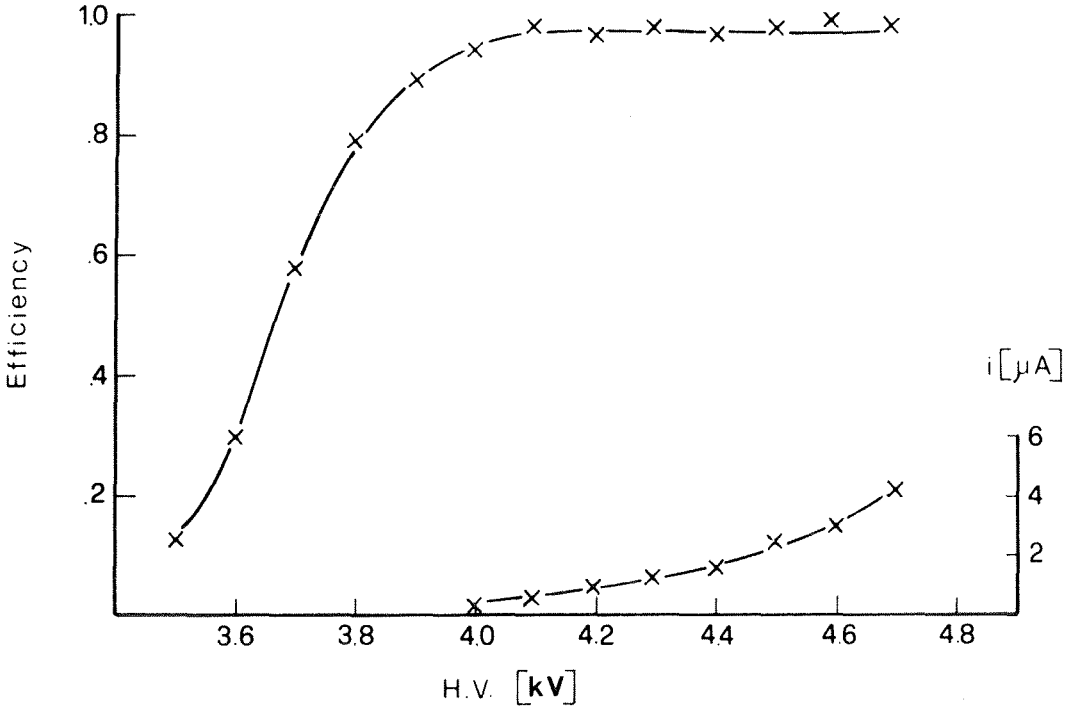

Gas Mixture **Ar** 83.8 %

Freon 0.8 %

Isobutane 15.4 %

V_{thr} = 2 mV

Fig. 6

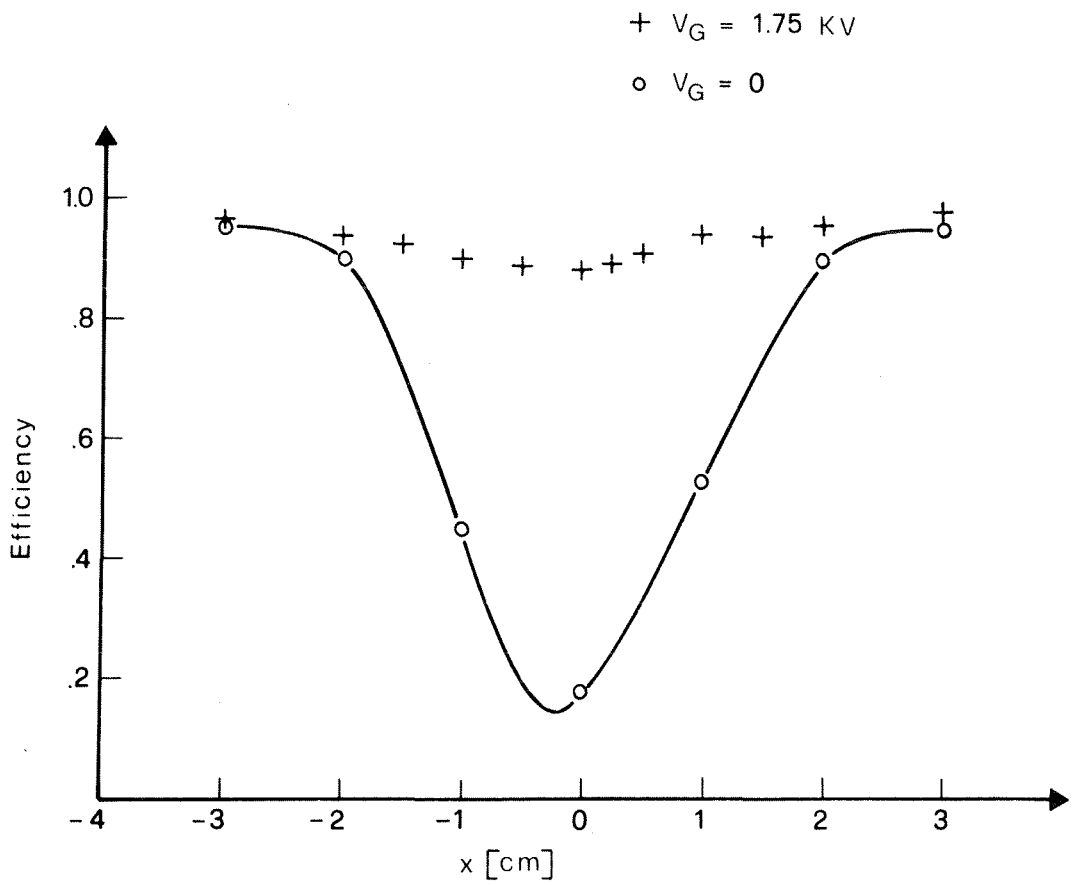

Gas Mixture **Ar** 74.25 %

Freon 0.75 %

CO_2 25.0 %

V_{thr} = 2mV

V_{ch} = 4.1 KV

Fig. 7

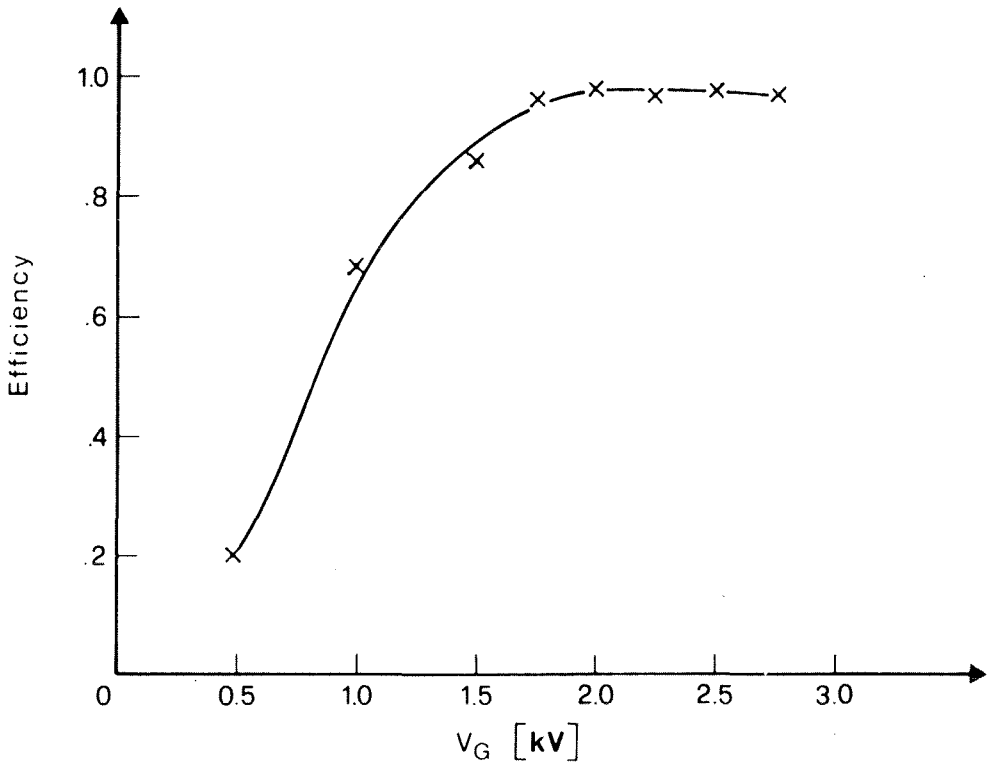

Gas Mixture **Ar** 74.25 %

Freon 0.75 %

CO_2 25.0 %

V_{thr} = 2mV

V_{ch} = 4.1 **kV**

Fig. 8

CHAMBER PROTECTION FAST SWITCH

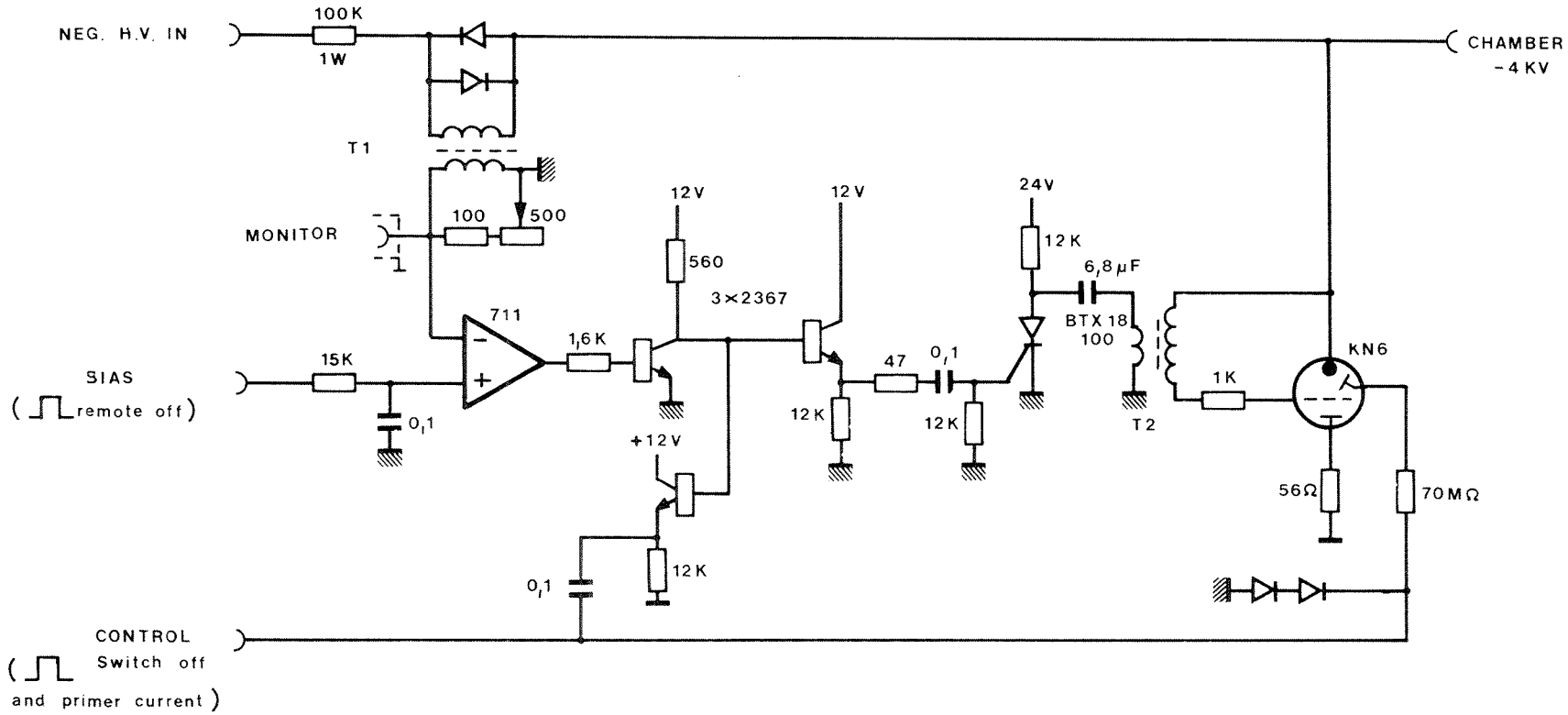

T1 : 250 turns
on potore 4C4

T2 : 4 : 120 turns
Ferrite 3E1
primary H.V. insulated

Fig. 9

CHAPTER 4

THE WA7 CALORIMETER AND MUON-DETECTOR

A. Outline of apparatus in the experimental zone.

For the position of the calorimeter and muon-detectors in the general WA7 setup, see Fig. 1.2.b. The detectors are denoted CAL + μ (1) . . and CAL + μ (2). Fig. 4.1 shows the sequence of the different elements in CAL + μ (1), all of which may be lowered up and down in slots in an iron frame. The calorimeter and muon-detector in each arm consist of iron slabs (220 x 210 x 10 cm^3), scintillator-hodoscopes (SH) and drift chambers (DC). The frame + 80 tons of iron, may be moved along the x-axis on rails by means of a hydraulic arrangement. Frames for SH's and DC's are not drawn. The ordering of the wire-planes in the DC's is indicated. U and V wires mean the same as for the WA7 proportional chambers (see Fig. 1.3). CAL + μ (2) in the recoil arm has the following sequence of elements going downstream:

19 iron slabs
1 SH, named R1
1 DC-plane, X-wires
7 iron slabs
4 DC-planes, Y, X, V and U-wires
1 SH, named R2

Also, CAL + μ (2) may move on rails along the x-axis.

The scintillator hodoscopes are labelled L1, and L2 and L3 in CAL + μ (1) (see Fig. 4.1) and R1 and R2 in CAL + μ (2). L1 and L2 are used in the calorimeter L2, L3, R1 and R2 for detecting muons. L1, L2, L3 and R2 are made up of elements of 12.5 x 100 x 2 cm^3.

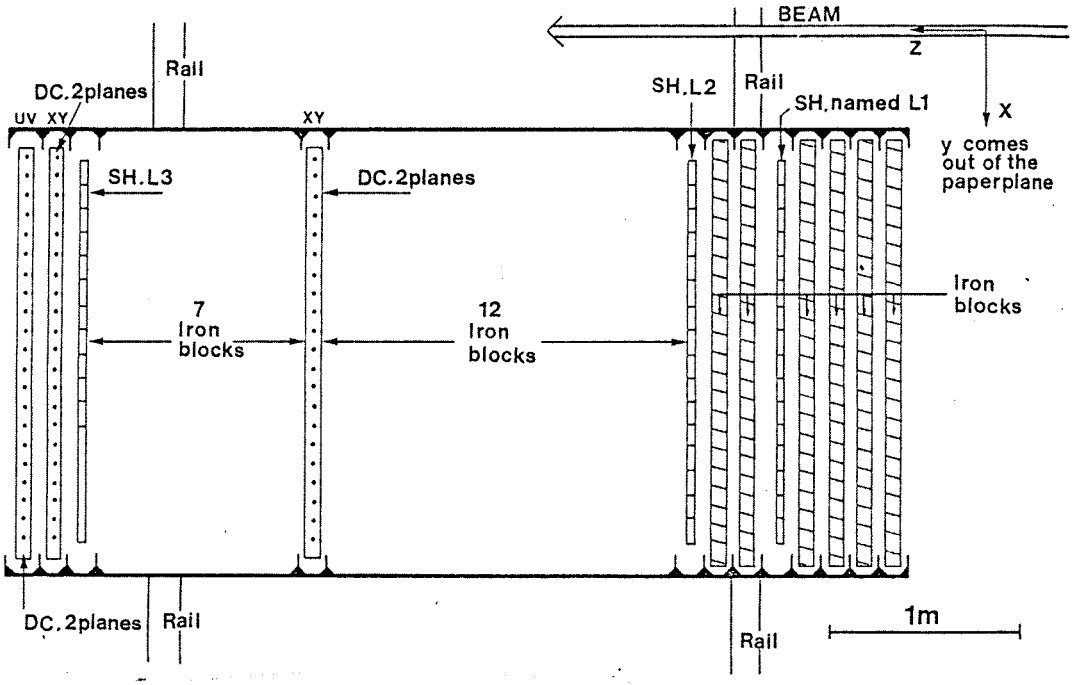

Fig. 4.1

Top view of CAL + μ (1). The scale is not correct for the thickness of the scintillator material (which is 2 cm).

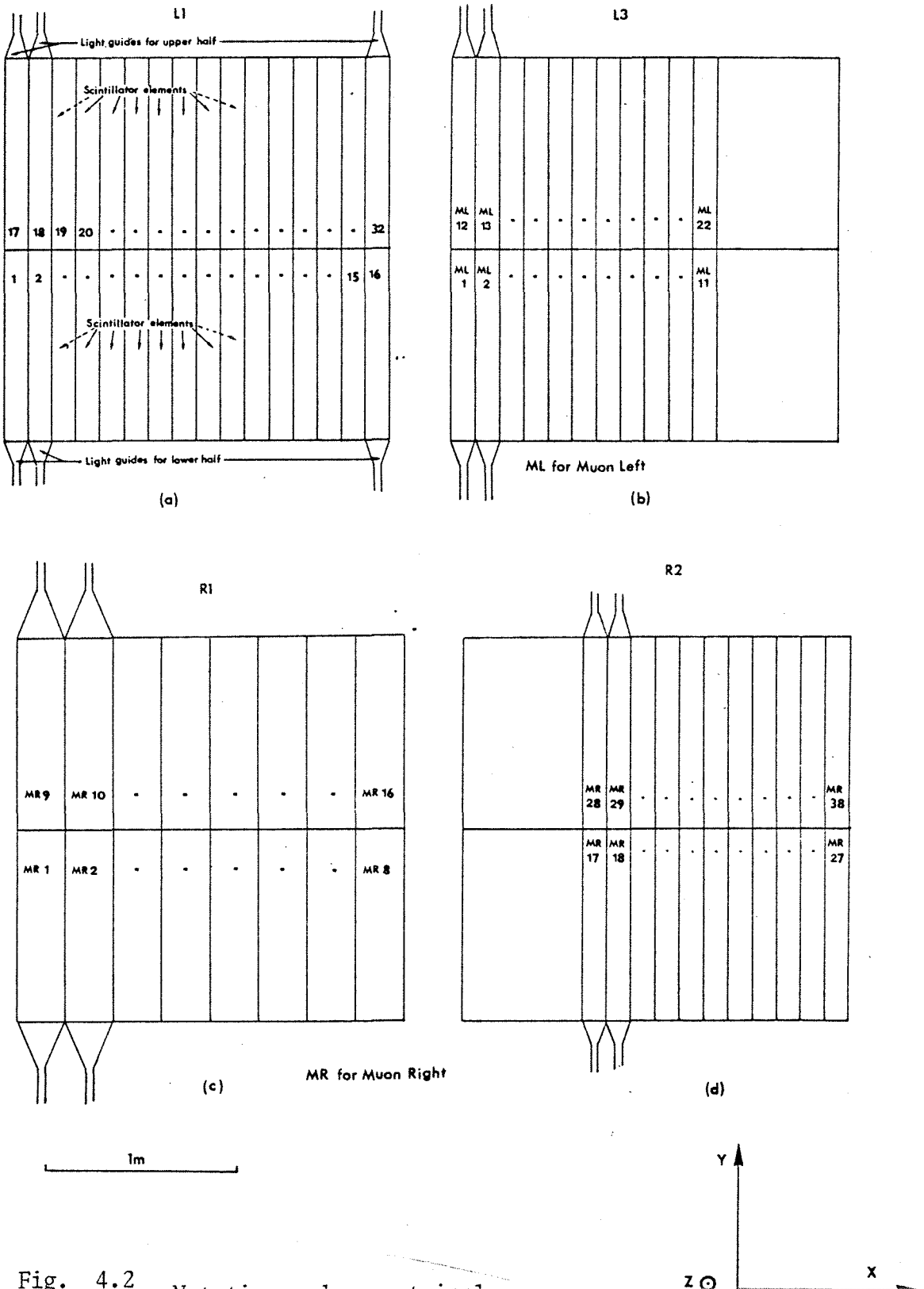

Fig. 4.2 Notation and geometrical arrangement for CAL + μ(1) and CAL + μ(2) scintillator elements. The beam comes out of the paperplane, L2 elements (not shown), runs from 33 to 64.

In L1 and L2 there are 32 elements in each plane, in L3 and R2, 22 elements. The labelling of the L1 and L3 elements is given in Figs. 4.2.a and b. L2 elements run from 33 to 64. R1 has 16 elements with dimensions, 25 x 100 x 2 cm^3. The labelling of the elements in the right arm is given in Figs. 4.2.c and d. The ordering of elements is with increasing x, y, and z. All counters are mounted on aluminium frames (which may easily be taken in and out by a crane). Notice that in L3 only the 11 positions closest to the beam are covered. Acceptance considerations for muon pairs from ψ-decay and shortage in bases led us to use only 12 elements in R1 (sometimes MR3 - MR8 + MR11 - MR16, other times MR2 - MR7 + MR10 - MR15). Accordingly we covered either positions 6 to 16 (as in Fig. 4.2.d) or positions 4 to 14 in R2.

We used Nuclear Enterprise plastic scintillator material some of which was old. Therefore it was necessary to cut and glue to get the desired dimensions. This together with the fact that the material was of varying quality, introduced big fluctuations in the light yield. For planes L3, R1 and R2 this was of no importance since they only act as threshold counters for the muon-detector (we only ask for a signal above a certain threshold voltage, a yes or no signal). However, for planes L1 and L2 where we wanted to use the analog information in the signals, this caused problems and slightly reduced the quality of the calorimeter. This will be discussed in section E.

Photomultipliers and bases:

In planes L1, L2, R1 and R2 we used the same bases as in H1/H2 (CERN PM supply type 4239), and for R3 we used some old resistor bases which were rather unreliable. L1 and L2 were equipped with Phillips 2232 B PM's, the three other planes had mostly 56 AVP's (some elements had XP 2020's). All bases of type 4239 were powered by low tension (-24V) from CERN's "PM supply control" type 4240 which offers nice monitoring possibilities. This was especially useful when doing precise voltage settings for calorimeter counters.

The drift chambers:

First some remarks in general about this detector type. They were developed in the beginning of the 1970's in an attempt to increase the spatial resolution when detecting tracks of charged particles. In fact one improved the resolution by a factor 10 compared to MWPC's, from ± 1 mm precision in MWPC's to ± 0.1 mm in drift chambers.

As in MWPC's a primary ionization is caused by a charged particle going through a suitable gas-mixture (very often the same as in MWPC's). The idea is then to make the electrons drift with a certain velocity V_e towards a well defined collection point called the sense wire, and then measure the time difference Δt between time of passage (given by fast scintillation counters) and time of arrival at the collection wire of the drifting electrons. Townsend[1] found that the drift velocity V_e of electrons in gases may be written as

$$V_e = \frac{e}{2m} t_c E$$

where e and m is the electron charge and mass respectively, t_c the mean time between collisions and E the electric field which the electrons experience. t_c depends in a complicated way on: gas type, its temperature and pressure, T and P, and finally on the electric field. Therefore with constant P and T and a uniform field, V_e is constant and the particle will have passed a distance $\Delta t \cdot V_e$ away from the sense wire. The accuracy of $\Delta t \cdot V_e$ will be limited by the precision of the Δt measurement, variations in V_e along the drift path (especially near the sense wire where the field is strongly non-uniform), diffusion of drifting electrons and lastly by the inherent width of the particle track. Below is shown a unit cell of a drift chamber with very nice performances, the resolution is ± 50 μm[2]. The chamber was built by the Charpak group at CERN. It was used to study multitrack separation, rate effects and the behaviour of drifting electrons in strong magnetic fields.

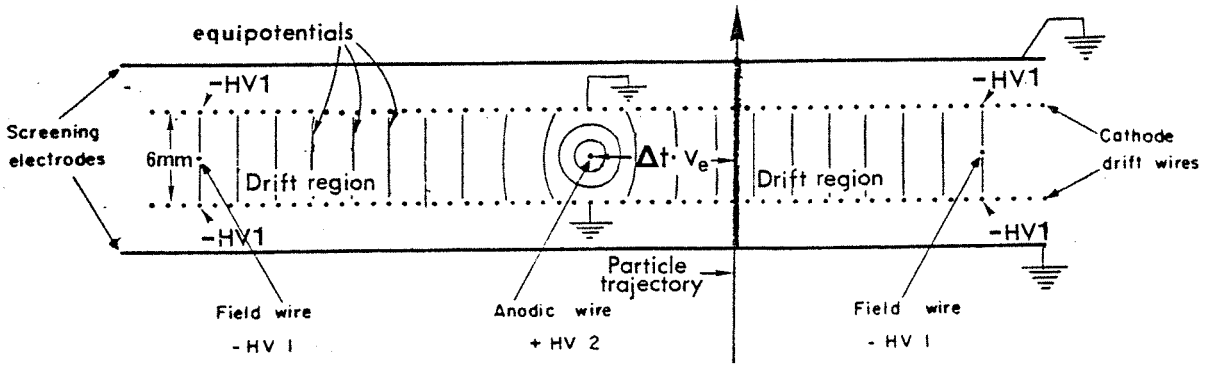

Fig. 4.3

Unit cell of a drift chamber [2].

The structure shown in Fig. 4.3 has since been used in several other drift chambers. Typical values for the pitch (distance between anodic wires, or sense wires) and the gap (thickness of the active part of the gas layer) are 50 mm and 6 mm respectively. The cathode drift wires (with tensions increasing uniformly as one approaches the anodic wire) make a near uniform field in the drift regions. The field wires separate consecutive cells. Near the anodic wire (at less than 0.1 mm) the drifting electrons will come into a very strong cylindric field which (as in MWPC's) by avalanche effects give the necessary multiplication so that the signal may be detected.

It is not possible to construct drift chambers with a uniform field throughout the entire drift region; around the anodic wire it has to be non-uniform, and also elsewhere in the drift cell it would be very difficult technically (especially for big chambers) to avoid local fluctuations in the electric field. However, with a good knowledge of the distance - time relationship ($s = s(\Delta t)$), which doesn't have to be linear as above) one would obtain the same precision as in chambers with a rigorous field uniformity. The inconvenience of a non-linear relationship may be avoided by choosing a gas mixture

which makes V_e independent of the electric field E. Data in ref. 3 (yellow CERN report by Sauli) shows that in a gas mixture of 38% isobutane (C_4H_{10}) and 62% argon, the drift velocity saturates at about 50 mm/μs when E > 1000 V/cm. Thus by keeping the field above 1000 V/cm throughout the entire drift region and also keeping the temperature, pressure and gas composition reasonably constant (for figures see ref. 3), one obtains a constant V_e. Notice that in this way one is also insensitive to time dependent field fluctuations.

The maximum drift time with the construction shown in Fig. 4.3 is $\sim$ 1 μs x 25/50 = 0.5 μs and also obviously, several planes are needed to define points and trajectories in space. This means that having recorded a start pulse, one has to open a gate of 0.5 μs so that all Δt's may be measured. So compared to MWPC's (where the strobe widths are around 50 ns), the amount of information received for a given particle flux, will be an order of magnitude higher*. This is one important limitation with drift chambers; track reconstruction becomes more difficult and costly (in computer time) as the number of digitizings (registered coordiantes) increases. Another limitation comes from the rather long deadtime (per cm length of wire), actually it is the length of that part of the anodic wire which is affected by the avalanche which sets the limit for the possible fluxes a chamber can take.

---

* Throughout one gate several Δt's from a single unit cell may be measured. This can be done by guiding successive stop pulses (which originally are generated at the anodic wire) to different scalers. All scalers start counting (a 500 Mhz clock) at the same time, but will stop after different periods of counting depending on which signal (which particle) generates the stop.

E.g. with a typical deadtime* t_d = 20 μs [2] and an event rate N for the affected area (= the length of the hot spot along the wire times the unit cell width (= the pitch)), the observed event rate will be given by,

$$N_o = Ne^{-Nt_d} \quad \text{(see (A2.4))}.$$

Demanding $N_o/N \gtrsim 0.9$ we get $N \lesssim 5.3 \times 10^3\ s^{-1}$. The length of the hot spot also depends on the avalanche size, 0.2 mm is a typical value [3]. With the above described drift chamber one can therefore support roughly $(5.3 \times 10^3/0.02) = 2.6 \times 10^5$ events per second per cm wire or 5.3×10^4 events $s^{-1} cm^{-2}$, and still have an efficiency around 90%. For a MWPC with 1 mm pitch the event rate per cm wire would have been ca. 50 times higher (the efficiency almost only affects one cell in both types of chambers).

In the main WA7 set-up, these limitations made using drift chambers impossible. Extensive treatment of drift chambers in references 2,3,4 and 5.

---

* This is not a deadtime properly speaking. It is rather a measure for how fast the inefficiency of the region drops from 1 to 0. A certain time after a 'hit', new showers may or may not trigger a new 'hit' depending on the individual shower qualities. High rates will lower the chamber efficiency. This may to some extent be compensated for by increasing the high voltage. Which shows that a lot of the lost signals are weak and not strong enough to be detected. Full efficiency is only restored when the affected zone is completely freed of positive ions. They drift slowly towards the negative cathodes and the clearing time will depend on how strong the avalanche was; in the Geiger-Müller operation, just before spark breakdown, the clearing time will be several hundred microseconds long, while in the usual semi-proportional mode of operation, it will be a factor 10 shorter (10 → 100 μs).

The WA7 drift chambers:

As part of our muon detector, drift chambers are fully usable. The maximum rate recorded per wire (with 10^8 incident on our H_2-target per burst and p(beam) = 92 GeV/c), is 10^5 per burst or 5×10^3 per burst per cm wire. These rates decrease quickly as one moves away from the wires closest to the beam. There were therefore no rate problems.

The construction is very simple. A cross section ($\perp$ to the sense wires) is shown in Fig. 4.4. As opposed to the usual case, the unit cells are here separated by cathode walls. The cathode walls are kept grounded, typical operating voltage on the sense wires was = 3 kV, and mostly the magic gas mixture (76.4% Argon, 20% Isobutane, 0.6% Freon and 3% Methylal) was circulated through the drift tubes. Each plane consists of 64 units cells, with a wire spacing of 3.08 cm, this gives a total width of 197 cm. For X and Y-planes the sense wires are $\sim$ 2 m long, for U and V-planes the length varies, the arrangement of unit cells is such that it covers areas where our muon-pair acceptance is most important (with 64 cells one cannot cover 2×2 m^2 in U and V-planes. Stainless steel was chosen as material for the sense wires because its thermal properties are close to those of aluminium.

The chamber with special preamplifiers were designed and built at the Niels Bohr Institute in Copenhagen. The rest of the readout system is identical to the one used for the WA7 proportional chambers. So one is not recording drift times, and the resolution is simply $\pm$ 1.5 cm. Because of multiple scattering (through 2.5 m of iron) higher precision is not needed.

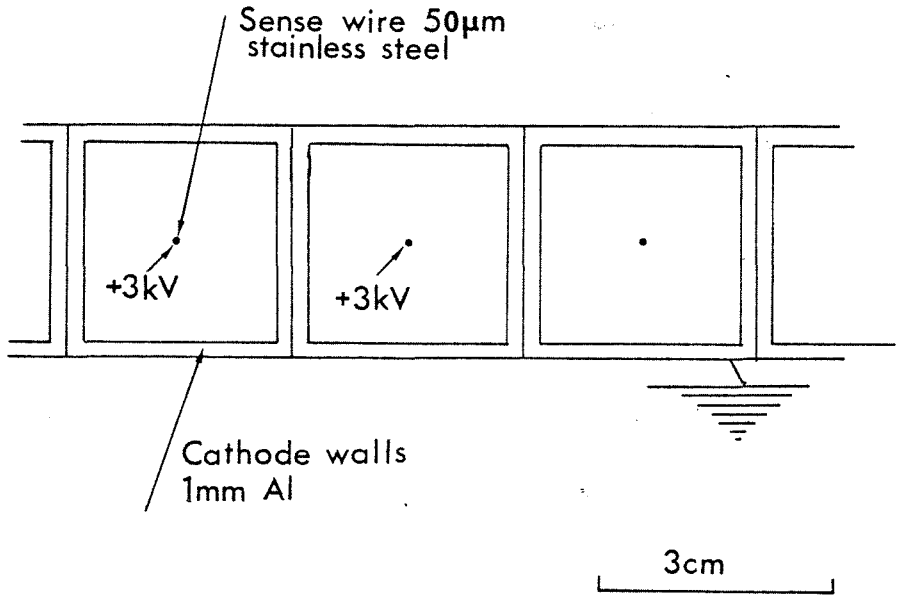

Fig. 4.4

Cross section of 3 unit cells of the NBI drift chamber

Remark on multiple scattering

Charged particles going through matter will be deviated from their incident trajectory by collisions of many kinds. For particles which interact electromagnetically, as for example muons, the collisions are of two types,

a) collisions with electrons (producing ionization or excitation),

b) radiation of photons produced when the particle is accelerated through a coulomb field (= particle-nucleus collision).

The contribution from radiation will be very dependent on the mass of the particle. For two reasons, first, a small mass m will be accelerated more (and hence radiates more) than a larger mass M entering the atom with the same impact parameter b (relative to the nucleus). Second, there is a $b_{max}(m)$ above which no radiation takes place, b_{max} is mass dependent and proportional to $(E_T/mc^2)^2$, where m and E_T are the mass and total energy of the particle, c, the velocity of light. The energy loss from radiation of photons increases with energy while the loss due to collisions is governed by the famous Bethe-Block formula*. These considerations qualitatively explain why electrons are so much faster absorbed when going through matter than muons. The energy loss for relativistic muons will stay small for all relevant energies (up to 1000 GeV). Not before one has reached several hundred GeV's will the energy loss due to radiation become as important as the loss due to collisions. Therefore when calculating trajectories for relativistic muons one considers all

---

* $$-\frac{dE}{d(x\rho)} = 0.6\,\frac{Z}{A}\,\frac{m_e c^2}{\beta^2}\left(\ln\frac{2m_e c^2\beta^2}{(1-\beta^2)\,I(Z)} - \beta^2\right) \qquad (4.1)$$

which is valid for heavy unit charge particles ($m_{par.} >> m_e$). (4.1) is given in units of energy per length per density (i.e., energy cm^2/g). ρ = density of material, m_e = electron mass, $\beta = v/c$ where v = velocity of the particle and c = velocity of light, Z, A = charge and mass number and finally I (Z) = the average ionization potential of an atom with charge number Z. Investigating the behaviour of $-dE/d(x\rho)$ one will find that β^{-2} is important at low values of β, bringing about a fast decrease in $dE/d(x\rho)$ with increasing β. It is only when β^2 is getting very close to 1 that the logarithmic term will introduce a slight increase in the energy loss (4.1 has a minimum for $\beta \sim 0.95$, varying at maximum some percent with Z). Notice that $dE/d(x\rho$ is only a function of the material and β. See chapter 2 for a more detailed presentation of (4.1).

collisions as elastic, and since muons are deviated very little in μ-e collisions, one may also disregard the muon energy loss. What is calculated is hence only the trajectory, its direction and coordinates relative to the incident particle trajectory with the traversed material thickness as the variable. Results[6] are shown in the figure below. The horizontal axis is proportional to θ, the angle between incident and outgoing particle projected into a plane parallel to the incident particle trajectory. P is the probability of observing the outgoing trajectory at a certain angle θ when the momentum of the incident particle is kept fixed.

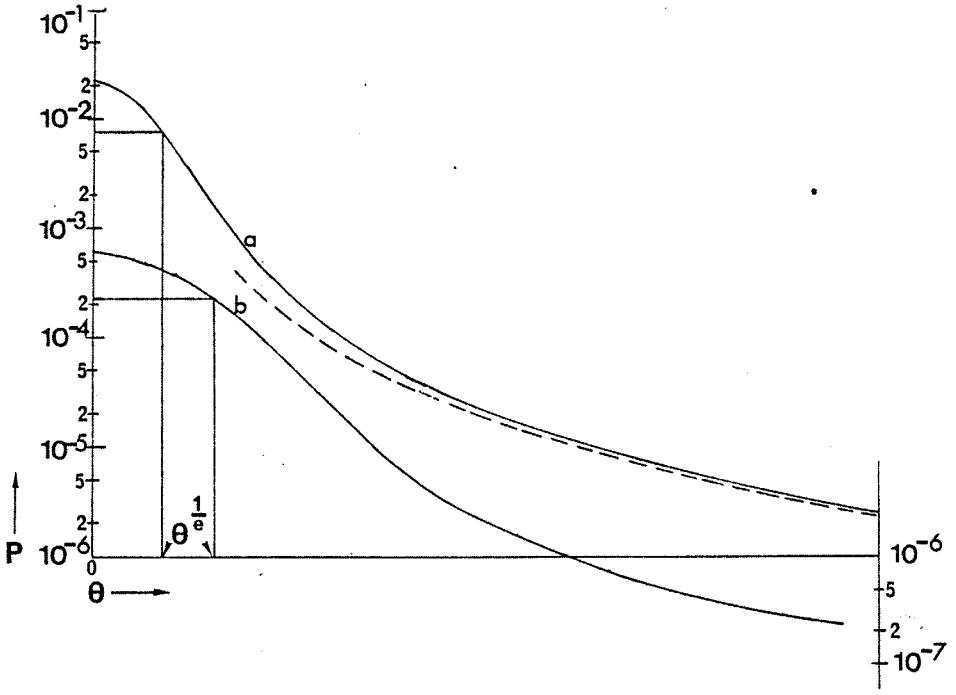

Fig. 4.5

a. corresponds to 8.3 μm of iron (s = 100 in ref. 6).

b. corresponds to 0.5 cm of iron (s = 60'000 in ref. 6).

The θ-values should be multiplied by 20 when going from a to b[6].

The normalization of the θ-axis may be found in the following way: for the angle $\theta^{1/e}$ where $P(\theta^{1/e}) = \frac{P(0)}{e}$ one uses the relation[7,8]

$$\theta^{1/e} = Z \frac{14 \text{ MeV/c}}{P\beta} \sqrt{\frac{L}{L_R}} \left(1 + \frac{1}{9} \log_{10} \left(\frac{L}{L_R}\right)\right) \left(1 + \frac{M^2}{Em_s}\right) \quad (4.2)$$

where Z is the charge and M the mass of the incident particle and E, P and β it's energy, momentum and velocity respectively. The scattering material has a thickness L, radiation length L_R and atomic mass m_s. With p = 10 GeV/c one finds for muons going through the above thicknesses of iron:

$$\theta_a^{1/e} = 0.0124 \text{ mrad} \quad \text{and} \quad \theta_b^{1/e} = 0.69 \text{ mrad}$$

Hence the scale on the θ-axis is roughly multiplied by a factor 20 when going from a to b.

The gaussian behaviour of the distribution for $\theta < \theta^{1/e}$ is interpreted as the result of many small angle elastic scatterings, this is called multiple scattering. The long tails come from multiple and a single scattering, the last becoming more important as the angle increases. The dashed line in Fig. 4.5 represents for case (a), the probability of a single scattering. There is a relation[7] between θ and the distance (projected into the same plane as θ) between the extended incoming trajectory and the actual position in space of the outgoing trajectory.

$$y_{proj} = \frac{L\theta}{\sqrt{3}} \quad (4.3)$$

where L still means the length of the scattering material. When L = 250 cm we obtain:

$$\theta^{1/e}_{L=250\,cm} = 15.4 \text{ mrad} \quad \text{and} \quad y_{proj} = 2.2 \text{ cm}.$$

We see from Fig. 4.5 that $P_a(\theta_a) = k_1 P_b(k_2 \theta_b)$ where k_1 and k_2 depend on L for a given material. This only means that as L increases the distribution blows up along the θ-axis. That is why it is interesting to define $\theta^{1/e}$. It should be noted that, $\theta_{mean} \approx \theta^{1/e}$, and that for two thirds of the distribution, $\theta < \theta^{1/e}$.

One may therefore conclude that the drift chambers will improve the resolution by at least a factor 2 for the X-coordinate [the scintillation counters give ± 6.25 cm, while the drift tubes will reduce this to ± 2.7 cm ($= \sqrt{1.5^2 + 2.2^2}$ cm)]. For the Y-coordinate, obviously, the drift chambers are essential.

---

* For a general discussion of multiple/single scattering phenomena, see ref. 6, and for an explanation of (4.2) see ref. 8.

B. Principles of a high energy calorimeter

It would be very difficult to describe in detail what happens when energetic hadrons or charged leptons impinge on several meters of iron. I will limit this section to the more essential features (energy resolution and shower parameters), with qualitative explanations.

Energetic particles hitting the calorimeter material (in our case $\sim$ 99% iron and 1% scintillator) will by electromagnetic and nuclear reactions, produce showers of secondaries. Let us assume that the whole shower will be contained within the stopping material, i.e. the particle looses all its energy to the calorimeter. As we have seen in chapter 2, charged particles going through a scintillator loose some of their energy: the loss is given by (4.2) if no particle nucleus interaction takes place*. A small fraction η, of this energy loss is converted into scintillation photons. The charge q, at the PM-anode, is proportional to the number of produced photons as long as their wavelength distribution is unchanged. By adding up all q's from counters which sample the shower, we will find a charge Q, which is directly related to the kinetic energy of

---

* For polystyrene, a much used scintillator material, the nuclear absorption length λ, with 5 GeV $\lesssim$ E proton, incident $\lesssim$ 25 GeV, is 68.5 cm. λ is a measure for how fast an inelastic nuclear reaction will occur. With λ = 68.5 cm the probability of reaction in 2 cm of such a scintillator is 1 - exp (-2/68.5) $\sim$ 3%.

In the case of reaction we may get substantial additional energy loss (and thus increased light yield) in the scintillator from secondary charged tracks. However, when triggering on straight through tracks, the energy loss is only governed by (4.1). With relativistic particles this energy loss is approximately energy independent, hence the light yield and the anode charge (q) will be rather well defined. We shall come back to anode charge distributions later when describing the calibration of the WA7 calorimeter. The origins of these distributions were explained in chapter 2.

the incident particle. This is so because the higher the energy the higher is the multiplicity in the shower. Assuming a proportionality between multiplicity and energy (i.e. doubling the energy will in the mean result in a multiplicity twice as high for all particles in the shower throughout the whole energy spectrum; there will be twice as many 10 MeV protons, 15 MeV neutrons etc. etc.), the wavelength spectrum of all light produced will be energy independent, and hence $Q \sim E$. We shall see later that data confirms a very near linear Q - E relationship. With or without linearity; knowing $Q = Q(E)$ for a certain particle type, means having an absolute calibration of the detector. The fact that we only sample the shower (therefore often called a sampling calorimeter), introduces fluctuations in Q for a given E.

In the following I shall mainly describe the gross features of hadron initiated showers. Important parameters for calorimeters and showers do not depend on the hadron type,* therefore no discrimination will be made when presenting the results. For hadron showers, big variations in the "seen energy", essentially, $n_{mean} \times$ (the ionization caused by fast and slow charged particles entering the scintillators), can be explained by the way in which the shower is initiated. The primary reaction between hadron and nucleus will produce a varying number of π^0's. While protons, neutrons, π^- and π^+'es will loose a lot of their energy in consecutive nuclear reactions, the π^0's only loose energy through electromagnetic interactions. This qualitatively explains why the π^0 showers will have a more well defined Q. For hadrons interacting strongly there are many channels of energy dissipation:

---

* As long as the energy is above some GeV's and the particle is charged.

a) production of more energetic secondaries,

b) of slow neutrons, protons and α's, E $\sim$ 8 MeV,

c) of fast neutrons and protons, E $\sim$ 165 MeV.

d) nuclear binding energy, fission products will often have weaker binding.*

We will only sample some of energetic secondaries and some of the protons. Therefore depending on how the nucelar cascading takes place, we may get important fluctuations. To summarize, the contributions to the energy resolution come from:

1) Spread in longitudinal coordinate of primary interaction; that part of the shower which reaches the sampling planes fluctuates.

2) The ratio between electromagnetic and hadronic component of the shower varies. It is these fluctuations between the electromagnetic and hadronic shower component, which is the ultimate limiting factor in the resolution. There are no remedy for these fluctuations, while others may at least be reduced.

3) The hadronic as well as the electromagnetic component themselves also fluctuate, the contribution from the hadronic being the most important. Here variations in the energy used for breaking up nuclei, play a central role.

---

* Some material like ^{238}U produce energy (mostly as neutrons and γ's) when fissioning. Therefore using uranium as stopping material (instead of iron), will mean more signals from the sampling counters which again, as we shall see, implies better energy resolution. Fabian and Willis have shown[9] that uranium produces a signal 40% bigger than iron and that this improves the resolution by a factor 2.5 (the relative energy resolution at 10 GeV for example, goes from 0.20 to 0.08).

4) Fluctuations in that part of the shower which escapes through the boundaries of the calorimeter (ν's , μ's and n's). However, calorimeters are mostly built big enough so that the energy loss out through the boundaries is at most some percent. In this case the effect on the overall energy resolution will be negligible.

When one wants to measure the energy in practice, this is done by adding signals from all counters which may have caught parts of the shower. The total signal I(t), then has to be time integrated yielding a total charge Q. It is common to define the charge unit as the charge of the signal which a minimum ionizing (straight through) particle produces in one counter (to be more precise, the position of the peak since we will observe a charge spectrum from such a particle). This unit will be denoted ep, for equivalent particle. Below in Figs. 4.6 and 4.7 are shown Q - measurements for two energies done at Fermilab with an iron test calorimeter[10].

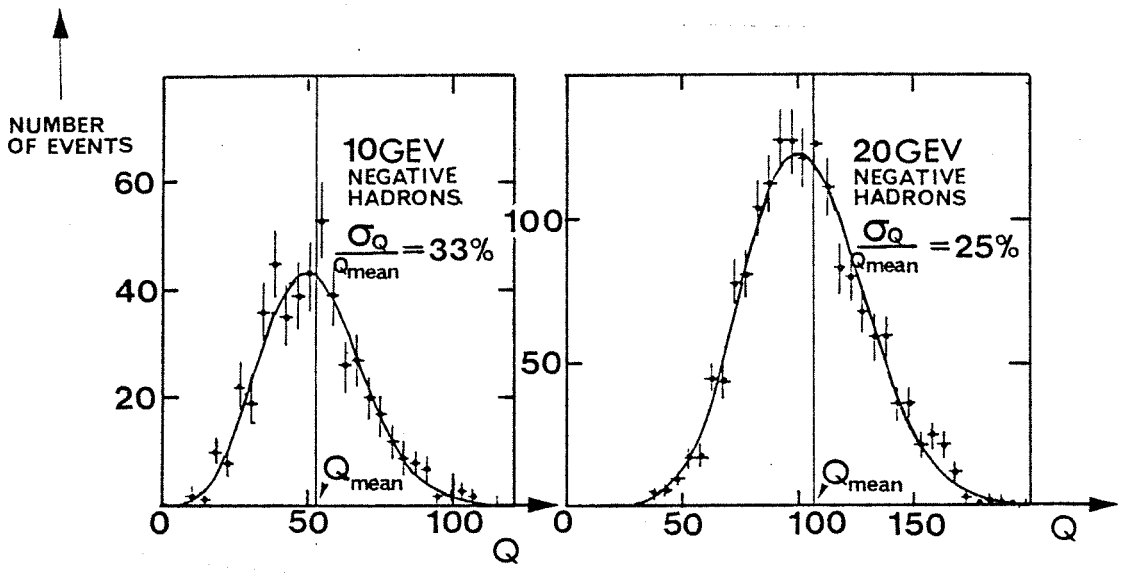

Fig. 4.6

Data from ref. 10

Q is in units of equivalent particules, ep.

The curves are best fitted with poisson distributions, values of $\frac{\sigma_Q}{Q_{mean}} \equiv \sigma_{R,Q}$ are given (σ_Q = one standard deviation). $\sigma_{R,Q}$ is the relative resolution of the total charge measurement. $\sigma_{R,Q} = \sigma_{R,E}$ because Q is propertional to E. This is seen to hold very well down to 1.5 GeV, cf. Fig. 4.7.

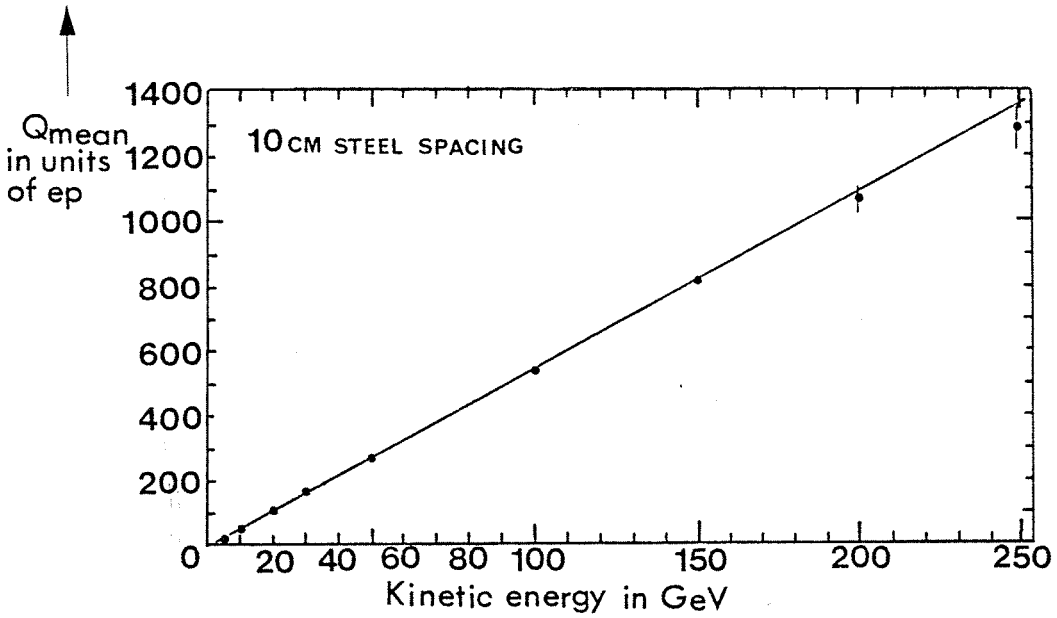

Fig. 4.7

Example of absolute energy calibration from ref. 10. The data points are obtained by measurements like the ones shown in Fig. 4.6.

The test calorimeter consisted of sandwiches of plastic scintillators (0.94 cm thick) and 10 cm steel plates. There were a total of 14 sampling counters. By appropriate constraints the background and shower leakage were minimized. This was done by 1), defining incoming beam well, 2), installing Pb-filter in the beam, 3), insuring that nothing fires the last counter and finally by 4), demanding that the shower doesn't die too quickly after its starting point (which would be a clear signature of an electron).

This last constraint was imposed by demanding sufficient signals in 3 counters after the primary interaction point. Possible shower leakage out the sides of the calorimeter is responsible for up to 6% energy loss (not seen), which again may worsen the energy resolution with 6%[11]. At 10 GeV this meant a 2% absolute increase of $\sigma_{Q,R}$. The rather big transverse energy loss is due to the reduced dimensions of this test calorimeter (the steel plates were 35 x 25 x 10 cm^3).

Many groups[10,12,13,14,15] have measured the important quantity $\sigma_{R,E}$ (the relative energy resolution) as a function both of energy and the sampling thickness s, of the stopping material.

The most interesting data are in Fig. 4.8. Error bars are not drawn. For the 10 GeV CITF[10] data the relative errors are $\sim \pm$ 50%, otherwise never larger than $\pm$ 10%, HPWF data[13] were taken with a huge liquid scintillator total absorption calorimeter, otherwise steel was used as stopping material. The advantage with a liquid scintillator is that the same medium acts as stopping and scintillation material, one therefore ensures that all the energy loss which may be seen, actually will be seen, which is not the case with a sandwich arrangement. CITF[10] and CDHSB[12] curves may be fitted very well with $E^{-\frac{1}{2}}$ dependencies, $\sigma_{R,E} = k(s)\ E^{-\frac{1}{2}}$. k seems to be a near linear function of s when $s \geq 15$ cm, see Fig. 4.9 (data from ref. 10).

The behaviour of $\sigma_{R,E}(s)$ and k(s) reflect the statistical nature of our measurements. Assume that Q is poisson distributed, then increasing the statistics by a factor 2 (by doubling E and hence Q) means decreasing $\sigma_{R,E}$ a factor $\sqrt{2}$. When reducing s to s/2, things are more complicated; with good sampling, $s \lesssim 15$ cm, Q will be a factor 2 higher which implies that $\sigma_{R,E}$ should be better by a factor $\sqrt{2}$ (from Fig. 4.9 one sees that $\sigma_{R,E}(10) \sim \sqrt{2}\ \sigma_{R,E}(5)$ and $\sigma_{R,E}(15) \sim \sqrt{3}\ \sigma_{R,E}(5)$). So for small s, $k \sim s^{\frac{1}{2}}$, which is as expected if one statistical parameter (i.e., the shower size Q) is

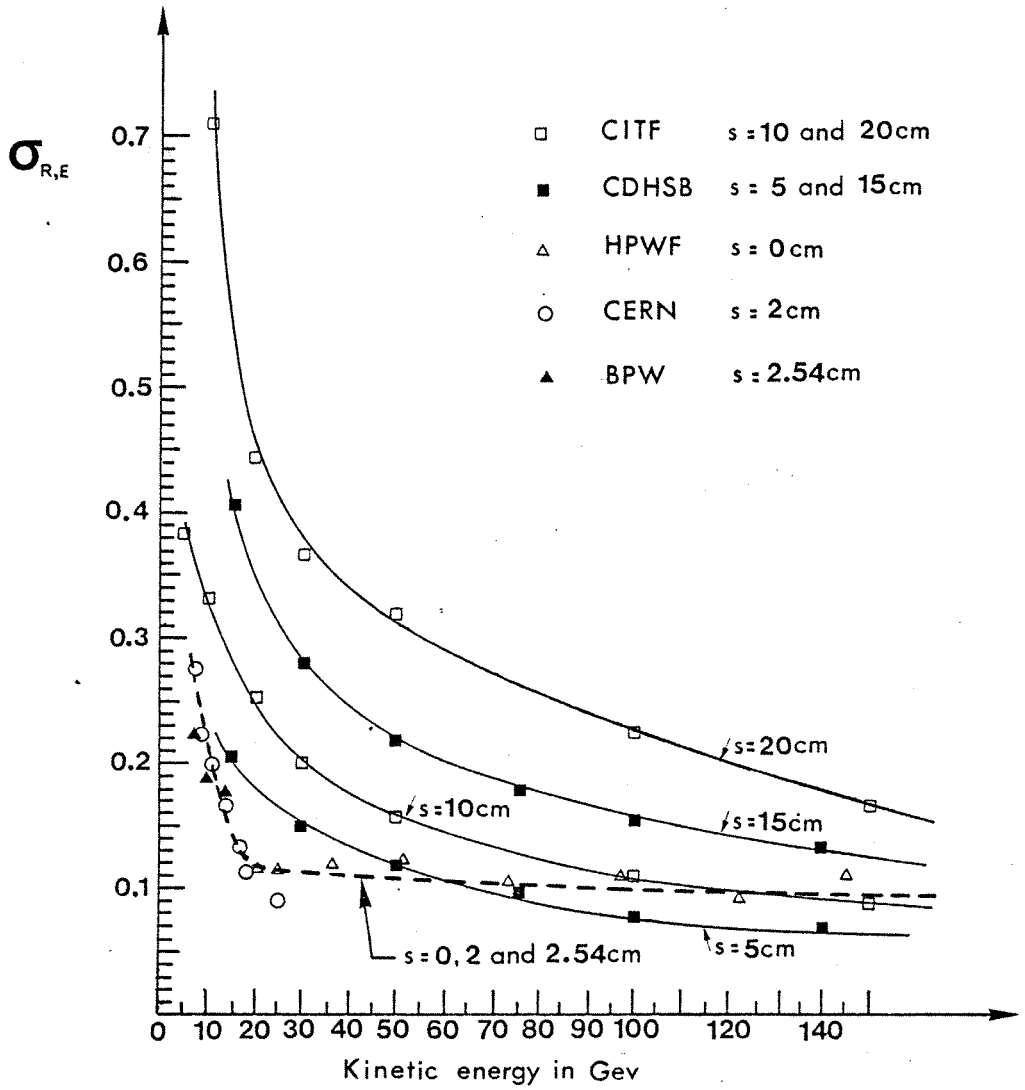

Fig. 4.8

Energy resolution versus energy for different values of s.
The data have been gathered from:
Caltech - Fermilab (CITF) ref. 10,
CERN - Dortmund - Heidelberg - Saclay - Bologna (CDHSB) ref. 12,
Harvard - Pennsylvania - Wisconsin - Fermilab (HPWF) ref. 13,
(CERN) ref. 14 and
(BPW) ref. 15.
HPWF data seem to be shifted especially at high energies.
This may be due to different stopping materials; all experiments except HPWF used iron. The dotted curve is drawn by hand along HPWF, CERN and BPW data points.

involved. For poor sampling, $s \geq 15$ cm, data[10], in the mean, still indicate a doubling of Q. A qualitative study of shower develepment curves (Fig. 4.10.a) will explain why we (for $s \geq 15$ cm) get a faster $\sigma_{R,E}$ dependence on s, $\sigma_{R,E}$ is roughly proportional to s, see Fig. 4.9.

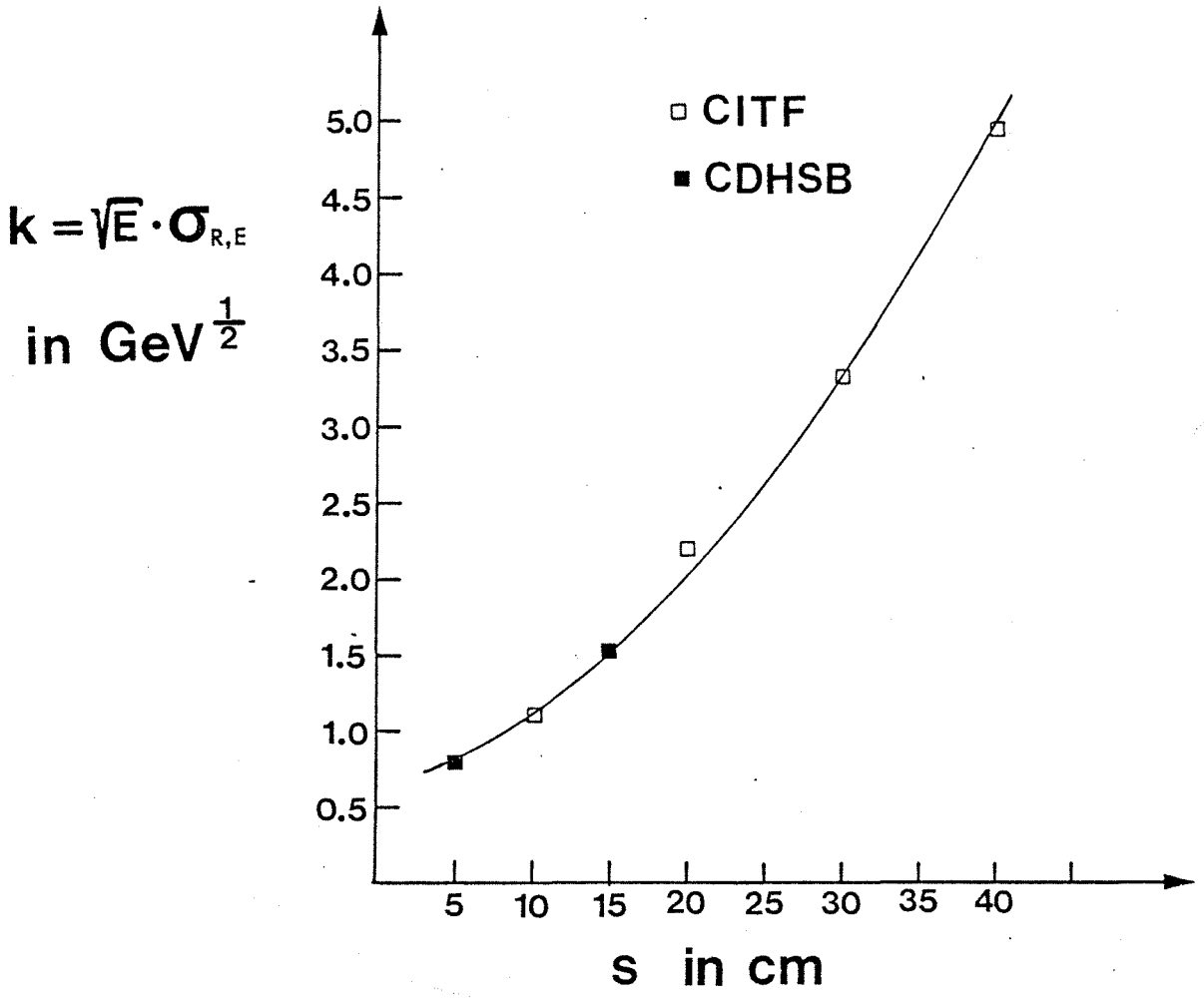

Fig. 4.9
k as a function of the iron slab thickness s. For fixed E, k is essentially the energy resolution. Data from refs. 10 and 12.

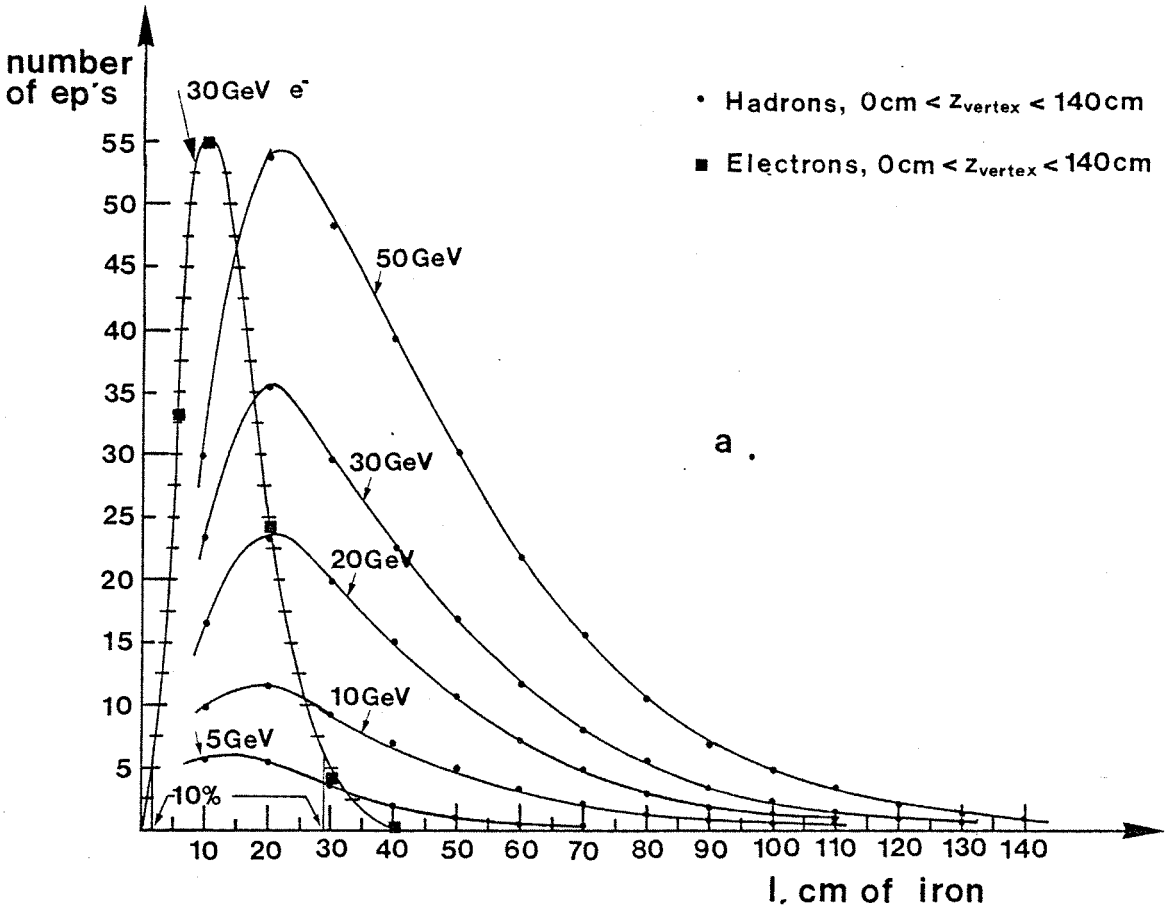

Fig. 4.10 a

All curves except the barred one are hadron data from ref. 10. The barred one is electron data from ref. 12. . z_{vertex} is the longitudinal coordinate of the primary interaction point in the iron, see fig. 4.11. The vertical axis gives the mean shower signal in units of ep, for the various incident energies.

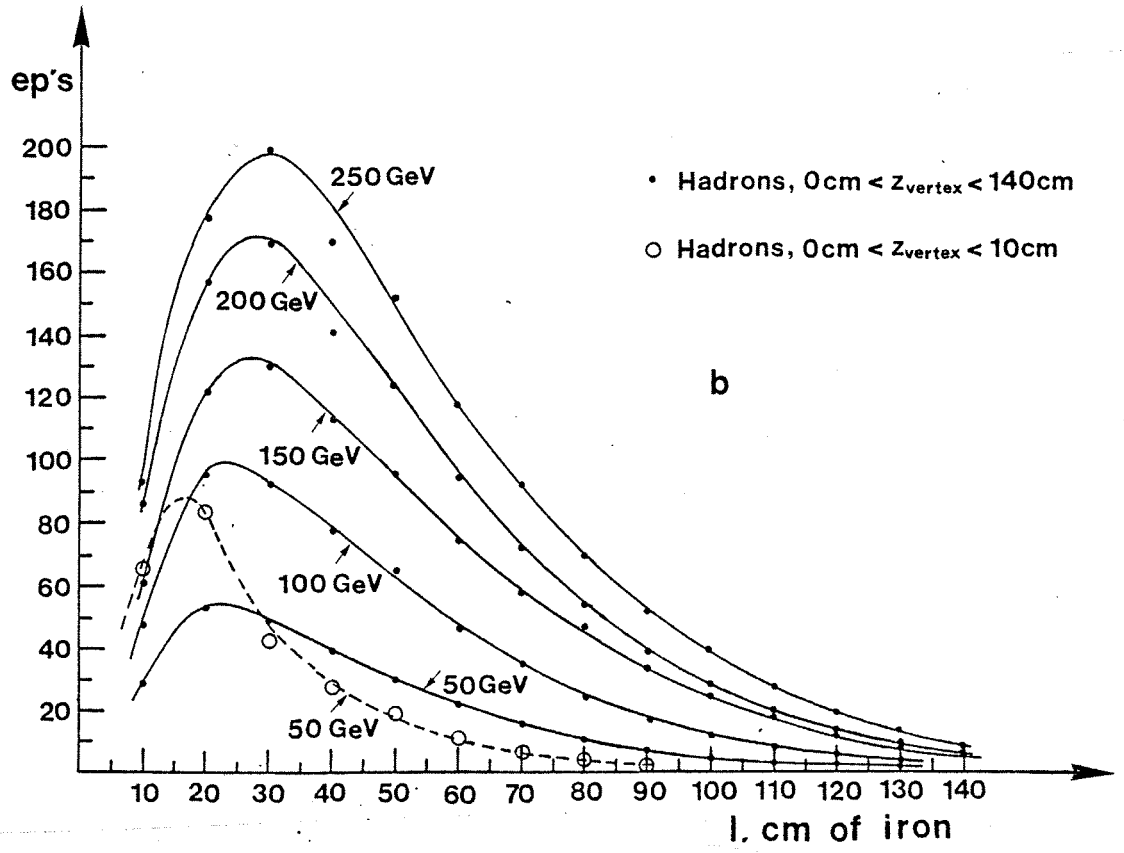

Fig. 4.10.b

All curves are again hadron data from ref. 10. While the fully drawn graph represents the shower signal with virtually no constraintes on the primary point of interaction, the dashed curve represents the case in which this point is limited to the first 10 cm of iron.

In Figs. 4.10.a and b are shown shower development curves for several incident energies[10]. The vertical axis is the mean number of equivalent particles (ep) after a certain length of iron. The starting point for the shower is assumed to be distributed as, $P(l) = \exp(-l/\lambda_{iron})$, where λ_{iron} is the nuclear absorption length (= 17.1 cm). Notice that we have good longitudinal containment, only for the highest energies may some percent escape out of the back. Comparing the two 50 GeV curves, we observe the smearing effect due to the spread of the first interaction point of the incident particle.

The s-dependence of $\sigma_{R,E}$ for large s may now be explained qualitatively in the following way. We have already seen that a varying fraction of the shower is electromagnetic, coming from π^o's which quickly ($\sim 10^{-16}$ sec) decay into two γ's, which again produce electron pairs and γ's until the energy falls below the threshold for pair production. What one observes is an electron-positron shower penetrating the scintillators. An energetic electron will cause the same type of shower. From fig. 4.10.a one sees that, depending on where exactly the shower started, one will get enormous fluctuations in the fraction of the electromagnetic shower which is sampled. The shower, in the mean, is 30 cm long, cutting at 10% of maximum shower development in both ends (see fig. 4.10.a). Therefore, with s = 10 cm one will sample it three times, with s = 15 cm twice and with s = 20 cm once or twice. Especially in the last case will the signal depend completely on where the shower started, these fluctuations are obviously no longer related only to reduced statistics, but also to the number of sampling points within the shower.

Notice how easy it is to descriminate between electromagnetic and hadronic showers, the former building up and dying much faster than the latter.

I shall end this general discussion about calorimeters with some remarks about transverse containement, in a plane orthogonal to the incident particle trajectory. Fig. 4.12.a and b show how the lateral shower develops at 50 and 140 GeV[12]. The two sets of curves in Fig. 4.12 are $\rho(r,\phi)$, which is the number of equivalent particles pr. cm^2 in r and ϕ (see fig. 4.11), integrated 90 cm along the z-axis (sampling every 5 cm and imposing a primary reaction in the iron at 6 cm < z < 30 cm), and I(r), where $I(r)\,\Delta r = \pi r \rho(r,\phi)\Delta r$, that is, the number of ep's in a ring with radius r and Δr = 0.5 cm around the z-axis. The curves are fits to the data from ref. 12.

At 50 GeV: $\rho(r,\phi) = A_1 e^{-b_1 r} + A_2 e^{-b_2 r^2}$

where $A_1 = 1.11$ ep, $A_2 = 13.23$ ep, $b_1 = 0.155$ cm^{-1} and $b_2 = 0.076$ cm^{-2}

At 140 GeV: $\rho(r,\phi) = A_1 e^{-b_1 r} + A_2 e^{-b_2 r^2} + A_3 e^{-b_3 r^2}$

where $A_1 = 1.76$ ep, $A_2 = 0.649$ ep, $A_3 = 55.25$ ep, $b_1 = 0.142$ cm^{-1}, $b_2 = 0.0128$ cm^{-2} and $b_3 = 0.1108$ cm^{-2}

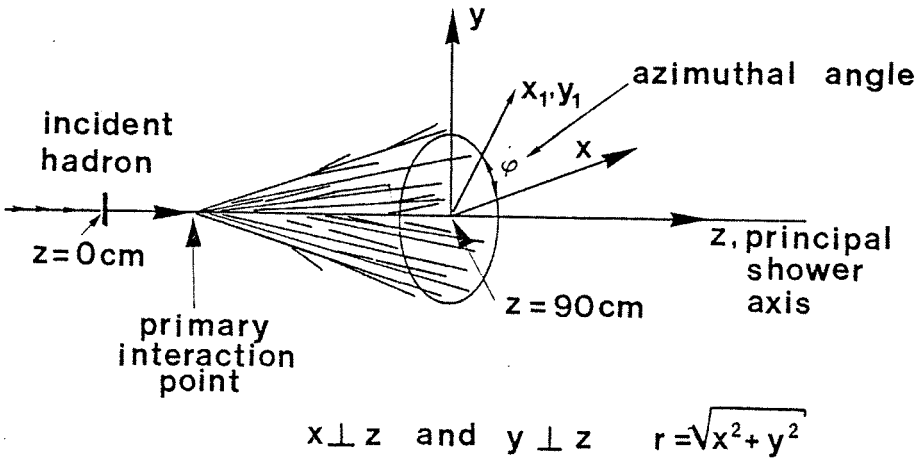

The shower is sampled at 5 cm intervals and the primary interaction point has to be such that, $6 < z < 30$ cm.

These parameterizations reproduce the data well, for 50 GeV to within ± 2% ($r < 25$ cm), for 140 GeV within ± 2.5% ($r < 30$ cm). Notice that there is a powerful central core which extends to $r = 7$ cm. Roughly 75% of the shower energy is deposited inside a circle with a radius of 7 cm. For $r < 7$ cm the ρ-distribution is mostly governed by the e^{-br^2} term, while outside the simple exponential (e^{-br}) takes over, I (r) therefore has long tails, 90% and 95% containement is reached at 15 and 20 cm respectively (see fig. 4.13). While the size of the shower core does not change with energy (HWHM, the half width at half maximum, is 3 cm at 50 GeV and 2.5 cm at 140 cm), certainly the intensity does; the core is more than 3 times as strong at the higher energy.

Also the extension of the tails is energy independent; for $r > 25$ cm the shower fraction located in the tails is the same at both energies, see Fig. 4.13. However, the tail-signal is energy dependent, for $r > 15$ cm the 140 GeV - signal is twice the 50 GeV - signal, see Fig. 4.12.

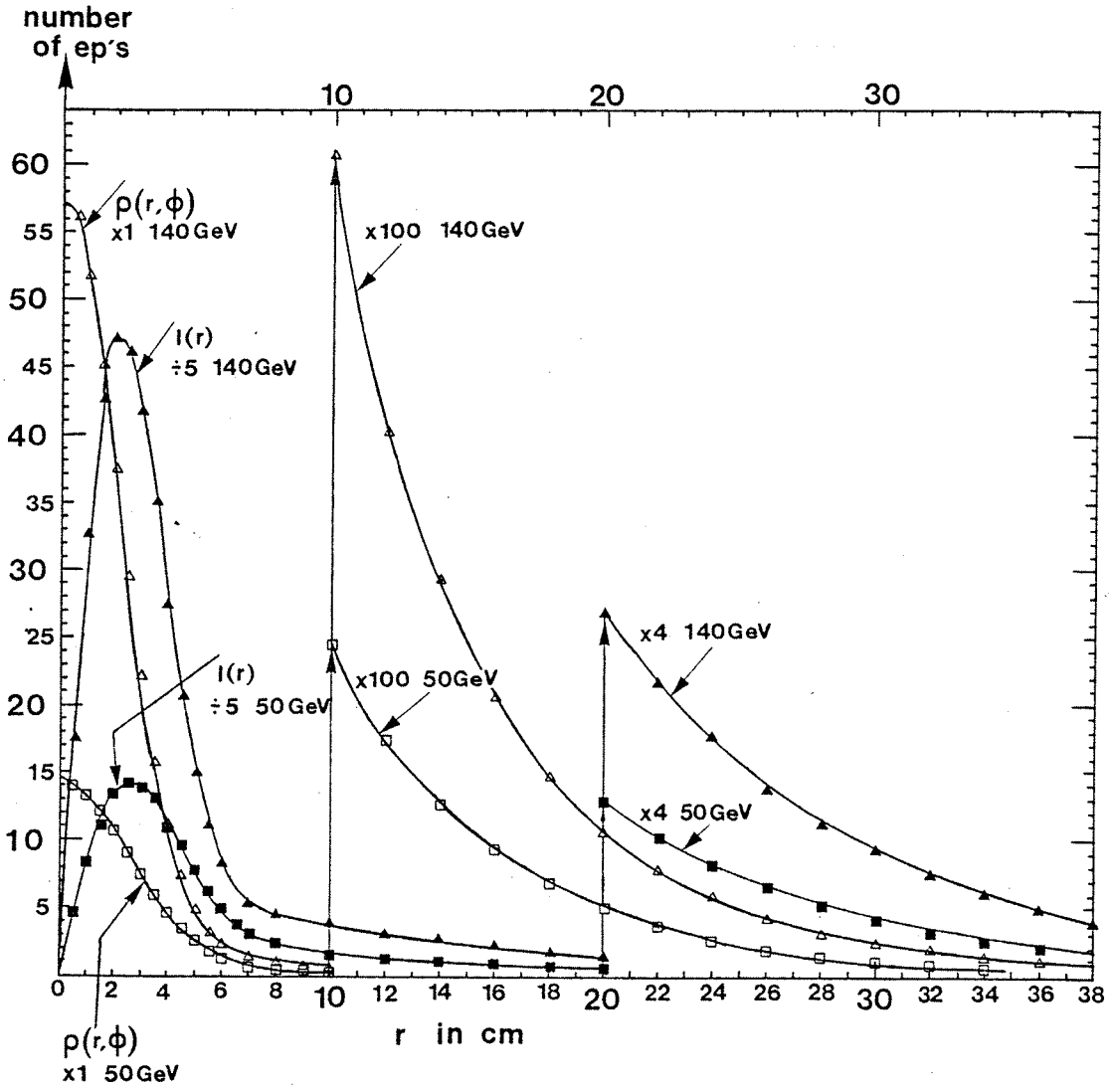

Fig. 4.12

ρ and I as a function of r (in number of equivalent particles) at 50 and 140 GeV. I is devided by 5 for 0 cm < r < 20 cm and multiplied by 4 for 20 cm < r < 40 cm. ρ is multiplied by 100 for 10 cm < r < 40 cm. The curves were obtained by fitting data from ref. 12. For more details and definitions of ρ and I, see the text.

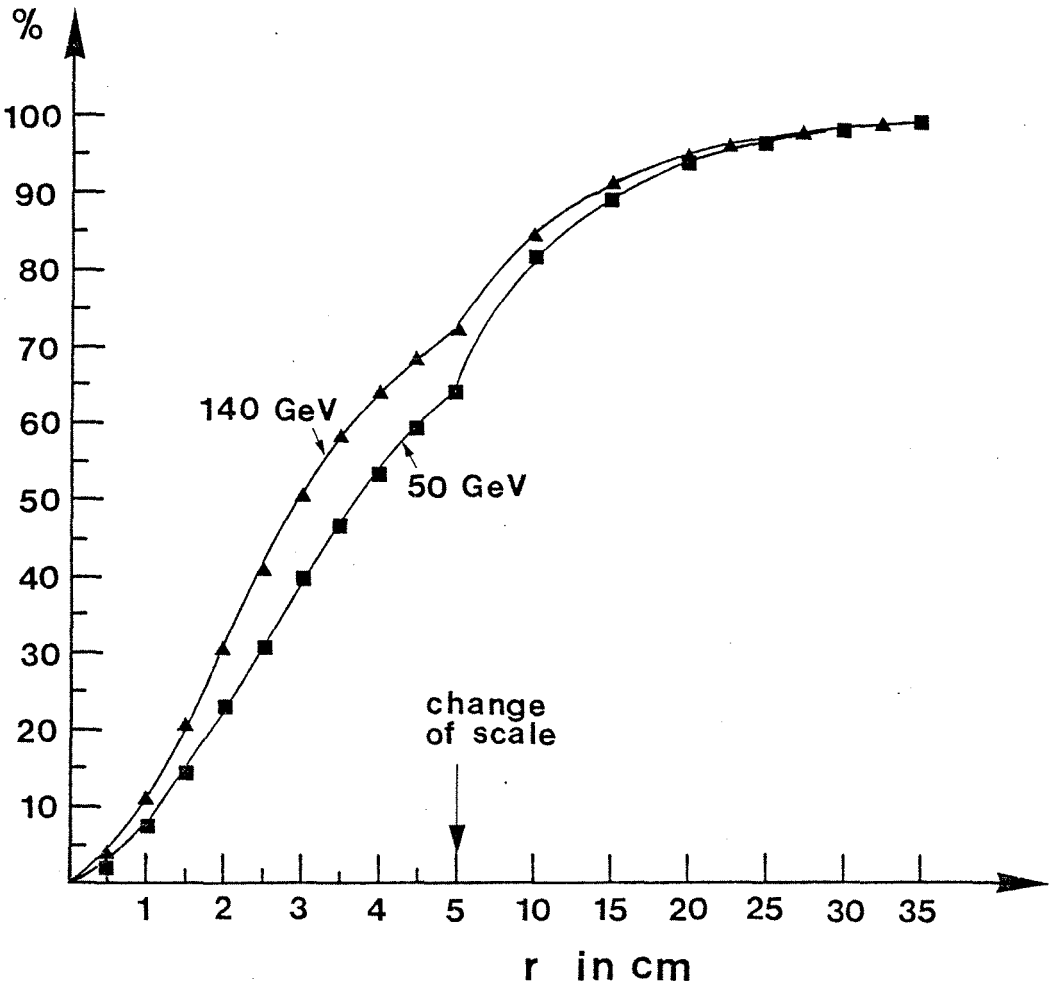

Fig. 4.13

Percentage of the shower contained inside a radius r around the principal shower axis.

C. Principle of a muon-filter, some cross sections.

Heavy materials such as iron act very efficiently as particle filters, only letting neutrinos and muons through. As already mentioned, this is due to the fact that these leptons rarely interact in such a way that they loose a lot of their energy. The proton-proton total cross section, σ_{pp}, above 5 GeV is ≈ 40 mb[7], and the total inelastic is close to 30 mb[7]. This should be compared with the muon-proton total cross section, $\sigma_{\mu p}$. For the process, $\mu p \rightarrow \mu + X$, where $|t|_{\mu} > 0.1$ (GeV/c)^2, $\sigma_{\mu p}$ is equal to roughly 3 μb with a muon energy of 10 GeV, (integrating data from refs. 16 and 17). As an example, compare the penetration of 10 GeV muons and protons in liquid hydrogen and iron.

A beam of particles traversing a material is attenuated according to

$$I = I_o e^{-n\sigma x} \qquad (4.4)$$

where I_o is the initial intensity, n the number of targets per volume (atoms, nuclei or nucleons) each with a cross section σ for causing the incident particle to be "lost"; meaning that the particle either is deviated too much in a collision, or simply lost in an inelastic collision. Therefore σ is not σ_{TOTAL}, but $\sigma_{TOTAL} - \sigma_{not\ lost}$ where $\sigma_{not\ lost}$ is the cross section for a scattering (elastic or inelastic) less than an angle $\Delta\theta$ of the incident particle. However, in this discussion it is unimportant to fix a $\Delta\theta$ and estimate $\sigma_{not\ lost}$ for the hadronic reactions at high energies; as mentioned above, the inelastic cross section is 3/4 of the total in pp-scattering at 10 GeV and therefore including or excluding $\sigma_{not\ lost}$, since it has mainly an elastic contribution, will not drastically alter the attenuation length $\lambda_p\ (H_2) = \frac{1}{n_p \sigma}$. Using $n_p = 4.23 \times 10^{22}$ cm^{-3}

---

* t is the 4-momentum transfer squared for the muon, that is $t \equiv (p_{after} - p_{before})^2 = (E_a - E_b, \vec{p}_a - \vec{p}_b)^2$

and $\sigma = \sigma_{pp} = 40\,mb$, we find $\lambda_p\ (H_2) = 591$ cm. For muon-proton reactions $\Delta\theta$ has to be fixed. This comes from the fact that the interaction is electromagnetic and therefore the cross section $\to \infty$ when $|t| \to 0$ (when giving hadron-hadron cross sections, naturally the electromagnetic contribution is subtracted). With a muon-momentum of 10 GeV/c the $|t| > 0.1$ cutoff corresponds to demanding a scattering $\Delta\theta$ of more than 32 mrad in the lab-system. Considering events with $\Delta\theta < 32$ mrad as "not lost", we get the attenuation length for 10 GeV/c muons in liquid hydrogen,

$$\lambda_\mu(H_2) = (\sigma_{\mu p}\, n_p)^{-1} = (3 \times 10^{-30} \times 4.23 \times 10^{22})^{-1}\ cm = 78802\,m$$

So protons are stopped a factor 10^4 faster than muons. For heavier materials one has to use the correct nuclear cross sections. The proton-Fe total cross section at 10 GeV, σ_p (Fe), is equal to 1.16 barn[7], yielding an attenuation length,

$$\lambda_p(Fe) = (\sigma_p(Fe) \cdot n_{Fe})^{-1} = (1.16 \times 10^{-24} \times 8.46 \times 10^{22})^{-1}\ cm = 10.2\ cm$$

σ_μ(Fe) may be split in $\sigma_{\mu,\,el}$ (Fe) and $\sigma_{\mu,\,inel}$ (Fe). From refs. 16 and 17 with $|t| > 0.1$ (GeV/c)^2, we find $\sigma_{\mu p,\,el} = 1.3$ μb and $\sigma_{\mu p,\,inel} = 1.5$ μb. May et al[18] have shown that $\sigma_{\mu,\,inel}$ is proportional to A^n where A is the atomic number of the scatterer, and n is a number very close to 1. So $\sigma_{\mu,\,inel}$ (Fe) $\sim 56 \times 1.5$ μb = 84 μb. To get an upper limit for $\sigma_{\mu,\,el}$ (Fe), assume that the nucleus is pointlike with a charge Ze. One may therefore use the famous Rutherford scattering formula* to obtain : $\sigma_{\mu,el}(Fe) < Z(Fe)^2 \cdot \sigma_{\mu,el} = 1.3 \times 26^2$ μb = 879 μb, where Z (Fe) is the atomic mass number for iron. $\sigma_{\mu p,elastic}$ was obtained by integrating ref. 17

---

* The differential coulomb scattering cross section is given by,

$$\frac{d\sigma}{d\Omega} = \frac{q_1^2\, q_2^2}{16E^2 \sin^4(\theta/2)} \qquad \text{where}$$

q_1 and q_2 are the charges involved. E and θ are the energy and angle of the scattered particle. In reality we have a charge distribution in the nucleus which lowers very much the cross section at a certain t-value compared to the cross section one would have had with a pointlike nucleus. (cont. next page).

data for 0.1 $(GeV/c)^2 < |t| < 0.85\ (GeV/c)^2$. This corresponds to the same θ-range, 32 mrad $< \theta <$ 95 mrad, for both μp and μFe scattering (the angles are small and the targetsvery heavy compared to m_μ). It is therefore correct only to multiply with $Z(Fe)^2$, without correcting for the (very small) change in the θ-range. σ_μ (Fe) < (84 + 879) μb = 963 μb which leads to λ_μ (Fe) > $(\sigma_\mu\ (Fe) \cdot n_{Fe})^{-1}$ = $(879 \times 10^{-30} \times 8.46 \times 10^{22})^{-1}$ cm = 13443 cm . Therefore in iron, $\lambda_\mu(Fe)/\lambda_p(Fe) \approx 10^3$. Inserting λ_μ(Fe) in (4.4), one sees that through 2.5 m of iron, one would loose < 1 - exp (-250/13443) = 2% of 10 GeV/c muons.

Notice that even if the μ-electron cross section is big (the cross section for scattering more than 1.8 mrad in the lab-system of a 10 GeV muon, is 0.4 mb[19]), this does not influence the absorption length. The electrons are so light that no matter the scattering angle in CM, when Lorentz-transformed to the lab-system this angle is always very small (the maximum scattering angle of a 10 GeV muon on an electron is 5 mrad in the lab-system!).

So, with a well defined coincidence between signals from the upstream and downstream side of a particle filter, one may very efficiently select muons (in WA7 we used H1, PR1, C1 and C2 as upstream detectors in the left arm, L3 as the downstream detector). There is a very small chance of a hadron punch through (see chapter 4B). However, ADC information from L2 and drift chambers hits, could be used to discard fake muon candidates off-line.

(cont.) Notice also that the Rutherford cross section is not correct even if the particles involved were pointlike. The reason is that the electron is a Dirac particle with spin; it is only at low energies ($M_{proton} >> E_{electron}$) and for small scattering angles, that $d\sigma/d\Omega$ would be correct. Otherwise a correction factor has to be added, however, this does not change the charge-dependence of $d\sigma/d\Omega$ ($= q_1^2 q_2^2$). The estimated upper limit for $\sigma_{\mu,el}$(Fe) is therefore still valid.

D. Use of the detector in the present set up; how a 5-plane and 14-plane calorimeter would affect the trigger rates.

From Fig. 4.1 one sees that the left arm is equipped with two planes in the iron (one after 40 cm, the other after 60 cm iron). This corresponds to two sampling planes in a calorimeter, their location being where an average hadron initiated shower has its maximum, see Fig. 4.10.a and b. The energy resolution with only two planes is very poor, and therefore the total signal cannot give any energy information. This should be evident from the discussion in chapter 4B. As an example, the mean number of equivalent particles (ep's) produced by a 15 GeV hadron after 40 and 60 cm of iron is 12.6 and 4.4 ep's respectively, but the corresponding root mean square fluctuations are 14.7 and 9.0 ep's[12]! With two planes the r.m.s. will be somewhat less than $\sqrt{14.7^2 + 9.0^2}$ ep's = 17.2 ep's (because the fluctuations are correlated). However, this does not make the energy information good enough to be useful. The momentum/energy is relatively much more precisely determined by off-line track reconstruction through a known magnetic field. The interest of (even only) these two planes comes from the fact that the signal given by hadrons is almost always very superior to all possible electron signals. As an example, running elastic scattering with a 20 GeV/c hadron beam incident, the forward particle (in the case of π p scattering) will at least have an energy of 10 GeV*, hitting the calorimeter it will in the mean produce 9.3 ep's in the two planes (see Fig. 4.10.a and b). The chances of producing less than one ep is less than 14%[20], this should be compared with the chances that a 20 GeV/c electron produces at least one ep in the two planes. In the mean a 20 GeV/c electron produces $\sim$ 0.2 ep's in a big enough scintillator located 40 cm inside the iron[12].

---

* The scattered pion may have less energy than 10 GeV, however, that would be scattering outside the acceptance at 20 GeV, which stops roughly at 90° in the center of mass system.

Since the probability distribution (for observing a certain number of ep's) is unknown, the actual probability of having more or equal to one ep cannot be given, but one can be sure that it is very low. In other words the discrimination between electrons and hadrons is very easily obtained by demanding an appropriate signal from L1 and L2. We shall come back to how this is done in practise in chapter 4E.

Up to now the main interest of these calorimeter planes has been the nearly 100% efficient vetoing of electrons (most of the electrons were of some GeV, and for these the veto was fully efficient). One has been able to reduce the trigger rate by roughly a factor two by imposing an appropriate threshold requirement on the total signal from the two planes. The effect on the trigger rate when changing the thresholds, will be studied in chapter 5B.

The Cerenkovs C1 and C2 select rather well hadrons with β ($=v/c$) above n^{-1}, where n is the refractive index of the Cerenkov gas. However, to be able to descriminate between pions and kaons with C1 and C2 at the relevant energies (for 20 GeV elastic scattering it is in the range from $\sim$ 10 GeV to $\sim$ 18 GeV), the refractive index has to be fixed so that the pion threshold becomes rather low and the trigger logic will accept pions with momenta down to roughly 5 GeV/c (see Fig. 4.14.a). It is therefore interesting to try to get rid of these low energy pions which make up an important fraction of the total spectrum. In addition, one may expect quite a lot of low energy hadrons and muons to satisfy the trigger conditions. In the following I shall study the momentum spectra in the forward arm for our three elastic trigger types, the pion, kaon and proton trigger. It will appear that a lot of low energy events satisfy the trigger conditions, which is mainly due to the low Cerenkov thresholds (for the pion and kaon trigger), and the non existance of momentum cuts for the proton trigger. So even at 20 GeV elastic scattering, a more fully equipped calorimeter could do very well to reduce the trigger rate. For the following studies of the momentum spectra, the incident beam is always +20 GeV/c.

1) For the pion trigger one demands a coincidence C1 * C2, even so, down to a momentum of 3 GeV/c there will be some population in the histogram (see Fig. 4.14.a). This may be an electron, but also a pion firing one Cerenkov properly, in this case C2 (which had a pion threshold around 3 GeV/c) and then, either a random coincident signal in C1 or more probably a related signal (which may come from a nuclear reaction, a knock-on electron, a desintegration of the particle etc.), will produce the coincidence. Below 3 GeV a coincidence between two improper Cerenkov firings is very unlikely, and this part of the spectrum is only made up of electrons.

2) For the kaon trigger one only demands one Cerenkov (C2), and as seen from Fig. 4.14.b, a very important fraction of the kaon triggers are low momentum signals. One would expect that electrons very easily could fire the kaon trigger, the only condition to be fulfilled being that the electron in the forward arm has a coincident signal from cedar 2 (see Fig. 5.9) which flags incoming kaons. And in fact for about 10% of the reconstructed kaon triggers, both C1 and C2 have fired.

However, studying these 'kaon-electrons' in detail, one finds that never will the track traverse or even pass in the vicinity of the fired mirror in C1, while the opposit is true for C2, here only 8% of the tracks pass outside the fired mirrors (in 3% of the cases of a C1 - C2 coincidence, apart from one good firing in C2 where the track is correlated to a fired C2 - mirror, there will be at least one additional non correlated mirror that fires). These triggers therefore are not electrons, but heavier particles such as muons, pions and kaons. The momentum distribution in Fig. 4.14.b also confirms this since the number of entries below the pion threshold (at about 3 GeV/c in C2) is very low. The coincident signals from C1 always came from either mirror C12 or mirror C15, see Fig. 1.2.b, that is, from the mirrors closest to the beam, where the chances of having random coincidences naturally are highest. Tracks originating from

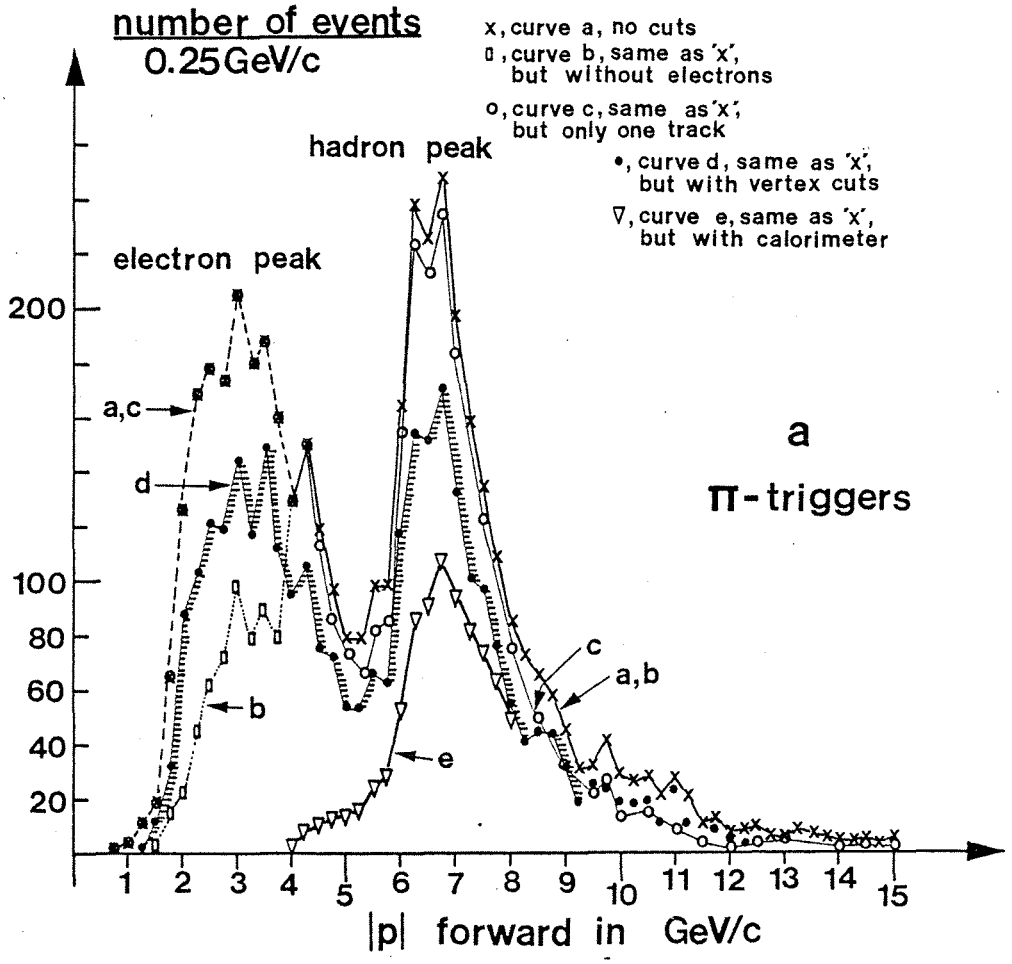

Fig. 4.14.a

The momentum spectra for reconstructed pion triggers from run number 1950, elastic scattering with + 20 GeV/c incident. For all curves is shown the absolute value of the momentum. In the case of more than one track the absolute values of the momenta are added. A comparison between curves a and c shows that multiple track triggers does not change the overall spectrum significantly (the mean increases by 6%, from 5.43 GeV/c to 5.76 GeV/c, when also including multiple track candidates). Demanding that at least one vertex is reconstructed within target (curve d) reduces the statistics by 32%), but does not alter the shape at all, the mean is at 5.75 GeV/c. However, the shape is drastically changed when electron candidates are substracted from curve a, the result is in curve b. An electron signature is given by a firing of both C1 and C2 which is not incompatible with the reconstructed track, in addition the $\Sigma|p_i$, forward| has to be less than 4 GeV/c, a cut which is clearly seen (curve b). The reduction observed when excluding unambiguous electron triggers, is most important for $|p| \sim 2$ GeV/c where it is more than a factor 5. The overall rejection is 20%. Curve e corresponds to the calculated spectrum imposing a signal of at least 30 equivalent particles from a fully equipped calorimeter in the forward arm (see text). The rejection is 68.8% or a factor 3.2. The rejection is more important the lower the momentum.

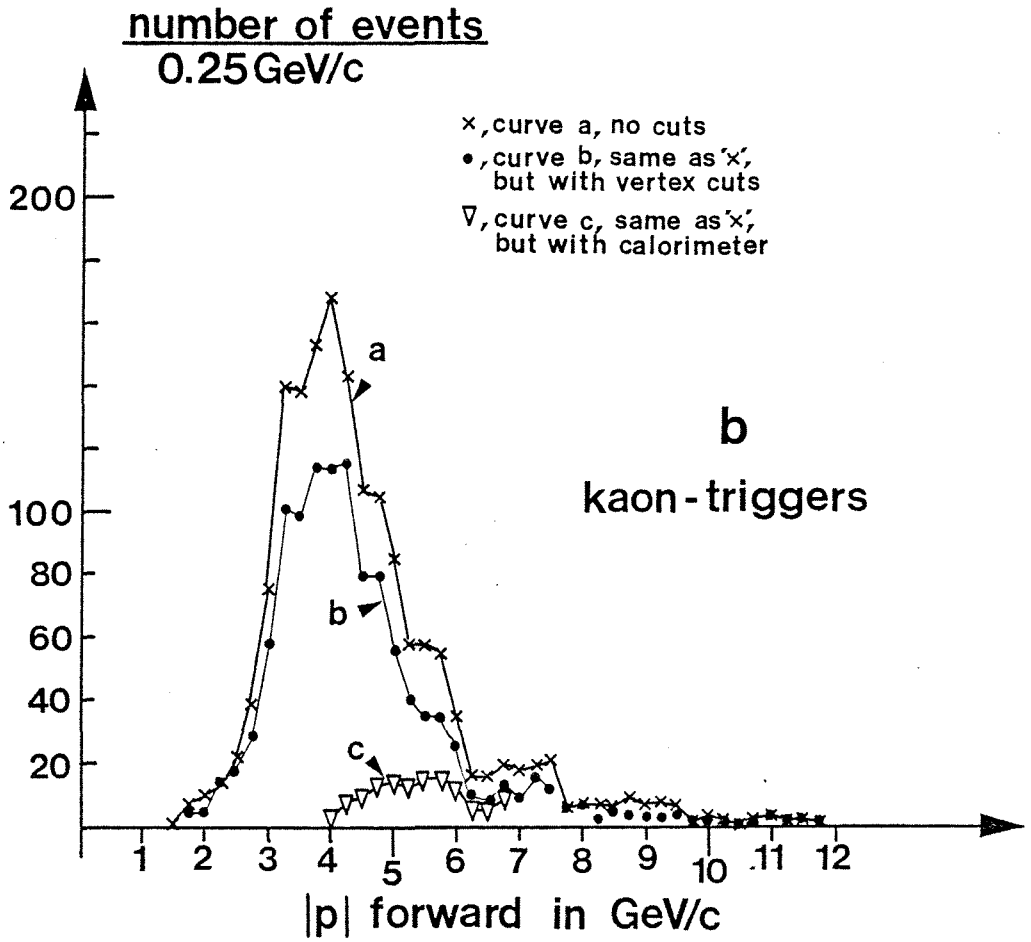

Fig. 4.14.b

The momentum spectra for reconstructed kaon triggers from run number 1950, elastic scattering, + 20 GeV/c incident. The horizontal scale is the same as in Fig. 4.14.a. 'Only-one-track-triggers' have not been shown as their spectrum is very similar to curve a which also includes 'multi-track-triggers', the difference between the mean values being only 6%. Although roughly 10% of the kaon triggers have a coincident firing of C1 and C2 none of these may be identified as electrons (see text). Therefore no cut due to electron contamination is shown. Like in the pion-trigger case, introducing vertex cuts only reduces the statistics (by 30%) without altering the shape of the distribution (curve b). Curve c shows what remains of the general momentum distribution (curve a) after having introduced calorimeter cuts (see text for details). The rejection represents 84.7% or a factor 6.5, the reason for the big difference between the pion and kaon case being that the kaon momentum is lower (in the mean), which again leads to a more efficient calorimeter veto (= higher rejection).

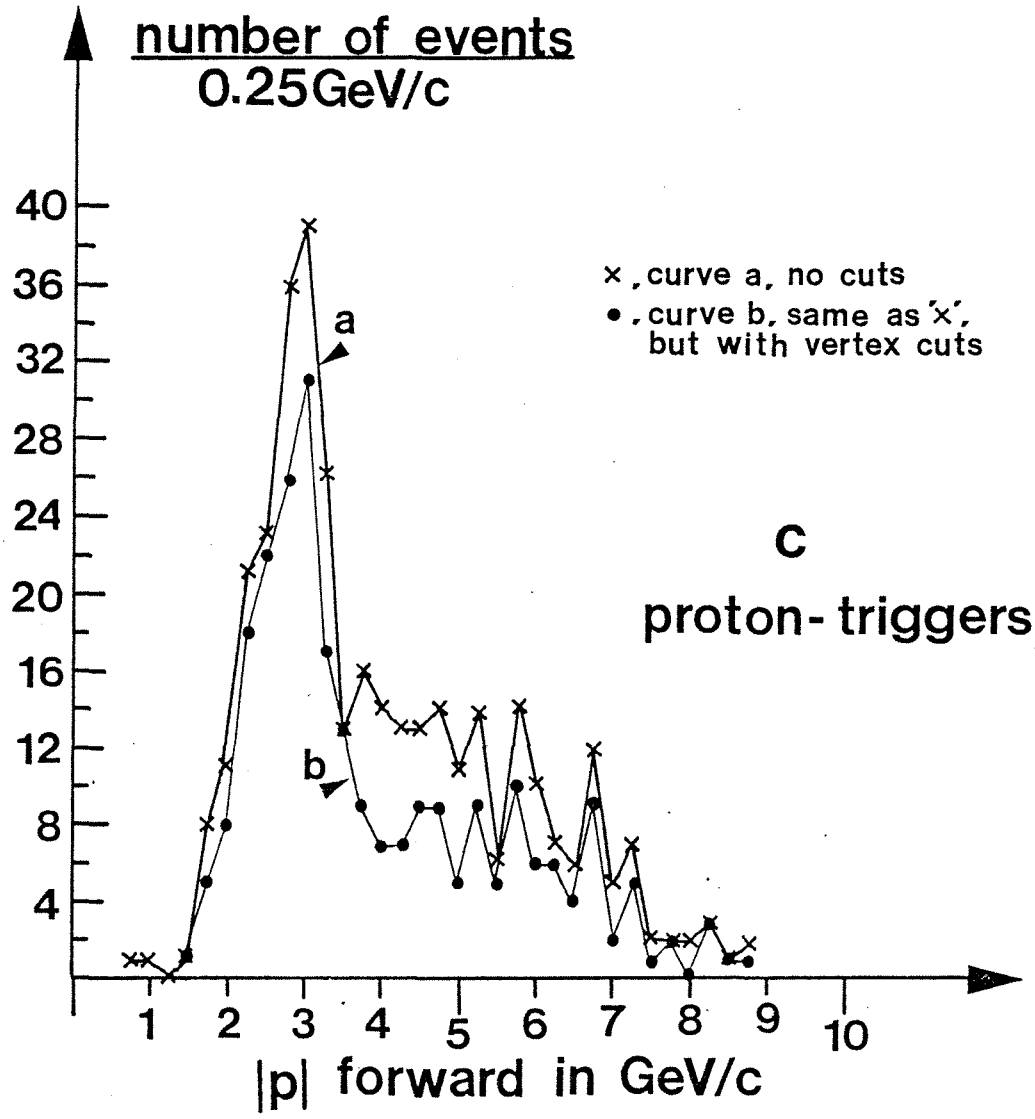

Fig. 4.14.c

The momentum spectra for reconstructed proton triggers from run number 1777, elastic scattering, + 20 GeV/c incident. The horizontal scale is the same as in the previous two figures. Only the effect of the usual vertex cuts has been shown (no change in shape, reducing statistics by 30%). Neither in this case do the 'only-one-track-triggers' behave differently. Because of the low statistics in the bins above 4 GeV/c, the calorimeter effect has not been drawn. However, the statistics is sufficient to conclude that it will cut drastically, notice that the mean momentum is as low as 4.4 GeV/c. In the text the rejection is calculated to be 85.5% or a factor 6.9.

this noise source cannot be reconstructed unless they fire the trigger-matrices (this is the way the reconstruction program is made, to minimize computer time) and actually absolutely none of the reconstructed tracks may be attributed to this noise source, and therefore very little may be said about it. C2 does give some information though, about the nature of these additional tracks (if they are tracks) that fire C1 and are inside our geometrical acceptance: If it is electrons, then there are very few of them; only in 8% + 3% = 11% of the cases might C2 have been fired by a non-reconstructed track (alone or together with the reconstructed track), and if due to hadrons, then their mean momentum must certainly be very low (only for 11% is the β above the C2 threshold). So contrary to what might seem a natural assumption, namely a rather big electron contamination of our kaon triggers, we observe a clean spectrum, at least when based on reconstructed events*. Compare Figs. 4.14.a-b, the difference in electron content is explained by the fact that demanding a C1 - C2 coincidence purifies the below 5 GeV/c spectrum well, and therefore makes the electron/hadron fraction much more important than in the kaon case where one allows hadrons down to 3 GeV/c. Also the cedar restriction defining an incoming kaon, thereby eliminating incoming electrons could play a role in reducing the electron background in the forward arm for the kaon trigger. Without a beam signal, decays, interactions upstream and halo particles, may produce coincidences that satisfy the trigger conditions, this should particularly be true for the pion triggers.

3) In the proton trigger one demands one cedar signal (cedar 1) coincident with, as usual (see chapter 1 or for more details, chapter 5), a fast trigger strobe (from scintillation counters) and a non firing of all cerenkovs (cedar 1 * fast strobe * $\overline{C1 + C2 + C3 + C4}$). Therefore there is no momentum cut in the trigger and the spectrum shown in Fig. 4.14.c is as expected. Naturally there can be no electron contamination in the proton trigger since neither C1 nor C2 are allowed to have fired.

---

* The reconstructed fraction represents 25% of all triggers written onto tape.

How much a calorimeter could reduce the trigger rate, depends on its resolution, how well it can separate particles of different energies. See Fig. 4.6: By imposing a signal of 50 ep's one will accept almost all hadrons above 20 GeV and reject half of the 10 GeV particles. Fixing a threshold of 30 ep's, we see from Fig. 4.6 that only 8.5% of the 10 GeV particles will not be accepted (by integration). Again using data from Ref. 10 and integrating the 5 GeV Q-spectrum, we find that at this lower energy only 3% will be accepted.

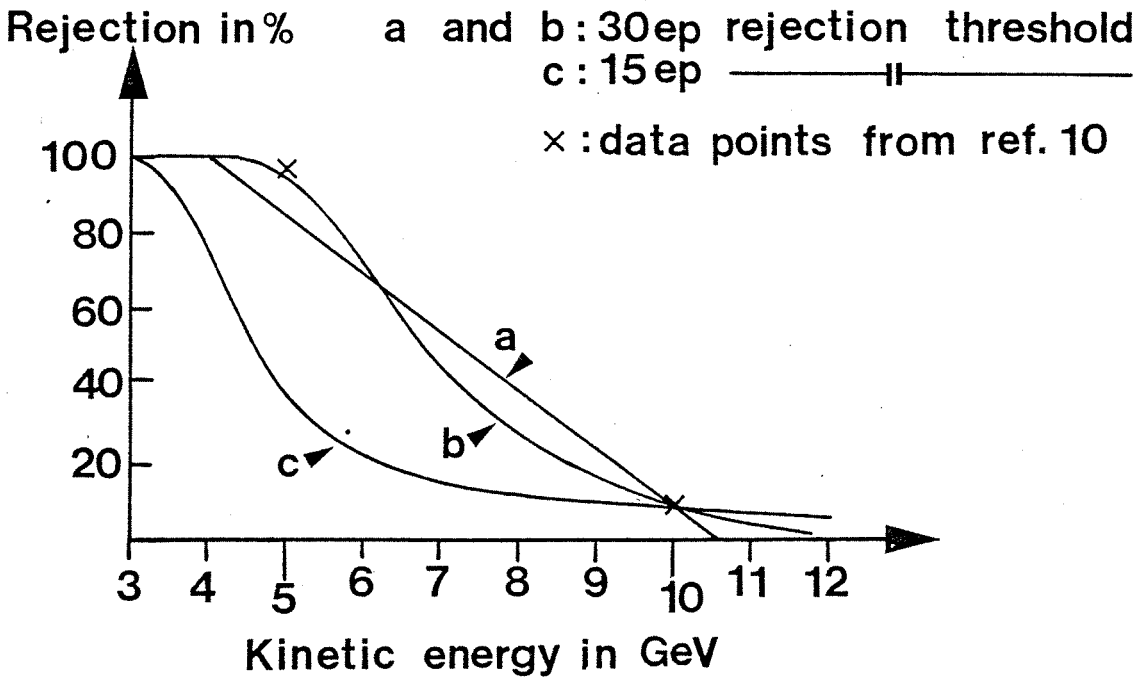

Fig. 4.15

Percentage rejected as a function of the particle energy a), assuming a linear relationship b), transferring the calculated curve from Fig. A4.4, 100% containement and c), transferring the calculated curve from Fig. A4.7, reduced containement. A comparison between a and b shows that the linear approximation is good. The rejection threshold is fixed to 30 equivalent particles for a and b and to 15 ep for c. The two data points are from Ref. 10, see the text and appendix 4.

These two data points are shown in Fig. 4.15. To calculate the effect of a 30 ep calorimeter threshold on the forward arm momentum spectra (see Figs. 4.14.a - c), one needs the rejection as a function of the energy. The results in table 4.1 are based on a linear relationship, curve a in Fig. 4.15. Below 4 GeV a 100% rejection has been used, above 10 GeV, it has been set to zero. The linear parametrization was fixed somewhat below the 5 GeV data point. This was done in order to avoid over-estimating the rejection: First, there is a big uncertainty associated with the 5 GeV data point and second, the correct rejection curve should approach 100% smoothly (hence a straight line through the two data points would necessarily lead to an over-estimation of the rejection). Notice that these cuts assume a fully equipped calorimeter which samples the shower at 10 cm intervals (iron as stopping material), the number of sampling planes being sufficient to measure a total signal Q which at maximum is 1% less than the real total signal (infinite calorimeter).

In figure 4.15 is also shown the rejection-energy relation which should have been used. Knowing Q_{mean} (E), one may calculate the rejection for all values of E, this was done afterwords (see appendix 4). However, as seen from Fig. 4.15, the linear approximation is good, and a recalculation of the calorimeter effects was not necessary for the conclusions we are going to draw here.

As seen from table 4.1, the momentum distribution for the forward particles, have been obtained from a rather small fraction of the total data sample (21% for the pion and kaon triggers, only 13% for the proton trigger). One may therefore expect that these distributions only partly reproduce the real spectra which are unavailable as long as one doesn't have 100% reconstruction of our raw data triggers.*

* There are many reasons for this low reconstruction efficiency. It is most often due to either: 1) an unsuccessful track reconstruction in the forward arm or 2), ditto for the recoil arm or 3), non existence of a good vertex candidate. Only if none of the three points are true, may the event be written onto the first data storage tape (DST1), where, among other things, the particle momenta can be found.

	Number of events without any calorimeter requirements, see a-curves in Figs. 4.14.a-c.				5) Mean Momentum (without cuts)
	1) $\|p\| < 4$ GeV/c	2) 4 GeV/c $< \|p\| <$ 10.5 GeV/c	3) $\|p\| >$ 10.5 GeV/c	4) $\|p\| >$ 0 GeV/c	
pion trigger	1478	2810	292	4580	5.8 GeV/c
kaon trigger	601	992	45	1638	4.8 GeV/c
proton trigger	196	160	9	365	4.4 GeV/c

	6) Number of events rejected (requiring 30 ep's) 4 GeV/c $< \|p\| <$ 10.5 GeV/c	7) Fraction rejected	8) Fraction of raw data triggers written on DST1
pion trigger	1673	68.8%	21%
kaon trigger	786	84.7%	21%
proton trigger	116	85.5%	13%

Table 4.1

In the first 5 and the last column is shown statistical information related to the a-curves of figures 4.14.a, b and c. The rejection is assumed to be a linear function between 4 and 10.5 GeV, below 4 GeV it's 1, and above 10.5 GeV/c, 0, see Fig. 4.15. The content of column 7), "the fraction rejected", therefore is the sum of columns 1) and 6) devided by column 4). The reduction factors for the three trigger types are in the order of above, 3.2, 6.5 and 6.9.

However, no bias is noticable when comparing the two proton spectra of Fig. 4.16, Both display the forward momentum, one only using triggers written onto DST1, the other is based on all triggers for which tracks were reconstructed in the forward arm, representing 50% of the raw data (compare with 13%). Sure enough, there is 50% left (triggers which don't have any tracks reconstructed in the forward arm),

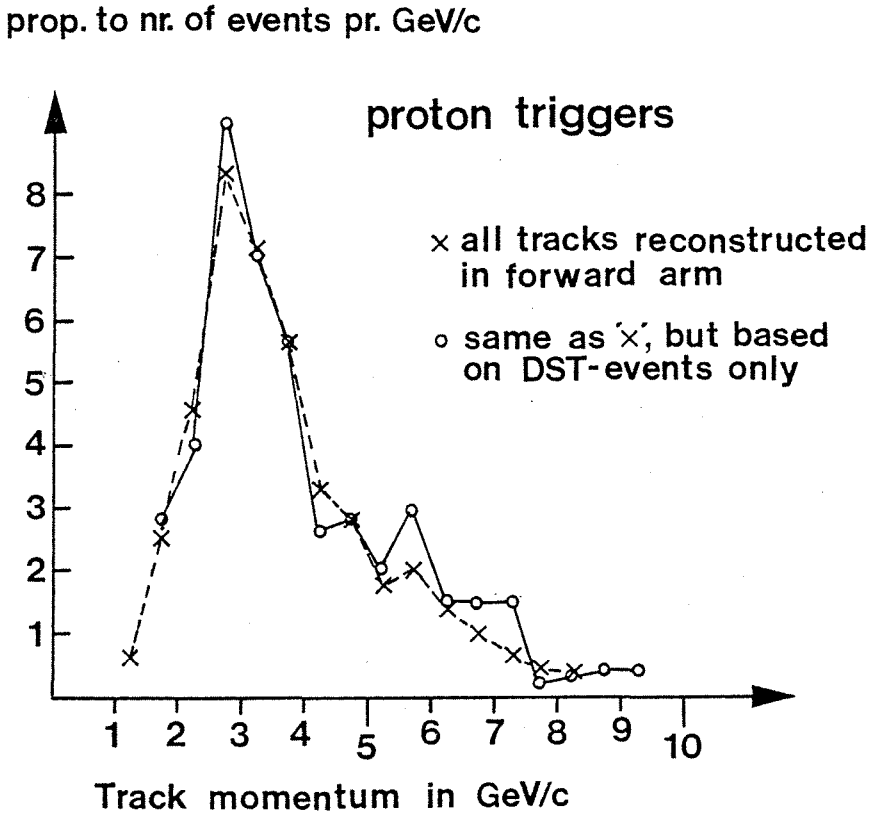

Fig. 4.16

The two curves show momentum spectra of the forward particle from run number 1777 (only proton triggers). One is based on DST1 data (229 tracks), the other on all reconstructed tracks in the forward arm (1043 tracks). Both curves are normalized so that the total number of entries is 100.

and the bias these may introduce on the forward momentum distribution is difficult to estimate. It is not evident that there should be any bias. Mostly, missing digitizings* is the cause when a track cannot be reconstructed. Therefore one would think that things should be uncorrelated, however, data seems to indicate a slight bias towards higher momenta for the reconstructed sample. This conclusion comes from a comparison of the momentum spectra of figures 4.14 with the known effect of the calorimeter on the trigger rate (see chapter 5B). As we shall see later, imposing even the lowest rejection threshold of one ep, one cuts away 60% of the triggers. Knowing that with a 'one ep threshold' few hadrons above 5 GeV/c are cut away and quite a lot below 5 GeV/c are kept - the probability that a 3 GeV/c hadron produces 1 ep in our 2 planes is roughly 0.5 - one can conclude, at least for the pion trigger (see fig. 4.14.a), that the momentum is too high when based on the DST1 sample. The kaon and proton distributions agree better with the observed 60% cut in the trigger rate. A lot of the lost pion triggers are probably electrons of rather low momentum (2-3 GeV/c) which easily may scatter sufficiently in the apparatus to be lost when reconstruction is tried. This argument could also be invoked for hadrons, the lower the energy the more likely is a deviation which makes a track lost, from 1), multiple and single scattering or/and 2), decay. It's importance has not been established, it is natural to assume that it plays a big role in the bias observed for the pion momentum, and a small role for kaon and proton triggers since their momentum spectra look reasonable (remember also that the electron contamination is very low for these trigger types).

To conclude, even if the figures in table 4.1 are based on a rather small fraction of the raw data, one is sure that a substantial reduction (a factor 5 to 6) is feasible in this particular case (yet very relevant for the WA7 experiment). The estimates are very likely to be modest. The effect could be even more dramatic at

* A digitizing = the duster center for a group of consecutive wires which all fire.

higher energies; because of better energy resolution one can introduce sharper energy cuts (the straight line in Fig. 4.15 becomes relatively steeper, this point has also been discussed in A4). Obviously the resulting forward spectrum (as a function of $\sum_i |p_{i,f}|$), hitting the calorimeter in an optimized geometrical position, should be known before one can say anything definite about the rejection factors at other energies. At higher energies the target produced multiplicity, will increase, also the solid angle covered by the calorimeter (in the CM-system) increases. These are factors which could reduce the rejection efficiency, however, it is $\sum_i |p_{i,f}|$ which is the decisive parameter. With a magnet in place and optimizing the geometrical position of the calorimeter for high-t elastic scattering, it is not easy to predict the energy dependence of $\sum_i |p_{i,f}|$, or rather the energy dependence of the fraction between 1), the mean signal produced by a "$\sum_i |p_{i,f}|$ shower" hitting the calorimeter and 2), the maximum rejection threshold (Q_{CUT}) compatible with the general efficiency requirements for the experiment.

Also, the effect of demanding a signal of 15 equivalent particles from the 5 first planes (after 10, 20 cm etc. of iron), has been calculated. The momentum spectra used were those of curves a and b in Fig. 4.14.a (for the pion trigger), and of the a-curves in Figs. 4.14.b and c (for the kaon and proton trigger respectively). By going down to only 15 ep's one accepts more low energy stuff (see curve c in Fig. 4.15.), and the rejection naturally will be less. The results are shown in the table below. In this case, with a somewhat limited shower containement, one would observe a decrease in the trigger rates corresponding to a factor 2, 2.5 and 3 for the pion, kaon and proton trigger respectively. To set the rejection threshold, one has to specify the loss of good triggers which is acceptable. A value of 8% for this loss fixed the thresholds to 15 and 30 ep for the two configurations discussed above (with 5 or 14 planes).

	Number of events without any calorimeter requirements.			
	[1] |p| < 3 GeV/c	[2] 3 GeV/c < |p| < 12 GeV/c	[3] |p| > 12 GeV/c	[4] |p| > 0 GeV/c
pion trigger	744	3671	165	4580
kaon trigger	94	1512	32	1638
proton trigger	102	258	5	365

	[5] Number of events rejected requiring 15 ep's |p| < 12 GeV/c	[6] fraction rejected
pion trigger	2188	48%
kaon trigger	1005	61%
proton trigger	248	68%

Table 4.2

In the 4 first colums is shown statistical information related to the a-curves of figures 4.14.a, b and c. The rejection applied is represented by curve c in Fig. 4.15. A small distinction compared to the previous case has been observed in that this rejection is applied to b-curve of the pion spectrum. The rest of the pion-spectrum (curve a minus curve b), is assumed to be electrons and are thererore rejected with 100% efficiency. The rejection is set to 1 below 3 GeV/c and to 0 above 12 GeV/c. Otherwise the fraction rejected is calculated the same way as before.

Notice, however, how much faster the full containement rejection (curve b Fig. 4.15) approaches zero than what is the case for the 5-plane set up (curve c). Therefore one sees that to have a fair comparison, the integral of the unwanted losses should be calculated in the two cases. For them to be equal, the 5-plane threshold would have to be much lower than 15 ep; and hence the performances of the full configuration is undervalued. The mean reduction factors are 5.19 and 2.52, using values in tables 4.1 and 4.2*; clearly from what has been said above, the actual performances is improved by more than the factor two (when going to 100% containement) which the figures above seem to indicate. No attempt has been done to evaluate the real improvement. To perform the necessary calculations one would need detailed knowledge of the tails of the charge distributions, (see appendix A4), and data on this have not been found. However, the two examples of above shows that big reductions in the trigger rate may be obtained with both setups. The main considerations when deciding on the size of such a calorimeter will be related to 1), the costs 2), the inefficiency (= loss of good events) combined with 3), the desired trigger rate reduction.

* * * * * * * * *

Ending this section I shall briefly explain the use of the muon detectors. These two detectors have been set up to detect muon pairs originating from the WA7 hydrogen target. Data were taken during 1978, and it is hoped that the present analysis will yield the production cross section for ψ with pion incident on proton**. This has not been measured before and is interesting physically because of

---

* For the weighting of the different trigger types, data with + 20 GeV/c incident have been used: π = 45%, K = 11% and p = 44%.

** It is not clear whether the kaon and proton beam intensity was sufficiently high to measure the corresponding cross section with these particles incident.

the clean target; it is easier to test different hypothesis for the production mechanism when the target is uniquely made up of protons. Otherwise the target would have been a bound proton neutron mixture, which would make the data more difficult to interpret.

We have seen in section C that muons penetrate matter surprisingly well. Actually only a very small fraction is lost when relativistic muons go through 2.5 m of iron, and also, very near 100% of all other particles will not produce any scintillator signal after this amount of matter, no matter their incident energy. Therefore our configuration is a very good muon filter.

The way in which a muon pair signal (muon trigger) is defined and produced (by the decision making logic), will be described in detail later. Here I shall only outline the way of selecting. To define tracks originating in the hydrogen target, we used the same signals as the general decision making logic. That is, possible event candidates are rejected/accepted according to the answer of complex coincidence units which use either H1 and PR1 signals, or H2 and PR2 signals, see Fig. 1.2.b. These units are programmed so that they will be fired by particles coming from the target and having sufficient momentum not to be lost through the magnetic field. Let the answer of these units be TR_{for} and TR_{rec}, for the forward and recoil arm, respectively. Now to the hodoscopes inside and after the two muon filters. In the forward arm a simple "yes signal" from at least one element in L2 and also from one in L3, was demanded. The recoil arm had to give a coincident signal from R1 and R2, however, with an additional constraint, namely that the fired elements should be compatible with a track coming from the target, let this response be TR_{iron}. A muon trigger then was defined as the firing of the following coincidence:

$$MUON = TR_{for} * TR_{rec} * TR_{iron} * L2*L3$$

Sometimes when this 'MUON-rate" became two high, we demanded in addition a signal from cedar 1 or cedar 2 (see Fig. 1.2.a), thereby limiting ourselves to events with kaons or protons incident. The correlations between R1 and R2 (that is, the elements in R2 which should be coincidenced with one R1-element), were established by tracking Monte Carlo generated muon pairs through the magnetic field and the rest of the apparatus. This muon trigger could run in parallel with other triggers (mostly elastic). It was mostly supposed to be running in a parasiting mode, hence the importance of limiting the 'MUON-rate" so that it would not disturb the general data acquisition. Information necessary for proper reconstruction of muon pair was - as in the general setup - stored for each accepted muon trigger and written onto tape. This comprised all the elastic data (chamber-, hodoscope- and Cerenkov-firings etc.) and relevant for the identification of muons; L3, R1, R2 hit patterns plus drift chamber digitizings. This last information obviously is crucial in that it permits to start off the search for good muon tracks with a relatively limited amount of digitizings in the MWPC's. The counter firings in and behind the iron defines a roughly cone shaped body in space which must enclose possible tracks originating in the target. Therefore track reconstruction is done using only those MWPC-digitizings (see footnote page 4 - 43) that cross the cone.

I shall describe and discuss the features of this muon trigger in chapter 5. Also how it was encompassed in the general decision making logic.

E. Installation and calibration of counters.

As we have seen in chapter 2, the signal from a scintillation counter varies in shape and size (even with only minimum ionizing particles traversing the scintillator). The general signal from a counter is therefore represented by a distribution called a charge- or simply a q-distribution. In the following I shall describe how such a q-distribution is obtained. The method was used when fixing the cathode high voltage for all photomultipliers (PM's) in H1/H2, PR1/PR2, L1/L2/L3 and R1/R2. Notice that what is measured is the distribution as a function of the charge produced at the anode, it is therefore only related to the size (and not to the shape) of the signal. We used the Lecroy multichannel analyzer (model 3001, it will be referred to as L3001) to measure the charge of the individual signals. Below is shown the NIM* -logic layout used. The notations are the same as used elsewhere which are defined systematically in the beginning of chapter 5.

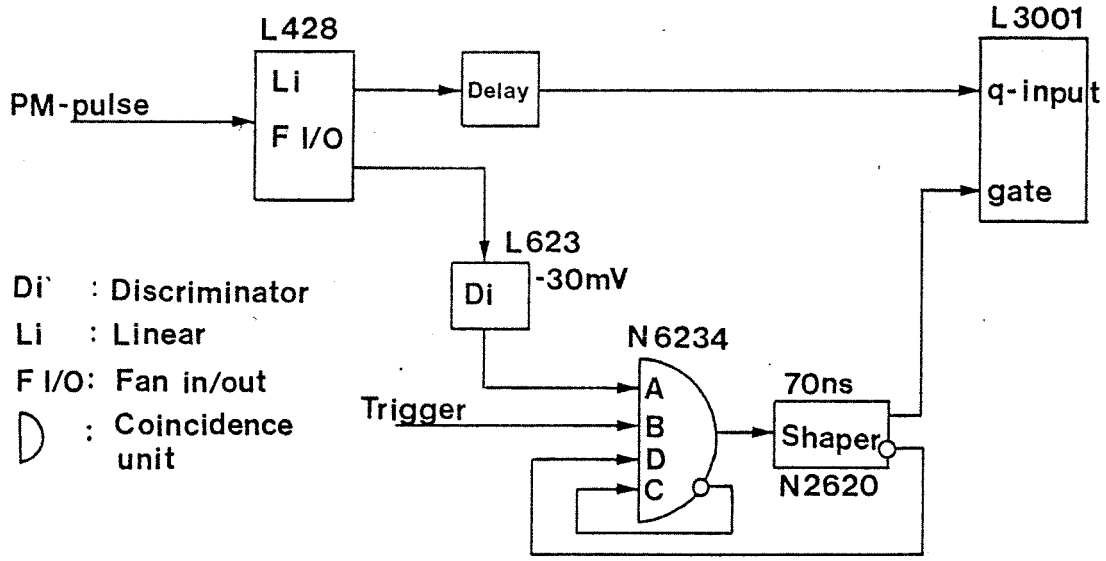

Fig. 4.17: Layout of the logic used to integrate analog PM-pulses.

* NIM for Nuclear Instrumentation Module which is a standardized system (concerning logic levels, crates and power supply) for handling fast logic and analog pulses.

An 'N' followed by a number refers to the classification of the CERN NIM-catalog while 'L' plus a number refers to Lecroy modules (which are also found in the CERN NIM-catalog). A signal enters a module with an arrow, the output is either 'normal' or the 'normal' is logically inverted, in this last case the output is marked with a ring.

Here is then an explanation of the layout in Fig. 4.17. The linear fan in/out sends out pulses which are equal to the analog sum of the input pulses (in this case there is only one input). One output pulse is sent off to be integrated, the other is sent off to the logic which 1), decides wether an integration should take place 2), if 1) is answered positively, generates a gate during which the actual integration takes place. 1) is answered by the coincidence unit, it demands a signal below - 30 mV from the PM which should be time correlated (in coincidence) with a trigger pulse from somewhere else in the experiment. Remember that the PM-pulses are negative (see chapter 2), and hence a threshold of - 30 mV for the discriminator implies that only pulses which produces a voltage below - 30 mV at the input, will trigger an output pulse. The choice of a good and correct trigger is vital to obtain a clean distribution. Most often the circumstances are such that one is interested only in a small fraction of the signals which trigger the discriminator. This is the case when only muon triggered L1/L2 pulses are to be analysed, or when it is the pulses of relativistic particles which interest us from the prompts (PR1/PR2). The smaller the fraction of interest, the more important is the trigger choice. I shall come back to the choice of trigger later in this section when dealing with high tension settings for elements in and behind the iron. An output from the N6234 coincidence unit will trigger the gate pulse, approximately 70 ns long. This pulse acts both as the start for the L3001-analycer and as the

actual gate during which the level at the q-input is integrated. The C and D inputs of the coincidence block the coincidence during the output of the gate pulse thereby ensuring a fixed gate width*. From Fig. 4.19 it should be apparant that this is important. The timing at the inputs of the coincidence is shown below, notice that it is done in such a way that the discriminated pulse is always the last (timewise) to fulfil the 4-coincidence (applies only to correlated pulses). Therefore both the q-input and the gate at the input

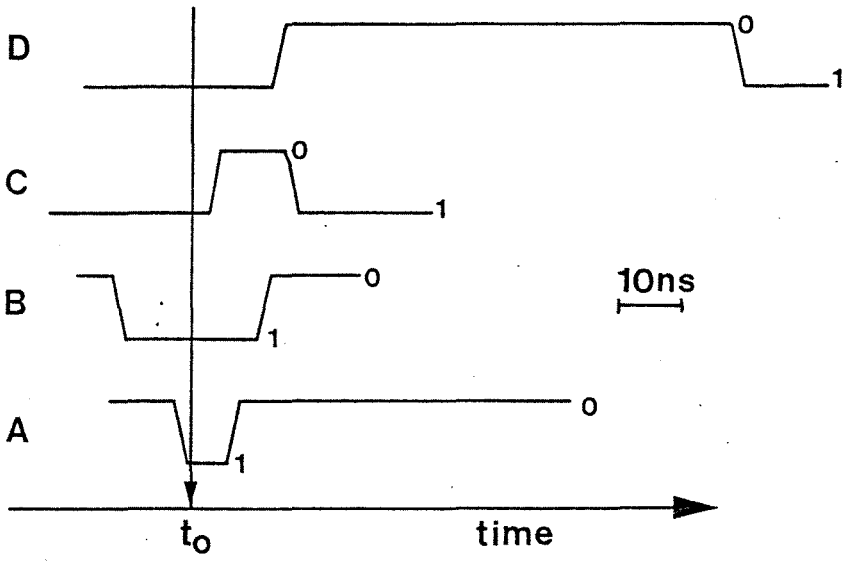

Fig. 4.18

Timing of signals at the input of the N 6234 coincidence (cf. Fig. 4.17). Notice that the full coincidence is satisfied at t_o (arrival time of A). '1' refers to logic 'yes' and '0' to logic 'no'. The veto blocks promptly and is efficient till the full gate pulse has been recorded by the L3001.

---

* With a working N2620 shaping unit this seems like an unnecessary precaution because this unit isn't updating i.e., it can not be retriggered during the output cycle, however praxis has shown that there are N2620's which don't work, and also possible updating replacements (for example discriminators).

of the L3001 are actually triggered by the same PM-pulse and their relative timing is determined by the setup and therefore needs doing only once. This is shown in Fig. 4.19. During subsequent q-distribution measurements it is therefore sufficient to check the timing of Fig. 4.18. The actual charge of the signal is given by

$$\frac{1}{R_i}\int_0^{70ns} V(t)\,dt \qquad (4.5)$$

where R_i is the input resistance of the L3001 (= 50 Ω). In Fig. 4.19 is shown an example of a typical V (t) - signal. The L3001 can be started by a push button, during operation it fills memory locations,

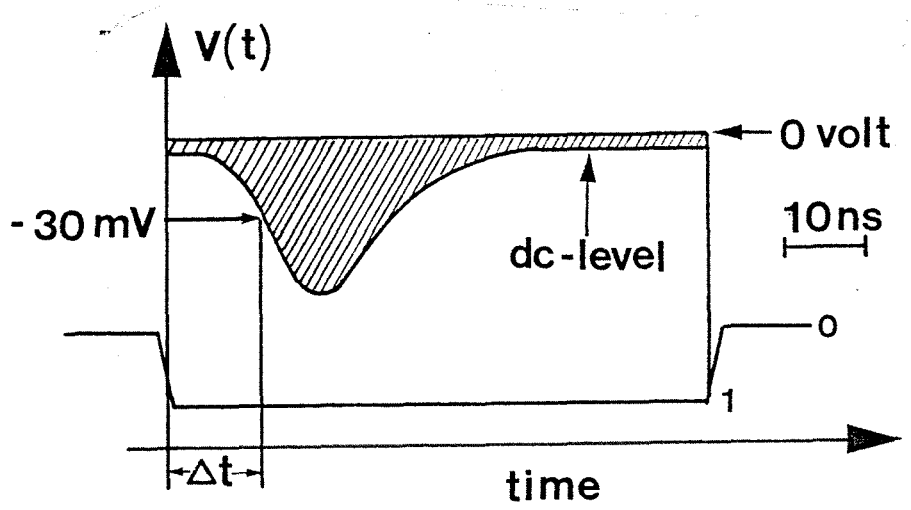

Fig. 4.19

Timing of gate and analog signal at L3001 inputs. The vertical scale is much bigger for the lower signal. Integration is performed during ∿ 70 ns and corresponds to the hatched area. Since the real PM-signal actually enters the L3001 on top of a dc level (some mV's high), changing the gate width also changes the integral, and therefore the gate width must be kept fixed. Notice that with the timing of Fig. 4.18 and a given logic layout, Δt is a constant, and independent of the precise arrival time of the trigger (B input, cf. Fig. 4.17).

each of which corresponds to a certain charge range (for instance, having recorded a signal of charge 2.5 pC, in a certain mode of operation the content of the 3rd memory location will be incremented by one, this location corresponding to $2 < q < 3$ pC). The deadtime of the module (during which it converts the registered charge into a binary word which is used for the filling operation), is around 20 μs . Therefore accumulating statistics may be fast and is actually only limited by the rate of the coincidence A * B. One can stop the process manually or by presetting a maximum memory content. And last, a very nice feature of the module, namely two outputs which may drive an oscilloscope, making possible a continuous display of the memory contents. Fig. 4.20 is a photograph of such a display.

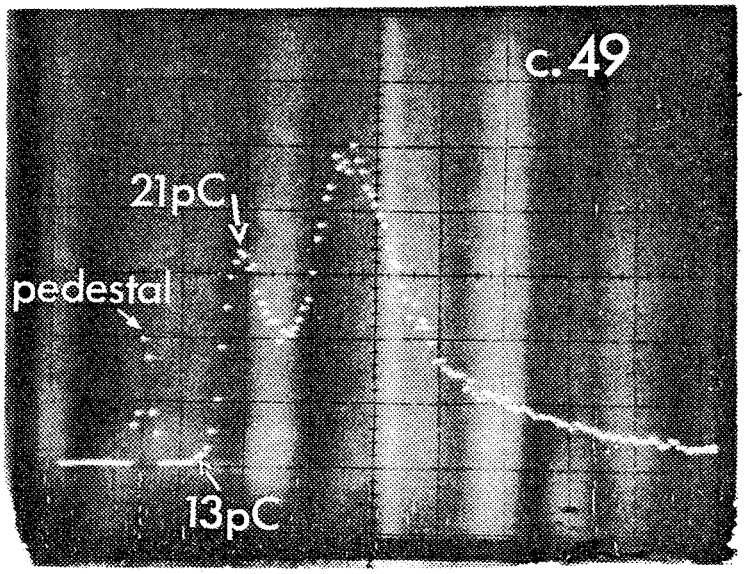

Fig. 4.20

Example of a q-distribution (counter 49 in L2, see Fig. 4.2). A threshold of -50 mV was used. The calibration of the horizontal scale is 1 pC (= 10^{-12} C) pr. dot. With the first peak defined as zero signal we see that 50 mV cutoff starts to affect pulses below 21 pC and becomes fully efficient below 13 pC. See the text for an interpretation of the spectrum.

To fix the absolute zero, notice that the signal produced by a particle traversing the scintillator naturally should start at zero (voltage) and also should fall down to zero after some time. However, many factors such as PM dark current, small deviations from the actual zero of the linear fan in-out output and last, the non calibration of the L3001 itself, explain the dc-level shown in Fig. 4.19. Therefore to obtain the real charge of a signal, one should subtract the integrated dc-level from the value of expression (4.5). There are two spectra superimposed in Fig. 4.20, one shows the zero measurement, it corresponds to the very sharp leftmost peak. One observes this when imposing only a B * C * D - coincidence (see Fig. 4.17). This is due to the fact that the 'A* B - rate' (even with a very bad trigger), always is much lower than the 'B - rate'. Therefore when starting the integration with the trigger pulse only, in most of the cases the gate is accompanied exclusively by the dc-level at the q-input. The extent to which random or/and correlated pulses from the counter fall within the gate, may be appreciated from possible peak asymmetry (around it's maximum). One should establish this zero pedestal for each high voltage setting since the PM dark current depends on the voltage applied. Note that it is the sum of several current sources which yield the final dc-level at the q-input. This level certainly depend on the overall resistance seen by the L3001, therefore to perform a precise q-measurement, care should be taken not to modify the logic layout during what is a two step procedure. The second step consists in obtaining a total spectrum (dc-level pluss signal). In Fig. 4.20, this corresponds to the two rightmost peaks. The sharpely increasing part between charges of 13 and 21 pC shows the effect of the 50 mV cutoff imposed by the discriminator. That this cutoff is sloping reflects the varying size and shape of pulses with the same amplitude. This second spectrum obtained through one measurement, contains two signal types 1), PM-noise signals, the -50 mV threshold cuts into an exponentially falling curve and 2), the signals which the trigger is

supposed to select (which in this case was muons traversing a calorimeter counter). With a rather elevated high voltage on the PM and a simple trigger, randoms (between A and B) were unavoidable and therefore quite a lot of noise pulses were analysed.

In the following I shall turn to the interesting details of the installation, first about the three hodocsopes used only for the muon detector (L3, R1 and R2), then about the calorimeter hodoscopes (L1 and L2).

As for all scintillation hodoscopes in the experiment except L1 and L2, the muon hodoscopes were used to give a 'yes' or 'no' answer only. That is, one wants 100% efficiency for relativistic particles, and one does not bother about the analog information of the signal. The tensions therefore, were fixed (using the method described above), so that the whole q-distribution would lie well 'above' a -30 mV threshold. Typical values were a cut off range from 7 to 10 pC, a maximum of the distribution around 20 pC (corresponding roughly to a -70 mV signal, see Fig. 4.35, and a FWHM somewhere between 7 and 32 pC. A schematic drawing with the significance of the values given above, is shown in Fig. 4.21. The physical meaning of the FWHM was discussed in chapter 2. Naturally, for those counters with wider q-distributions a higher peak position had to be chosen so as to have 100% efficiency. Therefore setting the high voltages as low as possible without loosing efficiency, we were left with peak positions varying from 15 to 35 pC. The big variations in response* mostly came from the scintillator itself. As already mentioned, these elements are of varying quality and also have been glued. Assuming that there are no fluctuations in the PM, we can obtain a measure for the performances of the element itself by calculating the average number of photoelectrons

---

* For the best element $FWHM/q_{max} = 0.37$, for the worst element this quantity was $32/32 = 1.0$, q_{max} is defined in Fig. 4.21.

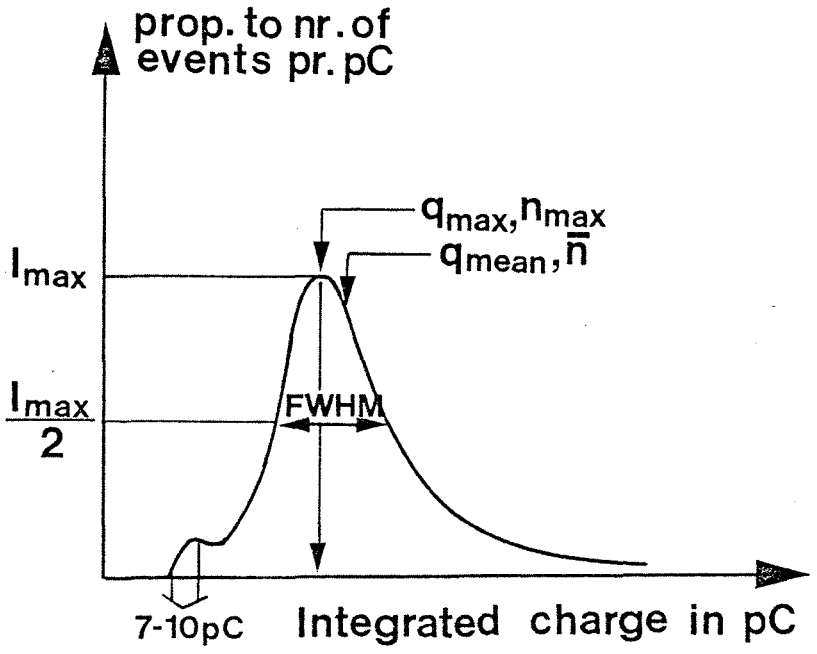

Fig. 4.21

q-distribution with notations used in the text. Note that the distribution is asymmetric and hence $\bar{n} > n_{max}$. '7-10 pC' corresponds to the usual 30 mV cut off range. A typical setting would be q_{max} = 20 pC (signals $\sim$ -70 mV). The actual anode signal is for most planes twice as big because half of it is lead to ground through a 50 Ω termination resistor at the base. For L1 and L2 the anode signal is 4 times the measured one, in Fig. 4.23 is shown the cabling which explains this.

produced on the photocathode, $\bar{n}$. By the above assumption, the observed q-distribution will be identical to the photoelectron distribution (where the variable is the actual number of produced photoelectrons). Here it is good enough to use a poisson distribution for q and hence,

$$\text{FWHM} = 1.177 \cdot (2\sigma) \text{ and } \sigma = \sqrt{\bar{n}} \qquad (4.6)$$

also $\bar{n} \approx n_{max} + 0.5$

we measured the fraction $\frac{\text{FWHM}}{q_{max}} \equiv f$ which is dimensionless.

Therefore $f = \frac{2 \times 1.177 \sqrt{\bar{n}}}{n_{max}} = \frac{2.35 \sqrt{\bar{n}}}{\bar{n} - 0.5}$

$$\Rightarrow \bar{n} = \frac{f^2 + a^2 + a\sqrt{2f^2 + a^2}}{2f^2} \text{ where } a = 2.35 \qquad (4.7)$$

Using the values of the best and worst spectrum (see footnote page 4-55), we find that $\bar{n}$ varies between 6.5 and 41.3 photoelectrons. This corresponds to, $\bar{n}$ = 23.9 photoelectrons ±270%, however, not all of this can be explained by bad scintillator elements. Certainly with only 6 - 7 electrons starting the multiplication, the PM response will itself fluctuate*. Hence the FWHM-fluctuations should be attributed to the varying quality of the scintillator-photocathode ensembles. In spite of the varying quality, 100% efficiency could be obtained for all muon-counters, the maximum tension required was somewhat above 2 kV (actually below -2kV).

As already mentioned, we define a trigger which would select the PM-pulses of interest. Due to the substantial amount of shielding iron, only muons could fire the planes in question (L3, R1 and R2), and the use of a trigger was therefore, simply to veto PM noise pulses. In the forward arm the out-put of the PR1 x H1R matrix was used, however, this would often be a too strict trigger for the elements furthest away from the beam in L3, making accumulation of statistics long. But simply or-ing some appropriate rings of PR1 or even better of L2 elements, was good enough.

---

* Such a low number of electrons at the photocathode implies important fluctuations in the conversion efficiency on event basis, which has nothing to do with the scintillator material.

Since L2 was installed after L3, this first plane wasn't actually used for the first high voltage settings, later on though, it was useful for checking L3. The procedure was more or less the same for the recoil arm. Here we had two planes (R1 and R2) which made the HV trimming faster; one of the planes was first roughly adjusted using an oscilloscope, the criteria being that most of the signals generated during the SPS 1.3 second long burst, should be at least 100 mV. This was good enough for this plane or parts of it to be used as a trigger for the other plane which could now be adjusted precisely. Next the roles were inversed; the settings of the first plane were refined using the second as a trigger. For some edge elements which did not overlap, we had to use PR2-rings instead.

While these trimmings might have been done in a simpler though cruder way, this was not so for the elements of the calorimeter planes. A shower will necessarily be split among the different planes and also among individual plane elements. Since it is the total charge which is to be measured ($Q = \Sigma q_i$), one has to ensure that all elements respond (in mean) as equally as possible. In this way the energy-deposition/signal fraction, will not depend on where the shower is located. Also one will minimize $\sigma_{Q,R}$ the most possible. As for all other counters in the experiment, L1 and L2 counters were checked for light-leaks and the PM's carefully focussed (see chapter 2). To have low noice level and stable operation, these checks are essential. We looked into the individual responses by using a radioactive source and an oscilloscope. Unfortunately it was far from uniform, examples of "best" and "worst" are shown in Fig. 4.22. Checking 'by eye' we confirmed that "yellowed" (old) and glued elements were the ones which attenuated a lot and reflected little. Notice that this will result in a widening of the q-distribution like the one observed for some muon counters. This will not affect the q_{mean} or Q_{mean}; by proper high voltage adjustements, all elements can be made to have

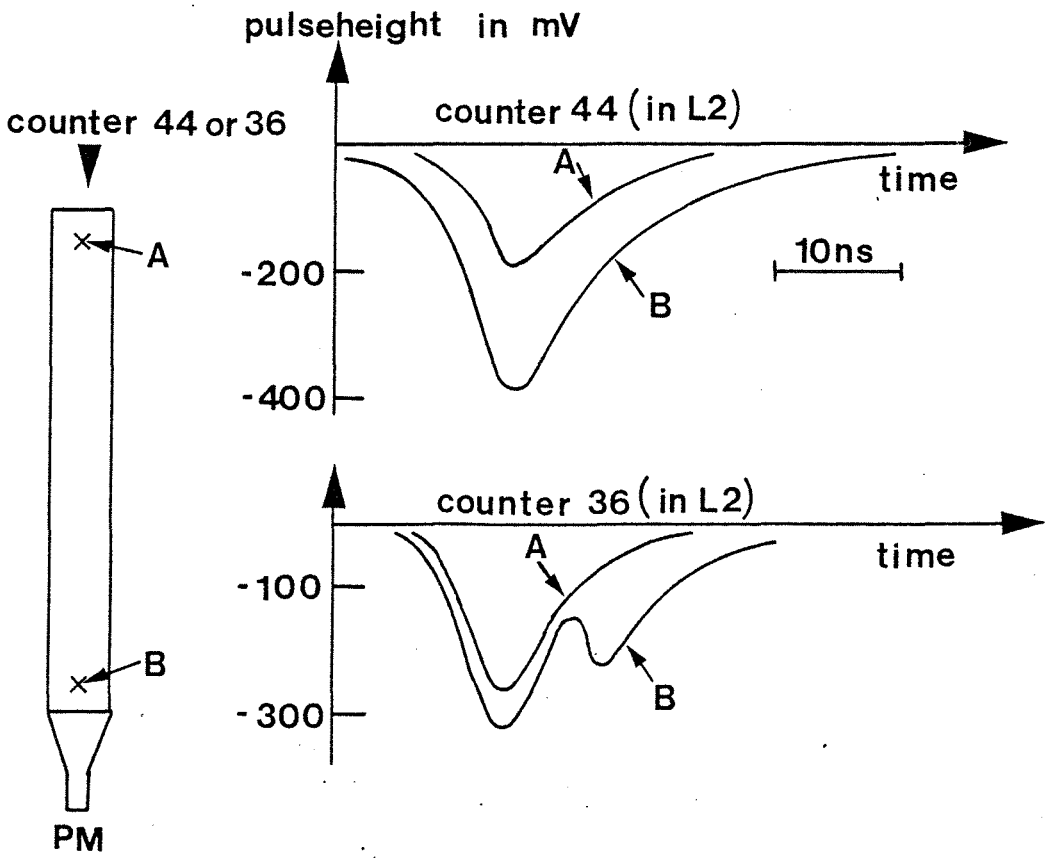

Fig. 4.22

Best and worst counters in L1/L2. The same high voltage (-1.63 kV) was applied to both elements. Either a radioactive source was placed in position "A" (furthest away from the PM) or in position "B". When triggering the oscilloscope only on the very highest signals, we observed very different behaviour for the two counters. Element 44 is bad, big attenuation, no reflexion, the opposite is true for element 36.

the same q_{mean}, however $\sigma_{Q,R}$ will certainly be affected. In particular, it will make $\sigma_{Q,R}$ a function of the coordinates of impact. Unfortunately this was the only scintillator material available at the time. With only 2 planes, the threshold signal which may safely be demanded (running at +20 GeV/c) is anyway very low, and even so the calorimeter cuts away

$\sim$ 50% of the triggers, see chapter 5. Therefore this non-uniformity is not a limiting factor, however, when extending the calorimeter to 5 planes or more, this contribution to $\sigma_{Q,R}$ should be determined; in this case it might be worth the effort to obtain a more uniform resolution.

One should have a common reference so that all counters can be made to respond the same way. We adopted the solution of many other experiments, i.e. by triggering on only minimum ionizing particles one obtains a q-distribution (which essentially is a mixture of a Landau and a Poisson distribution) for which the peak position is independent of the particle energy[23]. Therefore the corresponding charge was defined as 1 equivalent particle, 1 ep. Notice that this is also a very convenient definition: We studied the L1/L2 counters when fired by relativistic muons which naturally have varying momenta, therefore a q-distribution for muons is actually made up of the superposition of many distributions caracterized by different muon momenta. But the peak position stays fixed for all relativistic momenta (not so with the mean) and hence was used as the common reference. In this way identical counters will respond identically, and not identical counters (real life), will only have a common peak position. Obviously in our case with rather big counter related fluctuations in the FWHM, the best would have been to fix the mean (and not the peak) at one common charge. However, to do so, one would have needed a monoenergetic muon beam (to avoid variation in the mean due to different momenta). This was not feasible, besides resulting fluctuations in q_{mean}, which will be discussed in a moment, are very small, and the effect on $\sigma_{Q,R}$ is negligible for our purposes.

There are at least three considerations related to linearity which were considered so as to fix a good 1 ep calibration,

1. The individual signals are to be added linearly (in order to obtain Q). This operation is linear as long as the amplitude of the output signal does not exceed -1.5 V. Therefore the input amplitudes must be arranged in such a way that this voltage is rarely or never produced at the output. One could avoid this limitation by choosing another fanin logic, but the Le Croy modules used, offer a flexibility which is desirable in such set-ups. Relevant for the L127 FL's in Fig. 4.29 .

2. To permit a thorough off-line analyses of the calorimeter performances, all counters were individually q-analysed for each event written onto tape. CAMAC ADC's* performed the integrations with a resolution of 0.25 pC in the range from 0 to 256 pC. Ideally all counter signals should hence be less than 256 pC.

3. The liminations of the PM (Phillips XP 2232 B) and it's power supply. Using the CERN PM supply type 4239, it is the PM itself which becomes the actual limitation; the anodic dc-current should be well below 0.2 mA, and the linearity of an anodic pulse (with the amount of light incident on the photocathode) does not exceed 280 mA. The dc-limitation becomes more important with higher rates, while the ac-limination is related to the energy of the incident particle. The higher the energy the more likely are big splashes with high multiplicity in one single counter.

In order to evaluate these constraints the actual cabling and set-up has to be known, a drawing is shown in Fig. 4.23. To avoid reflections, one of the two anode outputs are terminated with 50 Ω. This is important when the analog information in the signal is to be

---

* ADC for Analog to Digital Conversion. The unit referred to above was a Le Croy model 2249A, 12 channels per CAMAC slot.

used. The signal is attenuated a factor 0.7* from the experimental zone to the "barrack" (25 m of RG 58 C/U coaxial cables). Here it's split in two again, one part of the signal is to be used in the fast decision making logic, the other is sent off to CAMAC for monitoring purposes. This last line was 360 ns long, 300 ns as RG 58 C/U, and 60 ns as 96-CEI-50-2-1. This last is the most used coaxial cable in fast electronics. The total attenuation for 56 AVP-pulses** along this 360 ns delay line was 0.31. A signal with an amplitude of

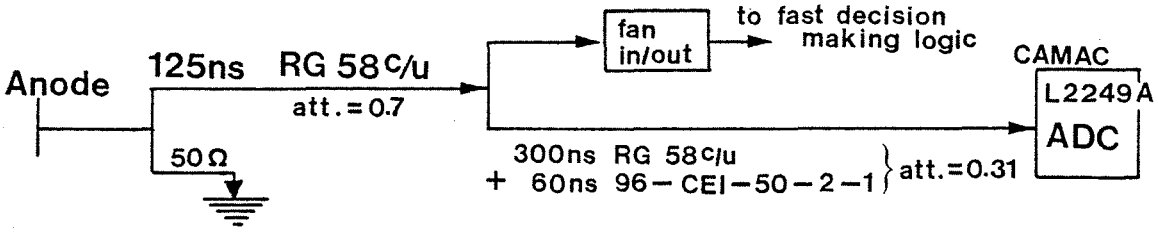

Fig. 4.23

Schematic layout of lines and logic associated with one single counter.

280 mA out of the PM will accordingly be reduced to ∿ 50 mA at the fan in-out input and to only ∿ 15 mA at CAMAC-level. This again means -2.5 V at the fan in-out and, (assuming a triangular signal with 60 ns base), a ∿ 450 pC signal for the ADC. One would think that several pulses will contribute to the fanned in signal. On the contrary, both due to low multiplicity and to the specific way of adding signals, the actual limitation at the first level of fanning in, is very close to -1.5 V as maximum allowed (one channel) input signal. At subsequent levels of fanning in (see Fig. 4.29) insertion of attenuators on the lines

---

* Measured with pocket pusler, which had signals 5 ns wide at half maximum (max. = - 0.7 V). Results agree with cabel producers specifications.

** 56 AVP is the kind of PM used in H1/H2 and to a large extent in PR1/PR2. The 56 AVP-pulses are very similar to the ones produced by the calorimeter PM's, the XP 2232 B.

was necessary to ensure linearity. Thus the most severe constraint are the points 1) and 2) of above. The choice of an optimal q_{max} was also affected by the PM power supply. The base delivers a maximum tension ranging from -1.5 to -3 kV. Scanning the individual counters we realized that at even the lowest voltage many counters worked very well and responded with a big q_{max}. We were therefore obliged to fix q_{max} rather high, at 70 pC to avoid having to install too many attenuators on the single lines. Even so we had to use 6 attenuators to reduce the biggest signals.

q-measurements were done as explained in the beginning of this section. This was performed with the configuration of Fig. 4.23 (the outputs of the fan in/out being used as shown in Fig. 4.17), and therefore when fixing q_{max} to 70 pC, this corresponds to a charge 4 times as big at the anode. Having low statistics it may be a rather tedious work to fix the maximum exactly at channel 70 (= 70 pC). To speed it up a bit we established the curve below (Fig. 4.24) yielding the relation q_{max} (PM-H.T.). This varies from counter to counter, but it helped nevertheless, in approaching the good setting faster. The inverse of the derivative is $9.3 \frac{V}{pC}$. 70 pC corresponds to $\sim$ -260 mV signals. To stay linear both in the logic and CAMAC with this setting (1 ep $\equiv$ 70 pC), individual signals should be less than 4 ep's. This was acceptable for the fast logic, we demanded that the total Q exceeds 1, or 2 ep at the most. However, generally this is not acceptable: 1), at higher energies (with for example 92 GeV/c incident) one can safely demand a Q well above 4 ep even with only two planes. Linearity should therefore be ensured so that the possible rejection of the calorimeter is fully exploited. 2), With q_{max} = 70 pC a lot of the ADC-information will be useless, from ref. 20 one can deduce the probability that a 15 GeV pion produces ≥ 4 ep* after 40 cm of iron; it is equal to 0.55.

---

* Remember that the ADC-range is given by $0 < q < 256$ pC for our ADC modules.

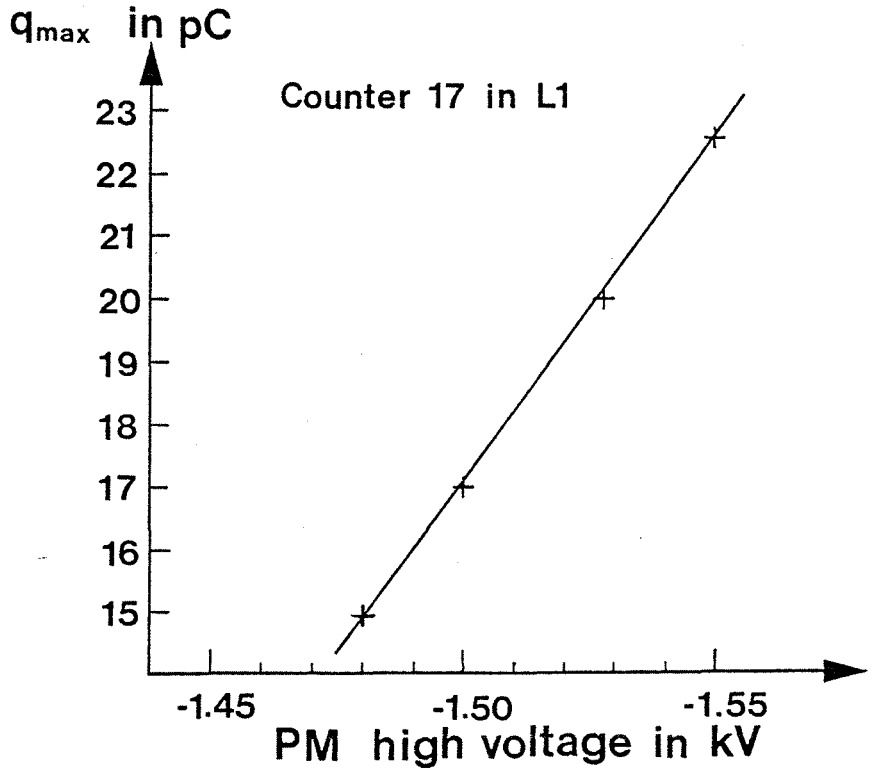

Fig. 4.24

Dependence of q_{max} on the high voltage applied to the PM. The derivative (assuming a linear relation) is ≈ 0.11 pC/V.

For a proper monitoring this is evidently not good enough and 3), as we shall see later, the dc-current increases with q_{max} which also forced us to lower the signal. This was made possible by adjusting an internal variable resistor of the base (PM supply type 4239) in that way reducing the minimum tension from -1.5 to -1.3 kV. We fixed the new q_{max}-value to 20 pC which was the minimum value compatible with no attenuators on single lines. This corresponds to a -70 mV signal, hence the fast logic could now accept signals of more than (1500/70) ep = 21 ep, and in CAMAC the

upper limit would be 256/20 ep = 12.5 ep. The actual limits are less severe; first, the total signal is very seldom fully deposited in one single counter and second, (concerns the logic only) the amplitude of a 21 ep signal is less than - 70 x 21 mV because a big signal is the sum of many signals which are not completely in time. Assuming as above, that one single counter receives the whole shower, the probability of producing $\geq$ 12.5 ep after 40 cm of iron is 28% (15 GeV incident) [20]. This is still rather high, but we settled for q_{max}=20 pc which was surely good enough in the fast logic and maybe somewhat high for monitoring energies above 15 GeV.

Concerning the dc-limitation of the phototube, see point 3) above, I shall come back to an example of how we calculated the dc-current of one phototube. The details are found in appendix 5. For several reasons (among others inexperience), this was done in a rather awkward way, piecing together data from different measurements. Actually what is here referred to as a dc-current, is a real dc-current plus the mean current produced by a whole range of PM-signals (represented by a q-distribution). In appendix 5 is calculated the mean charge produced per second by the PM on counter 18 when the incident beam momentum is -92 GeV/c. It is also shown that this charge for counter number i, may be parameterized as,

$$I_{ac,i} = 8.72\ q_{max}\ f_i\ I_B \text{ in (pA)} \qquad (4.8)^*$$

where q_{max} is the 1 ep calibration in pC, f_i is the counting rate of counter i above -30 mV normalized to the beam intensity, and finally is I_B the beam intensity (pr. burst = 1.3 second). f_i may be extracted from Fig. 4.30. In addition to I_{ac} comes the ever present dc-current. Typically I_{dc} = 50 μA (see A5).

---

* This is with a 92 GeV/c beam incident, and the calorimeter positioned so that the center of counter 17 is 122.5 cm away from the deflected beam (in x-direction). Counter 17 is placed 18.5 cm inside the iron along x and 40 cm inside along z, see Fig. 4.2.

For q_{max} = 20 pC, $I_B = 10^8$ burst^{-1} and i = 17 (closest to the beam), (4.8) yields $I_{ac,\ 17}$ = 124 μA or I_{17} = (124 + 50) μA = 174 μA. Therefore keeping in mind the dc-limitation of 0.2 mA (point 3) above), we see that at 92 GeV the upper limit for I_B and q_{max} is given by the figures just quoted. In fact, it would be desirable to lower q_{max} somewhat to allow for possible errors in the calculation and to be able to move the calorimeter closer to the beam. This ends the discussion about the choice of an optimal q_{max}-setting (q_{max} or lep was set to 20 pC with the set-up of Fig. 4.17, corresponding to 80 pC produced at the photomultiplier anode).

I shall now turn to the results. As already mentioned, the response from L1/L2 counters were far from uniform, this is reflected in a varying FWHM (Full Width Half Maximum). This variation is displayed in Fig. 4.25 both as a fonction of the FWHM (fig. a) and as a function of the number of photoelectrons produced at the PM cathode (Fig. b). Assume that the signals from minimum ionizing particles are poisson distributed, then relation (4.6) and (4.7) will give the correspondance between FWHM and n, the mean number of photoelectrons. Notice that this refers to a q-distribution produced by minimum ionizing particles only. All the counters were adjusted so that q_{max} = 20 pC. But because of the different FWHM's, the actual mean (above q_{max} since the q-distribution is asymmetric) will not be the same for all counters. Using (4.6) and (4.7) we calculated q_{mean}, which lies somewhere between 20.16 pC and 20.97 pC depending on the FWHM. Clearly this non-uniformity in q_{mean} represents a negligible contribution to the overall $\sigma_{Q,R}$. For the best element with a FWHM = 6 pC, $\sigma_{q,R}$ = 13%, which should be compared with $((20.97 - 20.16)/2)/20.97 \approx 2\%$. In addition, when several counters are added, all kinds of signals contribute, not only those from minimum ionizing particles. The counter related fluctuations will, due to the statistical nature of the huge number of photoelectrons, contribute very little to the overall calorimeter resolution. Shower inherent fluctuations can, however, not be avoided, and are therefore almost solely responsible for the observed $\sigma_{Q,R}$.

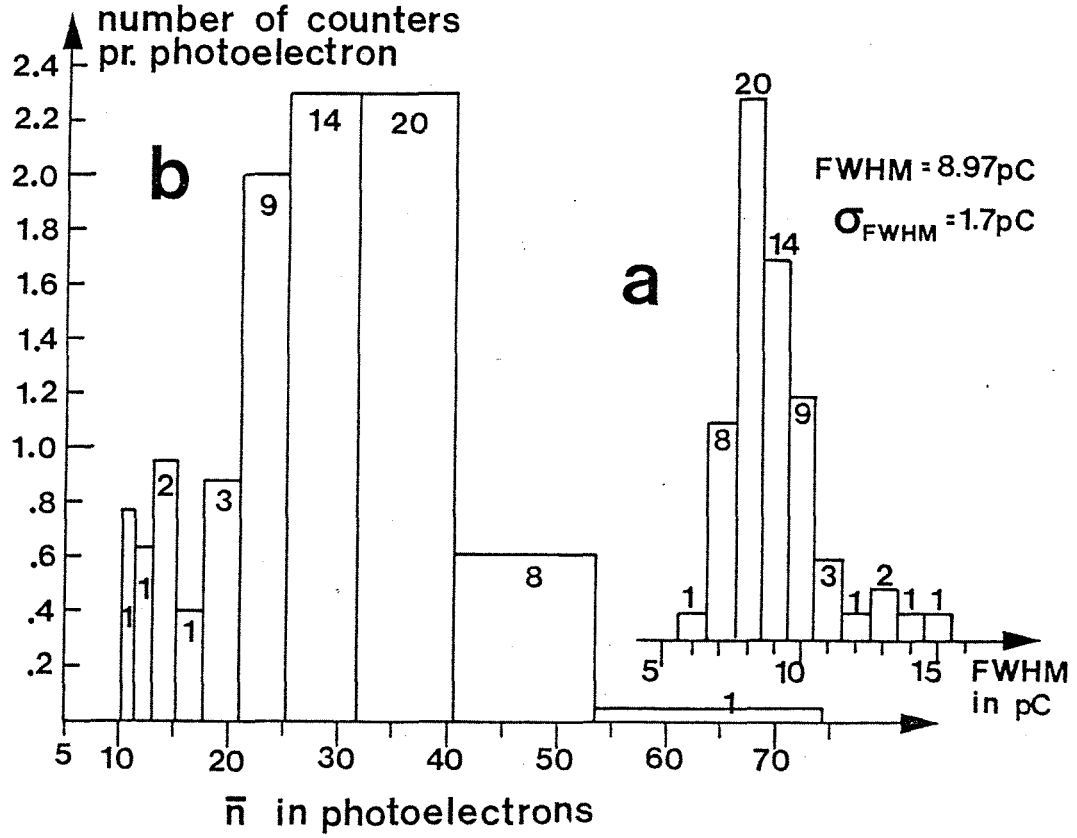

Fig. 4.25

a) The measured distribution of L1/L2-counters according to the FWHM of their q-distributions (with $q_{max} = q_{mean} = 20$ pC). The figures tell the number of counters per bin.

b) Same as a), but according to the number $\bar{n}$, of photoelectrons produced at the PM cathode. The normalization along the y-axis is pr. photoelectron.

Fig. 4.25.b reflects the real fluctuations in the quality among the counter elements. As already seen, some of this is due to a low photoelectron yield and may be compensated for by adjusting the high-voltages. However, the internal fluctuations in each individual counter evidently cannot be remedied. Nor can the fluctuations in FWHM's shown in Fig. 4.25.a, unless the scintillator material and PM's etc., are changed.

When summing the charges, $Q = \Sigma q_i$, this naturally affects $\sigma_{Q,R}$. To what extent, depends on the amount of light (the number of ep's) we are working with. For example with a 10 ep signal, envisaging 10 minimum ionizing particles hitting the worst counter (FWHM > 15 pC), what is the $\sigma_{q,R}$ for this signal ? With $q_{max} \sim q_{mean}$ = 20 pC and again assuming the min. ionizing signals to be poisson-distributed, a FWHM of 15 pC corresponds to σ(1 ep) = 6.4 pC and $\sigma(10\ ep) = \sqrt{10 \times 6.4^2}$ pC = 20.2 pC and σ_R(10 ep) = 20.2/200 = 0.1 . This should be compared to $\frac{6.4}{20} = 0.32$. Clearly working with big signals, the effect seen in Fig. 4.25 will simply disappear in the sense that the shower inherent fluctuations will dominate completely. Notice that the above estimation actually represents an upper limit for σ_R(10 ep); some of the shower particles that contribute to a 10 ep signal clearly are not minimum ionizing. Not being that, they will deposit more energy hence more light in the scintillator. In particular for electrons which are completely or very much stopped in scintillators, one cannot expect a poisson-like expression (with calibration: 'q_{mean} = 20 pC $\Rightarrow$ σ(1 ep) = 6.4 pC') to be valid any more. It is therefore more correct schematically to consider 10 ep as, N fully minimum ionizing particles plus 10-N fully stopped for which there are no fluctuation in deposited energy. In Fig. 4.26 below is shown a real q-distribution for counter 17, the high voltage is adjusted according to the peak position, and the FWHM is read directly from the display. Notice that the fraction FWHM/q_{max} should not depend on the high voltage, this was also verified to hold very well.

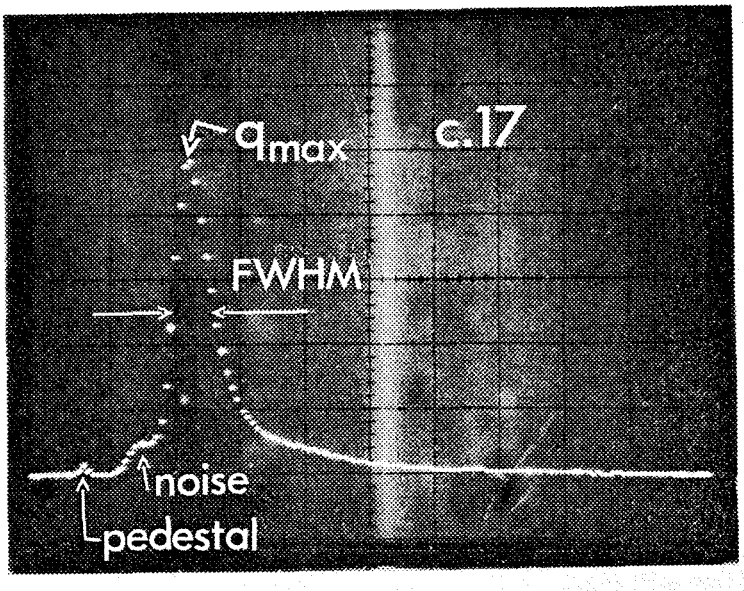

Fig. 4.26

q-distribution produced by minimim ionizing particles for counter 17. The resolution is 1 dot per pC, q_{max} = 20 pC (above pedestal), FWHM = 9 pC. Note the very low noise background.

We did several rate measurement. Below is shown single rates in L1, L2 and L3 running with positive particles incident at 20 GeV/c. The discriminators used on the lines from PM's to scalers, were all set to a threshold of -30 mV, in comparison remember that a minimum ionizing pulse on the average is -70 mV at it's maximum. All the rates given are normalized to the beam intensity. This was done by measuring the total beam intensity (with an ionization chamber) during each rate measurement. In the following a lot of rates will be given in units of counts per ionization chamber count ($\frac{c}{icc}$), the normalization of the ion(ization) chamber itself is roughly 75,000 beam particles per count. As seen from the figure, the innermost elements in L1, i.e. counters 1 and 17, are situated

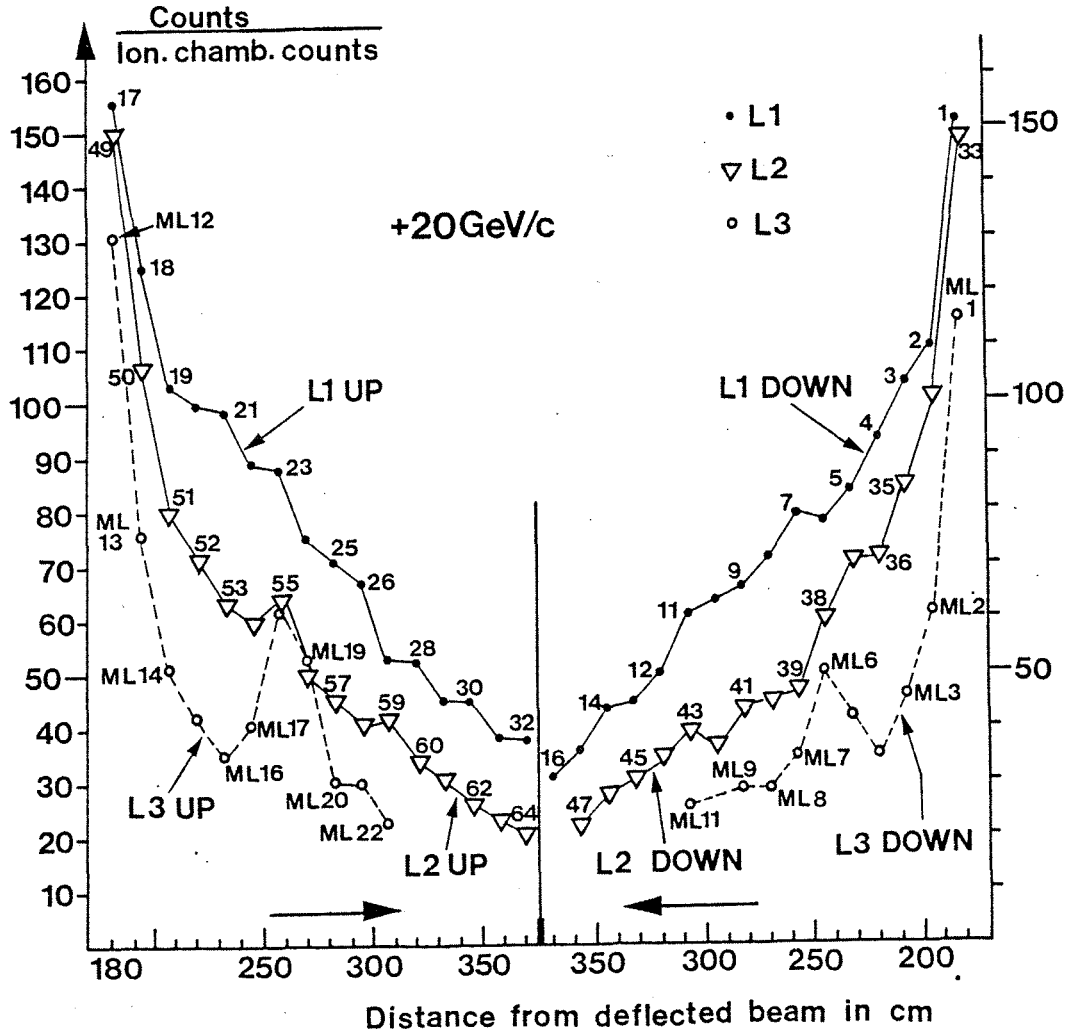

Fig. 4.27

Single rates in L1, L2 and L3 counters normalized to the ionization chamber (∿ the beam intensity). One ion chamber count = 75,000 beam particles. All figures/letters along the graphs refer to the counter notation of Fig. 4.2. Notice that counters with the same distance to the undeflected beam are drawn right above each other, this applies separately to UP and DOWN. The x-axis gives the x-coordinate (in the general WA7 coordinate system, see Fig. 1.3 of the counter centre, minus the x-position of the deflected beam at z = 1,364 cm, which is the z-position of L1. To get the actual x-distance of L2 and L3 counters to the deflected beam one has to subtract 1, respectively 10 cm from the values along the x-axis. Left out counters were either faulty or not mounted. Signal thresholds were set to -30 mV.

182 cm away from the deflected beam. (The innermost elements in L2, 33 and 49, are 181 cm away while in L3, MR1 and MR12 are 172 cm away, see text to Fig. 4.27). Doing some adding up one finds (per ion. chamber count):

L1 UP 1242(51.6%)	L1 UP 906(51.3%)	L3 UP 572(53.7%)
L1 DOWN 1167(48.4%)	L2 DOWN 860(48.7%)	L3 DOWN 494(46.3%)
L1 U+D 2409	L2 U+D 1766	L3 U+D 1066

(4.9)

Notice that the L2-part which is covered by L3 is equal to 1516 icc, which implies that $\frac{1066}{1516}$ = 70% of L2 counts over 30 mV, are muons. Clearly normalizing to the beam is not quite correct because the halo depends on details of the beam trimming (collimators, focusing etc), a fact which is seen in the "muon peak", somewhat larger in L3 UP than in L3 DOWN. This peak should obviously be seen in L2 as well, but here the signal is very weak and hence (with the same beam) the halo varies. These rates were measured with a beam of $\sim$ 3 x 10^7 per burst. One deduces, a small up-down asymmetry from the added rates, note that this and observed structures in L1, L2-rates are significant and may not be attributed to PM noise (the in-between burst rate of single elements is $\sim$ $1s^{-1}$!). Corresponding rate curves are shown in Fig. 4.28 for hodoscope planes R1 and R2 in the recoil arm, see Fig.1.2.b. Integration gives,

R1 UP 366.7 (54.4%)	R2 UP 476.2 (27.0%)	
R1 DOWN 307.6 (45.6%)	R2 DOWN 1289.4 (73.0%)	(4.10)
R1 U+D 674.3	R2 U+D 1765.6	

Again there is a clear up-down asymmetry, for R1 it is more or less the same as for L3, for R2 it's spectacular even if one subtracts possible noise peaks. Elements MR8 and MR16 (in R1) clearly receive a lot in through the sides, this was also the case

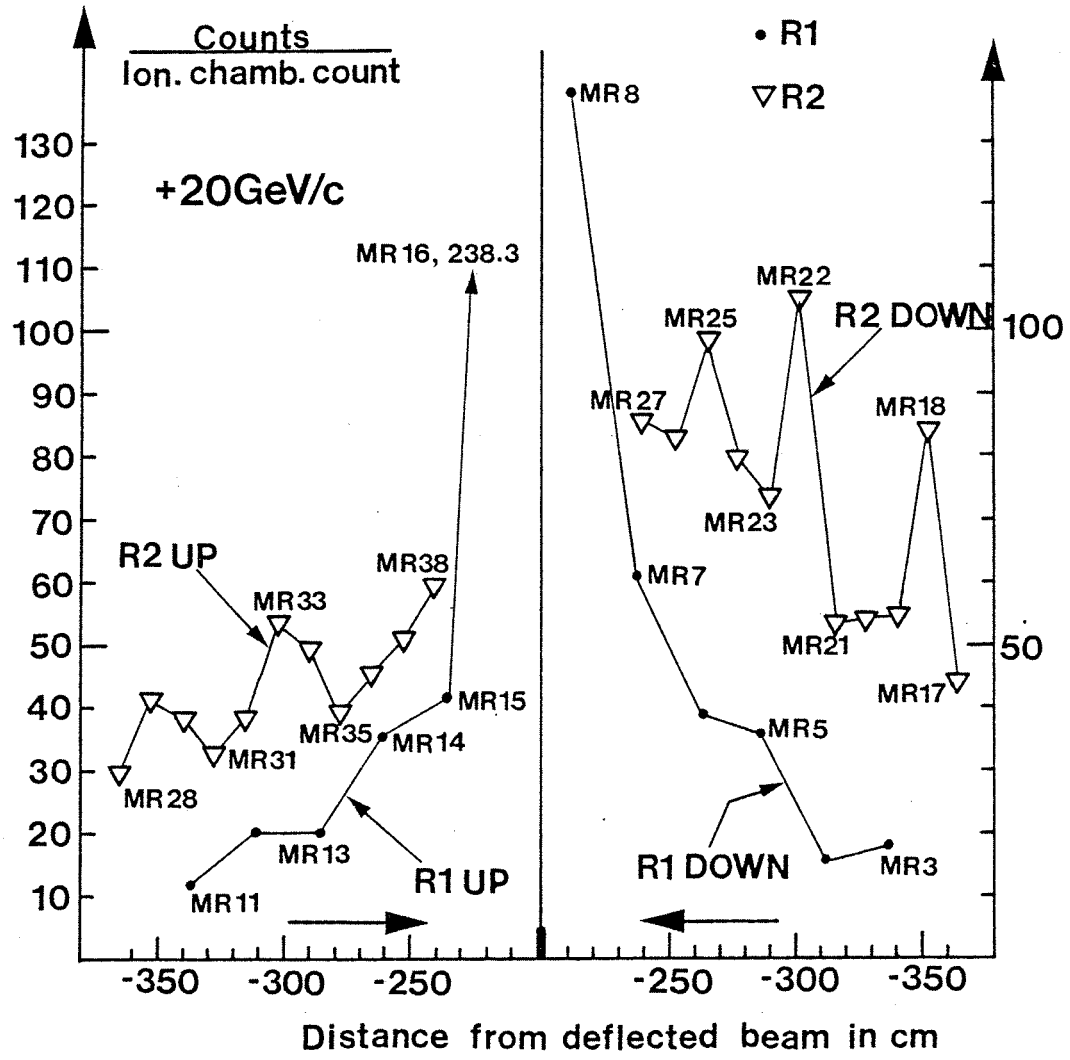

Fig. 4.28

Single rates in R1 and R2, counter notation from Fig. 4.2, same normalization as in Fig. 4.27. The x-distance is relative to the counter center and is in this case valid for both planes, both the beam deflection and the internal shift of R2 relative to R1 have been taken into account. Note up-down asymmetry and structures in R2, discussed in the text. In R2, the 4 positions closest to the beam were left free. Threshold at -30 mV.

for the innermost elements in L1, L2 and L3, see Fig. 4.27. The most interesting though, is the fact that in total, R2 counts much more than R1. One possible way of explaining this is to assume some second beam parasiting on our real beam, that by-passes our magnet and recoil calorimeter on the outside, and eventually partly backscatters from the concrete wall jutting out behind R2 (see Fig.1.2.b). This second beam might be asymmetric and could therefore also explain the observed up-down difference in the counting rate which in particular affects R2. A slight indication that some backscattering may be responsible is found in the fact that the fraction R2/R1 diminishes as one approaches the beam, this should be so because the wall extends 1.6 m only. Another possible explanation for this very much higher counting rate in R2, is particle leakage through the concrete shielding wall from the nearby very intense hyperon beam.

Concerning the peaks, nothing can be said about those corresponding to counters MR29, MR33 and MR25, it might be real structure as well as noisy counters. For counters MR22 and MR18 though, the high single rate could without doubt be attributed to bad PM focussing in the one case and to a wrong high voltage setting in the other.

Before proceeding to give equivalent rates with 92 GeV/c incident, I shall explain the logic which does the fanning in of both L1 and L2 signals. A layout is shown below. Basically there are two steps of fanning-in in order to produce the total L1 and the total L2 signals. Finally these two are added (linearly) to get the overall calorimeter signal, L1 + L2 . A calorimeter constraint would consist in demanding L1 + L2 to bypass a certain threshold value. Therefore the signals were distributed to discriminators with different settings. Out from the discriminators go what will be called, the 'CAL.YES'-signals, one only, may be used at a time in the decision making logic. The whole pulseheight pattern, however, was stored in CAMAC bit registers.

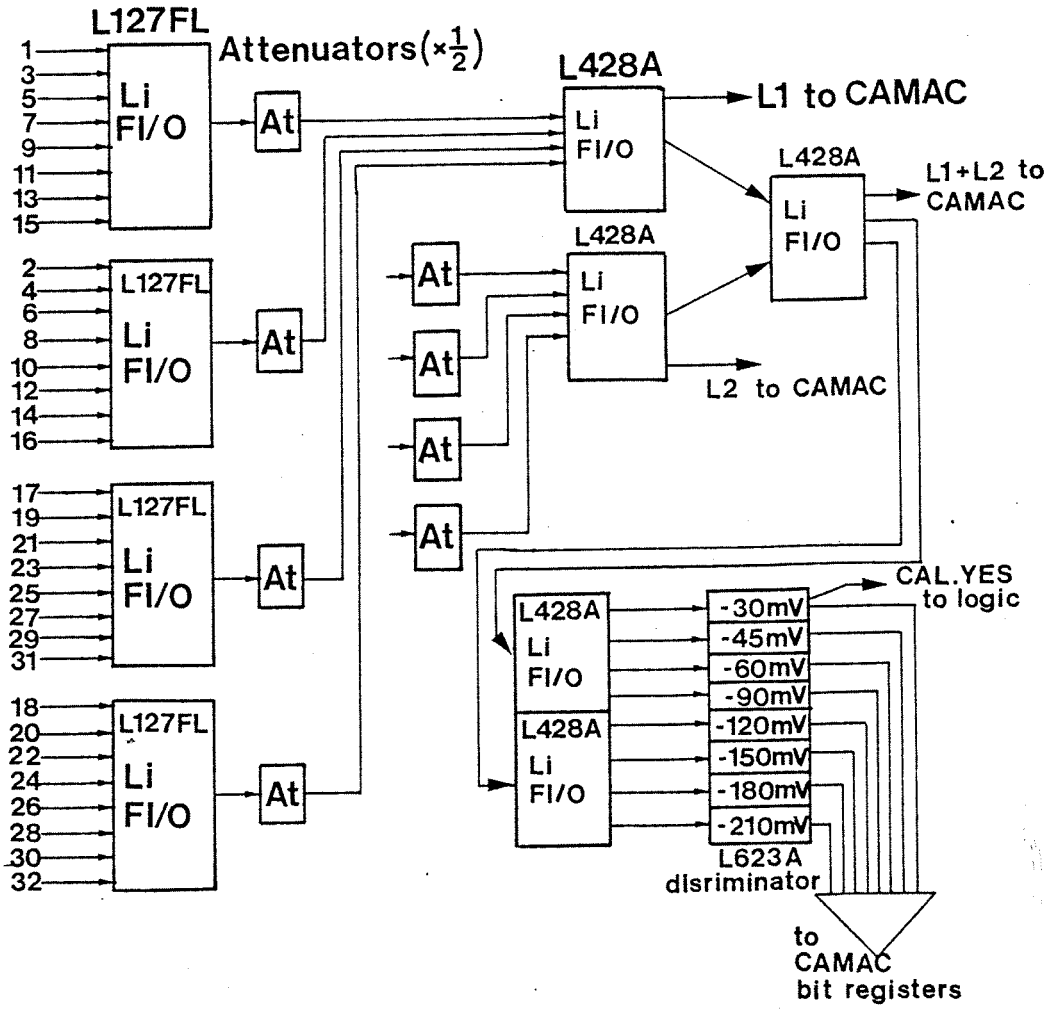

Fig. 4.29

Fanning-in logic for L1 and L2 counter signals. All attenuators divide by 2. Each discriminator channel has 3 outputs, therefore the CAL.YES signal may be taken from any of the 8 channels.

This information together with CAMAC ADC data (resulting from charge analyses), were used to check the calorimeter performances off-line, in particular its inefficiency and (by means of the bit registers), the rejection one would expect. I shall come back to this point later. Notice first that every other counter is connected to the

same L127FL unit, this was done in order to minimize the non-linearity/saturation of the unit due to big showers in the iron, secondly notice the attenuators; at the second step of fanning in one cannot avoid 'seeing' the full shower, hence the necessity of introducing 8 attenuators, each dividing the input signal by 2*. Only 4 are necessary because of linearity considerations, those are the ones serving L1, the 4 on L2 naturally follow; otherwise the L1 + L2 respons would not be linear along the z-axis. The first step in fanning in L2 counters is not shown in the figure, this is completely identical with what is indicated for L1. Because of the attenuation, observe, that demanding an L1 + L2 respons of 1 ep corresponds to roughly a signal greater or equal to - 35 mV. For the operation of this logic it was important to check that the dc-level out from the last L428A's actually was at zero, or more correctly that this level coincided with the zero reference of the discriminator. Two effects contribute 1), the sum of the PM dc-levels (mentioned in A5 and earlier in this chapter) and 2), an internal offset dc-level of the fan-in. An adjustable resistor permitted to set the dc-level out, to the discriminator zero (= general zero of NIM-crate power supply), which again ensures that the threshold applies to only the PM signal and not to 'something' plus this signal. I will discuss the timing of the signals in this set-up later (in connection with a discussion about pulseheight-charge relations of single and added signals).

-92 GeV/c rates for the 5 hodoscope planes are shown in figures 4.30 and 4.31. Again the signal threshold was set to -30 mV. Consider only the 3 planes in the forward arm. This time the inner-most L1-elements are located only 116 cm away from the deflected

---

* The L127FL stays linear for output signals $\leq$-1.5 V, and the L428A is linear for outputs $\leq$-2.0 V.

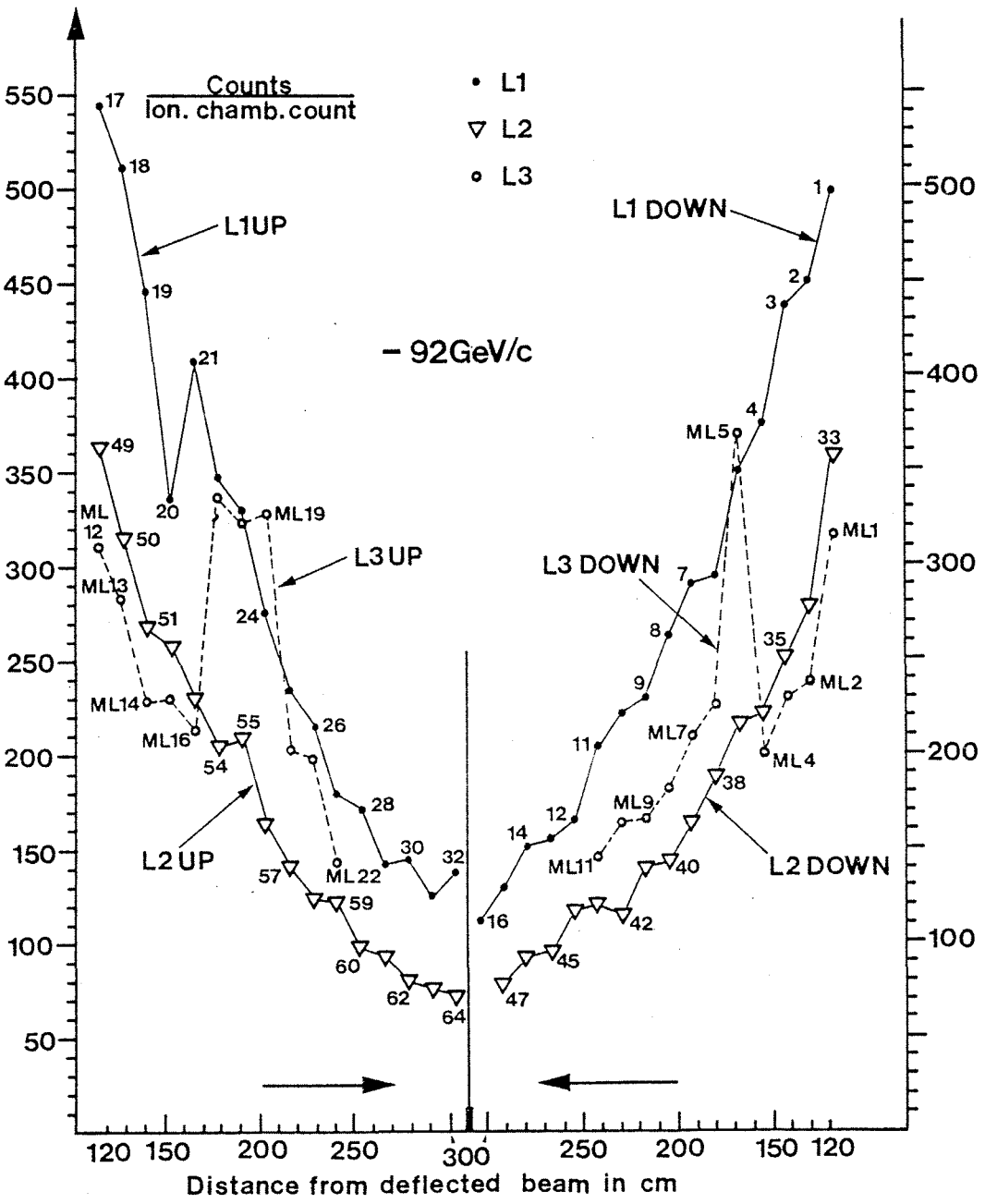

Fig. 4.30

Single rates in L1, L2 and L3 counters normalized to the ionization chamber (1 count ↔ 75,000 beam particles). The counter notation is taken from Fig. 4.2, and the x-axis distance refers to the counter center. Again counters with the same distance from the undeflected beam, are drawn above each other. This as we have seen, implies that one has to correct for the non parallelism of deflected and undeflected beam, the corrections are + 0.3 cm for L2 and + 2.2 cm for L3, now being positive since the beam is bent away from our counters. Threshold at -30 mV.

beam. Notice that all planes count more than at +20 GeV/c. At the same distance from the beam, it is roughly a factor 2.5 higher for L1-counters, ≈ 2 for L2 and as much as ≈ 4 for L3, this last fact indicates an important muon flux, probably from the halo. The integrated rates are,

L1 UP	4540 (51%)	L2 UP	2819 (52%)	L3 UP	2791 (53%)	
L1 DOWN	4322 (49%)	L2 DOWN	2569 (48%)	L3 DOWN	2443 (47%)	(4.11)
L1 U+D	8862	L2 U+D	5388	L3 U+D	5234	

All these figures are in units of counts (above -30 mV), per count in the ionization chamber ($\frac{c}{icc}$). L3 is seen to count a lot, comparing the rate of the 22 innermost elements in L2 with the L3-rate, one finds that L3 counts 14% more than the sum of these 22 L2-counters! Even after subtracting the two peaks (see Fig. 4.30), L3 counts 3% more than the L2-counters. It is not clear how much L3 (or L2) should count; L3 edge counters may 'see' particles which L2 does not see, also L3 is not shielded from the back and lastly, the rate measurements were not done at the same time, and hence we have normalization problems (the fraction, halo/beam may, as we have seen, vary). Therefore the 3 or even 15% is not that unreasonable. These halo/beam fluctuations are to some extent confirmed by the peak in L3 UP. To see this, observe that the peak is not seen in L2, but in L1, clearly the conditions change. The peak in L3 DOWN is probably due to high PM noise. Anyway it is safe to conclude that the halo must be almost the counting rate of L2 and could be as much as 70% of L1. One should convert the counting rate into a rate with a certain beam. For example, L3 = 5000 c/icc corresponds to a single rate of 2×10^6 per burst with 3×10^7 burst^{-1} incoming. Estimating the halo induced single rate in PR1 (see Figs. 1.2.b and 2.5), a modest guess would be around 4×10^6 burst^{-1} with the same beam.

Another way to get some information about our signals, is to look at the multiplicity in L1 and L2, that is; how often does different counters within the same plane fire at the same time. To do this we measured the single rate of the fanned in L1, L2 and L1 + L2 signals

of Fig. 4.29. With a -30 mV threshold and suppressing the attenuators, we measured,

$$L1 = 7939 \frac{c}{icc} \qquad L2 = 5786 \frac{c}{icc} \qquad L1 + L2 = 9659 \frac{c}{icc} \tag{4.12}$$

Using the figures in (4.11) the multiplicities are,

$$m_{L1} = \frac{8862}{7939} = 1.12 \qquad m_{L2} = \frac{5388}{5786} = 0.93$$

which shows that the multiplicity is very close to one, again confirming that the muon fraction both in L1 and L2 is important. Notice that this is a very simple way of calculating the multiplicity. For two reasons, first, it does not take into account the fact that in general L1 pulses are much bigger than single counter pulses and second, there is an important influx in the 7939 L1 counting rate of pulses that are exclusively the sum of single pulses below 30 mV. I shall treat the multiplicity phenomenon more in detail later on. In general a multiplicity below 1 should be impossible, however, in the simple way it's defined here, giving small and big signals the same weight as long as they are above 30 mV, this surely is possible. Some more information can be extracted from (4.11) and (4.12),

1) The fraction of L2-signals not firing L1 is,
$$\frac{9659 - 7939}{5786} = 30\% \text{ (1720 signals)}$$
These must mainly come in from the side firing the 4 innermost counters in L2.

2) The fraction of L1-signals firing L2 as well,
$$\frac{5786 - 1720}{7939} = 51\% \text{ (4066 signals)}$$

This is also an upper limit for the muon content in L1, assuming all coincident signals to be muons. This should be compared with the 70% estimation of above; the beam related fluctuations are hard to determine, but it would be reasonable to assume that the side

flux have been underestimated. That is, as for L2 a substantial fraction of the total L3 counting rate is not seen by the two other planes, this was not corrected for when calculating the muon fraction in L1 and L2. Hence the '70%' was too high, and the high rate of L3 compared to L2 (see above), is partly explained.

The last single rates to be presented are those of R1 and R2 counters in Fig. 4.31. The innermost R2 elements are located only

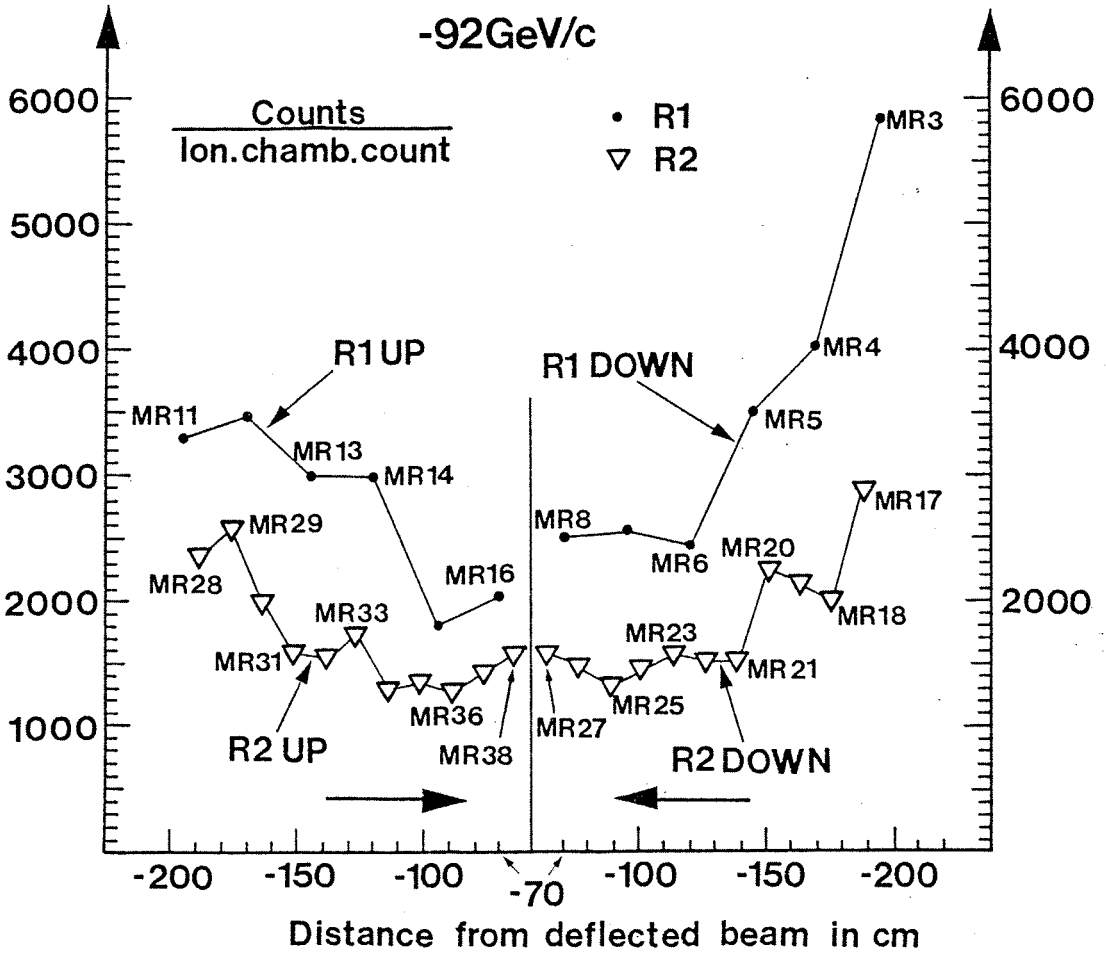

Fig. 4.31

Single rates in R1 and R2 normalized to the ionization chamber. Counter notation from Fig. 4.2, the x-axis refers to the distance between the x-position of the deflected beam opposite R1 (z = 1110 cm) and the counter center. For reasons discussed before, a 1 cm correction has to be used for R2 counters (z = 1230 cm). Threshold again set to -30 mV.

70 cm from the deflected beam. The sign of the beam and the direction of the magnetic field are such that halo and beam-particles are swept into the recoil arm. This may partly explain the very high recoil arm rates,

R1 UP	16711 (44%)		R2 UP	18797 (49%)	
R1 DOWN	20898 (56%)		R2 DOWN	19766 (51%)	(4.13)
R1 U+D	37609		R2 U+D	38563	

Again in units of $\frac{c}{icc}$. (4.13) implies for example, an R2-total rate of as much as 1.5×10^7 with 3×10^7 incident per burst (using 1 icc $\leftrightarrow$ 75,000 beam particles). Notice that the counters furthest away from the beam count the most, this indicates that a lot of these muons are of low momentum and hence are swept far out by the magnetic field. The deterioration of the beam quality (a low halo/beam ratio implying a good beam) at -92 GeV, is therefore also confirmed in the recoil arm. It could be due to bad beam adjustment, however, a lot of work was put into optimizing. Perhaps the beam-line itself could be blamed. Anyway, things should be checked more properly during the next -92 GeV run. This is necessary in order to understand well the rates of several trigger types (di-hadron, elastic and muon pair triggers, the two last will be discussed in chapter 5).

It is interesting to know the counting rates as a function of the discriminator threshold. Such a distribution is nothing but a "disguised" charge distribution, and since the total charge is proportional to the particle energy (see Fig. 4.7), one can deduce some information about the energy spectrum on each counter. For the relation between pulseheight (in mV) and charge of the signal, see Fig. 4.35. The distributions in Fig. 4.32 are "disguised" because one has to differentiate to get the q-distribution (with mV along the x-axis). This has been done in order to obtain the curves in Fig. A5.3. From this figure (and remembering that the pulseheight is directly related to the particle energy), one can

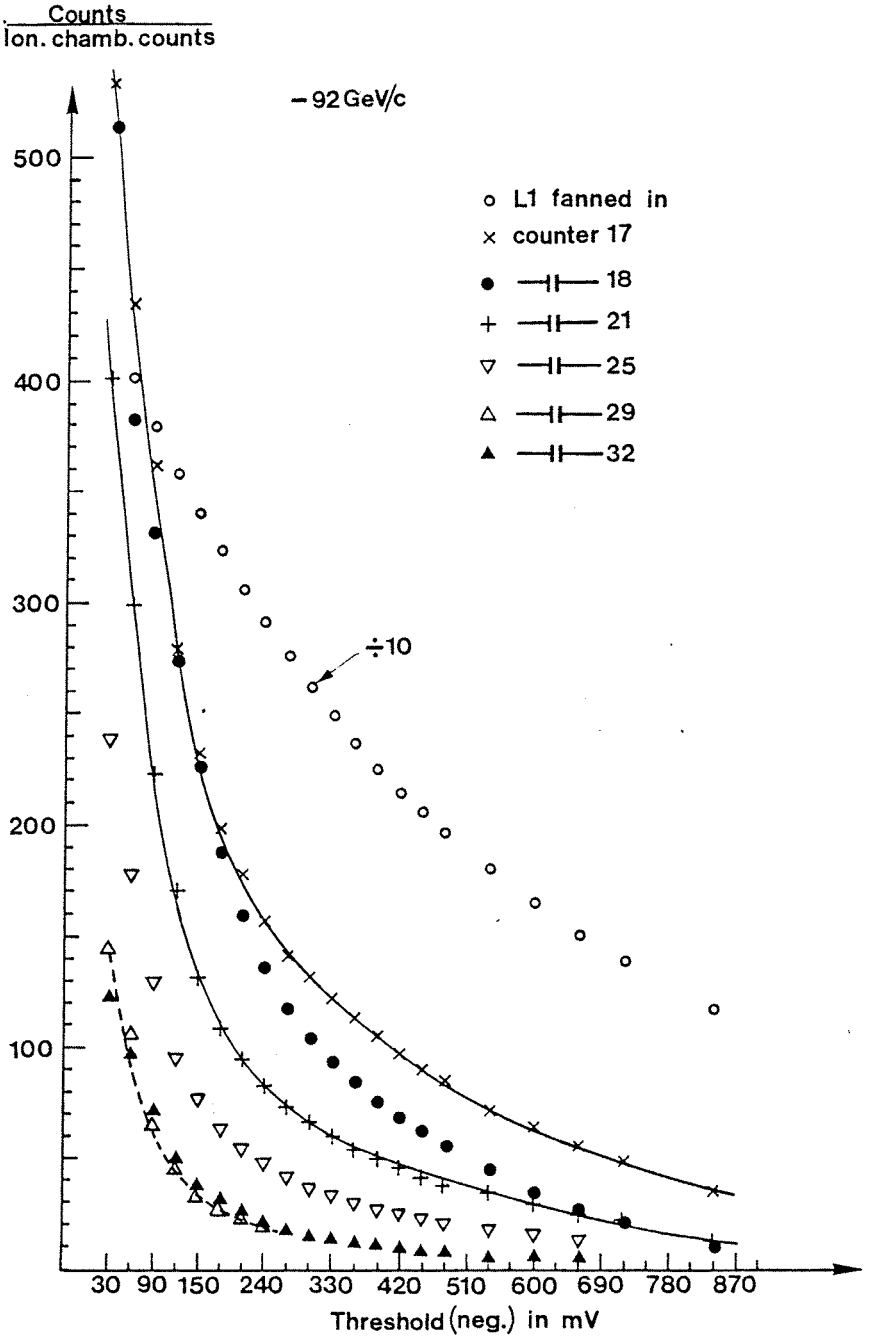

Fig. 4.32

Counting rates for different counters in L1 and 'L1 fanned in', as a function of the discriminator thresholds. The rates are normalized to the ion chamber as usual. The points for the 'L1 fanned in signal' are divided by 10. The intermediate behaviour exhibited by counter 18, is discussed in the text.

deduce that counter 29 and 32 'see' only 15% of the'high energy particles'which counter 18 see, for counter 25 this fraction is 33%. High energy particles are those whose signals exceed -200 mV, this cut is only motivated by the behaviour of data, see again Fig. A5.3. We have not established the relation between energy and single counter pulseheight, and it would be difficult to calculate; a single counter necessarily cuts into the shower (this fraction as we have seen, is energy dependent), and also the center of gravity of a shower moves into the calorimeter with energy. Hence, the fraction of the total signal seen by one single counter, depends on the energy. However, with data from ref. 10 we may set a lower limit for the '-200 mV energy equivalent'; they measured the mean signal after certain distances of iron for different incoming energies. Our '-200 mV' in the mean corresponds to a 2.6 ep-signal (Fig. 4.35). According to the measurements quoted above, the energy of the incident particle producing a 2.6 ep signal after 40 cm, is in the mean 5.5 GeV. Essentially this is found by interpolating between the 5 and 10 GeV - curves of Fig. 4.10.a. Now this corresponds to the entire shower after 40 cm, while we are only sampling a fraction of it with one counter. Clearly, 5.5 GeV is therefore a lower limit for the '-200 mV energy equivalent'.

Notice in Fig. 4.32, that counter 18 displays a mixed behaviour, for small thresholds it detects the low energy particles coming in from the side which also are seen by C. 17. However, for higher energies and thresholds the particles are more parallel with the beam, therefore only C. 17 will see some of these particles entering the iron along the calorimeter beam side, and C. 18 shows more the behaviour of C. 21 which surely is sufficiently shielded.

Apart from rate distributions for counters 17, 18, 25, 29 and 32, Fig. 4.32 also shows the same rates for the fanned in L1-signal with no attenuation, see Fig. 4.29. This makes it possible to obtain some information about the mean multiplicity in L1 averaged over all counters. By multiplicity is in general understood the number of

counters that fire at the same time. Often in counter experiments one may correctly assume that almost all particles involved are minimum ionizing and if this is the case, "multiplicity" is self explanatory; either a counter has fired or not (cf. the q-distribution of Fig. 4.26 for example). On the contrary, with distributions like the ones in Fig. 4.33 showing raw q-distributions, of L1 fanned in (no attenuation) and of a single counter, counters fire 'so and so much'. A more appropriate definition of multiplicity would therefore be, (the average total charge of L1 fanned in when counter i alone produces a charge q) devided by (q). Let this fraction be m (i,q). Notice that greater than 1 multiplicity is caused by two effects, 1), the particle induced shower in the iron spreads out, and very often covers more than one counter (they are only 12.5 cm wide) and 2), there may be more than one particle incident on the iron. With our data these two effects are non separable. In order to study their relative importance one would have to study off-line the information recorded by the ADC's. That is, establish the correlations between reconstructed tracks in front of the calorimeter and the actual counters which fire. However, this does have the inconvenience of studying only a selected sample, the events satisfying our trigger conditions. To be more specific, one should study off-line those events which satisfy the trigger conditions up to the level where the CAL.YES is supposed to be introduced (see Fig. 5.9), after that no biasing by further selection should take place before the events are written to tape. It is interesting to study m(i,q) because with a high intensity beam one will observe many events with high multiplicity incident on the iron. But it is not clear to what extent this will decrease the calorimeter rejection efficiency R (see A4). Put in another way, how much could be gained by selecting for discriminator testing only those counters which are hit by the shower, (to be termed 'fancy adding or fanning in')? Off-line results to answer this question do not exist since we have not accumulated such special data.

I shall now turn to the problem of calculating m (i,q), this will be based on the rates given in Fig. 4.32.

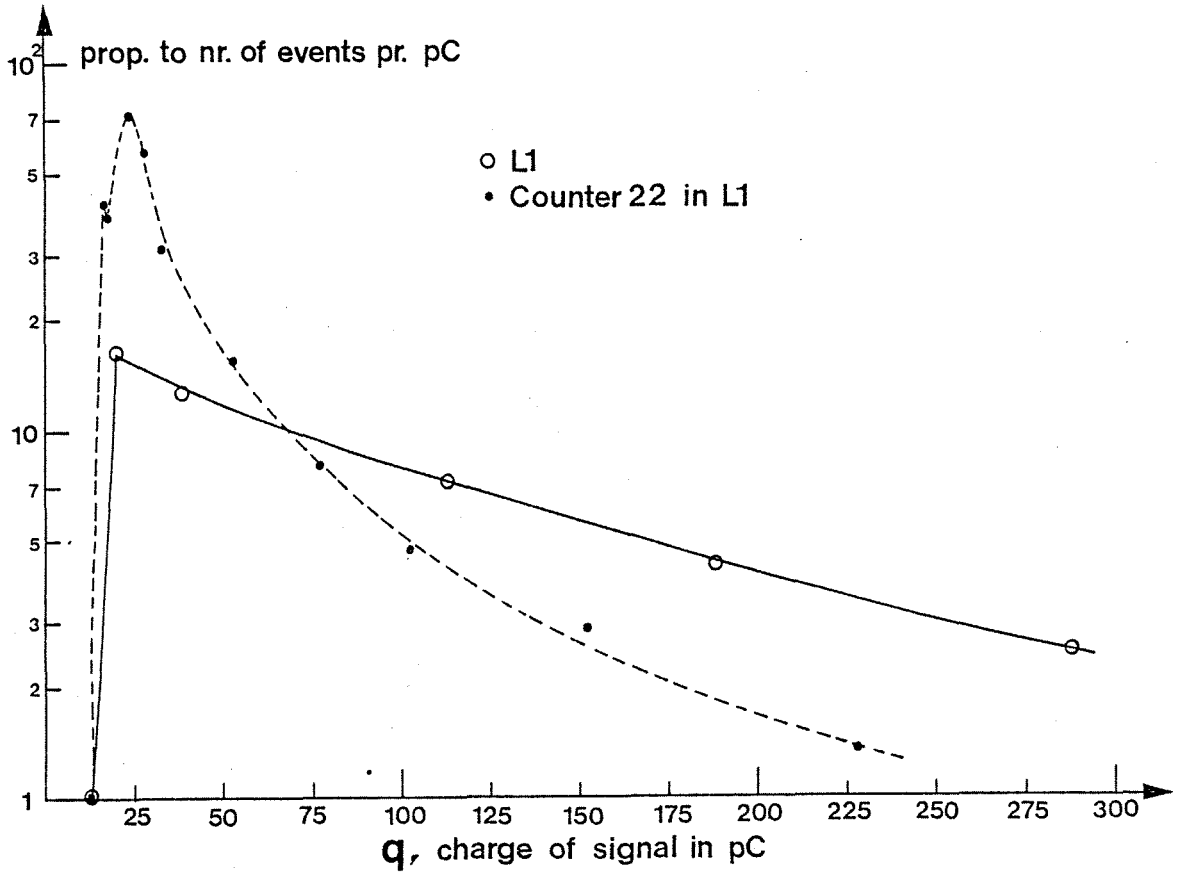

Fig. 4.33

Raw q-distributions for the fanned in L1-signal (o), and for the counter 22 - signal (•). 'Raw' meaning, no selection with trigger, see Fig. 4.17. The x-axis gives the integrated charge in pC. The unit along the vertical axis is arbitrary, but both curves are normalized so that the integrals are equal.

What is calculated is M ($h > h_o$) which is m (i, $h > h_o$) averaged over all L1-counters, and instead of studying M as a function of the charge q, it will be studied for pulses bigger than h_o (in mV). From Fig. 4.32 one can easily obtain the overall L1 single rate

above different thresholds (interpolating linearly to get rates which were not measured and assuming up-down symmetry). From this again is found the counting rate density (pr. mV and beam (icc)) CR_S (h), where S refers to single element. Let CR_A (h) be the counting rate density for the added L1-signal, also found from Fig. 4.32. Consider all entries in CR_A (h) such that $h > h_o$, assume that all of them are made up of at least one single signal above h_o. Then the mean multiplicity for pulses above h_o is given by

$$M\ (h > h_o) = \frac{\int_{h_o}^{\infty} h\ CR_A^n\ (h)\ dh}{\int_{h_o}^{\infty} h\ CR_S^n\ (h)\ dh} \qquad (4.14)$$

where CR_A^n and CR_S^n are supposed to be normalized,

$$\int_{h_o}^{\infty} CR_A^n\ (h)\ dh = \int_{h_o}^{\infty} CR_S^n\ (h)\ dh = 1$$

$M\ (h > h_o)$ tells to what extent a mean single signal above h_o is accompanied (within the PM resolution time, $\sim \pm 15$ ns) by other mean signals. But the assumption that never can a L1 added signal above h_o be made up exclusively of L1 single signals below h_o, is evidently wrong. Before integration of CR_A in (4.14) one should therefore subtract the fraction which comes from below h_o. Let the resulting function be, $CR_{A,C}$. That is, CR_A^n should be replaced by $CR_{A,C}^n$ in (4.14). This new distribution, cannot be calculated without knowledge of the multiplicity itself. However, I shall assume that the contribution of exclusively below h_o signals to CR_A (h), is only felt for $h < 3h_o$ and that the effect is linear between h_o and $3h_o$, i.e. :

$$CR_{A,C}(h) = \begin{cases} 0 & h \leq h_o \\ \dfrac{CR_A(3h_o)}{2h_o}(h - h_o) & h_o \leq h \leq 3h_o \\ CR_A(h) & 3h_o \leq h \end{cases} \qquad (4.15)$$

In Fig. 4.34 are shown results using both CR_A (curve a) and $CR_{A,C}$ (b). Notice that curve a represents a lower limit for the multiplicity; the denominator of expression (4.14) will increase with the type of correction considered above. Also, the correction which results from using (4.15) seems big. That is, remembering the shower size from section B one would expect the $3 \cdot h_o$ to be a bit high. Therefore the correct multiplicity is likely to be found in between the two curves. One may to some extent separate the two multiplicity effects. The multiplicity goes rather constant for $h_o > 250$ mV, this is a reasonable behaviour if only one shower is incident on the plane, it simply says that one single counter in the mean sees a constant fraction of the total shower independent of the particle energy (if there is a slight decrease for $h_o > 250$ mV, then this is caused by the shower becoming more forwardly directed with energy). Below 250 mV there is an increase in multiplicity which it is natural to ascribe to multiple showers within the resolution time. This is reasonable since a reduction in h_o implies lower mean energy per particle, which again in the mean, leads to a higher particle multiplicity.

Obviously the multiplicities could have been extracted without uncertainties had the measurements been done in another way. To avoid having to estimate $CR_{A,C}$ one should make sure that $CR_A(h)$ is measured only when at least one single counter triggers a discriminator set to h_o. Having determined $CR_A(h)$ for different h_o ($\equiv CR_A(h,h_o)$, where h is the threshold for the added one plane signal, and h_o is the single counter threshold), one may then find the multiplicity in a small $2 \cdot \Delta h_o$ interval,

$$m(h_o) = \frac{\int_o^\infty h\left[CR_A(h,h_o-\Delta h_o) - CR_A(h,h_o+\Delta h_o)\right]dh}{\int_o^\infty \left[CR_A(h,h_o-\Delta h_o) - CR_A(h,h_o+\Delta h_o)\right]dh}$$

$$\times \left\{ \int_{h_o-\Delta h_o}^{h_o+\Delta h_o} h \cdot CR_S^n(h)\, dh \right\}^{-1}$$

$$= \frac{\frac{\partial}{\partial h_o} \int_o^\infty h\, CR_A(h,h_o)\, dh}{\frac{\partial}{\partial h_o} \int_o^\infty CR_A(h,h_o)\, dh} \times \left\{ \int_{h_o-\Delta h_o}^{h_o+\Delta h_o} h\, CR_S^n(h)\, dh \right\}^{-1}$$

The difference between CR_A at $h_o + \Delta h_o$ and $h_o - \Delta h_o$ represents the added one plane distribution when all added signals contain at least one single signal with $h_o - \Delta h_o < h < h_o + \Delta h_o$.

In Fig. 4.35 is shown the much used relation between the actual pulseheight h, and charge q, for our PM-signals (type XP 2232 B, Philips), and also the equivalent relation for the fanned in L1-signal. The relations were obtained by doing q-measurements as described in the beginning of this section. The L3001 was simply triggered by the PM- or L1-signals when these bypassed the discriminator threshold h. See for example Fig. 4.20 to understand the effect of a threshold cut. So what is drawn in Fig.4.35, is the length of the straight cut, representing the fluctuation in charge with constant height. The bars representing the measurements for counter 18, lie nicely on a straight line. For h > 400mV,

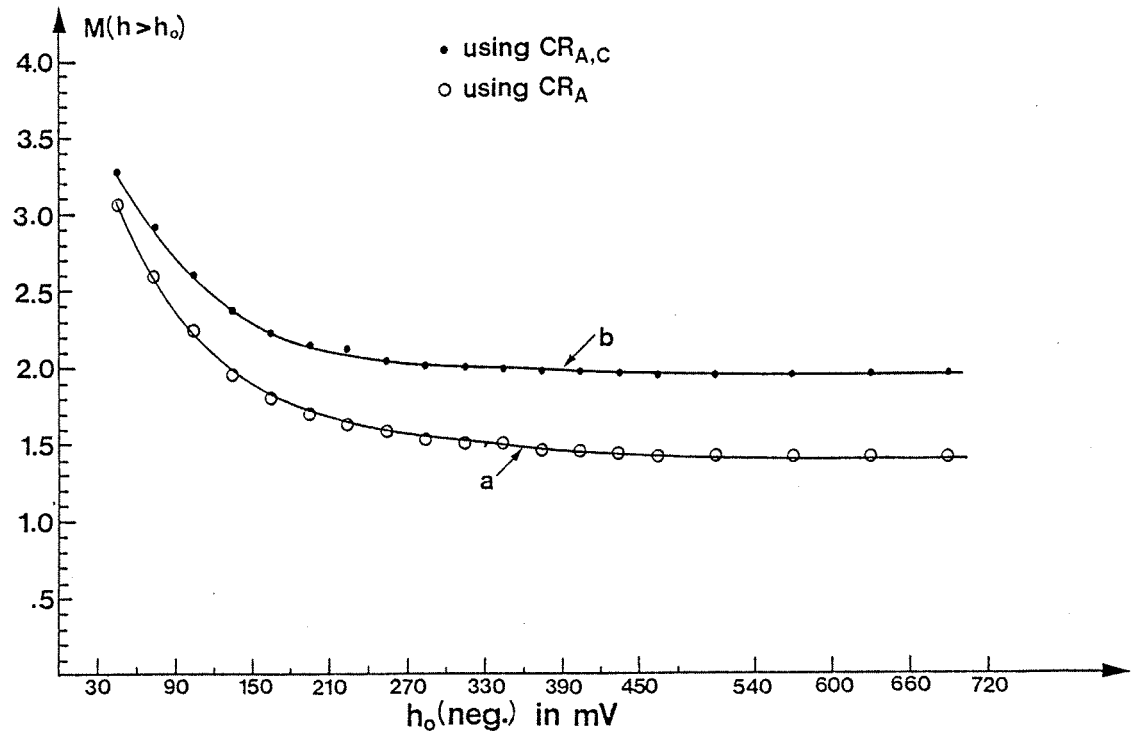

Fig. 4.34

Mean multiplicity in plane L1 for single signals $\geq h_o$. (o) - points show a crude calculation, (•) - points are the result of a correction which also sets an upper limit for $M(h > h_o)$, see text.

the charge was seen to saturate, i.e. pulses were partly cut by the integration gate when they became sufficiently high. The L1 response is shown by (•) - and (▽) - points, respectively representing relative cut length (width) and relative mean cut position (both compared to counter 18). The results displayed in the figure are relevant for the timing of individual signals, I shall therefore first explain some details about this timing.

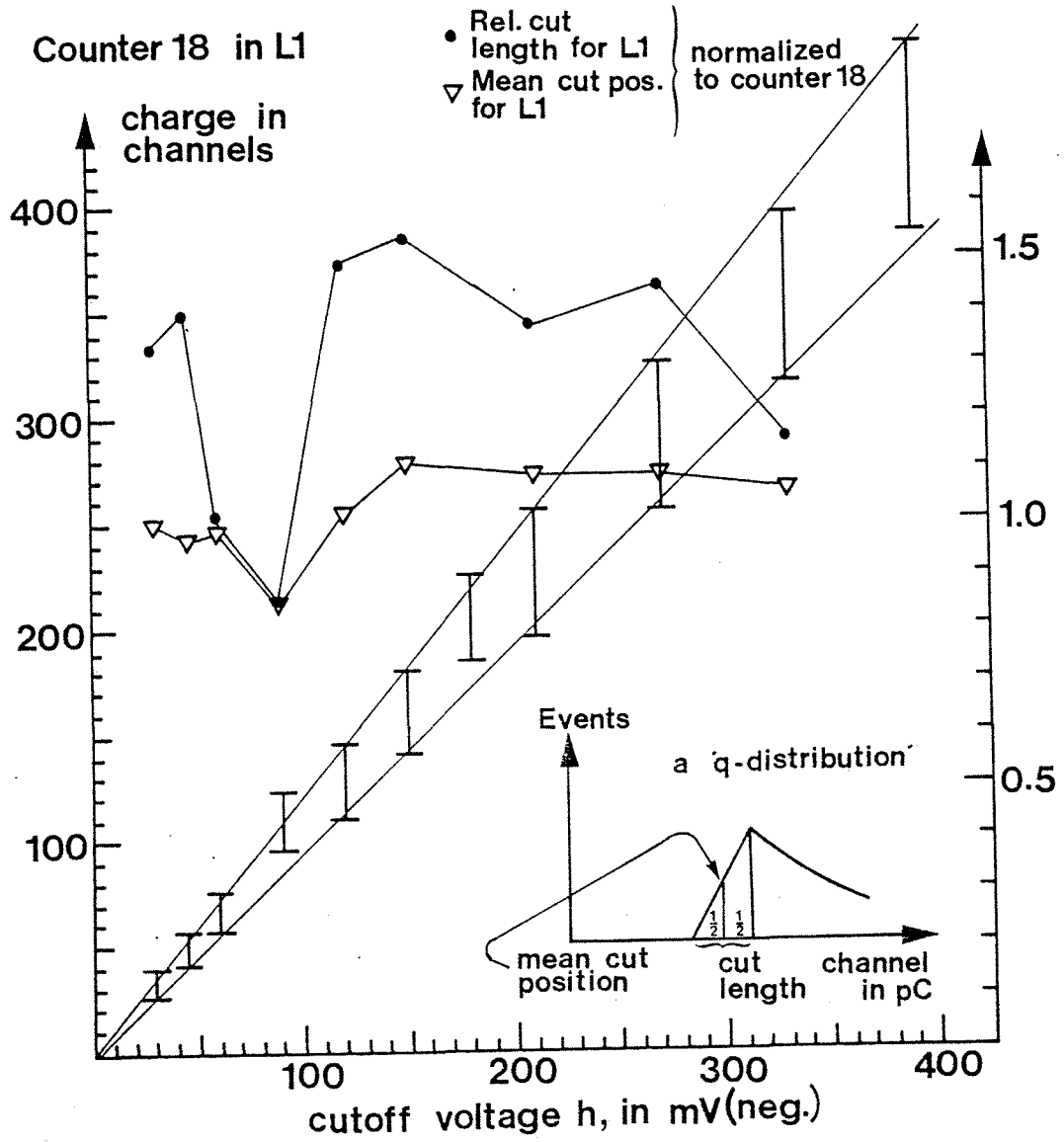

Fig. 4.35

Height versus charge of our PM-pulses, 1 channel = 0.25 pC. Bars give the exact charges of the cut length. The same is given indirectly for the fanned in L1 signal: (▽) - points represent (the mean cut position for L1) devided by (the mean cut position for counter 18), and (•) - points in the same way the relative cut length for L1 signals. For both curves, use scale to the right. Inserted is a general q-distribution with definitions of the terms used above and in the text.

Referring to Fig. 4.29, L1 and L2 signals were timed separately in such a way that equal height signals arrive at the same time at the first level of fanning in. We used the L3001 analyser to measure the time differences, the method has already been described in chapter 2F. The point is to make the fanning in as linear as possible in pulseheight, a non-linearity implies that the correlation between energy and pulseheight (threshold) deteriorates, and hence also the possibility to distinguish between different energies of incoming particles. For example, for a shower split equally between 3 counters (in charge and pulseheight) it would be nice to know that not only will the total charge be 3q (otherwise our fan in wouldn't work), but also that the total pulseheight is 3h. To obtain this, evidently the timing is crucial. In figure 4.36 is shown the relative time spectrum obtained when two (vertically) adjacent counters give the start and stop to the L3001. The FWHM is 2 ns wide. The threshold settings are the same for both start and stop pulses. Generally a shower is split unequally between adjacent counters, but in the mean it will be equally split. Also, it is reasonable to expect the splitting to be a symmetric distribution; for example, q (element 1) - q(element 2), should be distributed symmetrically around zero. This feature is nicely confirmed in Fig. 4.36.a, the width of the distribution certainly comes from individualities of the two counters, but also from the fact that the shower is unequally split (the bigger part triggers earlier than the smaller). Due to the symmetry, the peak position will correspond to signals with the same shape and height. Coincident timing of these signals (which implies that the maxima of the signals also will be coincident), was defined as good timing. This was the only reasonable choice since it implies minimum jitter between signals of different shape (and/or height). To set the timing, we first established the peak positions

for all counters on an arbitrary ns time-scale. This was done by measuring counter 2 relative to 1 and 3, next counter 4 relative to 3 and 5 etc. etc., now and then checking also the time difference between symmetrically positioned up/down counters. Next the timing was adjusted so that all peak positions would be found in the same bin on this time-scale. The final precision was good since the peak is so well defined, approximately ± .5 ns.

A check on the linearity of the total pulseheight, is the shape of the resulting signal, In Fig. 4.36.b are shown two ideal cases where the added signals have the same shape as their origin signals, in practise, however, the individualities of the different counters (different time constants for the scintillator material, different PM high voltage etc) plus incertainties in the timing

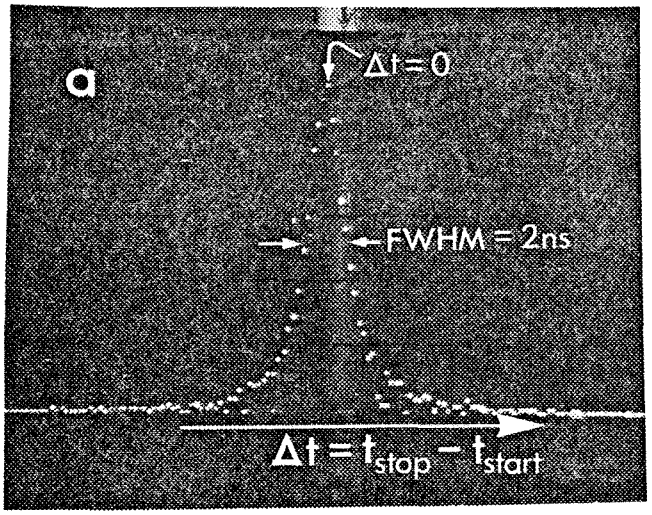

Fig. 4.36.a
TOF, or time of flight spectrum, between two adjacent counters in L1 (counters 14 and 15). One point represents 0.25 ns.

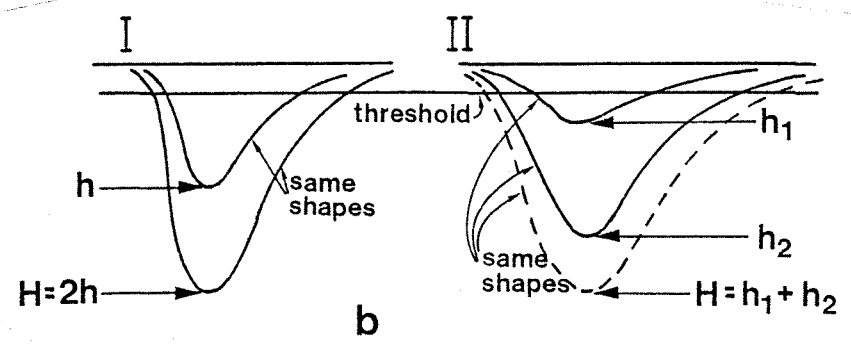

Fig. 4.36.b
Examples of how pulses from two adjacent counters produced by the same shower, add when I, the shower is equally split II, it is unequally split.

and threshold settings, all this makes the examples of Fig. 4.36.b ideal and in general $H < h_1 + h_2$. Results of the L1 timing is therefore indirectly shown in Fig. 4.35; at maximum, with the same pulseheight for L1 added as for counter 18 alone, will the charge of the added signal be 10% (at 150 mV) superior to the one of counter 18. This is important to establish because we want to use a threshold cut and not a charge cut on our elastic event candidates.

For example, demanding at least 5 ep (= 100 pC) in to our L1 fan-in's, is equivalent to demanding that 'L1 fanned in' is above $\sim$ 5 x 70 mV (1 ep = 20 pC $\sim$ 70 mV, see Fig. 4.35). There may be a reduction of up to 10% in the equivalent threshold cut due to reasons just discussed. Notice that this small change in signal shape not only reflects good timing but also that we are looking almost only at one event cases during the 100 ns integration gate. That is, additional random events falling within this 100 ns gate are time uncorrelated and would therefore with the same pulseheight increase the integrated charge. All these measurements were done with $\sim 10^7$ incident per burst and a -92 GeV/c beam.

Notice from the point of view of randoms, that a pure threshold cut is cleaner than a charge cut (which necessarily implies a gate of $\sim$ 50 ns). This brings me over to the deterioration in resolution due to a threshold cut as compared to a charge cut. When running with an elastic trigger, we are interested in the charge of the biggest shower which again is (in the mean), directly related to the energy of the incident particle producing the shower. The most correct is therefore to impose a charge cut on this shower only. A threshold cut would lower the energy resolution somewhat, hence a lower cut would have to be introduced unless one accepts the otherwise resulting increase in unwanted vetoing. This is so because pulses with the same charge have different shapes

(and hence heights). From the two straight lines in Fig. 4.35 one may deduce that the additional uncertainty in $\sigma_{R,E}$ (if the whole shower hits one single counter) due to a threshold cut, is approximately ± 12%. However, the situation is more complex because all counters are added. How would a threshold cut affect the trigger rate as compared to a charge cut in this case? There are two competing effects if a threshold cut is introduced, 1) the roughly 12% reduction in the effective cut level naturally increases the trigger rate while 2) the non-linearity in the addition of pulse-heights (as opposed to the case of addition of charges) will eliminate some of the background which a charge cut could not get rid of. That is, the inefficiency (or non-linearity) in pulse-height addition will mostly affect events with more than one shower incident on the plane, this is certainly the case for uncorrelated showers impinging within the resolution time of one specific shower, but this inefficiency may also be caused by correlated showers which develop differently in the iron (remember such a shower involves a lot of non relativistic particles). On the other hand the addition of counters within one single shower may be timed to add very well (see Fig. 4.36.a). The enhancement in the relative cut length observed for L1 signals in Fig. 4.35, may therefore be ascribed to fluctuations in shape which again, is mostly caused by the existence (or non existence) of additional showers. Notice the dips between 50 and 150 mV for both curves in Fig. 4.35. They may be explained by the relatively big influx of "relativistic signals" (from muons) in this interval; with the same height, "relativistic signals" (from minimum ionizing particles) produce a smaller charge than "other signals". Which is reasonable, because mostly the "other signals" are actually a sum of several light flashes in the scintillator (corresponding to some of the shower particles hitting the counter). The fact that the dip

value is below 1, is bizarre, however, again can the argument of varying halo conditions be invoked. To sum up, a threshold cut is less than 12% "worse" than a charge cut, probably equal in performance (rejection vs. inefficiency), this is true for cuts as high as 5 ep (for a single plane) and with a -92 GeV/c beam of at least 10^7 incident per burst. The relevant rates at this energy is given in figures 4.30 and 4.32.

We did not pursue these studies further, the conclusions are sufficient to impose a 1 or 2 ep threshold running elastic scattering with 20 or 30 GeV/c incident. The shower inherent fluctuations still are all important. With the situation of 5 planes covering the first 60 cm of iron these fluctuations decrease while non-linearity of pulseheight adding increases. But my guess would be that adding could still be performed very well with several planes. However, the effects of additional showers will be felt more (because more planes are located more upstream). Therefore with a bigger calorimeter trigger setup. the idea of 'fancy adding' should be considered (that is, apply the charge or threshold cut to only the fanned in signal of those counters hit by a shower). This is especially true if one wants to eliminate the charge/height related fluctuations by triggering on the charge of the fanned in signal. In this case, with a resolution time of ≥ 50 ns, the random rate may be felt to a much larger extent, remember that 10^7 is not a high intensity for high-t elastic scattering, and the fancy adding is likely to be the only remedy to make the charge cut 'win'.

The convenience of a charge cut should not be neglected, the work put into high precision timing and monitoring afterwards of $\sim$ 200 counters, is considerable, this is avoided if one does a charge addition, the signals should only fall fully within the

integration gate. The interest of developing a fast integration device etc, should be studied by finding how non-linear the pulseheight adding is. The guess of above, that this adding, even with many planes, is rather linear, is motivated by the fact that in the mean, only two planes after the primary interaction vertex will see most of the shower*. So for the main contributors to the signal there is not much 'room' for time fluctuations, the planes being < 15 cm apart. This will be treated to some extent in the last section of this chapter.

For completeness; the relative timing between L1 and L2 fanned in was measured and adjusted between the two last levels of fanning in, see Fig. 4.29. This was done by "eye", evidently a more precise method has to be used if and when the information relayed by the L1 + L2 - pulseheight is exploited. In our case, L2 was essential in order to see elastic candidates that reacted more than 40 cm into the iron (10%). The L1/L2 relative timing was unimportant both for this last efficiency consideration and for the overall rejection (almost fully done by L1).

* * * * * * * * * * *

Before ending this section I shall explain how the 'very fast logic' for selecting muon pairs were set up. In chapter 5 will be discussed the general fast decision making logic and in particular how this muon trigger and the CAL.YES signal were incorporated. The muon pair logic is shown in Fig. 4.37. In the recoil arm one element in R1 is coincidenced with an OR between 2,3 or

---

* From ref. 10: at 5 GeV this fraction is 90%, at 10 GeV it's 69%, at 20 GeV it's 65%, at 30 GeV it's 63% and finally at 50 GeV 55%.

4 R2-elements. The correlations were set up on the bases of Monte Carlo results. That is, first ψ's were generated randomely, but in such way that already existing data on the production mechanism was reproduced ($X_{||}$ and X_T-distributions in the center of mass system), then the ψ was made to decay isotropically (in its center of mass system) into two muons. These were then tracked through the magnetic field and down through the apparatus. Only those muon pairs which would trigger the elastic correlation matrices between H1 and PR1 and between H2 and PR2, were considered. These matrices, essentially define tracks coming from the target region. By selecting events where one specific R1 element has fired and plotting the track impact on R2, one could easily establish the R1-R2 correlations. At -92 GeV/c they were the following:

R2		R2
MR3 (MR11)	with	no elements
MR4 (MR12)	with	MR17, MR18 (MR28, MR29)
MR5 (MR13)	with	MR18, MR19, MR20 (MR29, MR30, MR31)
MR6 (MR14)	with	MR20, MR21, MR22, MR23 (MR31, MR32, MR33, MR34)
MR7 (MR15)	with	MR23, MR24, MR25 (MR34, MR35, MR36)
MR8 (MR16)	with	MR25, MR26, MR27 (MR36, MR37, MR38)

where up elements are in paranthesis. As we shall see, the constraint that the muon pair should fire the straight line matrices mentioned above, is also implemented in the logic, see Fig. 4.37 and Fig. 5.3. This is true for both arms. For the fast arm we demanded a signal from both L2 and L3.

Crucial for reducing the trigger rate was the coincidence between the two arms. It was done by demanding either a L3 UP/(R1 * R2) DOWN- or a L3 DOWN/(R1 * R2)UP- coincidence. This special way of making the coincidence was justified by the muon pairs being rather coplanar with the beamparticle, the ψ's being

produced mostly at very small angles to the beam. The loss in acceptance was 10%. But taking advantage of the coplanarity cut the accidental rate between the two arms by a factor 2. The total trigger rate was reduced somewhat less, 20-30% compared to the rate measured with a simple L3/(R1 * R2) - coincidence. Which is reasonable since it is only that half of the triggers which is made up of uncorrelated signals in each arm, which will be affected.

In Fig. 4.37 is also shown the beginning of the fast logic which was part of the general trigger logic. This includes the elastic trigger generation and also additional constraints which could be imposed on the muon pair trigger. Such as 1), demanding an L2 signal, (indicated with a dashed line in Fig. 4.37 because it actually enters the logic at a later stage) 2), demanding a certain Cerenkov combination to have fired 3), also that a cedar combination has fired and last 4), that the muon multiplicity is limited. These points will be discussed in chapter 5 since they are relevant for the general logic.

I shall mention some points concerning the timing of the signals in the set up of Fig. 4.37. First, most discriminators were set to a -30 mV threshold, for some, a bit higher to reduce the noise background. The width of all discriminator outputs were set to 15 ns. And the first level timing was done so that different counters fired by the same interaction in the hydrogen target, would produce coincident signals out from the discriminators. To do this, the prompts (PR1/PR2) were used as the time reference. As explained in chapter 2, all prompt elements were timed so that the time differences between a target reaction and the resulting prompt signals at their discriminator outputs, would all be the same.

Let this time reference be t_o, and let t in the following refer to the time at the discriminator output. We therefore measured $\Delta T_i \equiv t_i - t_o$ for all elements in L3 and R1. As before these spectra were obtained using the L3001 multichannel qVt analyser. To establish the ΔT_i's for R2 we used R1 as a reference. Finally all counters were made to have the same ΔT's by adjusting the cable length, the earliest possible (smallest ΔT), was chosen. Notice that instead of using PR1/PR2 as a reference it would have been better to have used the matrices H1 * PR1 and H2 * PR2, their timing also being set by the PR1/PR2 elements. Without changing the timing, one would have purified the sample by discarding a lot of the background which is observed when not imposing an H1 or H2-coincidence (particles which are non relativistic or originating outside the target). However, this more severe time reference drastically reduced the statistics, and since the signal is anyway clear enough to measure ΔT, although sitting on a higher background and being itself wider, no such improved ΔT measurement was done.

There are two reasons for fixing the timing in this way. First, the time jitter between the gate (produced by the fast strobe), and all the single counter signals at the CAMAC bit (or coincidence) registers (type L2341A), should be minimized and second, making all ΔT_i's equal largely facilitates further cabling and timing in Fig. 4.37. Some cable lengths are indicated, taking into account the internal delay of the 'Lo F I/Os', these cable lengths ensure correct timing at the inputs of coincidence units 1-5. The 15 ns signal width is necessary to have $\sim$ 0% inefficiency at the level of making the coincidences. That is, like shown in Fig. 4.38.a, it is a distribution which represents the time difference between two correlated signals. Such a distribution between R1 and R2 signals is very sharp, and it would be no problem to reduce the

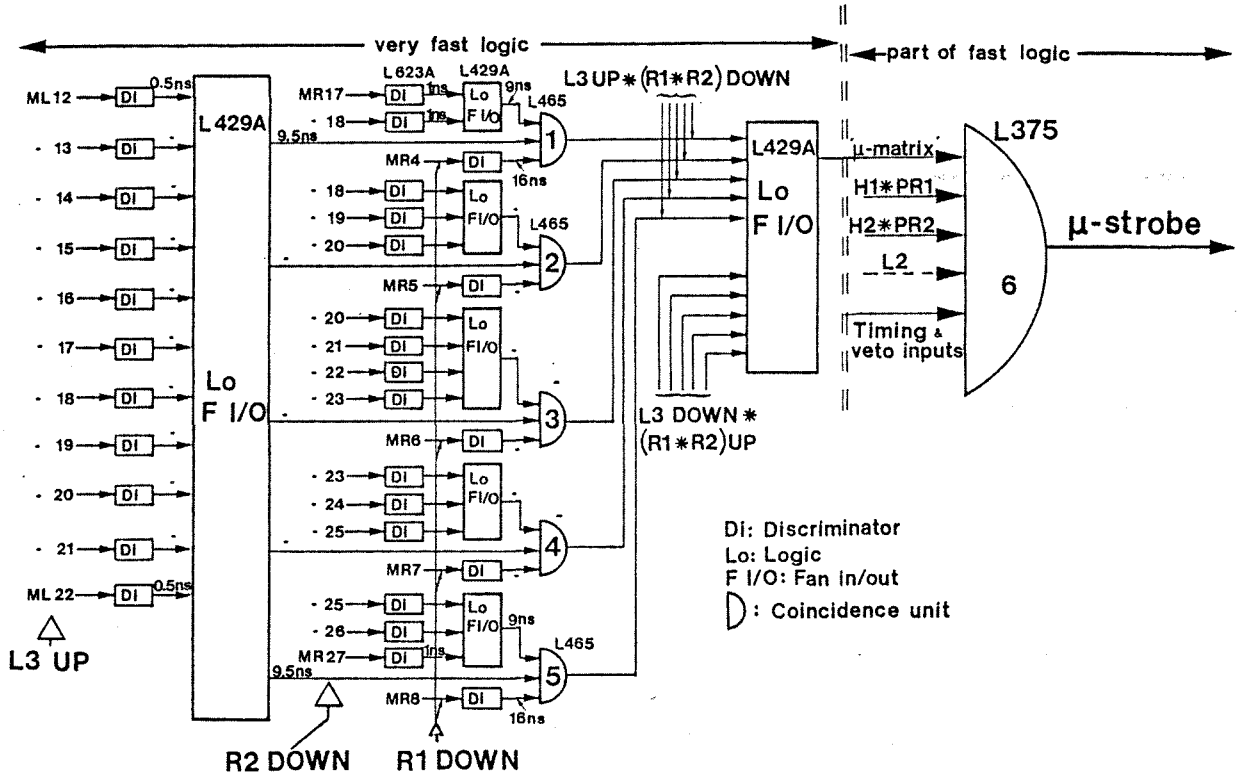

Fig. 4.37

The very fast muon pair trigger logic. In detail is shown only how L3 UP * (R1 * R2) DOWN is constructed, however, L3 DOWN * (R1 * R2) UP is constructed in a completely symmetrical way. Notice that the logic fan in/outs play the role of OR's. The fast logic is discussed in chapter 5. There are delay lines for all counters from discriminators to CAMAC bit registers. Logic fan in/outs are of type L429A. In the figure some counters seem to be equipped with more than one discriminator, this is not actually the case (the L623A discriminator is provided with 3 outputs per input), the reason for drawing like it has been done is purely technical.

signal width and still have ∿ 100% coincidence efficiency between these two signals. However, what matters to cut the muon pair trigger rate,is the coincidence between the two arms. Unfortunately, the time jitter between correlated signals in the two arms is as much as 20 ns. Therefore, with optimum timing to have ≈ 100% coincidence efficiency, the signal widths should be > 10 ns. This imlies that the minimum coincidence overlap is zero, typically it is 1 - 5 ns, see chapter 5B about veto counters. On basis of this the signal widths were fixed to 15 ns.

This brings me over to the next point, namely the timing at the input of coincidence unit 6. In Fig. 4.38.a is shown the start-stop time distribution between the 'μ-matrix' (see Fig. 4.37) and the coincidence between 'H1 * PR1' and 'H2 * PR2'. At the base the jitter distribution is 25 ns wide. Since the signal defined by 1) * 2) in Fig. 4.38.b, is very narrow, the μ-matrix signal width should also be 25 ns. Having fixed this width, the cable lengths are chosen so that $\Delta T_{max} = 2.5$ ns and $\Delta T_{min} = -22.5$ ns. This ΔT is defined in Fig. 4.38.b. Coincidence units 1-5 all have adjustable output widths, this saved using shaping units which would have introduced additional delay. As we shall see later, the μ-strobe had to be generated at the same time as an elastic strobe (relative to a target reaction). Therefore the timing of H1 * PR1 and H2 * PR2 could not be changed. Since in addition, the 'μ-matrix' arrived late ($\Delta T_{min} = -22.5$ ns is the absolute minimum possible), the logic had to be done as fast as possible. This was also the reason for choosing the earliest possible common timing (minimizing ΔT, see page 4-98).

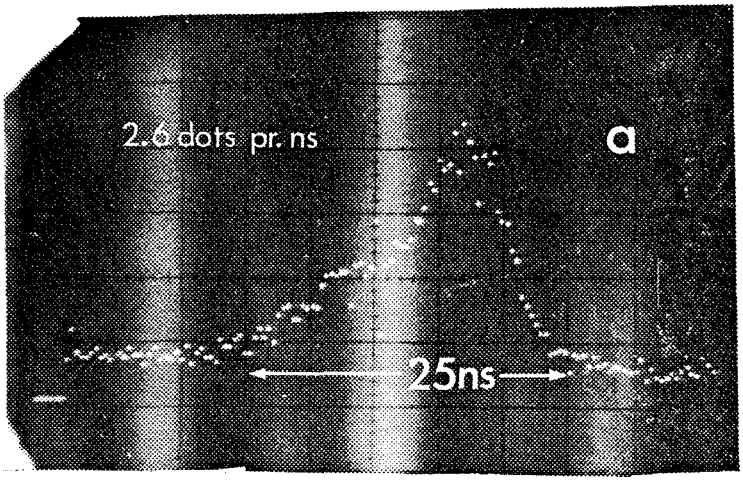

Fig. 4.38.a

Time distribution between two specific signals at the input of the strobe coincidence unit, see Fig. 4.37. The two signals are 1), μ-matrix and 2), (H1 * PR1) * (H2 * PR2). The second signal had to be generated by an additional coincidence unit inserted after the last 'Lo F I/O', see Fig. 4.37.

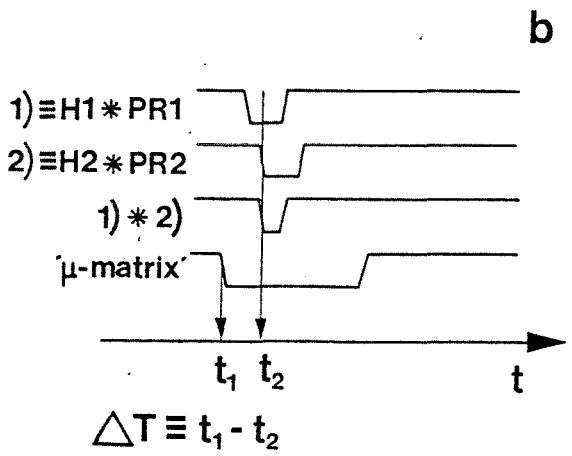

Fig. 4.38.b

Definition of ΔT. Notice that 1) * 2) simulates the real coincidence between H1 * PR1 and H2 * PR2 inside unit 6, see Fig. 4.37. The timing was done so that ΔT_{max} = 2.5 ns and ΔT_{min} = -22.5 ns (with the Fig. 4.37 set up).

F. Plans and future use.

As already mentioned, the calorimeter in the forward arm will be extended so as to be made up of 5 scintillator planes. This will allow to run with a higher rejection threshold, and the calorimeter should seriously start to veto low energy hadrons. For an estimation of the rejection as a function of energy, see Fig. A4.7. Applying the results of appendix 4 on the measured momentum spectra in the forward arm with 20 GeV/c incident, one obtains 48, 61 and 68% rejection for the pion, kaon and proton trigger respectively, see table 4.2.

The calorimeter may also be used when running with other triggers, to veto low energy particles. This is the case during di-hadron and medium-t data taking. The di-hadron trigger should select events with two outgoing hadrons (at $\sim 90^{\circ}$ in the CM-system and with high transverse momenta), while medium-t simply refers to elastic scattering in the intermediate t-range, from ~ 0.5 $(GeV/c)^2$ to ~ 8.0 $(GeV/c)^2$. Medium-t physics has been done with up to 50 GeV/c incident, and will be done at even higher momenta later. Some di-hadron data has already been taken at -92 GeV/c. So, the calorimeter is actually more useful for these triggers because the beam momentum is not limited upwards (as when doing high-t physics), by very low cross sections.

Now to some details about the new scintillator planes. They will each consist of 20 counters; we tried to minimize the number of channels due to expensive electronics. The 12 counters closest to the beam keep the original width of 12.5 cm, while the rest of the plane, 1.2 x 2 m^2, is covered by 8 counters 30 cm wide. Current limitations of the PM's limited the width of the elements closest

to the beam, while space (between iron and floor) limited the width of the ones furthest away. That is, the light guide is a triangular flat cone which brings the light from the cross section of the scintillator itself (12.5 or 30 cm, times 1 cm), down to the PM (diameter 4.4 cm), the angle between light guide and scintillator should be smaller than $\sim 25^{\circ}$, otherwise light may be lost. Hence, also space considerations set an upper limit for the scintillator width.

The material for the new planes is Plexipop, which is a doped plastic scintillator. With 1 cm thickness and a rather low conversion efficiency, the same particle will produce less light in this new material than in the Nuclear Enterprise (NE) material, which was used in L1/L2. Preliminary measurements indicate that minimum ionizing particles produce roughly 10 photoelectrons, confer Fig. 4.25. This naturally, will worsen the resolution, but not very much, as seen from the following quantitative example. Assume that for Plexipop, 10 photoelectrons are produced pr. ep, and that the same quantity is 40 for NE. What is then the scintillator related contribution to the overall relative resolution of signals which in the mean are 5 and 10 ep ? Notice first, assuming 100% containement with only 5 planes, that 5 and 10 ep correspond in the mean to very low incident energies, respectively 2.5 GeV and 3.5 GeV (from fit in Fig. A4.1). At such low energies the shower inherent fluctuations are enormous, at least ± 40%. However, the signals are even so, typical as rejection thresholds, see Fig. A4.7. If the total signal Q (which is proportional with the number of photoelectrons), is poisson distributed, then the interesting figures are given in the table below,

Mean Signal Q	material	$\bar{n}$	σ_n	$\sigma_{n,R}$	$\sigma_{Q,R}$
5 ep	Plexipop	50	7.1	0.14	0.424
	NE	200	14.1	0.07	0.406
10 ep	Plexipop	100	10	0.10	0.412
	NE	400	20	0.05	0.403

Table 4.3 $\bar{n}$ is the mean total number of photoelectrons produced at all photcathodes. If n is poisson distributed, then $\sigma_n = \sqrt{\bar{n}}$, is the roat mean square deviation which is relevant for the scintillator/PM - ensemble only. $\sigma_{n,R}$ is the relative r.m.s. deviation and lastly, $\sigma_{Q,R}$ is the overall relative charge (or energy) resolution assuming that the shower inherent fluctuations are ± 40%. The last column therefore, is found by calculating $\sqrt{0.4^2 + \sigma_{n,R}^2}$.

For both materials the scintillator/PM - related fluctuations are seen to enhance the overall resolution only slightly. We therefore found the 1 cm Plexipop good enough; the total number of photoelectrons produced is anyway considerable, and the small relative fluctuations in their number will hardly affect the overall resolution.

There are no plans to increase the number of planes beyound 5. As explained in appendix 4, it would be interesting both with respect to the rejection efficiency and to a possible energy determination (the calorimeter actually being an energy measurement device). Our beam line is foreseen for energeis up to $\sim$ 90 GeV. It is therefore only at the absolute highest energies that a fully equipped calorimeter may compete in energy resolution with an energy (actually momentum) determination based on tracking through a magnetic field. High costs and mostly rather low running energies, are therefore the reasons for not considering any 8,10 or 12-plane project.

The addition of the new counter signals will be done in a way similar to how it was done for L1 and L2. Naturally, this addition becomes less linear the higher 'the number of counters that fire pr. target interaction'. This last quantity increases with the number of planes, with the beam energy and the intensity. We will therefore study in detail shower multiplicities and the linearity of pulseheight addition when 5 planes are involved. Only these results will allow us to decide 1), whether "fancy adding" should be tried implemented and 2), if a fast q-integration of the added signal (fancy or non-fancy) is interesting. These data will be obtained during the Spring 1980.

Concerning fancy adding, evidently the best would be to fan out every single signal sufficiently so as to be able to add one x - z shower-cone for each element in the plane most upstream (like shown in Fig. 4.39). However, this is a big set-up, and instead of defining 16 regions to be added, see Fig. 4.2, reducing the number of regions to 3 or even to only 2, may also be interesting. The calorimeter constraint would then consist in requiring at least one region to produce a signal above threshold. Referring to Fig. 4.39, if there are two regions only, the two signals could be 1), all signals to the left of the cone + the signals from the cone, added, and 2), all signals to the right + the cone-signals, added.

To conclude I shall mention some possible features of a fast integrator. As for all ADC's, it will have to be a gated device. In principle one charges a capacitor, it's charge will increase continuously during the gate. This is also true for the voltage across the capacitor. This voltage (proportional to the charge), should be monitored without disturbing the process of charge build up. A charge cut could thus be implemented simply by imposing a threshold cut on the monitored

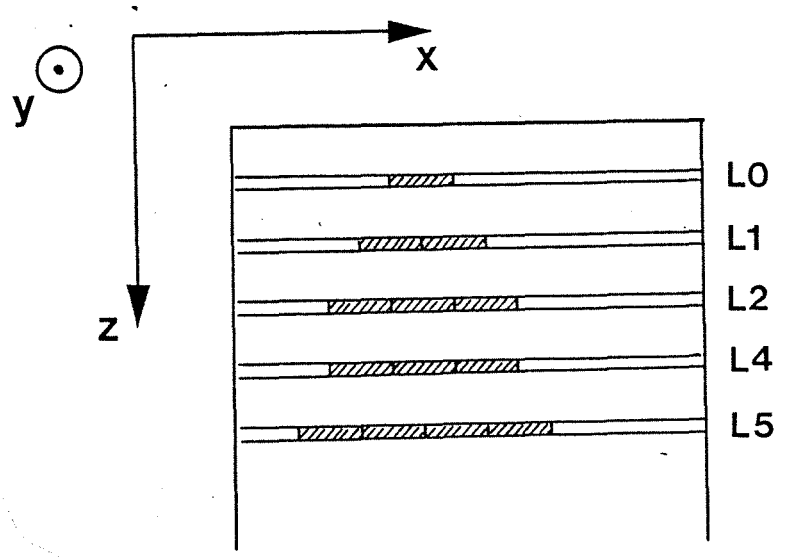

Fig. 4.39

Qualitative example of how one (of 16 possible) signals could be obtained with the fanciest adding. 1 vertical element (= a linear fan in of one up and down element) in L0, is added to two vertical elements in L1 etc. The geometry is such that a good particle hitting the hatched L0 element, always will develop a shower fully within the cone. 16 such signals would cover the calorimeter acceptance.

capacitor signal. After the termination of the gate, one has to inhibit the device until the capacitor is fully discharged. This will therefore be a deadtime which one has to take into account. The interesting parameter will be the time at which the integrator is again operationable compared to the time of a fast reset to the logic, see Fig. 5.3 and chapter 5B. The fast logic plus the event logic is blocked for $\sim$ 380 ns after the fast strobe creation. If the integrator may be ready within this period, then no extra deadtime is introduced. If so is not the case, one may

operate several integrators in parallel*. The principle would be to enable a second integrator with the fast reset. This second unit should see the same signal as the first, however, it is the only one which is enabled and has a completely discharged capacitor. With two instead of one integrator, the intrinsic integrator deadtime may be as such as $\sim$ 2 x 350 ns = 700 ns, without adding to the overall deadtime.

---

* Remember that anyway several such units have to be envisaged since some sort of fancy adding must be used. Otherwise such an integrator will not be advantageous.

G. References

1. Electrons in gases.
J. Townsend (Hutchinson, London, 1947).

2. Recent observations and measurements with high-accuracy drift chambers.
A. Breskin et al. (Nuclear Instruments and Methods 124 page 189, 1975).

3. Principles of operation of multiwire proportional and drift chambers.
F. Sauli (Yellow report 77 - 09, CERN).

4. Spark, streamer, proportional and drift chambers.
P. Rice-Evans (Richelieu, London 1974).

5. Evolution of the automatic spark chambers.
G. Charpak (Annual Review of Nuclear Science, Volume 20, 1970).

6. High-Energy Particles.
Bruno Rossi (Prentice-Hall, New York 1952).

7. Review of Particle Properties.
Particle Data Group (CERN 1976).

8. Some parctical remarks on multiple scattering.
Virgil L. Highland (Nuclear Instruments and Methods 129 page 497, 1975).

9. Proceedings of the Calorimeter Workshop May 1975.
Physics limitations on calorimetry.
C.W. Fabjan and W.J. Willis (CALT 68 - 502).

10. Calibration of a sampling total absorption detector designed for neutrino experiments.
B.C. Barish et al. (Nuclear Instruments and Methods 130 page 49, 1975).

11. Proceedings of the Calorimeter Workshop May 1975.
Photon - collecting hadron calorimeters.
F.J. Sciulli (CALT 68 - 502).

12. Performance of a magnetized total absorption calorimeter between 15 GeV and 140 GeV.
P. Bloch et al. (Nuclear Instruments and Methods 151 page 69, 1978).

13. A. Benvenuti, D. Cline, W.T. Ford, R. Imlay, T.Y. Ling, A.K. Mann, F. Messing, J. Pilcher, D.D. Reeder, C. Rubbia, R. Stefanski and L. Sulak (uncatalogued preprint).

14. A total absorption spectrometer for energy measurements of high energy particles.
J. Engler et al. (Nuclear Instruments and Methods 106 page 189, 1973).

15. F. Turkot, E. Harvey, T. Kondo, W. Kononenko, E.M. O'Neill, W. Selove, R. Diamond, A.R. Erwin, R. Loveless, M. Thompson, Univ. of Princeton internal report (uncatalogued).

16. Comparison of muon-proton and electron-proton inelastic scattering.
T.J. Braunstein et al. (Physical Review D6 page 106, 1972).

17. High-energy muon-proton scattering: one-photon exchange tests & High-energy muon-proton scattering: muon-electron universality.
L. Camilleri et al. (Physical Review Letters 23 page 149 and 153, 1969).

18. Scattering of 7 - GeV muons in nuclei.
M. May et al. (Physical Review Letters 35 page 407, 1975).

19. One-photon exchange processes and radiative corrections.
V. Gorgé et al. (Nuovo Cimento 27 page 928, 1963).

20. Calculated hadronic transmission through iron absorbers.
T.A. Gabriel and B.L. Bishop (Nuclear Instruments and Methods 155 page 81, 1978).

21. High energy particle interactions in large targets, Volum 1. Hadronic cascades, shielding, energy deposition.
A. Van Ginneken and M. Awschalom (FNAL, Batavia 1975).

22. Landolt - Börnstein (New Series I/7 1973)

23. General expression for the density effect for the ionization loss of charged particles.
R.M. Sternheimer and R.F. Peierls (Physical Review B3 page 3681, 1971).

CHAPTER 5

FAST ELECTRONICS

A. About NIM-logic and its principal modules.

This section is mainly meant to explain the different modules used in the logic, how they work and should be used. This is also relevant for the very fast logics that treat all the counter signals before being presented for the fast logic. It should be clear from Fig. 5.3 what is understood by the terms very fast, fast and event logics. The very fast 'elastic' logic was presented in chapter 2E, and the very fast muon pair logic in chapter 4E. Notations and abbreviations will also be defined here. NIM stands for Nuclear Instrumentation Module. It's a standardized mechanical electrical modular system to handle fast analog and logic pulses. The logic levels of the system are,

$$\text{logic 1} = \text{logic yes} = \begin{cases} -600 \text{ to } -1800 \text{ mV} & \text{at input} \\ -700 \text{ to } -900 \text{ mV} & \text{at output} \end{cases}$$

$$\text{logic 0} = \text{logic no} = \begin{cases} -200 \text{ to } 1000 \text{ mV} & \text{at input} \\ -100 \text{ to } 100 \text{ mV} & \text{at output} \end{cases}$$

Nominal values are -800 mV for logic 1, and 0 mV for logic 0.

In a decision making logic one may distinguish between modules playing an active role and those which are more auxiliary, for ex. shaping units, fan outs etc., that prepare the signals for the decision making. Here is first a discription of the two types of active modules.

Coincidence units

are often also called AND-units. Output is only produced if there is a time coincidence between logic yes leves at all enabled inputs. Most AND-units are constructed so that the user may easily select

the inputs which should be considered by the unit, hence one talks about enabling and disabling inputs. The outputs may either be linear or shaped. Linear means that the length of the output pulse is equal to the time overlap of the pulses at the enabled inputs. Shaped, on the contrary means that the length, out is independent of the input lengths, in most cases the output length may be set by the user. When special use is made of the length of the timeoverlap, that is, when linear outputs could not have been replaced by shaped outputs, this will be indicated by LO at the output. In both modes of operation a minimum timeoverlap between input pulses is necessary to trigger an output, around 2 ns (at -600 mV) for most units. Often

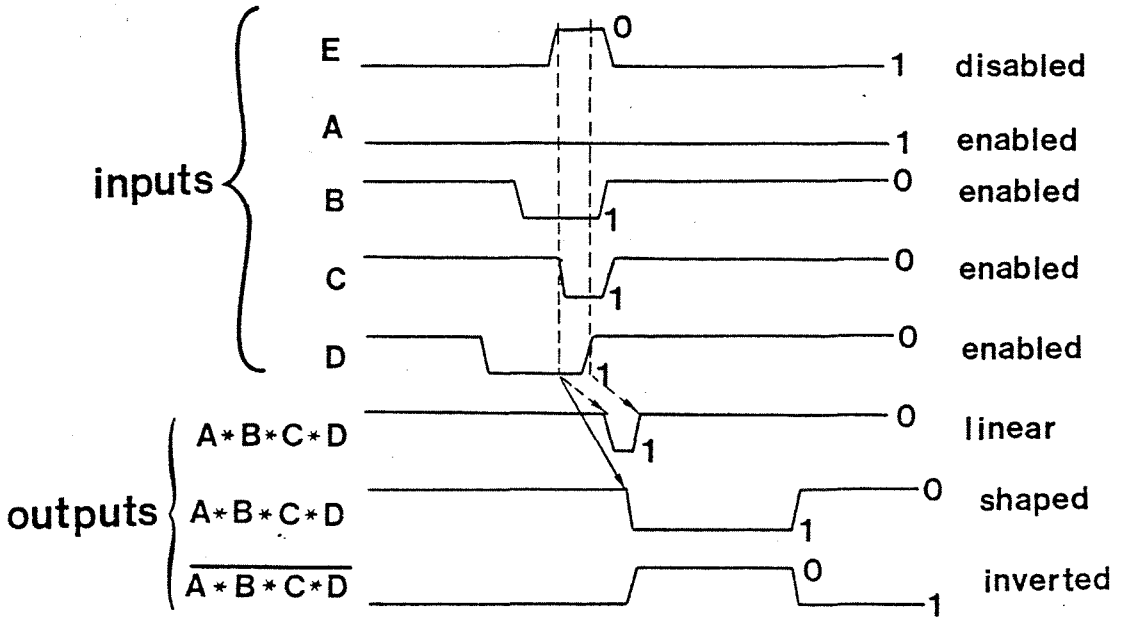

Fig. 5.1

Principles of timing with coincidence units. Notice that the internal delay to produce shaped outputs, is longer than when the outputs are linear. $\overline{A*B*C*D}$ is the logically inverted output.

there are, in addition to shaped and linear outputs, complementary or logically inverted outputs. This simplymeans that the standard

output is changed in such a way that 'logic 1' goes to 'logic 0' and vice versa.

Referring to Fig. 5.1, notice that if the E-input is enabled, the output is vetoed. This is one way to block a coincidence unit, applying a logically inverted signal which surely encloses the internally generated coincidence. However, often a special veto input is provided by the producer, in this case $\bar{E}$ has to be applied to the veto input in order to inhibit the output ($\bar{E}$ is E logically inverted). We used LeCroy* coincidence units L465 and L375, the first offering 3 4-fold coincidences per NIM-slot (2.7 cm wide), while the second is an 8-fold coincidence (per NIM-slot). These units are updating, which means that if the unit is retriggered during an output cycle, the output cycle is restarted without any change of level. We also used units N6234 and N6235 (CERN classification of NIM-modules). They are cheaper than the LeCroy modules, but not as compact and are not updating. The former is a 5-fold one slot module, while the latter is 2-fold with 3 channels per slot. AND-units are represented by half moons in this work, with inputs entering on the straight line section, the outputs are on the semi circumference.

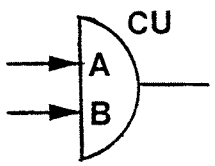

Logic fan in/outs or OR's

AND-units may be considered to perform multiplication of the input levels, either being '1' or '0' (hence the notation A*B*C*D in Fig. 5.1). In the same manner OR's (or logic fan in/outs) perform the logical addition of the inputs, '1' + '0' = '1', '1' + '1' = '1', '0' + '0' = '0' etc. Therefore output '1' is produced as long as there is input '1' on one or more of the inputs. As with AND-units, logic fan in/outs are equipped with logically inverted outputs. We used L429A and N4132 in our logics. Both act as an OR (which implies fanning in) and (not relevant for decision making) as a fanning out device at the same time. The L429A is flexible in that it permits more efficient use of the 16 inputs and 24 outputs. Operated as a 4-channel device; for each channel there are 4 inputs and 6 outputs (two of which are logically inverted), as a 2-channel device; 8

* All the quoted parameters for LeCroy NIM and CAMAC modules are from ref. 1.

inputs and 12 outputs (4 inverted) per channel and finally operated as a 1-channel device there are 16 inputs and 24 outputs (6 inverted). The N4132 fans in 6 inputs into 4 standard outputs plus one inverted. Unless otherwise noted, OR's will be symbolized as shown to the right. Lo F I/O will be the abbreviation for logic fan in/out.

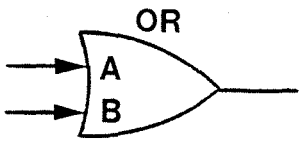

Next I shall turn to the auxiliary units; they are mainly made up of discriminators, cable timed shapers, timing units, linear fan-ins, attenuators and delayboxes. Complete specifications may be found in the 'EP electronics pool NIM catalogue'*, here only the main features of the modules together with WA7 relevant details, will be presented.

Discriminators (sometimes decision making)

Nearly all counter signals arriving in the barrack (for monitoring and data acquisition) are discriminated. One discriminates between pulses with different pulseheights (in mV), pulses passing the negative amplitude threshold will trigger standard NIM-pulses. Notice that it is the actual passing of the threshold dc-level towards lower voltages (more and more negative) that triggers an output signal. This means that a very long input pulse (longer than the preset output pulse), only will trigger the discriminator once. There will therefore be no multipulsing. Also normally, both threshold and output signal width are adjustable. As seen earlier, the counter threshold should be set in such a way that the noise/signal-ratio is minimized without reducing the counter efficiency. Discriminators therefore prepare a lot of counter signals for the logic. Also they are often used in the logic itself to shape or reshape logic pulses. And as we have seen and shall see, by vetoing pulses with pulseheight lower than the preset threshold voltage, discriminators actually also are decision making. This applies to the calorimeter and multiplicity logics.

---

* Issued at CERN.

We mostly used the LeCroy L623A and the N6009 (see CERN catalogue referred to above) discriminators. The LeCroy module is compact, offering 8 channels per NIM-slot, each channel featuring 3 outputs, adjustable width (6 to 60 ns) and threshold (-30 to -1000 mV). Also the N6009 has adjustable width (2 to 100ns) and threshold (-100 to -3000 mV), it has 4 standard outputs and 2 inverted, but occupies one whole NIM-slot. Both types are updating and can support very high rates (max. around $10^8 s^{-1}$). Notice that the updating feature ensures that logically no deadtime is present. However, when counting, since the level stayes up at '1' when updating takes place, losses will occur. See appendix4. Disciminator is abbreviated Di.

Cable timed shapers

are modules which may be used as pure shaping devices or as flip-flops. This will be clear from the following. Cable timed shapers have two types of inputs, one which through an internal discriminator triggers a logic '1' output, pulses arriving at this input while the output '1' is present will have no effect. The output level can be reset to logic '0' by a standard NIM pulse at the second type input only. The module can therefore be used as a discriminator/shaper with standard length output by simply letting one of the outputs trigger the RESET. The length of the output pulse is given by some small internal delay plus the time it takes before the output gets back to the RESET input. However, if the RESET pulse comes from somewhere else, the mode of operating is of a flip-flop type. We used the N2620 cable timed shaper. It has two SET inputs (one with -50 mV threshold, the other with -350 mV), one RESET input, 4 standard outputs plus 2 inverted. These shapers are always represented by rectangles. CT sh is short for cable timed shaper.

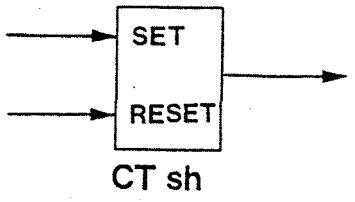

Timing units

are used either to produce long pulses (longer than 40 ns), or to produce a pulse after a fixed time interval ranging from 40 ns to, in practice, some seconds. A standard NIM pulse at the input will

produce a NIM output pulse; with the N2251 timing unit the output width = the fixed time interval, may be adjusted continuously between the values given above. There are 2 standard outputs, one inverted and the delayed pulse output also called the endmarker. This is a 5 ns pulse generated at the end of a standard output cycle. The endmarker permits generating signals after long time intervals. Naturally the caracteristics of the N2251 could be reproduced by a system of other units like CT sh's and Di's, but the amount of delay which would have to be introduced would make it, if not impossible, at least very space demanding. Also timing units will be represented by squares, and they are denoted TU's.

Linear fan-ins, fan-outs

All calorimeter counters are fanned in linearly, which means that the pulseheights of all inputs are added (as a function of time). We used two LeCroy linear fan in/outs, the L127FL and the L428A. The first device offers the possibility either of fanning in 16 inputs which are duplicated into 4 outputs, or of a 2-channel fan in/out where each channel fans in 8 inputs and has two outputs. The L428A is a '4-input/4-output' per channel, three times per slot. One should pay attention to the fact that the adding becomes less linear with increasing output current. If the pulseheight information is to be used care should be taken to adjust the dc-level at the output. This is especially true if the added signal is passed on to a discriminator.

Also cerenkov PM-signals were fanned out linearly. But this was done in a simple way not using the expensive LeCroy modules which for reasons of flexibility were employed in the calorimeter logic. Linear fan in/outs are Li F I/O's.

Attenuators/amplifiers

Attenuators are passive units which devide the input signal by a certain number above 1. This is done by means of resistors. Sometimes the N9300 attenuator was used in connection with the q-measurements. It attenuates between 0 and - 44.5 dB in steps of 0.5 dB. Remember that decibel (dB) is defined this way:

$$(x)\ dB = 20 \times \log_{10} \frac{V_{out}}{V_{in}}$$

Amplifiers were used on the cerenkov PM-pulses. This was done to be able to make a reasonable cut with discriminators which cannot be set to thresholds lower than -30 mV. An L335L was used for this purpose. Otherwise for q-measurements, we also used the L333 which offers 0 to 20 dB amplification in steps of 2 dB.

Delay boxes (N9053)

also are passive units which on a line may be used to insert time delay (adjustable in steps of 0.5 ns from 2.5 to 66 ns). Notice that the input signal necessarily is attenuated through the delay, for ex. with the cable types of the N9053 delay box (RG 58 C/U), 5 ns square pulses are attenuated 15% with the maximum delay setting. Signals from the 56AVP photomultiplier is attenuated 17.5%. Sometimes the delays in the logic are considerable and one may have to restore the attenuated pulses to standard NIM-pulses (with discriminators or shapers), this is especially true for short pulses.

Input to all types of units is symbolized with an arrow, ⟶ outputs are represented by the other lines 'leaving' the unit. If this is done through an open circle it means that the complementary, or logically inverted output is used. For the coincidence unit below, A*B is the standard output and $\overline{A*B}$ is the inverted.

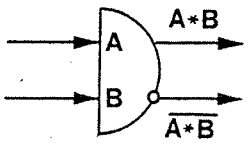

Text on lines is sometimes enclosed in a rounded rectangel, e.g.:

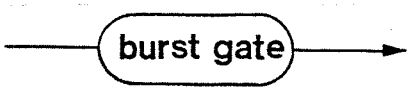

A common feature of many NIM modules is the bridged outputs. This means that one internal output is split in two as shown in Fig. 5.2. The module provides standard NIM output levels for an external load of 25 Ω. In other words,

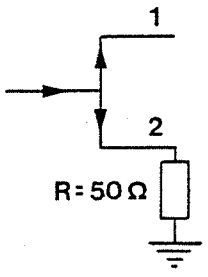

Fig.5.2
A bridged output.

if only one of the two branches is used and one wants to avoid reflections, the unused output should be terminated with 50 Ω as indicated. Bridging is most often shown as fully drawn lines (on the module front panels) between the two concerned branches. In this work bridging is normally not indicated and unused (bridged) outputs are always terminated with 50 Ω. However, when this feature is explicitly used, it has been indicated with a line interconnecting the outputs 'inside' the module, see for ex. coincidence units 1 and 2 in fig. 5.3. A signal applied to '1' in fig 5.2 will almost fully reflect at the junction (very high reverse impedance) and hence nearly the full signal is transmitted to the '2' out. This permits the ORing of several modules by cascading the bridged outputs, see the logic diagram for the H1/H2 and PR1/PR2 in chapter 2, Fig. 2.7.

B. The fast logic and the event logic for WA7.

The purpose of these logics is,

- To select as efficiently as possible event candidates, elastic, muon pair etc., on bases of the available counter signals.
- To store all relevant information about the selected events and about the running conditions.

It is natural to split the overall logic in three levels, the very fast logics, the fast logics and the event logics since the various detectors constraints are incorporated at three different levels.

The very fast logics consist of the decision making and signal preparation proper to the various detectors which precede the incorporation in either the fast logic or the event logic. These logics for instance, produce the outputs of the fast matrices, the calorimeter yes signal, cerenkov responses, Cedar responses etc.

In the event generation some constraints arrive earlier than others, this is the reason for making the event selection through a two-step procedure, the first being 'the fast logic', the second 'the event logic'. The fast matrices and some vetoes for instance, contribute in the fast logic, while the cal.yes and cerenkov signals arrive late and have to be incorporated in the event logic.

There are many advantages with such a two level decision making system. First, the most trivial, the length of chamber and scintillator delaylines to CAMAC may be minimized. The information is stored as soon as a gate may be generated and is kept until either transferred to the computer or, if the event in question is rejected by the decision making logic, simply erased. Second, the setup allows to make use in CAMAC of (at least) the counter data at a very early stage. In WA7, PR1/PR2 bit and multiplicity patterns (output from CAMAC) were used in the decision making. Also the chamber data were available very early, but could in our experiment not be used before an interrupt to the computer (or a processor) was generated.

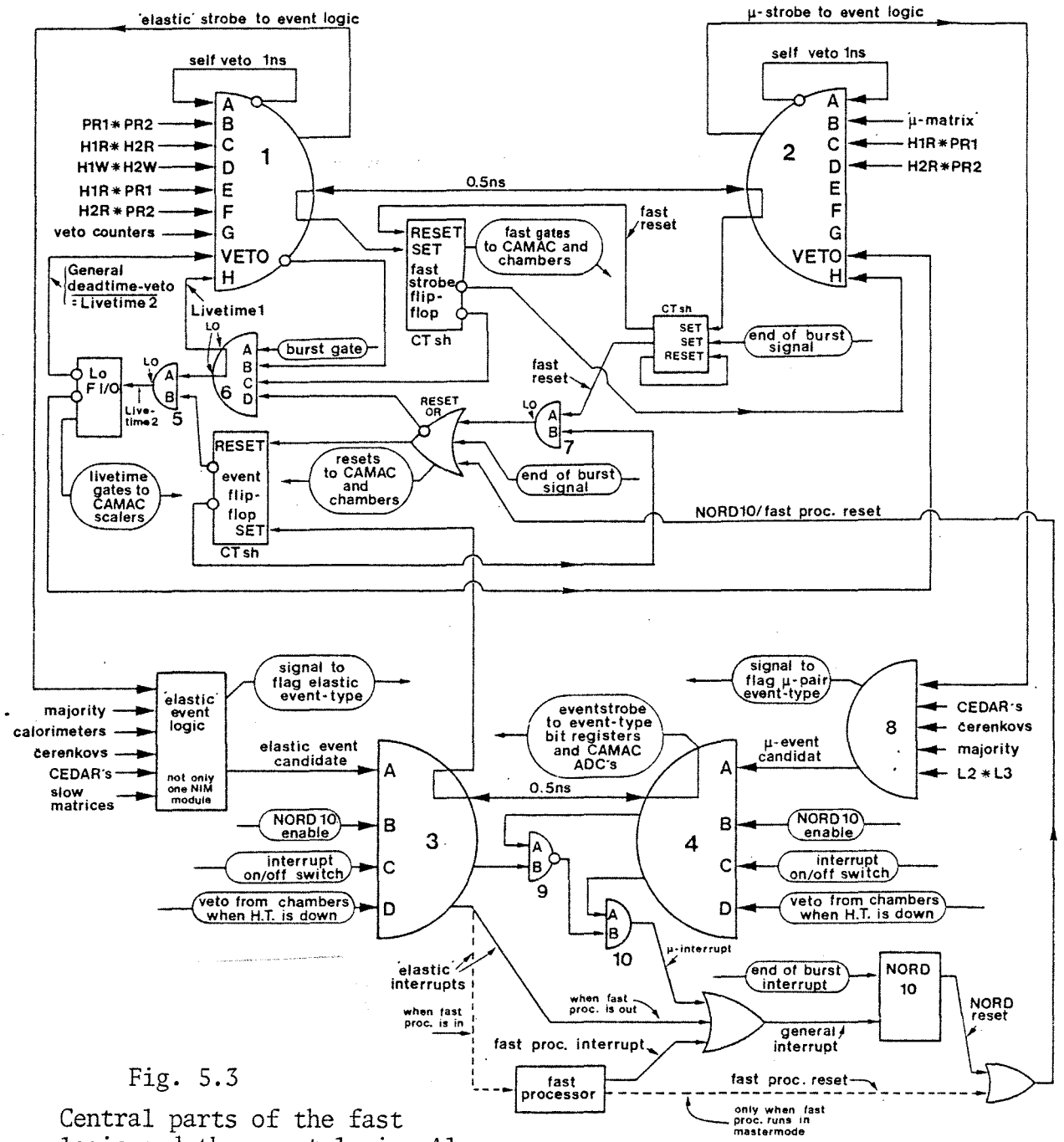

Fig. 5.3

Central parts of the fast logic and the event logic. Also shown is the position of the fast processor (fast proc.) and the computer (the NORD 10) in the system. The very fast logics have been presented elsewhere. All notations and abbreviations have been defined in chapter 5A. For a detailed explanation of the logics see the text. Here is a rough outline. First either coincidence unit (CU) 1 or CU2 produces a fast strobe which is sent off to the event logic (the CU8 or the box denoted: 'elastic' event logic). If the event is accepted in this part of the decision making logic, the control is passed onto the NORD or the processor (by means of interrupts) which will then decide what action to take. Otherwise the event logic will itself reset the logic and CAMAC so that the system again is prepared for a new event. Notice that the physics constraints are imposed...(cont. next page)

Fig. 5.3 shows the general fast logic and event logic with emphasis on that part which ensures correct timing and deadtime monitoring. I shall threrefore later come back to interesting details of how the physics constraints are formulated and incorporated. Veto counters, multiplicity, calorimeters, slow matrices and the elastic event logic itself are examples of this.

Now to an explanation of Fig. 5.3, since no delays have been indicated, Fig. 5.4 has to be used to understand the timing. First notice that three non physical conditions have to be fulfilled to produce either an 'elastic' strobe or a μ-strobe.

1) Ensured by the A-inputs, that no new strobe follows between 14 and 29 ns after the current one (self veto). See Fig. 5.4 and the explanation that goes with it.

2) That the fast logic is blocked during decision making in the event logic. Both strobe types will set the fast strobe flip-flop,and the same signal which sets the flip-flop will reset it automatically after a certain time delay (~380 ns). This delay is set so that it exceeds the full time interval of decision making in the event logic. This inhibit is done through the H-inputs of coincidence units 1 and 2. It is mandatory to block the system; a lot of information concerning the first fast strobe is stored in CAMAC and in RMH's (modules for the reception and temporary storage of MWPC data), these data should be protected until the event logic has decided whether or not the complete event should be written onto tape. Note that in addition to the fast strobe inhibit, the H-input of coincidence unit 1 also contains the conditions of,
   a) no self veto,
   b) a burst gate present and

...at 2 or 3 distinct levels (3 levels applies only to the selection of elastic event candidates); represented by CU1 and CU2 (first level), the 'elastic' event logic and CU8 (second level) and lastly by the fast proc. (third level, in mastermode only). The rest of the drawn logic is there to ensure correct timing and that no clashes will occur.

c) of no resetting taking place.

Condition a) is imposed in order to ensure overlap between the fast self veto entering coincidence unit 1 at A and the veto resulting from a non output from coincidence unit 6. Condition b) is selfexplanatory while c) was implemented to take into account a fast processor effect, this will be explained in a moment. Remark that using the linear output (LO) of unit 6 is essential.

3) That no strobe generation takes place during the readout and resetting performed by the NORD 10. If an interrupt is sent off to the computer (or the fast processor), then, for reasons to be explained later, the VETO-inputs of coincidence units 1 and 2 will become efficient and will relay the vetoing imposed through the H-inputs. Notice that the conditions b) and c) of above is present also in the VETO-inputs (by means of coincidence unit 5). The μ-strobe creation therefore is properly inhibited (there is time overlap between A and H-inputs). Also for coincidence unit 5 is the linear output vital. It is only when both the fast logic and the event logic (input A) and the NORD 10/(fast processor) (input B) are idle at the same time, that the experiment is 'alive' and ready to accept an event. With varying length of both inputs, the linear output becomes the only output which can always give the true livetime.

We have already studied to some extent what happens when a fast 'elastic' strobe or μ-strobe is produced (i.e., the generation of gates to CAMAC and the readout etc.). Notice that both strobe types trigger: A vetoing of futher strobe creation for both unit 1 and 2, moreover, fast gates to CAMAC and the chamber readout plus a reset of the fast strobe flip-flop. To connect the whole logic together one now has to study what happens if an event (of both types) is produced or not (= output of coincidence units 3 and 4).

Let us study the last case of no event first. In this case the event flip-flop stays reset which means that the B-input of coin-

cidence unit 7 stays up (at logic 1), and hence the reset entering at A will pass and erase all chamber and CAMAC information relevant for the current strobe. Also the strobe creation is blocked during the time of erasure (through the D-input of coincidence 6). However, this blockage could also be obtained by prolonging very little (less than 50 ns) the inhibit imposed by the fast strobe flip-flop. It is in the case of resetting CAMAC ADC's, a process that takes several microseconds, that this reset inhibit is relevant. However, since the ADC's may only be gated by an event, this is of no interst in this case when no event is produced. The event flip-flop is unaffected in the case of no event, and the logic is enabled as soon as the reset inhibits permits restauration of no veto at the VETO-inputs.

What happens in the case of an event or to be precise in the case of an interrupt, see Fig. 5.3? Notice that apart from the physics constraints imposed by the event logics, one demands that

a) the NORD 10 is enabled,
b) that the interrupt switch is in the on-position (used to stop the datataking temporarily to perform deadtime free rate measurements) and
c) that the voltages on the MWPC's are up so that only events with full chamber information will be read out.

The sequence of actions taken upon the generation of an 'elastic' or a μ-interrupt, is the following. The event flip-flop will be set, which ensures that coincidence unit 5 will be blocked also after the fast strobe inhibit is no longer efficient. Only a reset of the event flip-flop can reenable the system (by rendering the VETO-inputs of coincidence units 1 and 2 inefficient). Note that in this case (as opposed to the case of no event) the fast reset will not pass coincidence unit 7. Therefore the system is blocked until the fast processor or the NORD 10 resets the system. The two end of burst signals only ensures that nothing is 'hanging' in the logic when a new burst starts. These signals are generated ~1.4 seconds after the end of each burst gate. To explain the logic following

coincidence units 3 and 4, I shall briefly outline the role of the fast processor[2].

As already seen in chapter 2E, the fast and slow matrices very crudely defines elastic kinematics according to opening angle and coplanarity. The fast processor in principle does the same, but on the bases of the much more precise chamber information. It therefore constitutes a third level of decision making. The 'elastic' interrupt triggers the processor, which responds by reading (from the RMH readout modules) the hitpattern in chambers 3,4 and 6 (see Fig.1.2.b). Using this information it performs high speed tests, which simplified results in a yes or no answer. Now the processor may run in master or slave mode. In the last case (used for checking purposes) the processor will indicate its answer (yes or no) together with its NORD destinated interrupt. The NORD will then decide whether a full event readout should take place or not. In the mastermode on the contrary, only when a good candidate is found will the processor send an interrupt to the NORD which then performs a complete readout of the CAMAC and chamber data. Events that are rejected by the processor will result in a prompt reset to the logic. The interest of the processor resides in two facts,

1) it rejects bad events (55%),
2) this is done very fast, hence the deadtime is reduced (per event) which again means that less elastic events are lost per event.

For details about the processor performances, see ref. 3. Here are the main conclusions from some high intensity runs at -30 GeV/c (intensity ~ 5.0×10^7 burst^{-1}).

The accepted events represents 45% of the sample presented to the fast processor. This together with the fact that the mean analysis time (or deadtime) per event for the processor is of the order of 100 μs, while the NORD imposed deadtime (= time spent to transfer all CAMAC data to the NORD buffer) is in the mean 3.5 ms, means that the overall deadtime is roughly halfed with the processor in mastermode. This is verified independently by the measured increase

in livetime (from 0.64 to 0.84). Therefore, with the same incoming beamintensity roughly 30% more elastic events will be 'seen' (= (0.84 - 0.64)/0.64), this concerns the second point above. However, more interesting is the combined effect of 1) and 2) which implies that there are 3 times as many elastic interrupts written onto tape (per interrupt written onto tape) with the processor than without. This is particularly true for the WA7 experiment with millions of triggers to be analysed on big computers.

To come back to the logic, notice that coincidence unit 9 blocks 10 and hence the μ-interrupt in the case of a coincident μ and elastic interrupt, therefore ambiguity will never occur. Normally when the NORD 10 reads CAMAC and in particular ADC's (concerns cerenkov and calorimeter ADC's), the ADC's are automatically reset as they are read. This is the situation when every interrupt implies a complete readout. However, with the processor in mastermode, sometimes data stored in CAMAC will not be read, in such cases CAMAC and in particular ADC's have to be properly reset. As already mentioned this is time consuming (~ 2 μs for the L2249A ADC's), and in order to prevent the ADC's from being used before being cleared, the prompt fast processor reset is a long pulse, at least 2 μs. It keeps the D-input of coincidence unit 6 down sufficiently long. Finally notice the end of burst interrupt to the NORD 10. This triggers a special readout of scalers which are accumulated during the burst.

I shall mention the important sides of the timing not displayed by Fig. 5.4. Obviously the time jitter between the gates which are applied to CAMAC registers and the signals that enters the registers should be minimized. To ensure 100% efficiency, the gates should cover the full time jitter. Hence the gate widths are set according to this jitter. Many counters in the experiment see a very high particle flux. So to limit the number of irrelevant signals (accidentals) that sneek into the registers, the gate widths should at the same time be minimized. This is important both to have a clean data sample to work with offline and also,

as we shall see, in order to minimize the random multiplicity veto which work on the CAMAC bit registers. These considerations led to choosing the prompts, more precisely the PR1*PR2-signal, as the time definition of the strobe. In practice this was done by adjusting the relative time differences so that the falling edge of the prompt signal would (in the mean) always be centered on the other signals (inputs C,D,E and F of coincidence unit 1). The timing of the inputs of coincidence unit 2 has already been discussed, see Fig. 4.38.

Also in the event logics is a precise timing necessary. This is due especially to the gates for the CAMAC ADC's which should fluctuate timewise as little as possible relative to the analog input signals. Therfore in the continuation after coincidence units 1 and 2, the timing is done in such a say that it is defined by the strobe (in fact by the prompts). Notice also that this is the reason for bringing the 'elastic' strobe to the event logic, actually it is logically superfluous in that the elastic strobe is already required in the slow matrix logic.

Explanation of Fig. 5.4.

First some details about the very fast inhibiting of CU1 and CU2. Line 1 shows the actual coincidence at the CU1 inputs. And '2' shows the resulting output, the width is 20 ns, the transit time 13 ns. '4' shows the time interval for which the self veto ('3') is efficient. Notice that this depends on the mean width of the actual input coincidence (overlap) at CU1. There is a 7 ns interval after a first coincidence is established that no veto is efficient (compare lines 1 and 4). The L375 could be retriggered during these 7 ns, however this would be without effect. The unit is updating and hence the already existing output signal would simply be somewhat prolonged which would be without influence later on. Lines 5, 6,7 and 8 produce line 9 which is the livetime 1 (without interference from the NORD 10 computer or the fast processor). Actually with a 20 ns wide fast strobe the 'CU6 IN(B)' is superfluous (the 'line 3 veto' overlaps with the 'line 9 veto'). However, with

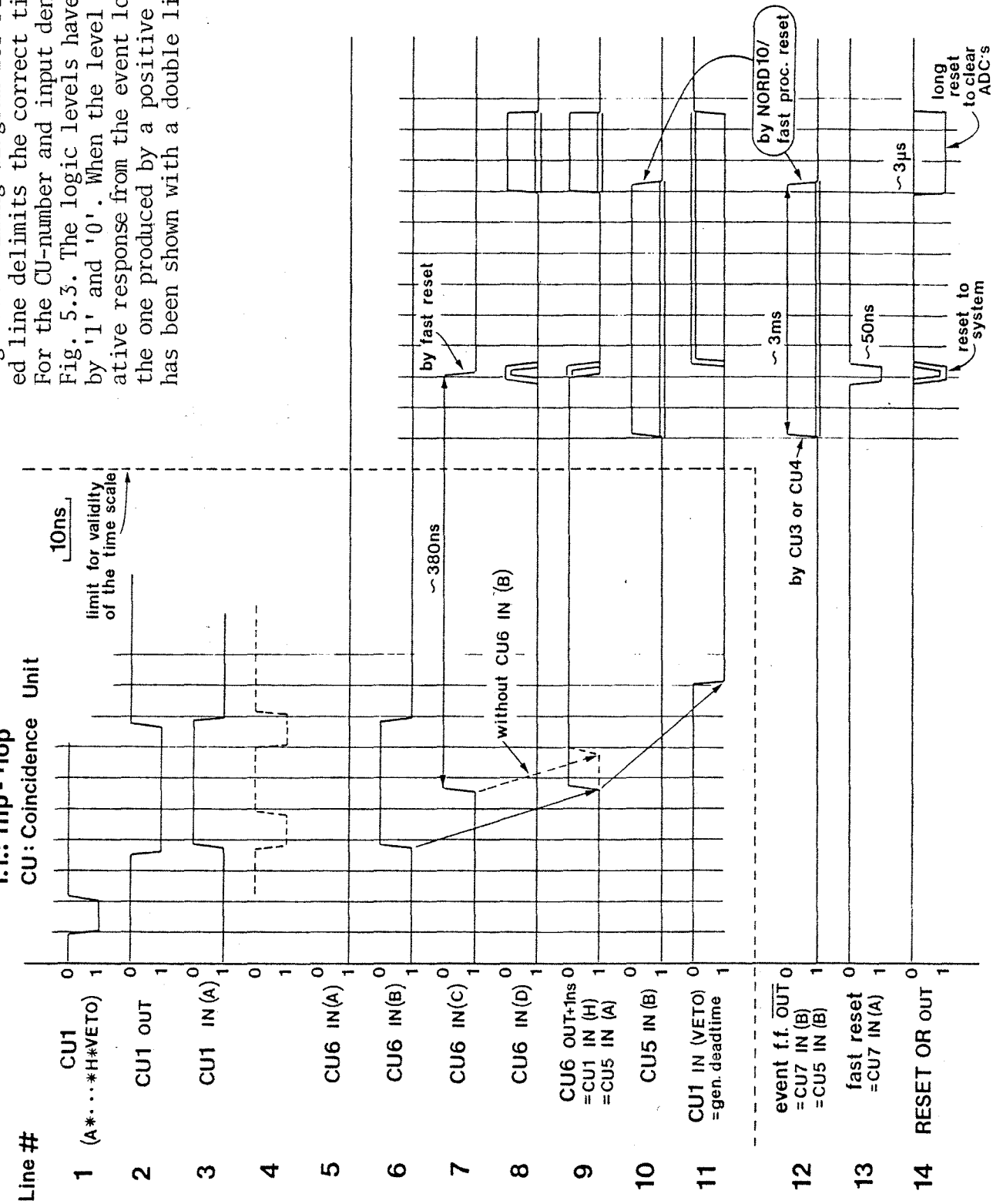

Fig. 5.4. Timing diagram for Fig. 5.3. The dashed line delimits the correct time scale area. For the CU-number and input denotation, see Fig. 5.3. The logic levels have been indicated by '1' and '0'. When the level produced by a negative response from the event logic differs from the one produced by a positive response, this has been shown with a double line.

shorter strober strobes (less than 15 ns) it would be necessary. CU2 is not inhibited exactly the same way as CU1, but the timing is done so that either no retriggering can take place, or it is without effect (for both CU1 and CU2).

In the following two cases are considered, 1), the event logics respond in a positive way and 2), in a negative way (= no event). When this last case differs from the first, it is indicated with a double line in Fig 5.4. After roughly 380 ns the strobe flip-flop is reset by the fast reset pulse. Now, in case 2) the fast reset will pass CU7 and produce fast resets to the system (line 14). It will slightly prolong the veto (line 9), after which lines 9 and 10 make the general deadtime veto inefficient (line 11). In case 2) the strobe flip-flop is also reset after roughly 380 ns, in this case though, CU7 is blocked by the event flip-flop and the fast reset will not pass ('12' * '13' = '14'). The event flip-flop being set also ensures that vetoing of CU1 and CU2 is maintained as long as the NORD 10/fast proc. are busy ('9' * '10' = '11'). A long reset pulse from the NORD 10/fast proc. has been drawn (3 μs). This is the situation when the fast processor runs in mastermode. If it rejects an event, the long reset pulse will sufficiently prolong the general deadtime (line 11), so that CAMAC ADC's can be properly cleared (again done by '9' * '10' = '11', see Figs. 5.3 and 5.4).

* * * * * * * * * * *

In the following will be considered the fast logic and the event logic separately. Both the implementation of the physics constraints and the performances (rates, efficiencies, random vetoing etc.), are treated. The logics relevant for the creation of a muon-pair interrupt won't be discussed here. A proper treatment of the problems encountered when setting up the 'elastic' logics will, due to the similarity of the two chains (see Fig. 5.3), make a detailed description of the muon pair chain superfluous. At the end of this chapter are given the rates for this second chain.

The fast logic

Here will be studied the effects of the inputs B - G of CU1, see Fig. 5.3, on the fast strobe rate. The veto counters (input G) are treated extensively. Optimizing such counters is not always trivial since it implies making a compromise; as we shall see, the veto signals affect both good (elastic) and bad strobes. The optimizing consists in keeping the effect on the good strobes low while, at the same time, getting the highest possible veto efficiency of the bad strobes.

It is very difficult to give typical values for the rates in the fast logic. Necessarily these depend on many parameters; beam-conditions, geometrical configurations of the apparatus, the functioning of the apparatus (unfortunately rather time dependent) and the programming of the fast matrices (inputs B - F, CU1) all influence the strobe rate. The presentation will therefore contain figures which are of specific validity. However, I shall try to extract general and interesting trends.

Here are for example the rates of the matrix outputs with -30GeV/c incident. The rates are normalized to the ionization chamber*.

$$
\begin{aligned}
A &\stackrel{\text{def}}{=} PR1 * PR2 = 1648 \text{ c/icc} \\
B &= PR1 * H1R = 3400 \text{ c/icc} \\
C &= PR2 * H2R = 2640 \text{ c/icc} \\
D &= H1R * H2R = 3012 \text{ c/icc} \\
E &= H1W * H2W = 2752 \text{ c/icc} \\
A * B * C * D * E &= 309 \text{ c/icc}
\end{aligned}
\qquad (5.1)
$$

---

* c/icc for counts per ionization chamber count. 1 icc corresponds to 75 to 80,000 beamparticles. The normalization has varied somewhat with time.

While at ± 20 GeV/c the same rates are,

+ 20 GeV/c	A = 629 c/icc	- 20 GeV/c	A = 1125 c/icc
	B = 1793 c/icc		B = 2700 c/icc
(5.2)	C = 1113 c/icc	(5.3)	C = 1875 c/icc
	D = 1369 c/icc		D = 2250 c/icc
	E = 2040 c/icc		E = 2250 c/icc
A * B * C * D * E =	68 c/icc	A * B * C * D * E =	100 c/icc

To get an idea of the size of these figures, or rather the efficiency of the matrices, remember that 1 icc = 75.000 beamparticles incident, and that out of these ~ 8% interact inelastically in the hydrogen target. This is easily found by knowledge of the total cross sections. The drop in intensity throughout the target is given by,

$$1 - \exp(-n\sigma x) \qquad (5.4)$$

where n is the number of protons per cm^3, σ is the inelastic cross section and x is the target length. The elastic cross section is disregarded since practically no elastic scattering may be seen by our apparatus; ~ 99% of the elastic events scatters very much forward, that is, the proton recoils into the magnet walls and the forward particle is too forward to be detected. In our case, using $n = 4.264 \times 10^{22}$ cm^{-3}, x = 100 cm and $\sigma(\pi p)$ = 19.3 mb, we find the intensity reduction to be 8%. Using only the pion cross section is justified by the fact that ~ 90% of our beam is pions. Therefore the rates given above should be compared with 0.08 x 75.000 = 6000 inelastic reactions per icc.

Comments to the rates given by (5.1), (5.2) and (5.3): Notice that in all three cases it is PR1 * PR2 which cuts the most. There are at least three reasons for this, 1), the prompts are situated furthest downstream which means that they see less of the low energy particles because these are swept away by the magnetic field, 2), the timing between the two prompt hodoscopes is tighter than between the other hodoscopes (this is possible since the time jitter bet-

ween arrival times of different prompt element signals, is very small) and finally 3), PR1*PR2 is made by correlating half rings in one arm (down or up) with half rings in the other arm (up or down); this is stricter than simply correlating full rings in the two arms (see Figs. 2.4-5). Also notice that the matrices all perform much worse at the higher energy. While the differences are rather modest when comparing simple matrix rates, this is not the case for the overall coincidence A*B*C*D*E. This is naturally ascribed to higher multiplicity, higher energy on the secondaries (hence they are swept less away by the magnetic field) and lastly to the increase in the γ-factor ($= (1 - \beta^2)^{-\frac{1}{2}}$), which implies that the secondaries will be produced in a more forward direction.

Next will be studied the effect of the veto counters, see Fig. 5.3, entering at the same level as the fast matrices. These counters block the strobe creation if at lest one of them fires. Elastic reactions in the target could not fire any of them and coincident signals are therefore a signature of non-elasticity. However, because of the non-zero time resolution and δ-ray effects, vetoing of elastic events may occur. It is very important to determine the losses due to unwanted vetoing since the cross sections have to be corrected accordingly. I shall show how these losses can be measured.

Notice that the presence of false coincident signals at non-veto inputs is of less importance; this effect may trigger fake strobes (rare), and very often will cause the CAMAC registers to contain a lot of irrelevant data. But with sophisticated off-line reconstruction, no elastic events are lost and no inelastic are accepted because of fake coincident signals. What matters on the contrary for the non-veto inputs is the efficiency, inefficiency being equivalent to a veto. This e.g., concerns signals from the matrices, calorimeters, cerenkovs and Cedars. For the track reconstruction, evidently also the chamber efficiencies count. Inefficiencies of course, should be included in the cross section evaluations as well. When carrying out the corrections both deficiencies and apparatus inherent inefficiencies are considered. Deficiencies will not be

considered here in spite of the importance of such a study. It would reveal the reliability of the experimental setup as well as the efficiency of the monitoring system which necessarily goes with such a complex experiment (a dead PM should be found as soon as possible!). Apparatus inherent inefficiencies are treated in the chapters of the relevant detectors. As opposed to the deficiencies, proper inefficiencies in principle may be disregarded in the logics; all the signals are treated with sufficient margins (concerns widths and delays) so that an event which has fired all relevant detectors properly, could not be lost because of logic related inefficiencies. However, it could be lost due to deadtime or random vetoing. I shall come back to the details of the veto counters.

During the high-t elastic scattering data taking periods we used at most three sets of veto counters, entering the G-input of CU1, see Fig. 5.3,

1) 4 counters surrounding the beam as shown in Fig. 5.5.a. These were located just downstream of the second Cedar, see Fig. 1.2.a, and would veto some of the events where a), the beam-particle had interacted upstream of the counters or/and b), the beamparticle did not aim onto the hydrogen target.

2) 2 counters inside the magnet, see Fig. 5.5.b. Some events with associated production of low momentum particles were rejected by the constraint that none of these counters should have fired.

3) Up to 12 wedge elements in H1/H2, see Fig. 2.4.b. The kinematics for elastic events plus the geometrical acceptance define particle trajectories which cannot depart too much from the median plane (y=0). Therefore, for ex. with -30 GeV/c incident, could only elements 4,5,6 and 7 in both H1 and H2 fire as the result of the passage of elastically scattered particles. Most of our -30 GeV/c data were taken using a trigger that imposed that there were no simultanuous hits outside the area covered by the elements mentioned above. These outside elements were 1,2,3,8,9 and 10 for both hodoscopes.

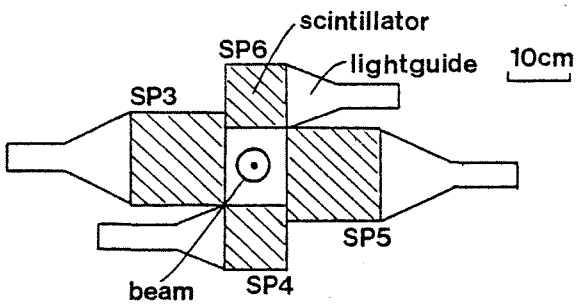

Fig. 5.5.a.

Configuration of the veto counters between the second Cedar and the hydrogen target. The scintillators are 1 cm thick.

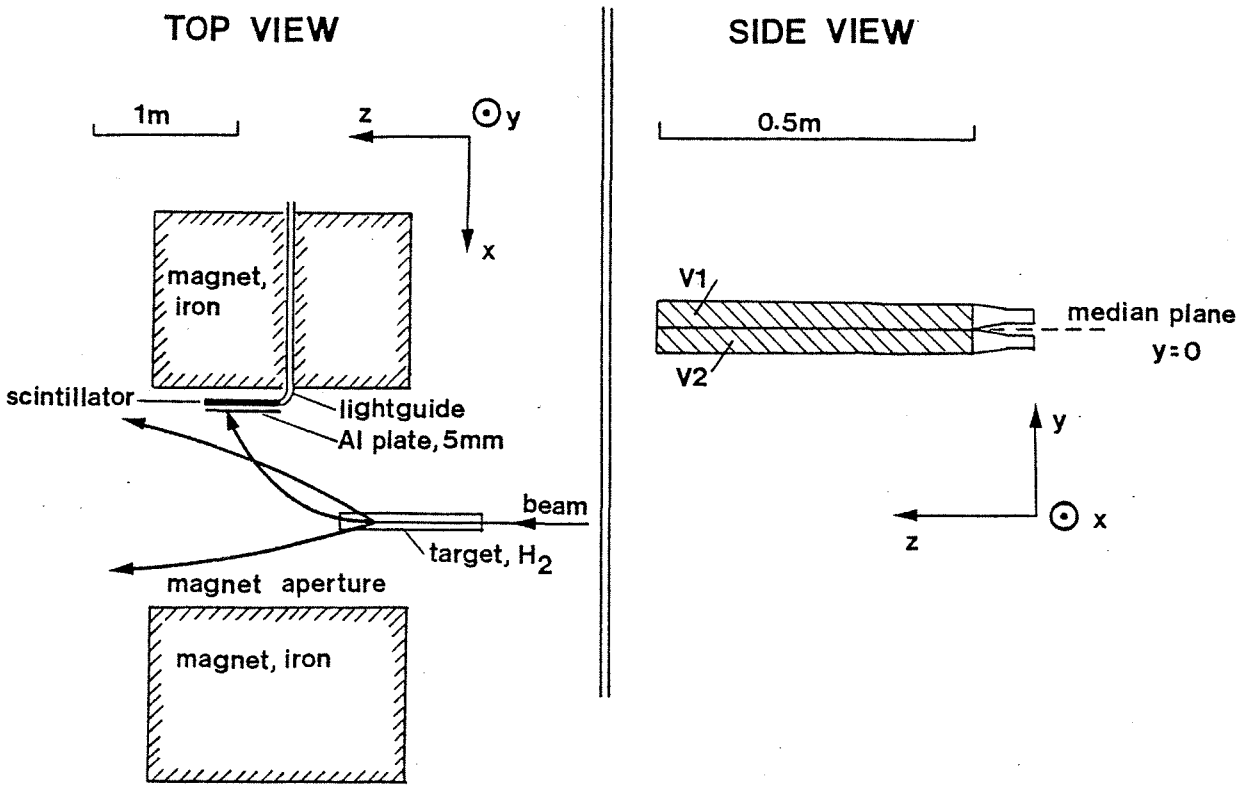

Fig. 5.5.b.

Top and side view of the two veto counters inside the magnet aperture. Notice the 5 mm aluminum plate which stop low energy electrons (δ-rays). The scintillator thickness is 1 cm. The magnetic field is vertical and the bending therefore is horizontal.

Before proceeding to give some results concerning the efficiency of the vetoes, the two central signals in a veto process will be presented. These are the veto signal which is either a logic '0' or a logic '1' signal, and the coincidence signal which is always a logic '1' signal. In the following they are referred to as 'the veto signal' and 'the logic 1 signal'.

Often the logic 1 signal will be of varying length. In the case of CU1 (Fig. 5.3) for instance, this signal is the logic sum of all the inputs except the G-input. The detailed effects of the veto signal depend on the type of inputs/outputs which are used. If a non-veto input is used (which means that the veto signal has to be a logic '0' signal), then a near complete time overlap between the zero level of the veto signal and the -800 mV level of the logic 1 signal is necessary to ensure vetoing (applies to both types of outputs, linear and shaped). This is also the situation if the veto input is combined with a linear output (in this case, however, the veto signal should be a standard non-inverted pulse). On the other hand, when the veto input is used together with a shaped output, only a minimum time overlap with the leading edge of the logic 1 signal is necessary. For example, with the CU L375 only shaped outputs exist and the veto signal should in this case overlap the leading edge plus at least ~3ns of the logic 1 signal if the veto input is used.

Let t_w be the average minimum width of the logic 1 signal which the veto signal must overlap for the veto to be effective. When linear outputs or/and non-veto inputs are used, t_w = (the average duration of the logic 1 signal) - 2 x (the minimum duration of the same signal which would produce an output)*. This mimimum time overlap between the input signals is 3-4 ns for the 375L LeCroy CU. Let t_v be the length of the veto signal, and finally let t_j denote the time jitter between the two signals. These definitions are easily understood by considering Fig. 5.6, which shows a constructed jitter spectrum. ΔT is defined as the maximum time difference between the falling edge of the logic 1 signal and the rising edge of a

---

* The minimum coincidence overlap, one in each end of the logic 1 signal.

correlated veto signal (notice that it is inverted in Fig. 5.6). As shown in the figure, $\Delta T=0$ when the distribution starts at the same time as the logic 1 signal. Δt is the time difference between the rising edge of the veto signal and the falling edge of the logic 1 signal for fixed ΔT. In these definitions the logic 1 signal is understood to mean the the effective or reduced logic 1 signal, represented by the width, t_w. It is seen that ΔT is a measure for the relative timing of the two signals, while Δt is the relevant variable for discribing the TOF-spectrum between the two pulses for

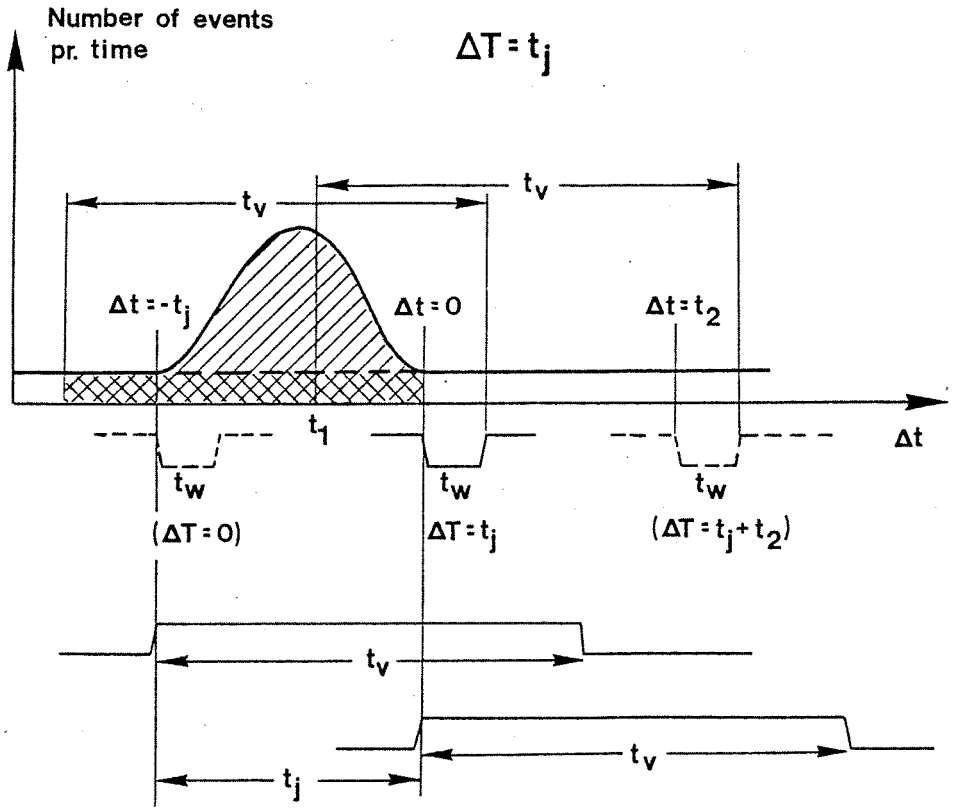

Fig. 5.6

Constructed example of a time of flight (TOF) spectrum between a logic 1 signal and a veto signal. The logic 1 signal is understood to be the reduced signal of width t_w, see the text. Notice that the relative time of the logic 1 signal for fixed ΔT is fixed (i.e., Δt=constant) while that of the gate varies. Obviously in real life the absolute time of both vary. For details see the text.

a given value of ΔT.

In the figure all the correlated veto pulses (represented by the hatched area of the distribution) will be effective; t_V is sufficiently long so as to always cover t_W. There are also uncorrelated veto signals which will be effective, shown as the shaded area. However, for the second logic 1 signal drawn with a dashed line ($\Delta T = t_j + t_2$), not all the correlated veto pulses will be effective, actually only those which arrive after $\Delta t = t_1 = t_2 + t_W - t_V$, will completely cover the second dashed pulse.

Remembering the definition of ΔT and referring to Fig. 5.6, one may study the veto efficiency due to correlated veto signals, ε_c, as a function of ΔT. Assume that $t_V \geq t_j + t_W$, correlated veto signals will start to be felt for $\Delta T > 0$. ε_c will then increase and the maximum vetoing is reached when $\Delta T = t_j$, ε_c stays flat for $t_j \leq \Delta T \leq t_V - t_W$, and drops to zero during the jitter time interval; $\varepsilon_c = 0$ for $\Delta T \geq t_V - t_W + t_j$.

Unfortunately, in addition to the correlated vetoes, there are, as we have seen, uncorrelated (or 'random') vetoes. The 'efficiency' of these will be denoted, ε_{uc}. ε_{uc} depends on t_V and the single rate of the veto signals; a random coincidence with sufficient overlap becomes more probable with increasing width and rate. Notice that because of the randomness, ε_{uc} should be ΔT-independent.

ε_c and ε_{uc} may be measured at the same time by variation of the relative time delay between the two signals, i.e. ΔT (the time of the logic 1 signal is varied relative to whole jitter distribution, see Fig. 5.6). Let me come back to the WA7 veto counters.

Referring to Fig. 5.7, the efficiencies may be found by plotting $R \stackrel{def}{=} \text{scaler1/scaler2}$, as a function of ΔT. 1 - R is the total veto efficiency which may be split in two as shown in the same figure, $1 - R = \varepsilon_c + \varepsilon_{uc}$.

In what follows, the data from Fig. 5.7 are analysed, hence the results will contain the efficiencies for the combination of veto-counter sets 1) and 2), see above. The linear approximation is confirmed to be good outside the time interval, t_1 (see Fig. 5.7), in

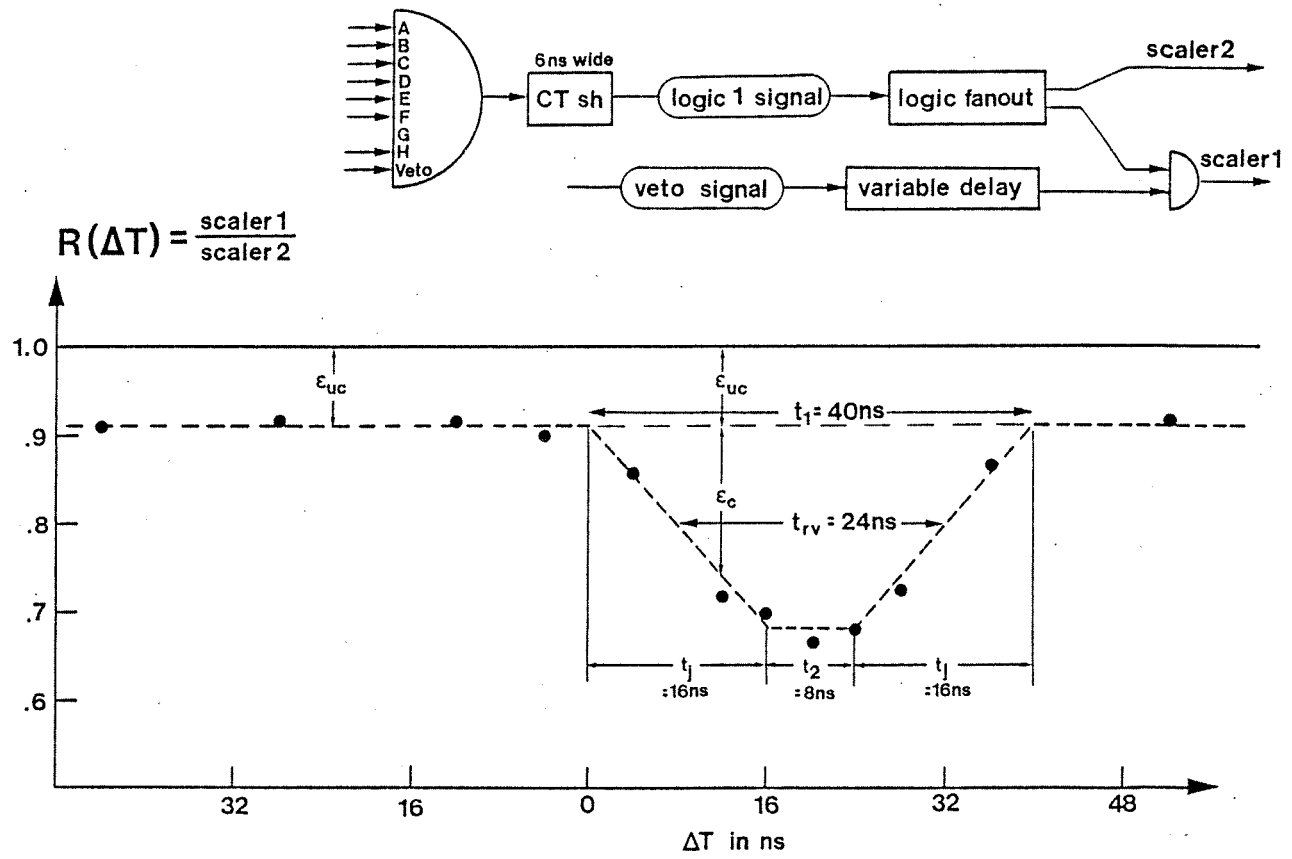

Fig. 5.7

Example of a veto efficiency measurement. In this particular case the two signals entering the simple logic are the following,

1) the logic 1 signal = the signal represented by the coincidence: A*B*C*D*E*F*H*VETO of CU1 in Fig. 5.3, reshaped afterwords to a 6 ns wide signal.

2) the veto signal = the OR of SP3, SP4, SP5, SP6, V1 and V2, see Figs. 5.5.a and b.

Data points are shown and the dashed line has been drawn by hand. Throughout the whole time scale are the data seen to be fitted rather well by straight line sections. The interpretation of what is random and correlated vetoes is also indicated.

which also correlated vetoing occurs. The random veto is seen to be as much as 9%. Which are the decisive parameters for ε_{uc}? Due to the randomness of ε_{uc} these must be the single rate of the veto

counters, N_V, and the actual time width, t_{rv}, associated with each logic 1 signal during which a random veto would be effective.

Notice that t_{rv} like a lot of the other time variables, actually can only be represented properly by a time distribution. t_{rv} is therefore understood to be the mean of the t_{rv}-distribution. The fluctuations are caused by 1), variations in t_v and 2), variations in t_w (due to the jitter between the signals producing the logic 1 coincidence signal). Concerning point 1) observe the following. The veto signals originate from 6 different counters. Even if all their discriminators are set to the same width, fluctuations in t_v will be present. This is due to overlap between different rather coincident signals, both at the level of the discriminators and later at the level of the ORing of the veto signals.

The relation between ε_{uc}, t_{rv} and N_V (to be developed below) is simple and may be used to check the measurements. Using the same arguments as in appendix 2, we find that the chance of having no effective veto of the logic 1 signal (i.e., $1 - \varepsilon_{uc}$) is,

$$(1 - t_{rv}/t_b)^{N_V} = \exp(- N_V t_{rv}/t_b)$$

where t_b is the duration of the beam spill. If $N_V t_{rv} \ll t_b$,

$$\varepsilon_{uc} = N_V \frac{t_{rv}}{t_b} \qquad (5.5)$$

t_{rv} can be extracted from Fig. 5.7. Obviously $t_{rv} = t_v - t_w$ (where, for reasons explained above, one should actually write, $\bar{t}_{rv} = \bar{t}_v - \bar{t}_w$). From above, also $t_1 = t_v - t_w + t_j$ (see Fig. 5.7) and $t_2 = t_v - t_w - t_j$ so that $(t_1 + t_2)/2 = t_v - t_w = t_{rv}$. Notice that while t_1 and t_2 may not be read with good precision from Fig. 5.7, this is not the case with t_{rv}. t_{rv} is exactly the full width at half minimum of the correlated veto pulses, the only condition being that full veto efficiency is reached for some value of ΔT or simply that $t_v \geq t_j + t_w$.

Assuming t_b=1.3 sec and complete randomness of the veto single rates during the burst (which implies that there is no structure in the beam), deducing t_{rv}=24 ns from Fig. 5.7 and using a single rate

N_v=3.2 x 10^6 burst^{-1}, one finds ε_{uc}=0.059. This is 34% below the on-line measurement of 9%. Some off-line analysis work was done to find the reason for this discrepancy, however, without success. One problem is that the the values quoted for N_v and t_b are averages for one whole run (typically 1 hour of data taking, ~400 SPS bursts and $2 \cdot 10^{10}$ incoming particles on the H_2-target). Another possible source of error is the assumption of no beam structure. However, when taking into account the effect that the efficient spill duration is shorter than the actual one, ε_{uc} does not change very much. The figures for the run in question are,

$$N_v = 3.2 \times 10^6 \text{ burst}^{-1}, \quad t_b = 1.91 \text{ sec}, \quad D = 0.687 \text{ and}$$
$$t_{be} = t_b \cdot D = 1.31 \text{ sec}$$

Here t_{be} is the efficient spill duration and D is the dutycycle parameter. Both values were obtained through the off-line analysis, more details about this in appendix 2. The value for t_{be} shows that the assumption of a 1.3sec flat spill is very good. However, it may be that during the 10 minutes of recording the curve displayed by Fig. 5.7, t_{be} was significantly smaller. Unfortunately this is only a hypothesis.

To conclude about this simple veto (made up of scintillators SP3-SP6, V1 and V2, see Figs. 5.5.a and b), notice that the total rejection (= $\varepsilon_c + \varepsilon_{uc}$) is at most 33% out of which up to 9% may have been due to random vetoing.

Next will be studied the effect of the wedge elements in veto. As in the case of above a delay curve was established yielding the reduction* as a function of the relative timing of the two signals, see Fig. 5.8. In this case the agreement between the measured random veto ε_{uc} and the one calculated using (5.5), is better.

Approximating as in Fig. 5.7 with straight line sections one finds t_2 = 10 ns and t_j = 8 ns. Hence $t_1 = 2t_j + t_2$ = 26 ns, $t_{rv} = (t_1 + t_2)/2$ = 18 ns and $t_w = t_v - t_{rv}$ = 2ns. To get the real

---

* 'Reduction' is the fraction of events which passes a test (for ex. a veto test) and 'rejection' is the fraction which doesn't pass.

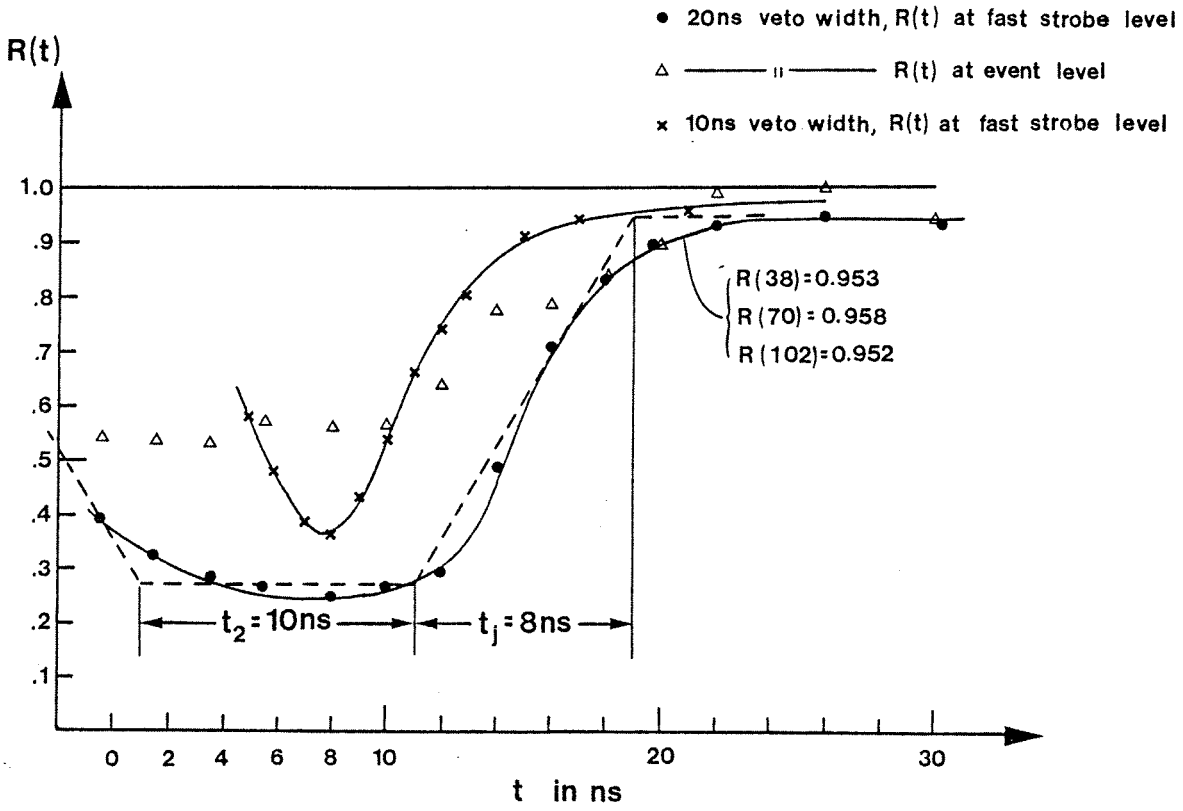

Fig. 5.8

On-line measurement of the effect of using the outer wedge elements in veto. The horizontal axis is the delay between the veto signal and the logic 1 signal plus a suitable time constant. The vertical axis gives R defined by R=(rate with veto/rate without veto). The normalization is explained in the text.

width of the logic 1 signal, twice the minimum time overlap of 3-4 ns (for CU 375L) has to be added. One therefore obtains 8-10 ns for this mean width, which is in rather good agreement with the widths of the PR1/PR2-signals (6-8 ns); notice that both t_{rv} and the minimum time overlap cannot be determined precisely. The H1/H2-signals also participate in the definition of the logic 1 signal, but don't influence the overlap because of their 15-20 ns widths.

Now to the caculation of ε_{uc}. During the Fig. 5.8 measurements typically $N_v = 2.6 \times 10^6$ burst^{-1} and $t_{be} = 1$ sec. Hence,

$$\varepsilon_{uc} = N_V \frac{t_{rv}}{t_{be}} = 2.6 \times 10^6 \times \frac{18 \times 10^{-9}}{1} \; 100\% = 4.7\%$$

in good agreement with what was observed.

Also shown in Fig. 5.8 is the response with a 10 ns wide veto signal, nearly full veto efficiency is attained. 10 ns covers 2 ns more than the full range in jitter (8 ns), even so some inefficiency will be present due to the long logic 1 signals (> 8-10 ns). Moreover the random veto drops roughly to the half (~2%), as it should. Therefore, to minimize the random veto and still have full veto efficiency, a width of 15 ns was chosen. This implies a reduction of 25% for the fast strobes. At the event level R is seen to be around 50%. The measurement was performed without the computer deadtime, which means that the only deadtime present in the system is the one imposed by the fast logic, ~380 ns per fast strobe, the livetime 1, see Fig. 5.3.

Before proceeding to evaluate the effect of the veto counters for the data acquisition, some details of the measurements related to Fig. 5.8 will be given. As opposed to the previous example of Fig. 5.7, in this case the logic 1 signal was not reshaped. The veto signal (shaped to a standard width pulse), was applied directly to the first coincidence unit (as during real data taking). For each t-value in Fig.5.8 we measured the number of strobes and events for a certain incoming beam (corresponding to 4096 icc), and to normalize, devided by the corresponding number of strobes and events with no veto present. 'With and without veto data' were not obtained at the same time (very impracticable). The calibration of the number of strobes and events against the the beam was therefore established independently. To use this calibration to normalize above one has to assume that both the event and strobe number depend linearly on the beam. The validity of this assumption can be checked from the figures in table 5.1. Fluctuations in the strobe numbers are small, $\pm$ 1%, while the events fluctuates as much as $\pm$ 5%. One may therefore expect the normalization of R(t) to be better at the fast strobe level than at the event level (both for what concerns the overall

Measurement number	1	2	3	Mean
Beam (icc)	4096	4096	4096	
Strobes (x 10^3)	871	879	864	871.3
Events	1353	1312	1351	1338.7

Table 5.1

Number of recorded strobes and events for 4096 icc, 3 independent measurements with no veto at the fast strobe level. The mean number of strobes and events were used for the normalization of the data points in Fig. 5.8.

normalization and the one related to each data point). As we shall see later, in fact the eventrate is not intensity independent. Due to increasing random multiplicity veto*, the number of events per icc is not constant, but falls with increasing beam intensity (see Figs. 5.12.a and b). The multiplicity veto was imposed at the event level and hence does not influence the strobe rate. This non linearity in the event rate is both the reason for the overall normalization error of R(t) at the event level, and for the apparant fluctuating normalization in each data point. Notice that even if the three measurements of table 5.1 are based on the same number of incident beamparticles, the respective intensities very likely are not the same. Obviously to have precise results stable beam conditions would be necessary (applies to both the intensity and the dutycycle).

Let the OR of the three sets of vetocounters be called 'the prompt veto' (it arrives promptly and hence could be implemented early in the logic, at the fast strobe level). One more important point related to the multiplicity veto should be mentioned. Notice that the prompt vetoes actually also impose a multiplicity constraint (in particular the wedge elements). There is correlation between the prompt and the multiplicity vetoes, both will sometimes be

---

* The multiplicity veto will be explained in detail later. It was introduced to veto events which fire too many elements in H1R/H2R and PR1/PR2, more than two tracks from the target being a signature of inelasticity.

be triggered by the same particle. This correlation explains the fact that the reduction is less at the event level.

I shall come back to the general aspects of the prompt veto in connection with the data acquisition. From table 5.2 is deduced,

The reduction in strobe rate $R_S = 59/276 = 0.21$
The reduction in event rate $R_E = 0.12/0.27 = 0.44$

Notice that again has the linearity of the rates versus the ionization chamber been assumed; the three columns of table 5.2 correspond to three independent measurements. Some of the reduction is due to random vetoing,

At the fast strobe level: 257/276 = 0.93
At the event level: 0.26/0.27 = 0.96

	Prompt veto out of time	Prompt veto in time	No prompt veto
Strobes per icc	257	59.0	276
Events per icc	0.26	0.12	0.27
icc per burst	855	796	878

Table 5.2

'Out of time' for the wedge vetoes would for example mean that $t \approx 70$ ns in Fig. 5.8. The event rate is as usual recorded without computer deadtime and icc is the standard abbreviation for ionization chamber count(s).

The 0.07 random veto agrees rather well with the prompt veto single rates and signal widths. The total single rate of the prompt vetoes with a beam of 850 icc, was 5.1×10^6 per burst, roughly 3.1×10^6 on the wedges and 2×10^6 on the beam and magnet anti counters. The efficient veto widths were $t_{rv} = 13$ ns for the wedges and $t_{rv} = 24$ ns for the other veto counters. Here the first figure is deduced from $t_{rv} = t_v - t_w$, where t_v is set in the fast logic to 15 ns and t_w has been taken from Fig. 5.8, in the same way also the second width (= 24 ns) was based on the delay curve measurement in Fig. 5.7. And finally with an efficient spill $t_{be} = 1$ sec (from appendix 2), one

finds the following random vetoes,

$$\varepsilon_{uc,1} = 3.1 \times 10^6 \times 13 \times 10^{-9} = 0.043$$
$$\varepsilon_{uc,2} = 2 \times 10^6 \times 24 \times 10^{-9} = 0.048 \text{ and the total}$$
$$\varepsilon_{uc} = 1 - (1 - \varepsilon_{uc,1})(1 - \varepsilon_{uc,2}) = 0.086$$

Some correlation between the three sets of vetocounters (which would lower ε_{uc}) may explain the small discrepancy between measured and calculated random vetoing. The difference between fast strobe level and event level results (0.93 versus 0.96), also come from correlations in the system. As we shall see, the random multiplicity veto is very important, for a beam intensity corresponding to 1000 icc per burst, it is as much as 60%. This random veto is present for all measurements in table 5.2, hence the correlation fraction between prompt and multiplicity random veto is already included in the figure 0.27. It is reasonable to assume that roughly half of the prompt random vetoes (mainly from the wedges) would anyway have produced a random veto at the event level through the multiplicity logic.

There are two related and interesting consequences for the data acquisition. First, the number of triggers written onto tape is reduced (means less data to be analysed off-line, important because of the very substantial amounts of data that we had). Second, due to reduced deadtime (comes from the lower rates at both the strobe and the event level), less good events are lost. The improvements may therefore be represented by the resulting increase in the ratios defined by,

$$f = \frac{N_g}{N_I} = \frac{\text{number of good interrupts written onto tape}}{\text{number of all interrupts written onto tape}} \quad \text{and}$$

$$g = \frac{\text{number of good interrupts written onto tape}}{\text{number of incident beamparticles}}$$

To calculate this one needs the relative deadtime $\stackrel{def}{=} t_D$. Typically the deadtime per interupt ($=t_d$) is 3.5 milliseconds. Note that the interruptrate, N_I, is somewhat lower than the eventrate, N_E,

due to the computer deadtime. Actually the two rates are connected in a very simple way, assuming N_I to be proportional to N_E and to the relative livetime, we find,

$$N_I = N_E(1 - t_D) = N_E(1 - N_I \frac{t_d}{t_{be}}) \qquad (5.6)$$

where t_{be} is the efficient burst duration, hence

$$N_I = \frac{N_E}{1 + N_E \frac{t_d}{t_{be}}} \qquad (5.7)$$

Like above t_{be} = 1 sec will be used, and the beam intensity is set to 850 icc per burst, somewhat above the mean intensity for the whole - 30 GeV/c data taking period, even so a lot of the data were taken at this very high intensity. Let primed variables refer to 'with prompt veto' and double primed to 'without prompt veto'. Data to be used in the calculation of f'/f" and g'/g" are found in table 5.3 below.

	Prompt veto in time	No prompt veto
N_E per burst	103.02	229.50
N_I per burst	75.85	127.27
$t_D = t_d N_I / t_{be}$	0.27	0.45

Table 5.3

The eventrates have been taken from table 5.2 and are scaled by the beam intensity. N_I is calculated from equation (5.7).

Using (5.6),

$$f' = \frac{N_g'}{N_I'} = \frac{N_g'}{1 - t_D'} \cdot \frac{1 - t_D'}{N_I'} = \frac{N_g'}{(1 - t_D')N_E'}$$

Obviously the fraction f does not depend on the livetime; the dead-time does not distinguish between good and bad events. Therefore

$N_g/(1 - t_D)$ is the good (=elastic) eventrate. Now

$$\frac{N_g''}{1 - t_D''} = \frac{1}{0.97} \cdot \frac{N_g'}{1 - t_D'}$$, the reason that the good event-rates differ being the small 3% random vetoing at the event level due to the prompt vetoes, see page 5 - 33. Since,

$$f'' = \frac{N_g''}{(1 - t_D'')N_E''}$$, we find

$$\frac{f'}{f''} = 0.97 \frac{N_E''}{N_E'} = 0.97 \frac{229.5}{103.2} = 2.25$$

Let α be the scaling factor between the ionization chamber and the beam intensity, then

$$g' = \alpha \frac{N_g'}{850} \quad \text{and} \quad g'' = \alpha \frac{N_g''}{850}$$

$$N_g'' = 0.97\, N_g' \frac{1 - t_D''}{1 - t_D'}$$, which inserted into the expression for g" allows to find,

$$\frac{g'}{g''} = 0.97 \frac{1 - t_D'}{1 - t_D''} = 0.97 \frac{1 - 0.27}{1 - 0.45} = 1.28$$

So nearly concluding we see that the on-line filtering becomes more than twice as efficient while the absolute number og good events will increase by 28%.

There is, however, one important point left to be investigated. It concerns the corrections that has to be applied in the cross section calculations, and which come from the losses of good events. Per definition of randomness, the 3% losses found from table 5.2 (at the event level), are random and should be taken into account. Not discussed so far is the possibility that correlated veto signals could veto good events. Several mechanisms could be responsible. Suppose that there are two outgoing particles, one incoming beam-

particle and that the reaction is elastic. Even so more particles which are physically correlated may be present,

1) The beamparticle interacts upstream of the target and produces additional particles. If the collision is sufficiently soft, the beamparticle may continue into the target where it interacts elastically.

2) The outgoing particles produces δ-rays.

3) The outgoing particles interacts with atom nuclei on their way through the detectors.

4) Decays of the scattered particles.

5) Radiation which eventually converts into e^+e^- pairs.

Unfortunately there are no data available so that the importance of point 1) could be estimated. Concerning the second point notice that this is only relevant for the wedge vetoes, the veto counters in the magnet being shielded by 5 mm of Al. Also, because of the magnetic field, these δ-rays have to be produced close to the wedge counters, otherwise they are trapped in the field and loose their energy there.

I have done some investigations which will reveal the importance of points 2) to 5) in connection with correlated but unwanted wedge vetoes. The conclusions, based on analysed data, will be that this veto is practically zero. Notice that this only means that these veto counters do not introduce the necessity of additional correction factors; in our off-line data analysis we only reconstruct 25% of all the triggers written onto tape, hence it is very probable that good events which due to points 2) to 5) are vetoed by the wedges, would anyway have been rejected because of unsuccessful track reconstruction. However, beforehand it was not clear to what extent the new veto would overlap with the always present reconstruction inefficiency, this in particular concerns points 2) and 3). One reason for the uncertainty was the rather poor momentum determination ($\pm$2% at 20 GeV/c), which implies rather loose cuts on the selected events and hence also the possibility that soft reactions along the

particle trajectories will not prevent the event from being reconstructed. Anyway, as the following will bear out, very few such events were seen.

Three event samples were chosen. It would have been preferable to have measured the vetoing with a sample made up of elastic events only. Low statistics made this impossible. Data samples I and II (see table 5.4) differ from III with respect to the wedge veto, the former were accumulated without the wedge veto. Samples I and III also differ from II, this is related to the event selection criteria. To have as clean events out from the target as possible, two constraints were imposed,

1) The vertex should be located well inside the hydrogen target.
2) The total number of digitizings in CH1, the first MWPC downstream of the target, should at most be one greater than the total number of digitizings used (for the reconstruction of the two outgoing tracks) in the same chamber.

Samples I and III differ from II in that for the two first, all 5 planes in CH1 worked properly, while for sample II, the second x-plane was dead.

Data sample	Mean intensity per burst (icc)	Number of events considered	Number of events with fired wedge	P	σ_P
I	509.07	113	15	0.133	0.034
II	720.07	176	20	0.114	0.025
I + II	613.91	289	35	0.121	0.021
III	627.54	389	31	0.080	0.014

Table 5.4

P is the probability that at least one of the outer wedge elements fires (in the CAMAC bit registers). Only events fulfilling the two constraints mentioned above are considered. σ_P is one standard deviation including only statistical errors.

The philosophy for extracting the correlated unwanted veto is as follows. For data sample III the wedge veto is in, it will be assumed to be 100% efficient which means that all (outer) wedge signals that enter the CAMAC bit registers will be random. This will be clearer in a moment. For data sample I and II no wedge veto is present, hence both random and correlated signals will set the registers. To find the correlated fraction one only needs to subtract the probability P_{III}, see table above, from for example P_I. However, the intensities as well as the gatewidths should be taken into account, which means that the P's of table 5.4 should be adjusted before subtraction. The probability of a random signal setting the register is proportional to the gatewidth and the wedge veto single rate (which again is proportional to the beam intensity). The mean width of the wedge signals was 15 ns and of the register gates, 38 ns. Some overlap is necessary for the signals to be registered, typically this is 3 ns. Hence the maximum jitter of a wedge signal relative to the gate is (38 + 15 - 3 - 3)ns = 47 ns. But if the random wedge pulse falls within $t_{rv} = t_v - t_w$ = (15 - 2)ns = 13 ns, then no fast strobes are generated and no events are read out. So the 'effective random gate width' is (47 - 13)ns = 34 ns for sample III and 47 ns for samples I and II. Therefore to find P(random) for data samples I and II, one should scale with the beam intensity and multiply P_{III} with 47/34. Hence,

$$P_I(\text{random}) = 0.08 \times \frac{47}{34} \times \frac{509.07}{627.54} = 0.089\ (\pm 0.016)$$

$$P_{II}(\text{random}) = 0.08 \times \frac{47}{34} \times \frac{720.07}{627.54} = 0.126\ (\pm 0.023)$$

$$P_{I+II}(\text{random}) = 0.108\ (\pm 0.019)$$

The probability given in table 5.4 for data samples I, II and I+II is a combined probability P_{12} of observing a random or a correlated signal within the gates. Knowing one of the probabilities P_1 (= P(random)), the second P_2 (= P(correlated)) is found by this formula,

$$P_2 = (P_{12} - P_1)/(1 - P_1)$$

since the combined probability is given by,

$$P_{12} = 1 - (1 - P_1)(1 - P_2).$$

From this is found the correlated probilities,

$$P_I(\text{corr.}) = (0.133 - 0.089)/(1 - 0.089) = 0.048$$
$$P_{II}(\text{corr.}) = -0.014$$
$$P_{I+II}(\text{corr.}) = 0.015$$

Converting to N(corr.), the number of events with correlated signals present in the wedge veto counters, we find,

$$N_I(\text{corr.}) = 0.048 \times 113 = 5.4\ (\pm 4.3)$$
$$N_{II}(\text{corr.}) = -0.014 \times 176 = -2.5\ (\pm 5.2)$$
$$N_{I+II}(\text{corr.}) = 0.015 \times 289 = 4.3\ (\pm 7.6)$$

The event selection criteria were very simple (vertex and digitizings in CH1 should be OK), and the event samples can therefore only partly simulate elastic events. In particular, no momentum cuts were made (would again have resulted in too low statistics), and no care could be taken to avoid neutrals. Possible bias arising from not applying momentum cuts, has not been studied. One should think that if any, the bias in the non elastic sample would be towards higher correlated vetoing; lower momenta implying higher total cross sections, higher decay probabilities and higher mean number of associated neutrals. Probably the bias is very much inferior to the statistical and systematic errors in the results presented above.

The correlated and unwanted wedge vetoing was therefore neglected, its importance being very small. Corrections which had to be applied were only due to randoms.

The event logic

At the fast strobe level the physics constraints were imposed in a very simple way, by means of one single coincidence unit for the elastic as well as the muon pair strobe creation chains. In each case all the matrices and vetoes entered the same unit. The logic is

more developed at the event level. Some words will be said about the muon pair event logic at the end of this chapter.

The elastic event generation is shown if Fig. 5.9. Both the slow matrices and the multiplicity logic work with the bit information from the CAMAC registers. There are hence three outputs from these registers, one to the CAMAC dataway used in case the event is read out, a second for the slow matrices and the third is for the multiplicity logic. The last output is special and works as follows. For each coincidence between the register gate and a single input, a level of -100 mV is set. The '-100 mV outputs' are linearly added in two groups, each corresponding to 8 inputs. By cascading the two outputs of one module, one adds linearly the '0 mV/-100 mV'-levels of the corresponding 16 single inputs. Therefore, in the blow up of the multiplicity logic (in Fig. 5.9), each input to a linear fan in/out, represents some integer multiple of -100 mV, corresponding to the number of coincident hits in a hodoscope. In this connection notice that the resolution of the coincidence is roughly defined by: The single element signal width + the gate width. The rest of the multiplicity logic should be easy to understand. All 4 levels from the 4 hodoscopes are linearly fanned out, and the outputs distributed to separate discriminators. Their levels are set so as to separate ≤ 1 firing from ≥ 2 firings, ≤ 2 from ≥ 3, etc. In the figure the most used multiplicity constraint is shown, it requires that,

$$(PR1 \leq 2) * (PR2 \leq 1) * (H1R \leq 2) * (H2R \leq 2) = 1$$

which may also be expressed as,

$$\overline{PR1 \geq 3 + PR2 \geq 2 + H1R \geq 3 + H2R \geq 3} = 0,$$

or simply that nothing comes out of the OR, see Fig. 5.9. Due to the logic that follows, the multiplicity signal has to be shaped. With a 40 ns gate for the H1/H2 registers, the jitter between the fast strobe and the multiplicity inputs of CU1 (Fig. 5.9), becomes about the same, ~40ns. Since, in addition, the time of the pulse out of CU1 should always be set by the fast strobe pulse, it is important to shape (lengthen) the multiplicity veto. The reason that the

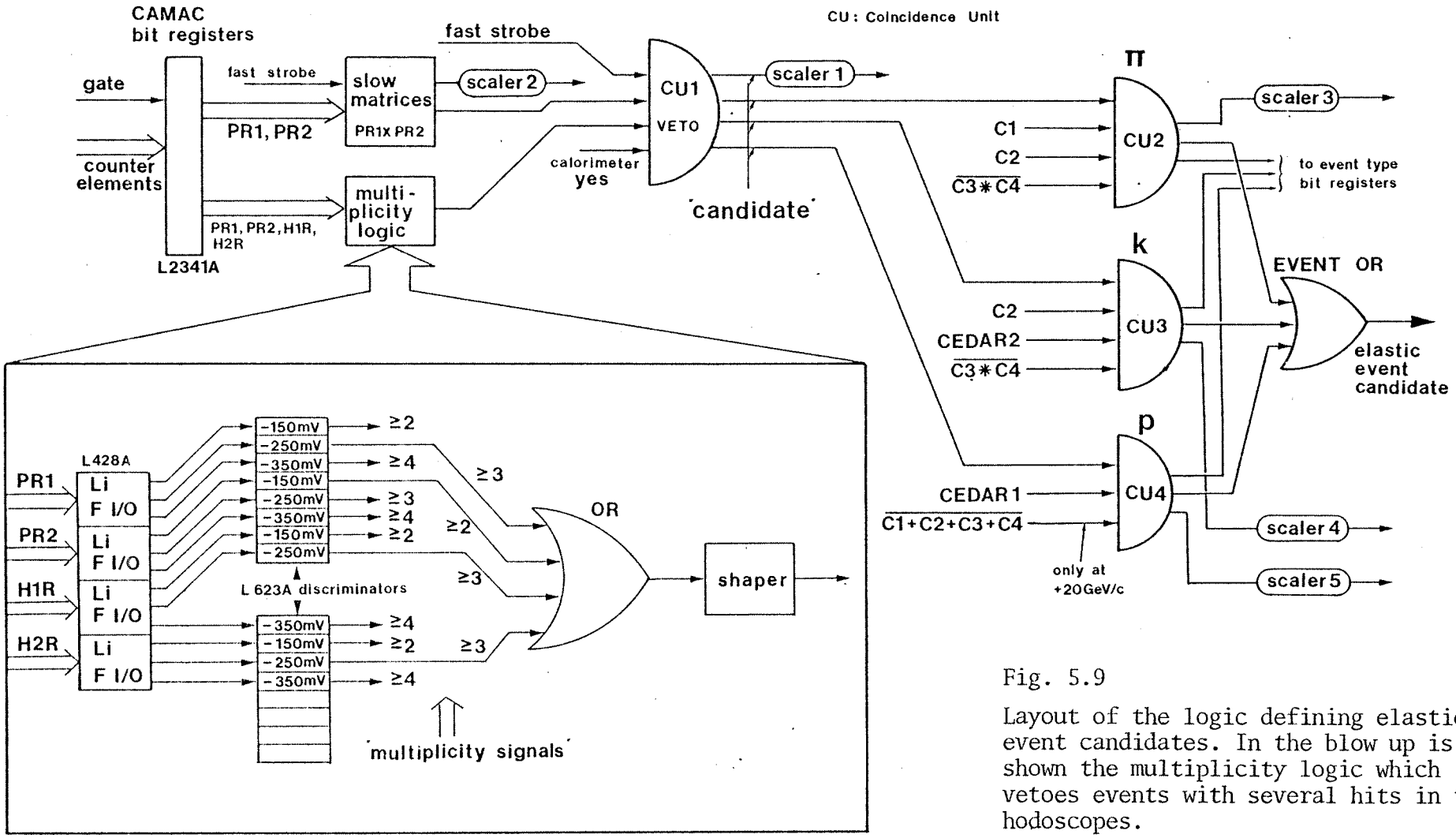

Fig. 5.9

Layout of the logic defining elastic event candidates. In the blow up is shown the multiplicity logic which vetoes events with several hits in the hodoscopes.

fast strobe should define the timing throughout the event logic (also for CU2, CU3 and CU4), has already been mentioned. If the event OR produces a NORD interrupt (not always the case because other parts of the system may be busy, see Fig. 5.3), then the CAMAC ADC's will be gated, both the calorimeter and cerenkov ADC's. The timing of this gate relative to the analog input signals, should be as precise as possible, hence the effort put into keeping the small time jitter of the PR1/PR2, also in the event logic. For the same reason also the slow matrix signal and the 'calorimeter yes signal' were shaped and timed so that they would always overlap the leading edge of the fast strobe signal.

The physical significance of the calorimeter yes signal has been discussed. I shall be brief about the slow matrices*. There are two, each consists of 2304 (= 48 x 48) programmable nodes. They were used to correlate one single PR1 element with some single elements in PR2, the programmed correlations (enabling/disabling nodes) were based on the kinematics of elastic events (opening angle and coplanarity). The slow matrices therefore in principle do the same as the PR1 * PR2 fast matrix, however with finer geometrical resolution.

We took data with three incident particle types, pions, kaons and protons. The rate of candidates (defined in Fig. 5.9), was too high for the data acquisition system. Cerenkovs and Cedars were therefore also used in the trigger logic.

First about the selection of πp elastic event candidates. A coincidence between C1 and C2 was a signature of a possible pion in the forward arm. C1 and C2 thresholds for pions running at $\pm$20 GeV/c, were set to 6 and 3.1 GeV/c, and running at -30 GeV/c, to 7.3 and 3.1 GeV/c. If at the same time the recoiling particle is a proton, then neither C3 nor C4 should fire. The proton thresholds at $\pm$20 GeV/c were set to 20.8 GeV/c for C3 and to 33.0 GeV/c for C4, and at -30 GeV/c to 20.7 GeV/c for both cerenkovs. C3 and C4 were therefore used in anti. However, to reduce the random veto rate, only when

---

* Made by Jean-Claude Lacotte, LAPP, Annecy.

there was a coincident firing of C3 and C4 would a veto be imposed.

With ±20 GeV/c incident the kaon thresholds in C1 and C2 were at 21.3 and 11 GeV/c, with -30 GeV/c the corresponding thresholds were 25.8 and 10.9 GeV/c. Notice that the choice of threshold is mostly based on particle identification considerations. Clearly for the kaon events one could only demand a C2 signal. In addition, the same recoil arm veto (as for π-events) was imposed, and also a beam signature was required. Cedar 2 was set to flag incoming kaons.

Lastly to the case of proton events. With a positive beam the proton content is important, also the proton-proton cross sections are well known. So to limit the proton event rate, a strict veto was imposed, demanding that none of the cerenkovs fired (thresholds being for protons 40.5, 20.8, 20.8 and 33.0 GeV/c for C1 - C4). On the contrary with a negative beam the antiproton content is low and Cedar 1, flagging incoming protons, would reduce the rate drastically. The proton event was therefore simply defined by 'candidate * Cedar 1' with negative beam polarity, see Fig. 5.9.

For the pion and kaon event generation, notice that only when the beamparticle scatters into the left arm and the recoil particle into the right, can the event be accepted. Hence the terms 'forward' and 'recoil' arm.

Rates in the event logic

Next will be studied the performance of this logic. In detail is discussed the effect of the slow matrices and the multiplicity logic. Notice that the decision of these elements depend highly on the bit registers since they provide the necessary data to be used when making a decision. Hence the crucial role of the timing and the width, t_g, of the bit register gates.

Fig. 5.10 shows the effect of the slow matrices relative to the fast strobe as a function of the average beamintensity, given in units of icc per burst. Each (x,y)-entry is the mean of data accumulated during one whole run. There are three bands of data, one where the reduction due to the slow matrices is 72%, a second where the reduction is 62% and a third one with 46% reduction. The upper band shows results from a period during which the logic was defi-

cient; the width of the bit register gates (see Fig. 5.9) which are generated by the fast strobe, were erroneously set to 30 instead of 12 ns. A comparison between the two sets of data should therefore reflect the sensitivity of the slow matrices to random coicidences. The relative random coincidence rate agrees rather well with the relative gate widths. Drawing in Fig. 5.10 the two straight and dashed lines by hand, one finds the inclinations: 0.106 per 1000 icc and 0.044 per 1000 icc for the upper and middle data bands respectively. The fraction, 0.106 : 0.044 = 2.41, should be equal to the ratio between the widths, (30 : 12)ns = 2.5, (actually one should have used the gate widths + something, where this last

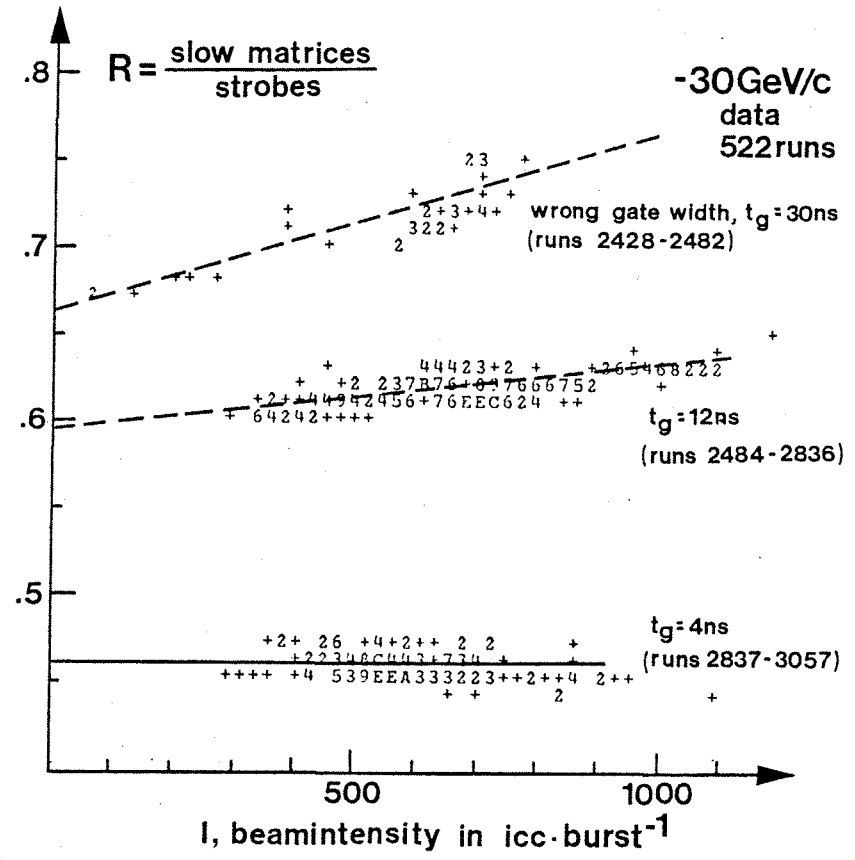

Fig. 5.10

R is the number of triggers accepted by the slow matrices normalized to the number of triggers which are input to the same matrices. Notice that both scalers (counting the nominator and denominator), actually are livetime gated so that R is still the true reduction (cf. Fig. 5.3). t_g is the gate width applied to the CAMAC bit registers.

has contributions from the individual prompt signal widths and also, but negative, from the required time overlap to set the register). 7 ns has been used below for this additional interval of sensitivity. In this case the width ratio becomes (37 : 19)ns = 1.95, which is worse than the 2.5-ratio just found. However, the systematic errors are big, coming from the way in which the lines were drawn, and also from the changes in running conditions. In fact the variations in R for a fixed intensity and gate width, are not negligible, hence R (and dR/dI as well) do, to some extent, depend on other variables than I and t_g.

In the lower data sample no intensity dependence may be seen, this is due to the very narrow gate to the PR1/PR2 bit registers, t_g = 4 ns.

Notice that clearly the 3 lines drawn by hand do not extrapolate to the same value for R at I = 0. This means that there is some inefficiency present in the slow matrices. In fact this may be due, not only to the slow matrices themselves, but also to the fact that not all correlated signals are accepted by the coincidence registers. Using the straight line extrapolations in Fig. 5.10 to find the intensity independent reductions (=R(0)), one may calculate the combined inefficiencies of registers and slow matrices. To be able to normalize, assume that the inefficiency is 0% for t_g = 30 ns. One then finds 10.4% inefficiency for the middle data sample (t_g = 12 ns), and as much as 30% for the lower sample (t_g = 4 ns).

First will be looked into the possible register related inefficiency. Some information about the TOF-spectrum (TOF, for time of flight) between the 'PR1 $\geq$ 1 signal' and the gate signal, may be deduced from the delay curves in Fig. 5.11.b. The results are from on-line measurements performed by two members of the WA7 collobration, Maurice Poulet and Michel Yvert. The curves give the rates of 'PR1 $\geq$ 1' etc., devided by the gate rate (= fast strobe rate) as a function of the relative time delay between the gate and the single signals from PR1. What was varied therefore, was the arrival time of the gate at the CAMAC register, see Fig. 5.9. Notice that 'PR1 $\geq$ 1' actually is 'PR1 $\geq$ 1 * gate' because this rate is monitored from one of the mul-

tiplicity discriminator outputs, (PR1 ≥1 is obtained by setting a discriminator threshold to for example, -50 mV). The pulses from PR1 which are physically correlated with the gate, are seen in Fig. 5.11.b as the very clear signals sitting on high backgrounds.

Knowledge of the TOF-spectrum (or simply the jitter spectrum,

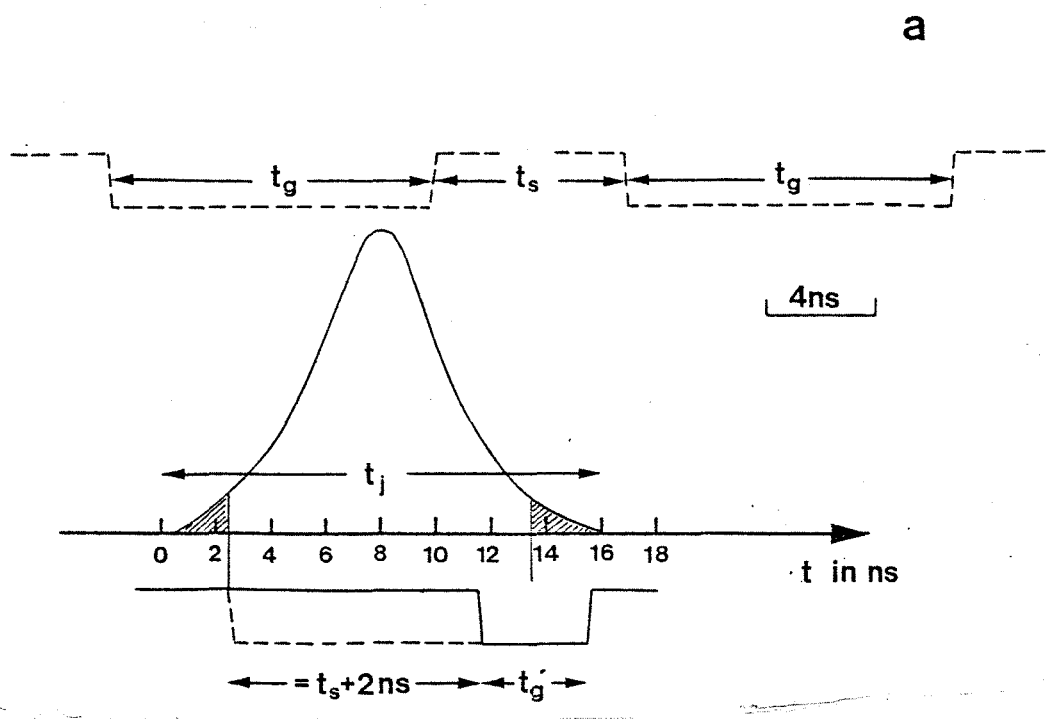

Fig. 5.11.a

The distribution is a constructed yet typical jitter spectrum, for ex. of all PR1 single signals which are correlated with the bit register gate, relative to the gate itself. Here the timing of the gates is fixed while that of the single signals varies. The ordinate naturally is the number of single signals per time, and refers to the starting point (falling edge) of the single signals. In the figure an average single signal width (at -100 mV), t_s', of 11 ns has been assumed. This is 2 ns off the predicted value, see the text, however, there is room for at least 0.5 ns uncertainties in several variables, FWHM, t_g, t_s' and in the overlaps. The two dashed gates (t_g = 12 ns) are positioned relative to the spectrum so that exactly half of the single signals will set the bit registers, corresponding to t_1 and t_2 in Fig. 5.11.b. This may be used to measure t_s. Under the timescale is shown the optimum position of a 4 ns gate. Notice that the sensitive width is $t_s + t_g'$ since a minimum overlap of 2 ns is necessary to set the register. Hence the last half of the gate is insensitive and the hatched area corresponds to inefficient signals. t_s is the active signal width, see the text for a precise definition.

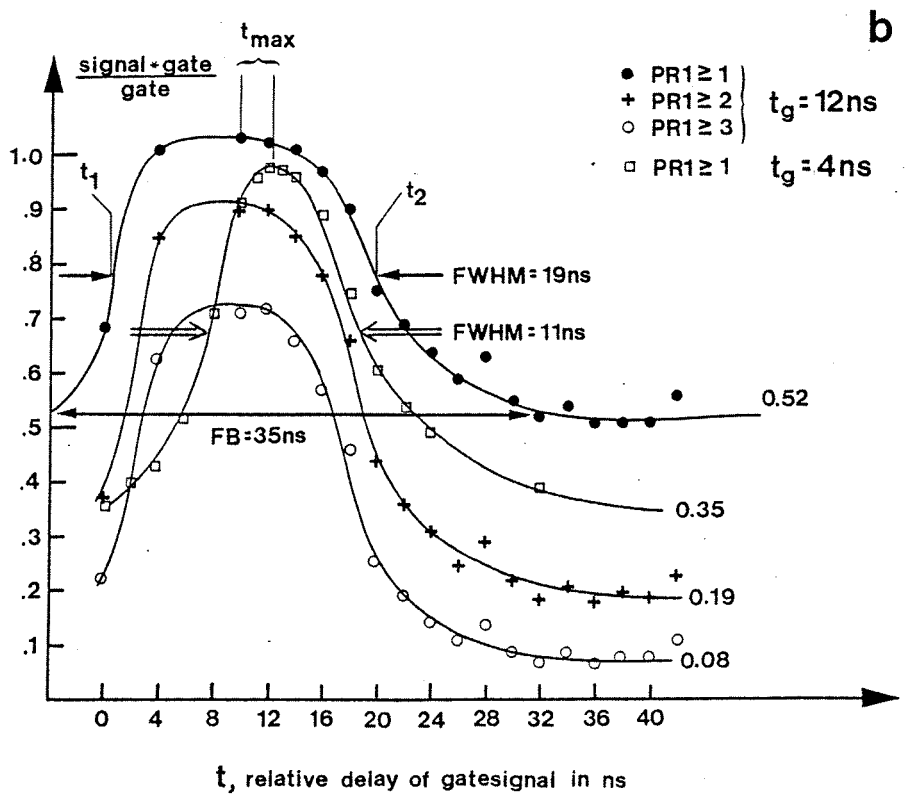

Fig. 5.11.b

Different delay curves obtained on-line (by M. Poulet and M. Yvert). The horizontal scale is the absolute time delay between the gate and the signal in question + an arbitrary time constant. Along the vertical axis is the ratio between two rates: gate * signal and gate. If the time constant for the horizontal axis is zero, the correct absolute timing of the gate is given by t_{max}. The curve obtained with t_g = 4 ns is from run number 2837 (at -30 GeV/c), the three other curves are from run number 2725, also -30 GeV/c data.

more appropriate since this term reflects the significance of the spectrum, while TOF refers more to the method used to obtain it) and the gate width, allows to calculate the efficiency, or in other words, the size of the accepted spectrum fraction, see Fig. 5.11.a. Normally the maximum value of the delay curve will yield the efficiency directly. However, in the case of Fig. 5.11.b there are obvious normalization problems; the curve which represent PR1 ≥1 and t_g = 12 ns data, attains 103%! I'll try to establish some facts about the jitter spectrum, which in turn will confirm the drop in

efficiency (at least for t_g = 4 ns). This information will be extracted independently of the background level, hence only by using the correlated signals.

First to the determination of t_s, the mean active signal width, t_s = 7 ns was used above to find the correct sensitive width for randoms, $t_s + t_g \equiv t_d$. One will loose in both ends of the gate if the time overlap is insufficient, therefore t_s is the difference between (the mean prompt singel signal width, t_s') and 2 x (the minimum time overlap between t_s' and the gate which would set the register). t_s' =(6-8)ns at half maximum (= -400 mV), and t_s' = (8-10)ns at -100 mV, which is also the sensitive level for the registers. The minimum overlap is 2 ns (at -100 mV for the register inputs, see specifications for bit register type LeCroy 2341A). $\bar{t}_s$ therefore should be equal to $t_s' - 2 \times 2$ ns = 5 ns. In this connection remark (by considering Fig. 5.11.a), that if the gate is wide enough so that full efficiency may be ensured, then t_1 and t_2 in Fig. 5.11.b correspond to the two dashed signals in Fig. 5.11.a. In each position will exactly half the spectrum be 'seen'. Hence t_s = FWHM - t_g = 7 ns. Note that if some inefficiency is present, the 7 ns will be an upper limit for t_s. t_s = 7 ns is true for both PRI $\geq$1 curves in Fig. 5.11.b. The agreement with the estimated value of t_s (= 5 ns) is not bad. In the following t_s = 7 ns will be used, hence the assumption of t_s' = 11 ns in Fig. 5.11.a.

Second to the jitter width, t_j. The full base width, FB, for the t_g = 12 ns curve is approximately 35 ns. Using this value for FB will, as we shall see, lead to concluding that the registers are 100% efficient when t_g = 12 ns. However, 40 ns could also be a good value for FB. In this case not only for t_g = 4 ns would the registers be inefficient, but also slightly when t_g = 12 ns. The main conclusion will be, irrespective of the choice of FB, that the register inefficiencies probably on their own may explain the drop in efficiency observed in Fig. 5.10.

Now assume that FB = 35 ns. Evidently, when increasing the relative delay of the gate signal, see Fig. 5.11.a, correlated coincidences start to count when $t = -t_g + (t_s' - t_s)/2$, and they are

present as long as $t < t_j + t_s' - (t_s' - t_s)/2$. Hence $FB = t_g + t_j + t_s$ and $t_j = FB - t_g - t_s = (35 - 12 - 7)ns = 16$ ns. What does this imply for the delay curves? Since $t_g + t_s = 19$ ns, it means that the whole jitter can be covered, and hence that 100% efficiency should be the situation when $t_g = 12$ ns. This again implies that the delay curve should be flat during a time interval equal to $t_g + t_s - t_j = (12 + 7 - 16)ns = 3$ ns. The curve should in addition increase and decrease during t_j nanoseconds. The PR1 ≥ 1 and $t_g = 12$ ns data, agree rather well with these predictions. When $t_g = 4$ ns only, the efficient span of the gate is $t_s + t_g = (4 + 7)ns = 11$ ns. It is clear that in this case the registers cannot be fully efficient. So, if the efficiency is 100% with $t_g = 12$ ns, what is then the '$t_g = 4$ ns efficiency'? To avoid the normalization anomally, assume simply that there is a 3% shift in the background (in Fig. 5.11.b), which, for example, could have been caused by noise generated in the multiplicity discriminator. Therfore, subtracting 3% in both curves, one obtains maxima at 100% and 94%. To calculate the inefficiency one has to take into account the background,

$$ineff(t_g = 4 \text{ ns}) = (1 - 0.94)/(1 - (0.35 - 0.03)) = 0.09$$

In this connection, observe that if a symmetric and triangular jitter distribution is assumed (see Fig. 5.11.a)), and with $t_j = 16$ ns and $t_s + t_g = 11$ ns, then the inefficiency becomes 0.1. Which is also an upper limit for this inefficiency; from the delay curves one sees that the early and late correlated signals approach the background smoothly, so the tail of an assumed triangular distribution must be overestimated. The closeness of measured (0.09) and calculated (0.10) values for the inefficiency therefore may indicate that FB is underestimated, FB > 35 ns. $FB(t_g = 12 \text{ ns})$ is not easy to extract from Fig. 5.11.b. As the following will bear out, also $FB(t_g = 12 \text{ ns}) = 40$ ns is a plausible estimate. In this case the jitter would be $t_j = FB - t_s - t_g = (40 - 7 - 12)ns = 21$ ns. Since for $t_g = 12$ ns, the sensitive width $t_d = 19$ ns, only some very small inefficiency will be present. Assuming the jitter distribution to be triangular sets an upper limit of 1% for the inefficiency. The very small

inefficiency implies that the estimate of t_s = 7 ns, is still valid. The 40 ns estimate is also seen to agree with data; the durations of reaching ~ full efficiency and equally zero efficiency are close to t_j (= 21 ns), the flat top (with t_g = 12 ns), may be considered as slightly rounded (which would mean that 100% efficiency is not quite reached) and last, FB(t_g = 4 ns) clearly $\geq$ 32 ns (from Fig. 5.11.b) which implies that FB(t_g = 12 ns) should be $\geq$ 40 ns. The inefficiency increases with the full base width (FB). As above, a triangular jitter distribution may be assumed, which in this case (t_j = 21 ns and t_g = 4 ns), sets an upper limit of 22.5% for the inefficiency.

There is another independent check on the 9% inefficiency found above. Could, for example, wrong background levels change it significantly? Correctiong for the 3% anomally, these levels are 49 and 32%. With the following parameters: the PR1 single rate at the input of the registers, N, the width $t_s + t_g = t_d$ and the effective spill, t_{be}, one may calculate the background. In table 5.5 below are given the relevant parameters for the two runs in question. Using an

Run number	t_g (ns)	t_d (ns)	t_{be} (sec)	Intensity, I (icc burst^{-1})
2837	4	11	0.95	853
2725	12	19	0.99	592

Table 5.5

Data from high t elastic scattering at - 30 GeV/c. The method used to obtaine t_{be} is outlined in A2.

argument from appendix 2, one finds that the probability that at least one <u>random</u> PR1 pulse sets a register, is given by,

$$P = 1 - \exp(- Nt_d/t_{be})$$

where N may be replaced by kI if I (the beam intensity) is propertional to N. Setting P(t_g = 12 ns) = 0.49 and = 0.43 one may calculate k and hence P(4 ns). The results are shown in table 5.6. Notice the discrepancy between calculated (44%) and experimental

	P(12 ns)	ineff(12 ns)	k (x 10^{-5})	P (4 ns)
I	0.49	0%	5.93	0.44
II	0.43	10.5%	4.95	0.39

Table 5.6

$k = (-t_{be} \ln(1 - P))/(t_d I)$, t_{be} in seconds, t_d in ns and P = P(12 ns).

(32%) values for P(4 ns), this may be due to non-linearity between the beam (I) and the PR1 single rate (N), also to the fact that I and t_{be} are averages over whole runs while the curves in Fig. 5.11.b are based on much smaller data samples and finally to uncertainties in the estimate of t_d. Assuming the same discrepancy for both sets of background levels (I and II), let us calculate the effect of the 6% level shift on ineff(4 ns). We have observed that the calculated value for P(4 ns) lies 38% above the experimental value, for level I. For level II, due to the assumption above, this means lowering P_{II}(4 ns) by 38% as well, therefore $P_{II,exp}$ (4 ns) = 0.39(1 - 0.38) = 28%. Hence, if the background level for t_g = 12 ns is shifted by 6% (43 instead of 49%), this implies that the level for t_g = 4 ns has to be shifted by 4% (from 32 to 28%) for the two levels to be consistent with rates etc. of table 5.5. If $P_{II,exp}$(4 ns) = 28%,

$$\text{ineff(4 ns)} = \frac{1 - (0.94 - 0.04)}{1 - (0.32 - 0.04)} = 14\%$$

The inefficiency increases from 9 to 14% when shifting P(12 ns) by 6%. This is only the situation in the extreme case of PR1 being alone responsible for the 10% drop in efficiency, see Fig. 5.10 t_g = 12 ns and compare with the value of 10.5% in table 5.6. Therefore the inefficiency is clearly limited upwards, downwards it is more unclear, but judging from Fig. 5.11.b, it could not be below 5%.

Clearly also PR2 is important for the overall efficiency of the slow matrices. The PR2 $\geq$1 signal exhibits a behaviour like the one for PR1. With ~10% register related inefficiency for each of the prompts, it is not unreasonable to assume that the 30% drop observed

in Fig. 5.10 may completely be attributed to the registers alone. This is also a natural conclusion, the CAMAC registers, which the slow matrices read, are either set or not set during the gate. There is therefore no need in the following slow matrix logic to do the coincidencing so tight and fast that losses could occur.

The inefficiency of the register/slow matrix ensemble being irrefutably established, how should one correct for it in the cross section calculations? Unfortunately this is tricky because the inefficiency values found from Fig. 5.10, cannot be used. For the following reason. The signals in Fig. 5.10 represent all events which fire a strobe and hence also a PR1 pulse, very inelastic reactions, high multiplicity events, etc., in particular events with non-relativistic secondaries. Naturally the elastic events make up a very small fraction; the inefficiency for the elastic events could be 0 as well as 50% without changing the overall inefficiency of 30%. Obviously the crucial question is: what would the jitter spectrum of Fig. 5.11.a look like for a sample of elastic events? We did not read out any such TOF information on event basis (which together with the knowledge of t_d, would have allowed to calculate the correction which should be used). $\pm$5.5 ns (t_d = 11 ns) may be enough; at -30 GeV/c the apparatus and the acceptance were such that the maximum jitter arising from different pathlengths (from the target to the prompts, all particles assumed to be relativistic, v = c), was $\pm$1.5ns, at +20 GeV/c the same quantity was $\pm$3 ns. However, remembering that there is also jitter in the scintillators as well as in the photomultipliers, it is clear that an effective gate width of 11 ns puts very severe demands on the cabling and timing work, and on the stability of the PM-response (remember that the timing depends on the pulse amplitudes).

Another useful information from such a jitter spectrum would be the exact optimum timing. That is, if the delay curve of Fig. 5.11.b in some way is biased relative to the curve one would have produced with only elastic events, then fixing the absolute delay at the maximum may be slightly wrong.

In the end no corrections were made to the cross sections. This is surely correct for the $\pm$20 GeV/c data taken with t_d = 19 ns, however, for the last half of the -30 GeV/c data (t_d = 11 ns), this is not so clear.

The multiplicity veto (MV),
which is another important part of the event logic, will also be studied in some detail. The MV is supposed to veto inelastic events with many particles incident on at least one of the 4 scintillator hodoscopes, H1R/H2R and PR1/PR2. All particles should be produced in the same target reaction. The implementation in the decision making logic has been explained, see Figs. 5.3 and 5.9. Here will be studied the effect of the MV on the trigger rate plus the aspects which will allow to understand the behaviour of R(I) displayed in Figs. 5.12. For a more extensive treatment also including a proposal of a continuous on-line monitoring facility (of the unwanted random MV, RMV), see reference 4.

First to the effect of the MV on the trigger rate. In Fig. 5.12.a is shown the measured reduction, R ≡ scaler 1/scaler 2, see Fig. 5.9, as a function of the beam per burst, I. Nearly all our data at -30 GeV/c is gathered in the figure (> 95%). The overall reduction is seen to lie between 0.5 and 3.5%, corresponding to a rejection of 96.5 to 99.5%*. R essentially reflects the effect due to MV's, see footnote. There are 4 main reasons for the obvious data band structures,

1) The strictness of the multiplicity requirement was altered.

2) The event sample which is presented for the multiplicity check was not always the same. This would happen if the criteria for the fast strobe creation (and hence also for the creation of the bit register gates), were changed. The introduction of the wedge vetoes, see above, is an example of this. Also simply altering the gate widths will affect R, we shall see why.

3) Faults/ deficiencies/breakdowns in the apparatus occured and were discovered/repaired, unfortunately not always right away.

4) The cal.yes input of CU1 Fig. 5.9, was enabled/disabled.

---

* Actually the data in Fig. 5.12.a partly shows the combined effect of the MV and the calorimeter (confere Fig. 5.9, sometimes the cal. input of CU1 was enabled). However, the cal. reduction has separately been verified to be constant with I, at -30 GeV/c equal to ~0.5.

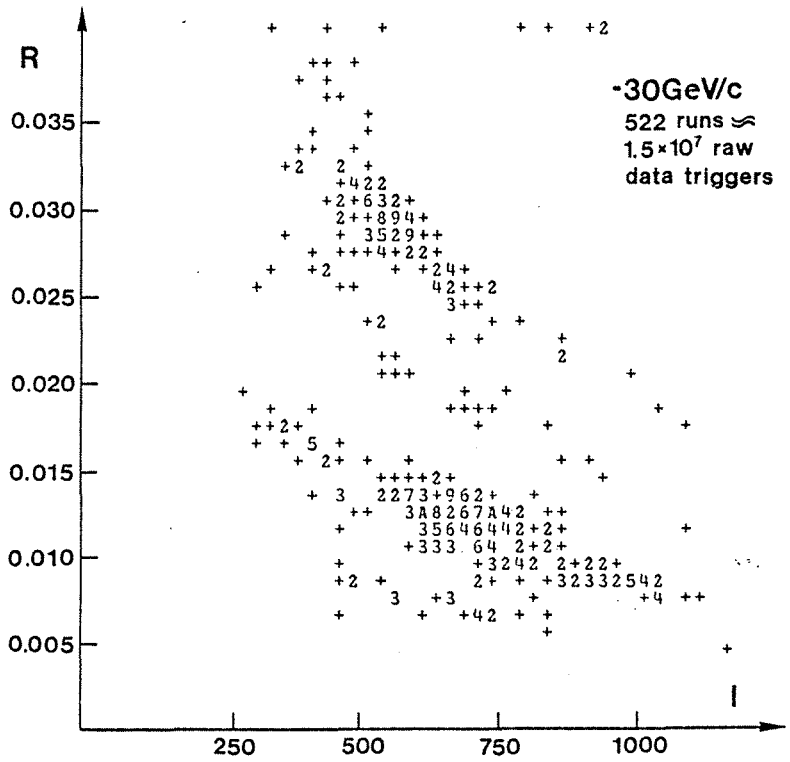

Fig. 5.12.a

The reduction in the trigger rate due to the MV as a function of the beam intensity (in units of icc/burst, 1 icc ≈ 75,000 incident beamparticles). Each entry represents the mean reduction during one whole run.

Studying the data taking conditions in detail (mostly using the experiment logbooks), one may decompose the Fig. 5.12.a data in run sequences with (at least for what concerns the MV), stable conditions. Fig. 5.12.b for instance, shows R for runs 2515 - 2677 (no calorimeter). Here R varies between 0.8 and 1.6%. The importance of the MV should be noticed, obviously it is crucial in the trigger rate reduction, one could not do without it.

Also notice the clear drop in R with I. This brings me over to the second item, the understanding of R(I), which will lead to an estimation of the RMV.

What is the expected R(I)? If the MV vetoes only the events

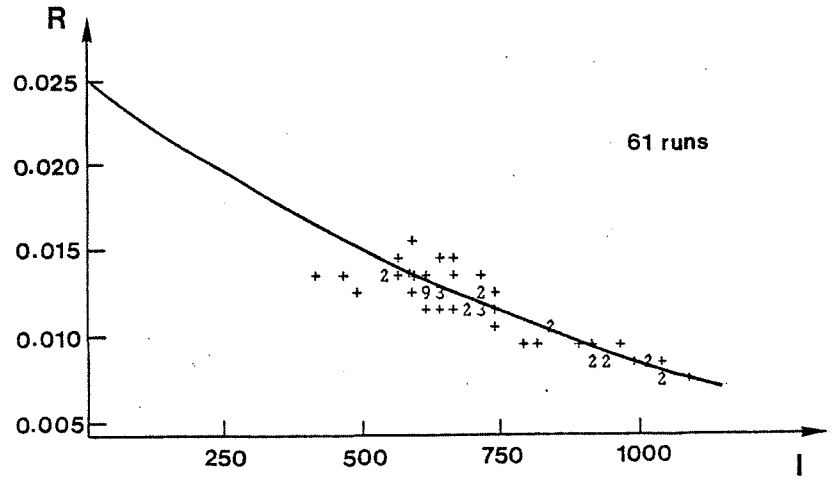

Fig. 5.12.b

R versus I for one data band (runs 2512 - 2677) extracted from the data sample in Fig. 5.12.a. $R_C = R(I = 0) = 0.025$.

it is supposed to veto (i.e. inelastic events), then R should be intensity independent. Because in that case, scaler 1/I, reflects a physical cross section, the probability that a beam particle interacts in the target and produces secondaries which will satisfy the constraints imposed by CU1, see Fig. 5.9. The same argument naturally applies to, scaler 2/I, too. Hence R should be flat if the multiplicity veto only rejects a well defined fraction of our inelastic events. However, this is not observed. The drop in R with I is interpreted as resulting from the increasing probability of one or more random hodoscope firings, coincident enough with the actual event to produce an MV. This probability of 'a random coincident enough firing', is related to two variables, an overall singlerate S, which in a complex way depends on the single rates of the 4 hodoscopes and the actual multiplicity constraints, plus an average efficient register gate width, t_g. The measured reduction R of Figs. 5.12.a and b, therefore is a combined effect of correlated and uncorrelated (= random) MV's. Let the two corresponding reductions be R_C and $R_u = R_u(t_g, S)$, then,

$$R = R_C \cdot R_u \qquad (5.8)$$

Notice that R_c does not depend on S *. How is R_u related to t_g and S? We have already used the following argument several times. The probability that all the random vetosignals during 1 second will not veto, is given by,

$$R_u = (1 - t_g)^S = e^{-tgS} \tag{5.9}$$

If we assume that S ~ I, then S(I = 0) = 0, and the data in Fig. 5.12.b may be fitted with $R = R_c \exp(-kI)$ where k is a constant proportional to t_g. The cross sections should be corrected by mulplying with the factor,

$$C \equiv \frac{R_c}{R} = \exp(kI) \tag{5.10}$$

Details of the normalization work for elastic data at high t, based on the method outlined above, may be found in the forthcoming thesis by Kjell Brobakken, Department of Physics - University of Oslo. Two important remarks should be made.

The first is related to the difficulties in using, $C = \exp(kI)$. The good correction is given by the factor $C = R_c/R$. However, the difficult and crucial problem is to find a parameter, X in our data, for which there is a one-to-one correspondance with R. Notice that since the gatewidths involved were constant, X can only be dependent on S. If then, the value X_o of X, so that $X(S=0) = X_o$, is known, R_c is simply found by extrapolating the R(X) data-points to $R(X_o)$. Hence, for a certain data run with $X = X'$, $C' = R(X_o)/R(X')$. Above we have set $X = I$ and $X_o = I_o = 0$, and assumed $S \sim I$. This last assumption implies (5.10), i.e., that C is exponential and independent of R_c. Unfortunately the correspondance in our data is not good enough to confirm the exponential behaviour of R, see Fig. 5.12.b. I have tried to replace I with the actual beam intensity (per second and not per burst; the spill duration varies) and corrected for the beam structure (see appendix 2). However, the correspondance between X and R isn't noticeably improved. One very probable reason is that the halo affects S, but does not depend linearly on the beam. Still another source of

---

* Due to the fact that the cal.yes input of CU1 Fig. 5.9, is sometimes enabled, R_c will, for some data, also include the calorimeter reduction of $\approx 50\%$.

error could be the incorrectness of assuming that, $I = I_o = 0 \Rightarrow S = 0$. For example with high noise rates on single channels, $S > 0$ when $I = 0$. Usually the noise is of no importance, but with defect electronics, this may very easily not be the case.

The second remark. Actually the method is not quite correct, event if all assumptions hold. The reason is that R reflects the effect of the RMV on our triggers and not on elastic events. This will lead to overestimating C. The reader is again referred to ref. 4.

Now will be given a discription of a direct RMV-measurement (as opposed to above where R_u is found indirectly through a fitting procedure where several assumptions are necessary). Unfortunately the method employed cannot be used while taking data.

Let the multiplicity requirement be the one most commonly used, i.e., $H1R \leq 2$ and $H2R \leq 2$ and $PR1 \leq 2$ and $PR2 \leq 1$, otherwise the event is rejected. The timing of all the register gates were then completely shifted (so that none of the hodoscope signals that participated in the fast strobe creation would set any register). We next assumed that the multiplicity configuration of elastic events is, H1R = H2R = PR1 = PR2 = 1, which, now that the gates are shifted, means that the rate of the configuration defined by, $H1R \geq 2$ or $H2R \geq 2$ or $PR1 \geq 2$ or $PR \geq 1$ (inclusive or's), actually is the RMV-rate. Hence the ratio between this rate and the fast strobe rate equals $1 - R_u = P_{rmv}$, the probability of a RMV. Actually P_{rmv} will be slightly underestimated; elastic events, due to δ-rays, may result in a total of more than 4 hodoscope firings which naturally enhances the chances of randoms producing a MV. Estimates in ref. 4 limit the possible error to ~10%. In Fig. 5.13 is shown such a P_{rmv}-measurement; the ratio between the two rates as a function of I (neither corrected for varying spill duration nor for possible beamstructure). The two curves clearly display the significance of the gate width, the wider the gates the more probable are RMV's. It should be noted that the correlated single signals will not be affected by the change in gate width, their time jitter with respect to the gate is small. Hence the change in P_{rmv} is purely due to randoms. The effect (= increase in rate) is 19% at the event level, 12% at the interrupt level. Remember that an interrupt

is an event which is accepted by the computer and hence written onto tape. The reason that the effect is smaller at the interrupt level is related to the computer deadtime. Since the accepted fraction drops with the number of events - see (5.7), the deadtime is propor-

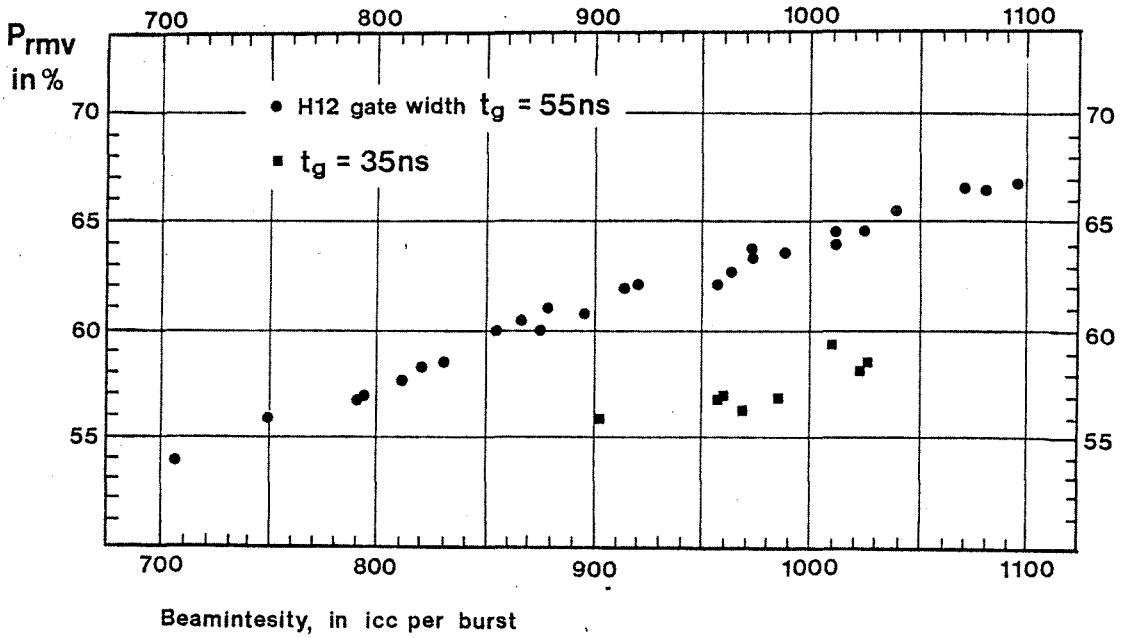

Fig. 5.13

P_{rmv}, the probability of a RMV versus the beamintensity (icc·burst^{-1}). The normalization of the ionization chamber is the usual one, 1 icc = 75,000 beam particles. The widths t_g, are the effective sensitive widths ≈ the actual gate width + the mean H1/H2 single signal width. The method employed for the measurement is described in the text. The multiplicity requirement was H1R ≤ 2 and H2R ≤ 2 and PR1 ≤ 2 and PR2 ≤ 1, the beam momentum -30 GeV/c and the PR1/PR2 gate width (12 + 7)ns = 19 ns.

tional with the number of interrupts - the 19% increase cannot be fully taken advantage of; it generates more deadtime, hence fractionally less events are accepted. The 19% figure is found directly from Fig. 5.13. For instance, for I = 1000 icc, $P_{rmv}(t_g = 55) = 0.64$ and, $P_{rmv}(t_g = 35) = 0.57$. Hence the effect is found to be,

$$\frac{1 - 0.57}{1 - 0.64} - 1 = 0.19$$

which was used to calculate the effect at the interrupt level. With an eventrate of 125 per burst, a deadtime per event of 3.8 ms and a 1 second effective spill, this increase of 19% translates into 12% at the interrupt level (using formula (5.7)).

The calorimeter.

The calorimeter constraint is imposed through coincidence unit 1, see Fig. 5.9. As explained in chapter 4E (see for instance Fig. 4.29), the presence of the cal.yes signal signifies that the linear sum of the signals from all the calorimeter counters (in L1 and L2), bypasses a certain voltage threshold which, essentially, is an energy threshold. The resolution with only 2 sampling planes (one after 40 cm, the other after 60 cm of iron) is poor, and the mean energy cut level therefore had to be very low. Otherwise, as we shall see, too many good events are lost.

I shall first make some comments related to the geometrical acceptance of the calorimeter, then will be given the relevant figures for its reduction (= effect on the trigger rate) and inefficiency.

The calorimeter unfortunately did not cover the full acceptance as defined by the rest of the apparatus at ±20 GeV/c. This corresponds roughly to: $50^{o} < \vartheta_{CM} < 100^{o}$ *. Hence, to avoid loosing events at ±20 GeV/c, the cal.yes signal had to be redefined as shown below.

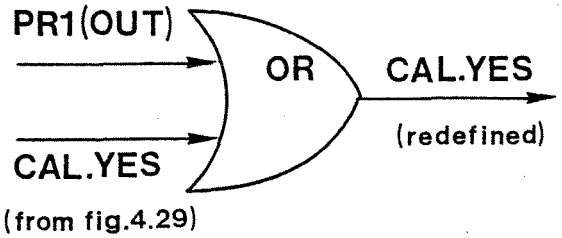

Fig. 5.14
Cal.yes signal redefined.

---

* ϑ_{CM} is the scattering angle of the beam particle in the center of mass system.

Roughly half of the solid angle defined by the PR1 hodoscope could not be covered by the calorimeter. An OR between the corresponding PR1-elements is denoted 'PR1(OUT)' in Fig. 5.14. At -30 GeV/c we let the calorimeter set the acceptance, thereby slightly reducing it compared to the acceptance of the rest of the apparatus, however, with an obvious advantage in the trigger rate reduction.

In Fig. 5.15.a is given the results at +20 GeV/c. One curve (x), shows the overall reduction, the other (·), the reduction which would result if only tracks impinging on the calorimeter sensitive part of PR1 are considered. These reductions are measured by counting simultaneously event and event * cal.yes, hence

$$R_{cal} = \frac{\text{event} * \text{cal.yes}}{\text{event}}$$

'Event' was defined in Fig. 5.9, event is the rate of scaler 3 + scaler 4 + scaler 5. 'Event * cal.yes' was the output of a coincidence unit not shown in the figure. Comparing the two curves in Fig 5.15.a, it is evident that redefining the cal.yes signal seriously affects R_{cal}, the reduction due to the calorimeter. This is ascribed to the high multiplicity on PR1.

The situation is more favorable at -30 GeV/c where, as just mentioned, PR1(OUT) ~ 0 (the geometrical acceptance, due to the Lorentz contraction, increases with the beam momentum). Hence the reduction is lower at the higher momentum, compare upper curve in Fig. 5.15.a with the curve in Fig. 5.15.b.

A general feature of the 3 curves is an important reduction at the very low thresholds. This shows that a big fraction of our triggers is made up of either very low energy hadrons or/and electrons. Since little is gained by increasing the threshold, data were taken with loose threshold constraints, mostly demanding only -30 mV ($\approx$ 1 ep). In this case the effect of the calorimeter is seen to be 0.75 and 0.50 reductions for the low and high momentum respectively.

These reductions naturally cannot be had without some calorimeter inefficiency, see appendix 4. K.E. Johansson has evaluated this inefficiency as a function of the incident momentum[5]. Great care had to be taken so as to select only events with a good momentum determination for the forward particle. Using a discriminator

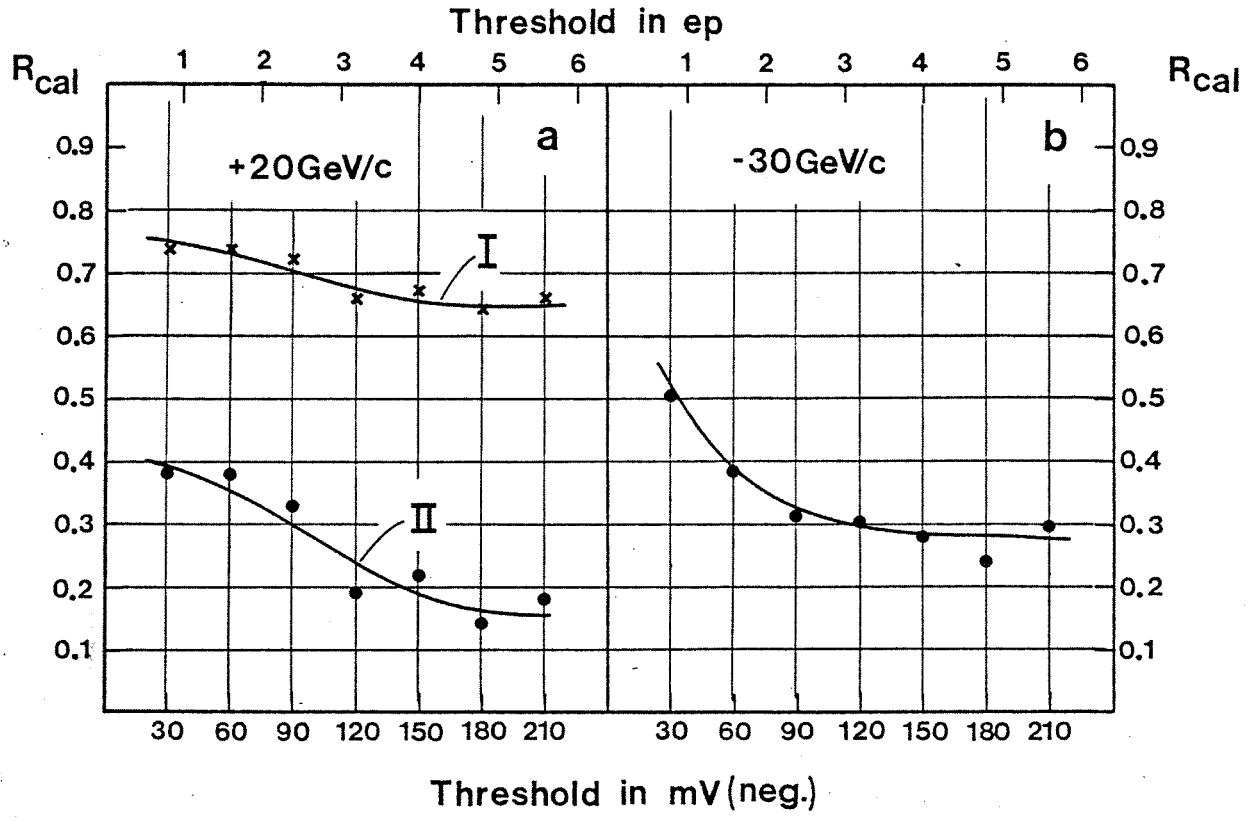

Fig. 5.15

The horizontal scale is the threshold imposed on the added calorimeter signal, given either in units of ep's (1 ep by definition is the charge of the signal of 1 minimum ionizing particle in 1 counter) or simply in mV.

Fig. a, reduction when the beam momentum is +20 GeV/c. Curve I: the cal.yes signal is redefined as in Fig. 5.14, R_{cal} is the fraction between two rates,

$$R_{cal} = \frac{\text{cal.yes} * \text{event}}{\text{event}}$$

Curve II: only those events with no particles incident on PR1(OUT) are considered. The cal.yes signal is not redefined, and the cal.yes * event - rate now is normalized to the rate of, event * $\overline{\text{PR1(OUT)}}$,

$$R_{cal} = \frac{\text{cal.yes} * \text{event}}{\overline{\text{PR1(OUT)}} * \text{event}}$$

Fig. b, reduction when the beam momentum is -30 GeV/c. The cal.yes signal is not redefined and R_{cal} is (cal.yes * event) over (event). No redefining is needed, this is due to the increased calorimeter acceptance, see the text.

bitpattern stored in CAMAC (see Fig. 4.29), the inefficiency is easily obtained by calculating 1 - $\varepsilon_{cal}(p,i)$, where ε_{cal} is the calorimeter efficiency,

$$\varepsilon_{cal}(p,i) = \frac{\text{number of times that bit 'i' fires when } p-\Delta p < p < p+\Delta p}{\text{number of times that } p-\Delta p < p < p+\Delta p}$$

In Fig. 5.16 is shown $\varepsilon_{cal}(p,1)$ and $\varepsilon_{cal}(p,4)$ corresponding to ph = -30 mV and -90 mV respectively. In addition are shown Monte Carlo

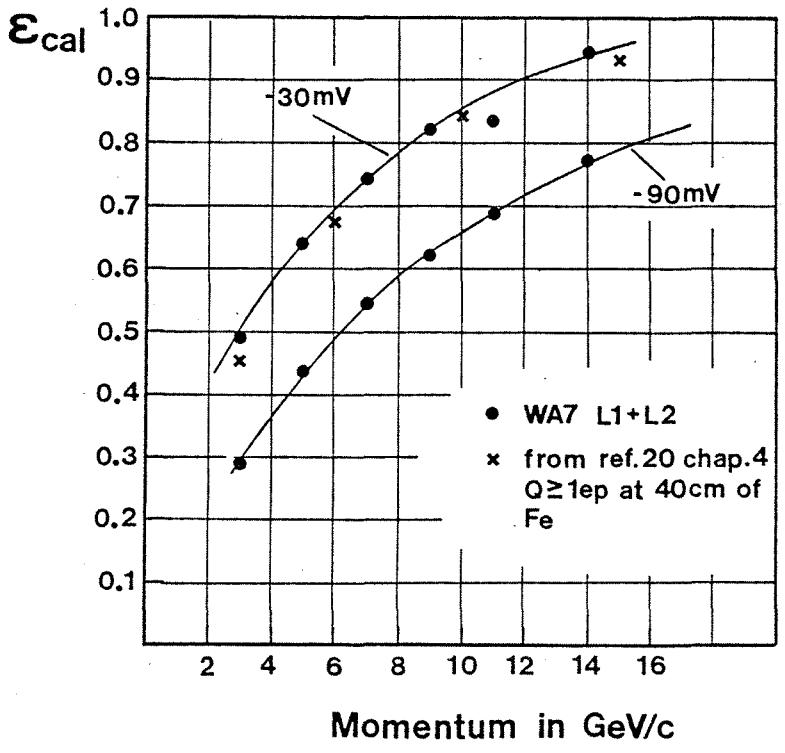

Fig. 5.16

Crosses (x) represent the calculated probability for observing at least a 1 ep - signal at 40 cm of iron. Points (•) represent the measured WA7 calorimeter efficiency for two threshold values, ph = -30 mV and ph = -90 mV. In this case the summed signal, L1 + L2, was used.

shower simulation results due to T.A. Gabriel et al., see ref. 20 chapter 4. They show that there is good agreement between their calculations and existing experimental data. Also our data agree well with their Monte Carlo predictions. To see this, two points should

be made,

1) The probability that $|ph(L1 + L2)| > 30$ mV $\approx$
   the probability that $|ph(L1)| > 30$ mV.
   The reason for this is connected with the second point,

2) From Figs. 4.29 and 4.35 it is seen that our 1 ep calibration
   is '1 ep corresponds to -37 mV (= -75/2 mV)'.

In order to contribute to the inequality of the two probabilities in 1), the shower must be small in L1 ($|ph(L1)| < 30$ mV), but still fire L2 so that $|ph(L1 + L2)| > 30$ mV. This is not inconceavable (for ex. could fast neutrals be reponsible; the charged shower fraction being practically zero at 40 cm of iron, L1 would fire less than -30 mV, if, at the same time, the neutral fraction converts late enough so that only L2 will see the secondary shower, then this will contribute to the inequality of the two probabilities in 1)), but very improbable. Hence the probability of at least a 1 ep signal after 40 cm of iron, corresponds roughly to the efficiency when requiring $|ph(L1 + L2)| > 30$ mV. The ref. 20 calculations are seen to lie systematically below our measurements. This may be due to the slight calibration discrepancy (our data should have been taken with a -37 mV threshold).

The calorimeter inefficiency was taken into account in our cross section calculations. $1 - \varepsilon_{cal}$ was set to 0.05 for the -30 GeV/c data. At this momentum our geometrical acceptance covered a momentum range from 18 to 26 GeV/c for the forward particle, cf. Fig. 5.16. For details about this work, see ref. 7.

At +20 GeV/c the calorimeter performances were not fully understood. Therefore, during actual data taking, it was only used on the proton trigger (the cal.yes signal was connected to CU4, see Fig. 5.9). The proton-proton elastic cross section had already been measured by other people, however, we did not want to risk compromising the π^+ K^+ data. For the proton data $1 - \varepsilon_{cal} = 0.2$, was used, see ref. 6.

The cerenkovs and Cedars.
The signals from these detectors are used in the event logic as shown in Fig. 5.9. Cedar 1 flags protons and Cedar 2, kaons, hence the incident particle may be identified. The thresholds for the 4 atmospheric cerenkov counters C1 - C4, are arranged in such a way that elastically scattered pions should fire C1 and C2, kaons should fire at least C2, and the recoiling proton should never fire either C3 or C4. With the cerenkovs one imposes a velocity constraint,

$$\beta = \frac{v}{c} \geq \beta_{threshold} = \frac{1}{n}$$

where n is the refractive index of the cerenkov radiating medium, in our case, gas mixtures. This again implies different momentum thresholds for the various particle types (due to their different masses). For example, the onset of the accepted pions in the forward arm is clearly seen to be situated at p_π = 6 GeV/c (at -20 GeV/c, see Fig. 4.14.a). Due to electrons and cerenkov noise, also events with momenta below 6 GeV/c for the forward particle were accepted.

The reductions which result from the cerenkov and Cedar constraints are shown in Figs. 5.17.a-c. Scalers 3, 4 and 5 count respectively the π, the K and the proton event rates, scaler 1 is the common normalization given by the rate of the 'candidate', see Fig. 5.9. As usual the beam intensity (per burst) is along the x-axis. Some dependence on the intensity seem to be present for all 3 event types. However, detailed studies of the data taking conditions reveal that when they were constant, also the plotted ratios were constant. The observed increase in the ratios is due to the mixing of different databands (like the ones displayed in Fig. 5.12.a).

The reasons for the existance of the databands are similar to the ones invoked above to explain the databands in Fig. 5.12.a.

1) The event sample presented for CU2, CU3 and CU4 was not always the same, see Fig. 5.9. For example will the following modifications to the logic lead to sudden increases/decreases in R_π, R_K and R_p,

   a) Introduction of the wedge vetoes (⇒ small increase in R_π, R_K and R_p).

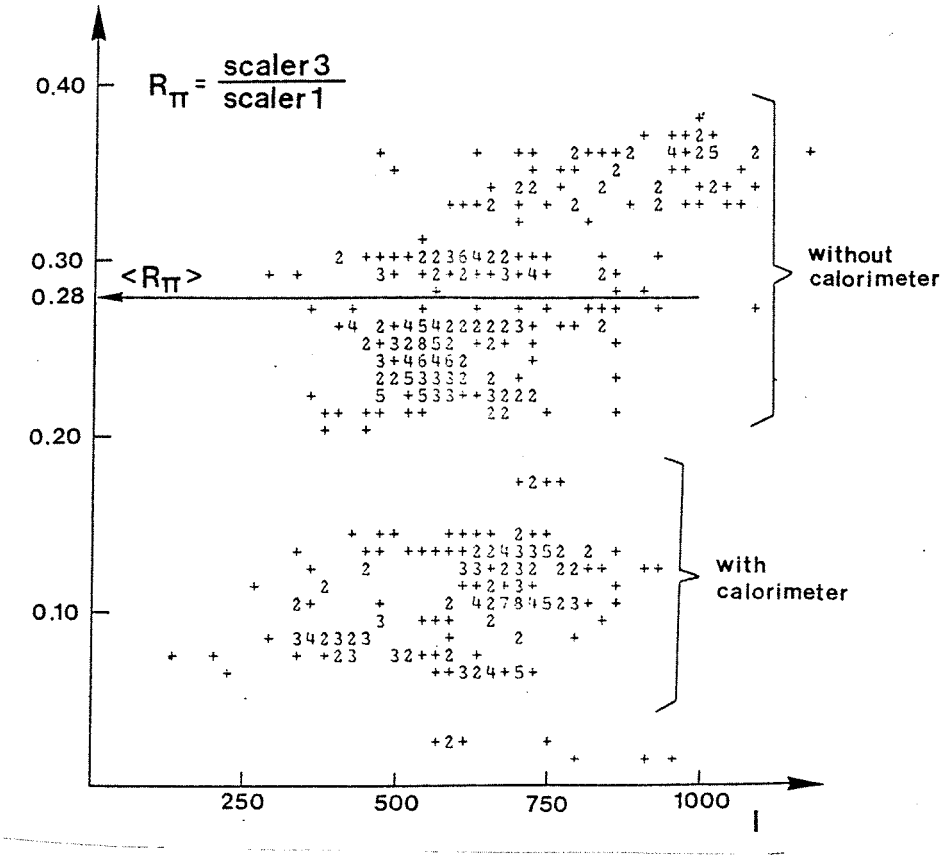

Fig. 5.17.a

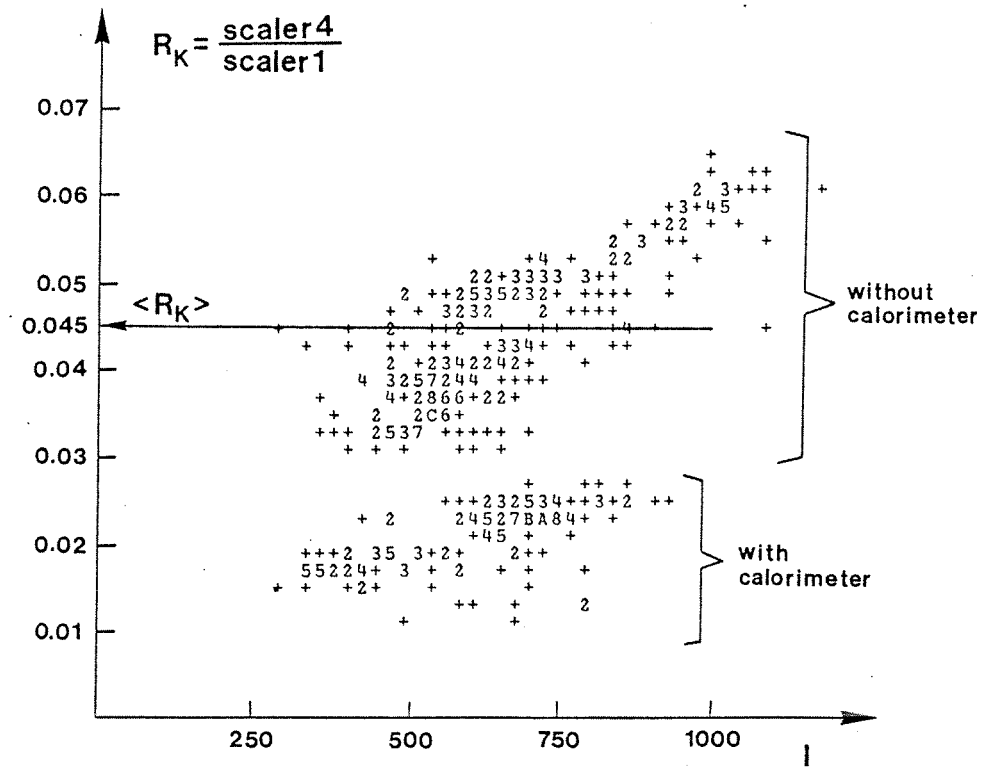

Fig. 5.17.b

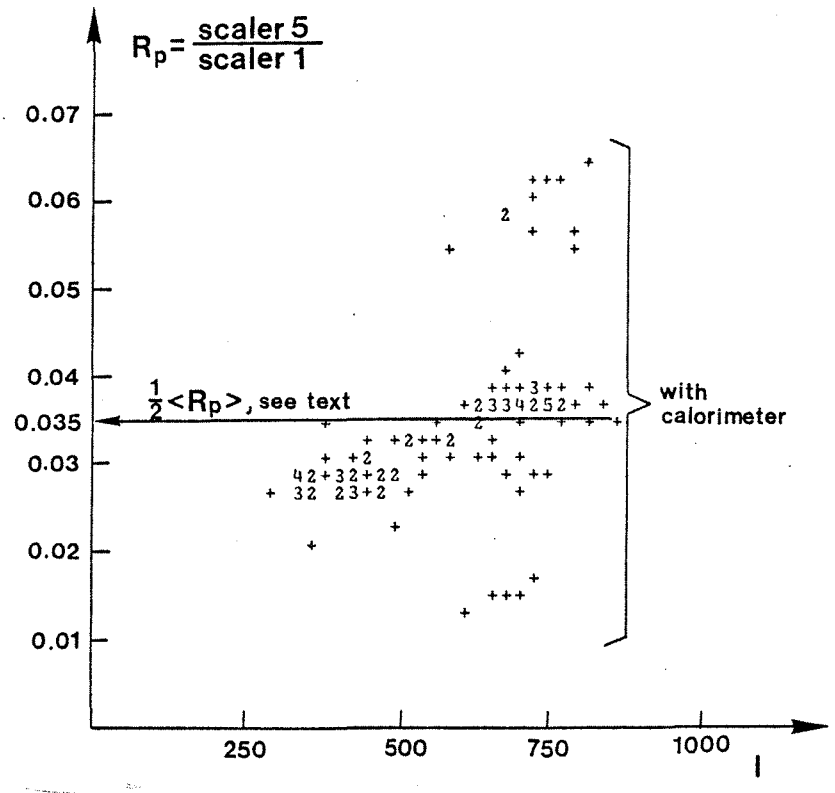

Fig. 5.17.c

Fig. 5.17.a-c. Reductions due to cerenkov and Cedar constraints for the π, K and p trigger. The abscissa is as usual the beam intensity (per burst) and the ordinate, the mean reduction per run. Each entry is based on the data from one whole run. A definition of scalers 1 - 4 is given in Fig. 5.9. For part of the π and K data the calorimeter was effective and for the p data it was always effective. The scatterplots represent more than 95% of our -30 GeV/c data.

b) Introduction of the recoil or the forward calorimeter in the candidate generation of CU1, Fig. 5.9 (⇒ increased reductions).

c) Loosening the multiplicity requirement ⇒ increased multiplicity for the candidates ⇒ the C3 * C4 veto becomes more efficient ⇒ R_π and R_K decrease.

2) The cal.yes signal (forward calorimeter) was switched so that it is input to CU1 instead of to CU2, CU3 and CU4. This lead to a clear increase, a factor 2, in R_π and R_K. The two main structures in Figs. 5.17.a and b are caused by this change in the logic.

3) The essential cerenkov and Cedar parameters were subject to

both volontary and involontary changes. This could be the pressure in the Cedar counters, the electronic threshold for the C1 - C4 counters, the refractive indexes of the same cerenkovs, the readout of both Cedars and cerenkovs etc.

The three relevant reductions are seen to be,

$$< R_\pi > = 0.28, \; < R_K > = 0.045 \text{ and } < R_p > = 2 \times 0.035 = 0.07$$

Here the data with an 'effective calorimeter', meaning that it is input to CU2 and CU3 in Fig. 5.9, have been excluded. To obtain $< R_p >$, the observed mean reduction has been multiplied by a factor 2 so as to be left with only the Cedar reduction. The overall reduction is (in the mean),

$$R_{CER} = < R_\pi > + < R_K > + < R_p > = 0.395$$

There is some overlap between the different trigger types (e.g., if Cedar 2 fires in coincidence with a π-trigger, then both a π and a K-trigger will be generated), but this ovelap is small.

As seen from R_π, the cerenkov constraints do not result in a substantial reduction. The C3 * C4 veto has separately been measured to be responsible for the rejection of 40% of our π and K events. Hence,

$$R_{\overline{C3 * C4}} = 0.6 \text{ and } R_{C1 * C2} = \frac{0.28}{0.6} = 0.47$$

For the K-trigger almost the whole reduction is caused by Cedar 2, while for the p-trigger, Cedar 1 is on its own responsible for the full reduction (at -30 GeV/c). The effect of Cedar 1 therefore, is the same as R_p, $R_{CED1} = R_p = 0.07$. Assuming that the Cedar 2 effect scales with the kaon content in the beam ($f_K = 0.03$ and $f_p = 0.021$, from ref. 8), one may find R_{CED2},

$$R_{CED2} = R_{CED1} \cdot \frac{f_k}{f_p} = 0.1$$

Since $R_K = R_{\overline{C3 * C4}} \cdot R_{C2} \cdot R_{CED2}$, we find

$$R_{C2} = 0.75$$

Conclusions for the 'elastic' fast logic and event logic.

Summing up the reductions in both logics, I shall give results for run number 2978 at -30 GeV/c. The values are representative for the -30 GeV/c data sample.

1) Fast correlation matrices (FM), confere equations (5.1)

$$R_{FM} = \frac{272}{6000} = 0.0453$$

The 6000 figure corresponds to the calculated number of beam induced interactions in the target when 1 icc is incident ($\approx$ 75,000 beam particles). The interaction probability is 0.08. '272' is the measured number of A * B * C * D * E - coincidences (cf. (5.1)) per icc. When this number is slightly smaller than the one given in (5.1) (= 309 per icc), this is most likely due to time fluctuations in the data taking conditions. The '309-rate' was the average throughout run number 2690.

2) The prompt veto (pr.v.) including some of the H1/H2 wedge counters in veto,

$$R_{pr.v.} = 0.021,$$

which is taken from table 5.2.

3) The slow matrices (SM),

$$R_{SM} = 0.4605$$

see Fig. 5.10.

4) The forward calorimeter (CAL) with a -30 mV threshold,

$$R_{CAL} = 0.5$$

which is taken from Fig. 5.15.b.

5) The multiplicity veto (MV),

$$R_{MV} = 0.05364$$

6) The cerenkov requirements (CER),

$$R_{CER} = 0.301$$

This R_{CER} value differs from the one given above (0.395). The reason is that here as opposed to above, we have excluded the the p-trigger.

Unless otherwise is explicitly stated, these reductions come from scalers (like the ones in Fig. 5.9) whose rates are written onto tape after each burst. For run 2978 the average intensity per burst was 604 icc = $4.53 \cdot 10^7$ out of which 8% interact in the target. The starting point therefore is $3.6 \cdot 10^6$ interactions, and we are left with,

$$N_E = R \cdot 3.6 \cdot 10^6 = 126 \text{ events per burst, where}$$

$$R \equiv R_{FM} \cdot R_{pr.v.} \cdot R_{SM} \cdot R_{CAL} \cdot R_{MV} \cdot R_{CER} = 0.0000354$$

N_E is in good agreement with the number of interrupts, N_I, and the average total deadtime per burst, t_D. To see this use equation (5.7). For run 2798 the effective burst duration was t_{be} = 1.026 sec, the number of interrupts N_I = 83.0 burst^{-1} and t_D = 0.316 sec. Solving for N_E (in (5.7)), we find,

$$N_E = \frac{N_I}{1 - t_D/t_{be}} = \frac{83.0}{1 - 0.316/1.026} = 120 \text{ events}$$

The discrepancy between the two N_E - values is probably due to errors in the estimate of t_{be}. Also, overlap between the π and K triggers could be responsible. If $R_{CER} < R_\pi + R_K$, then R is too big and consequently the event rate would be too high. To aid visualize, the development of 10^5 target interactions throughout the logics have been shown in Fig. 5.18. The horizontal scale is logarithmic.

Rates in the logic which defines muon events.

The rates which will be given were typical at -20 GeV/c when muon pair and elastic data were recorded in parallel. With the muon pair event simply defined by the μ-strobe in Fig. 5.3 (= μ-matrix * (H1R * PR1) * (H2R * PR2)), these events would represent 5 - 10% of all events, the elastic dominating with 90 - 95%. Typically the beam would be used in this way,

- $2.5 \cdot 10^7$ beam particles incident per burst.
- $2.0 \cdot 10^6$ target interactions per burst.
- 185 μ-matrix firings per burst.
- 10 μ-matrix * (H1R * PR1) * (H2R * PR2) per burst ($\equiv$ μ-event).
- 3.5 μ-event * C2 * C3 per burst.

- 0.75 μ-event * C1 * C2 * C3 * C4 per burst.

and - 110 elastic events per burst.

Mostly we ran without the cerenkov constraints since this would reduce our small muon pair acceptance even more.

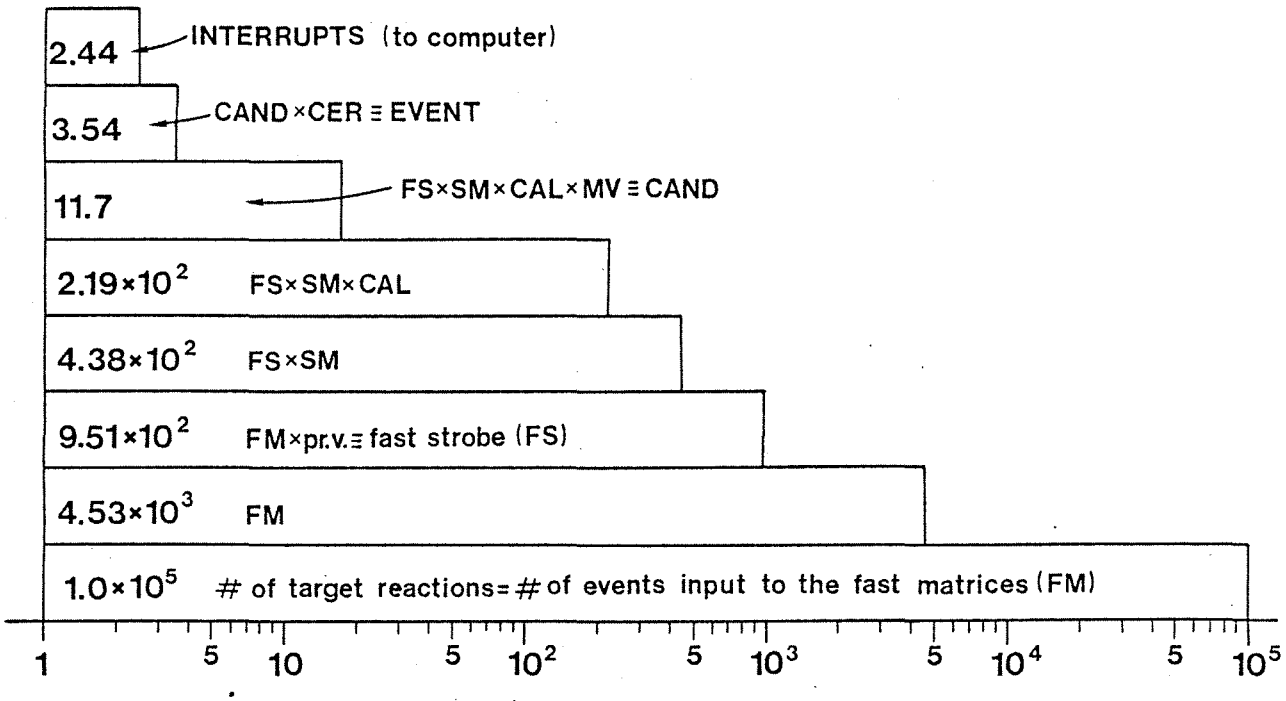

Fig. 5.18

Statistics at the different levels in the logic. 10^5 events are input. At each level is marked the type of test (filtering mechanism) and the corresponding number of accepted events. Notice that the accepted events from one level are input to the next (the one above). This example is from run number 2978 at -30 GeV/c. The last reduction from EVENT to INTERRUPT is due to computer deadtime. Note that 10^5 target interactions corresponds to $10^5 : 0.08 = 1.25 \cdot 10^6$ beam particles incident on the target.

C. References

1. Fast - pulse instrumentation.
LeCroy Research Systems (Catalogue, fall 1977).

2. A hardwired processor for on-line event filtering in an experiment studying 2-body reactions at high momentum transfers.
Ivar Gjerpe (Thesis, Institute of Physics, Univ. of Oslo, March 1981 & ELAS 147, internal WA7-report, CERN Febr. 1981).

3. Results from runs with the fast processor.
I. Gjerpe (ELAS 137, internal WA7-report, CERN 1980).

4. The multiplicity veto (MV) and in particular, the random multiplicity veto (RMV), in the WA7 CERN experiment.
K. Kirsebom (Submitted to Institute of Physics Report Series, Univ. of Oslo, May 1981).

5. The calorimeter cookery book.
K.E. Johansson (ELAS 123 with addendum, internal WA7-report, CERN 1980).

6. Results from +20 GeV/c high-t analysis.
K. Brobakken et al. (ELAS 135, internal WA7-report, CERN 1980).

7. Results from -30 GeV/c high-t analysis.
K. Brobakken et al. (ELAS 136, internal WA7-report, CERN 1980).

8. Summary of the high-t data taking and trigger conditions.
K. Brobakken (ELAS 138, internal WA7-report, CERN 1980).

CHAPTER 6

CERENKOV COUNTERS IN GENERAL AND IN WA7

A. In general

As always the detection of a charged particle is based on some of the energy deposited by the passing particle in the detector medium. In this case the well known cerenkov light is detected. This is produced by all charged particles when their velocity is above the velocity of light in the detector medium. This is a situation which occurs when relativistic particles just below the velocity of light in one medium of propagation (which could be $\approx$ vacuum), suddenly enter a new medium with an index of refraction, n_{medium}, 'sufficiently' above 1. The velocity of light in a medium is given by, $c_{medium} = c_{vacuum}/n_{medium}$. Hence the condition for light emission, $v_{medium} > c_{medium}$, may also be written as,

$$\beta_{medium} = v_{medium}/c_{vacuum} > 1/n_{medium}$$

The angle of emission is given by[1],

$$\cos\vartheta(\lambda) = \frac{1}{\beta\, n(\lambda)} \qquad (6.1)$$

where the angle depends on the wavelenght of the emitted light because n, the refractive index of the light emitting medium, is wavelenght dependent. The intensity of the emitted light is given by[1],

$$\frac{dN_\gamma}{d\nu\, dL} = 2\pi\alpha \frac{z^2}{c} \sin^2\vartheta(\nu) \qquad (6.2)$$

where α is the fine structure constant (≈ 137), ze is the charge of the particle, L the length of the radiating medium and ν, the frequency of the emitted light, $\nu = c_{medium}/\lambda$. Due to the relation between λ, ν and c, (6.2) may also be written this way,

$$\frac{dN_\gamma}{d\lambda\, dL} = 2\pi\alpha z^2 \sin^2\vartheta(\nu) \frac{1}{\lambda^2} \qquad (6.3)$$

For the experimentalist the interesting quantity is the photomultiplier signal, or in other words how much cerenkov light can be made to participate and with what efficiency in the generation of the PM-signal. Here, first the collecting and focussing of the light onto the PM photocathode plays an important role, and afterwards also the PM performances are essential (in particular the quantum efficiency of

the photocathode = the conversion efficiency as a funtion of the wavelength of the incident light). Naturally the lenght of the cerenkov medium (the radiator), is proportional with the PM-signal. As the PM-signal one often uses the number of photoelectrons produced at the cathode, N_e, which is independent of the PM high voltage. The number of photoelectrons per lenght may be found by integrating $dN_\gamma/(d\lambda\, dL)$ multiplied by a weighting function which takes into account both the light transmission and cathode efficiencies. In the wavelength range for which photocathodes are sensitive ($200 < \lambda < 600$ nm), the refractive index varies very little. Hence (by (6.1)), also $\sin^2\vartheta(\lambda)$ is a constant with respect to λ, and without intergrating one sees that the photoelectron yield can be parameterized as follows for unit charge particles,

$$\frac{dN_e}{dL} = A \sin^2\vartheta \qquad (6.4)$$

A is the factor of proportionality which reflects the quality of the optics and the photocathode.

Notice from (6.1) that light is produced as long as $\beta\, n(\lambda) > 1$. For a given value of β, only photons with $\lambda > \lambda_{thr}$ will be emitted. λ_{thr} is defined through, $\beta\, n(\lambda_{thr}) = 1$. Since n varies very slowly with λ, for the photocathode the emission of light or not, corresponds to a sharp velocity threshold. In the threshold region, for a given cerenkov, slightly increasing β will result in λ_{thr} moving across the PM-sensitive spectrum completely (from the red to the violet side).

The detection of cerenkov light is used in two ways,

1) To establish that the velocity β of a particle is above the the threshold velocity β_{thr}, defined by, $\beta_{thr} = 1/n$. This is the simplest way of detection. Used in this way, the detector is called a threshold cerenkov counter.

2) By measurement of the angle of emission ϑ, which only depends on ϑ if n is constant, one can actually determine the particle velocity $\beta = 1/(n\cos\vartheta)$. In this case the detector is a differential cerenkov counter.

B. Cerenkovs in WA7

The Cedars

In Fig. 1.2.a are shown Cedars 1 and 2. These are differential cerenkov counters which may be set so as to detect one specific particle type when the beam momentum is given. For details about the Cedar counters, see refs. 2 and 3. By means of high precision focussing of the emitted cerenkov light, only light at a certain angle will be seen by the 8 PM's. The Cedar is set to fire on a certain particle type by adjusting the gasuous pressure; since n is pressure dependent one may fix the angle of emission so that only particles with a certain velocity will be detected. This again means identifying the particles since the beam is monochromatic.

By means of two Cedars we flagged the two minority beam particles (i.e., kaons and protons). This information were used for three purposes

1) In the event logic. To reduce the rate we demanded a coincident firing from Cedar 1 in the generation of a proton event, and a firing in Cedar 2 for the kaon event, see Fig. 5.9.

2) The hitpattern in the Cedars were recorded for each interrupt. These bitpatterns were used in the off-line analysis. In the case of an elastic event, the bitpattern should be compatible with the expected pattern from an elastic event.

3) The two Cedars were used for monitoring the incident flux of the minority beam particles, this was necessary for the absolute normalization of the cross sections.

The cerenkovs (C1, C2, C3 and C4)

These detectors are located downstream of the target, see Fig. 1.2.b. They are threshold cerenkov counters. A brief description will be given. For details see refs. 4 and 5. The essential parameters are given in the table below.

Knowing the factor of proportionality A, in equation (6.4), and the refractive index (from table 6.1), the yield of photoelectrons may easily be calculated. Inserting (6.1) in (6.4), one

Cerenkov	Radiation length m (L)	Volume m^3	Photomultiplier type	Thresholds (in GeV/c)					
				± 20 GeV/c			- 30 GeV/c		
				π	K	p	π	K	p
C1	4.6	39	RCA 8854	6.0	21.3	40.5	7.3	25.8	54.0
C2	3.4	45	RCA 8854	3.1	11.0	20.8	3.1	10.9	20.2
C3	1.86	17	58 DVP	3.1	11.0	20.8	3.1	11.2	20.7
C4	2.6	31	RCA 8854	4.9	17.3	33.0	3.1	11.1	20.7

Cerenkov	Refractive index; $(n-1) \times 10^6$		Size of reflecting mirrors (cm × cm)
	± 20 GeV/c	- 30 GeV/c	
C1	269	183	70 × 100
C2	1013	1013	80 × 80
C3	1013	1013	80 × 80
C4	405	1013	70 × 100

Table 6.1

Main parameters for the WA7 threshold cerenkov counters. The photomultiplier diameters are 5".

finds,

$$N_e = AL\left(1 - \frac{1}{n^2\,\beta^2}\right) \qquad (6.5)$$

where, $\beta^2 = p^2/(m^2 + p^2)$. $A \approx 100\ cm^{-1}$ for our 4 cerenkovs. A pion with $p = 15$ GeV/c, for example, would produce 21, 66, 36 and 19 photoelectrons in the four cerenkovs respectively (using the refractive indexes of the ± 20 GeV/c beam momentum).

Notice that N_e is a linear function of β. For relativistic energies, $\delta_\beta \equiv 1 - \beta \ll 1$ and $\delta_n \equiv n - 1 \ll 1$, hence from (6.5),

$$N_e = AL\left(1 - (1 - \delta_n)^2(1 + \delta_\beta)^2\right) = AL\left(2\delta_n - 2\delta_\beta\right) = 2AL\left(n + \beta - 2\right)$$

The emitted cerenkov light is reflected from mirrors which are mounted on the downstream walls of the cerenkovs. The dimensions in x and y (rotated 45° for C2) are given in table 6.1. These mirrors

are concave and are focussed onto parabolic mirror cones (Winston cones[6], 35 cm in diameter) surrounding the photocathode of the 5" phototubes. This extra light capturing was necessary because of the rather large angular spread of the cerenkov light; due to the extension of the H_2 - target along z, the elastically scattered particles will hit the cerenkovs with varying angles of incidence.

The treatment of the cerenkov pulses is schematically shown in Fig. 6.1. As for the Cedars, the cerenkov signals are used in

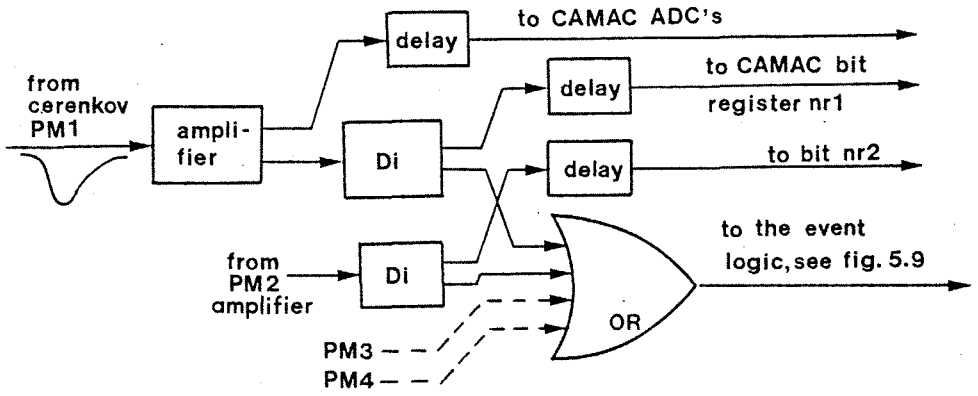

Fig. 6.1

Schematic layout of the cerenkov relevant logic. Information about each mirror firing is both stored analogically (in ADC's) and digitally (bit) in CAMAC. The signal which is used in the event logic, in general is the OR of all mirrors in one cerenkov. The bit-information is gated by the fast strobe and the ADC's are gated by the event logic, actually by the interrupt, see Fig. 5.3.

the event logic, see Fig. 5.9. The stored information again is used in the off-line analysis to identify the outgoing particles. For the forward arm, elastically scattered pions should fire both cerenkovs (C1 and C2), kaons should fire at least C2 and protons should fire none. The cerenkov thresholds were set so that they would match the the momenta defined by our geometrical acceptance. For the recoil arm cerenkovs (C3 and C4), the thresholds were set so that these counters could be used in veto. Therefore the proton momentum threshold should be well above the maximum momentum of a recoiling proton.

Especially for the pion trigger did the cerenkov constraint (we demanded a C1 * C2 - coincidence) matter for the trigger rate reduction, see the final part of chapter 5B.

C. References

1. Cerenkov counter technique in high-energy physics.
J. Litt and R. Meunier (CERN, Geneva 1973).

2. Monitoring of SPS secondary beams.
J.V. Allaby and C. Borel (CERN/Lab. II/EA/74 - 5).

3. The Cedar project (CERN/Lab. II/EA/74 - 4).

4. Cerenkov PM's. Test with wavelength shifters and high voltages.
P. Carlson (ELAS 68, internal WA7-report, CERN 1977).

5. Gases/gas-mixtures for cerenkov counters.
P. Carlson (ELAS 97, internal WA7-report, CERN 1977).

6. Angular dispersion of particles in the cerenkov counter C3 due to the extension of the target.
Jakob Haldorsen (ELAS 87, internal WA7-report, CERN 1976).

APPENDIX 1

Some remarks concerning probability.

Given a random sequence of N identical events (for ex. timewise random) in an interval of length 1, what is the probability for observing m events inside a specified interval x?
Such a sequence might be obtained by 'dropping' the N events one after the other randomly into [0,1], see Fig. A1.1. There are many such event sets of m events inside x and N - m outside. For ex., the first event into x, the second outside, third outside, · · ·, $(N-1)^{th}$ inside and the N^{th} outside.

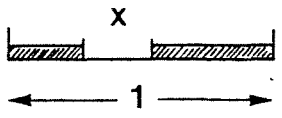

Fig. A1.1

The probability for observing one specified such set is,

$$P_o(x,m) = (1-x)^{N-m}\, x^m$$

How many such, to us indistinguishable, event sets with exactly m events inside and N - m outside, are there?

Assume that absolutely all the N events are distinguishable (it makes sence to talk about the first event, the second, etc., after all the N events have been 'dropped', see above). Then the total number of event sets (with m inside and N - m outside x) is equal to the number of possible configurations of m balls among N distinguishable balls. To find this number of configurations, reason as follows,

At the first pick one may choose between N balls,
at the second pick one may choose between N - 1 balls, etc. and
at the m^{th} pick one may choose between N - m + 1 balls.

This gives a total of $N(N-1)\cdots(N-m+1)$ ways of picking m balls. For each way we are left with m balls (events inside x). However, these m balls will be the same m balls for several ways of picking (the way defined by, the red ball, the blue ball etc., is identical to the one defined by, the blue ball, the red ball etc.). There are many ways of picking to one configuration, this number is easily seen to be, m! Hence the number of configurations of m balls among N (= the number of indistinguishable event sets of m events inside x and N - m outside) is,

$$\frac{N(N-1)\cdots\cdots(N-m+1)}{m!} \equiv \binom{N}{m} = \frac{N!}{(N-m)!\; m!}$$

Therefore the probability of observing an eventset of N events, only specified by having m events inside x, is given by:

$$P(x,m) = (1-x)^{N-m}\, x^m \binom{N}{m} \tag{A1.1}$$

which is only a general term in the polynomian expansion

$$1 = (x + (1-x))^N = \sum_{m=0}^{N} \binom{N}{m} (1-x)^{N-m}\, x^m \tag{A1.2}$$

so that the probability is normalized. With this distribution, what is the average m ($\equiv \bar{m}$) ?

$$\bar{m} \equiv \frac{\sum_{m=0}^{N} m\, P(x,m)}{\sum_{m=0}^{N} P(x,m)} = \sum_{m=0}^{N} m\, P(x,m)$$

By calculating $\partial/\partial x(\sum_{m=0}^{N} P(x,m))$ and setting the result equal to zero, see (A1.2), one finds,

$$\bar{m} = Nx \tag{A1.3}$$

as it should be; on the average, Nx events out of N fall into the x-interval. What happens to P(x,m) when $x \to 0$ and $N \to \infty$? Due to (A1.3), (A1.1) may be written as,

$$P(x,m) = \binom{N}{m}(1-x)^N\, \bar{m}^m\, (1-x)^{-m} \frac{1}{N^m}$$

Since $(1-x)^N \to \exp(-\bar{m})$ when $N \to \infty$,

$$P(x,m) \underset{N \to \infty}{\to} e^{-\bar{m}}\, \bar{m}^m \binom{N}{m} \frac{1}{(N-\bar{m})^m} = \frac{e^{-\bar{m}}\, \bar{m}^m}{m!} \frac{N(N-1)\cdots(N-m+1)}{(N-\bar{m})^m}$$

Here the last factor, $[N(N-1)\cdots(N-m+1)]/[(N-\bar{m})^m] \to 1$ when $N \to \infty$. It may be shown mathematically that the speed of convergence is given by, $\sim m^2/N$. Hence, for $m^2/N \ll 1$,

$$P(\bar{m}/N,m) = \frac{1}{m!}\, e^{-\bar{m}}\, \bar{m}^m \tag{A1.4}$$

which is called the Poisson distribution.

What does this probability actually mean? This is easier to see if one considers the original variables somewhat differently. Let $x \to x_t = L_t x$, where x_t and L_t now are absolute time intervals. The question is still:

What is the probability that m out of N events fall inside x_t, where L_t is the whole time interval accesible? Now let $L_t \to \infty$ and $N \to \infty$ in such a way that, $N/L_t = \bar{m}$. m is then the mean number of events in a unit time interval [t,t+1]. Since $x_t = xL_t$, $L_t = N/\bar{m}$ and $\bar{m} = Nx \Rightarrow x_t = 1$. When $L_t \to \infty$, $x \to 0$. It is therefore more instructive to rewrite the poisson expression of (A1.4) as,

$$P_{\bar{m}}(m) = \frac{1}{\bar{m}!} e^{-\bar{m}} \bar{m}^m \qquad \text{(A1.5)}$$

which now has got a clear interpretation,

> If an infinit number of events are spread out randomely in $0 \leq t \leq \infty$ with density $\bar{m}$, then $P_{\bar{m}}(m)$ is the probability that in any [t,t+1] one observes m events.

How can one arrive at the Poisson distribution directly when assuming $N = \infty$, and that all the events are spread out randomly over an infinite interval with density $\bar{m}$?

Let us consider the probability of not observing an event, P_o. The change in probability, dP_o, in a short time interval dt, is proportional to $-\bar{m}$, to dt and also to P_o.

$$dP_o = -\bar{m}\, dt\, P_o \quad \Rightarrow \quad P_o = Ce^{-\bar{m}t}$$

where $C = 1$ because the probability should be 1 for $t = 0$.

$$\bar{t} = \frac{\int_0^\infty te^{-\bar{m}t}\, dt}{\int_0^\infty e^{-\bar{m}t}\, dt} = \frac{1}{\bar{m}}$$

So we see that with this distribution there is a mean time difference, $\bar{t} = 1/\bar{m}$, between events, which corresponds to an event density of $\bar{m}$. The probability for observing one or more particles after a time t is given by,

$$1 - P_o(t) = 1 - e^{-mt} \equiv P_{N_E > 1}(t)$$

This probability can also be written as

$$e^{-\bar{m}t}(e^{\bar{m}t} - 1) = e^{-\bar{m}t} \sum_{m=1}^{\infty} \frac{\bar{m}^m t^m}{m!}$$

It is easy to show that one can identify each term, $e^{-\bar{m}t}\frac{\bar{m}^m t^m}{m!}$, in the sum as the probability of observing m and only m events in the time interval [0,t]. I shall show how one can do this for m = 1. Let this probability be P_1. In Fig. A1.2 is shown an example of one single event occuring in [0,t]. The probability of observing this event is equal to,

$$P_0(t')\,dt'\,\bar{m}\,P_0(t-t') = e^{-\bar{m}t'}e^{-\bar{m}t+\bar{m}t'}dt'\,\bar{m}$$
$$= e^{-\bar{m}t}\,\bar{m}\,dt' \qquad (A1.6)$$

$P_0(t')$ is the probability of non-observation in [0,t'], $dt'\,\bar{m}$ is the probability of observation in [t',t'+dt'], this term is the sum of the first two terms in the Taylor expansion of $P_{N_E\geq 1}$ around 0 which is correct since dt' is infinitesimal, and finally $P_0(t-t')$ is the probability of non-observation in [t'+dt',t]. P_1 is found by integrating (A1.6),

$$P_1 = \bar{m}\,e^{-\bar{m}t}\int_0^t dt' = \bar{m}\,t\,e^{-\bar{m}t} \qquad \text{qed}$$

The probabilities, P_N, N > 1, may be found in an analog way.

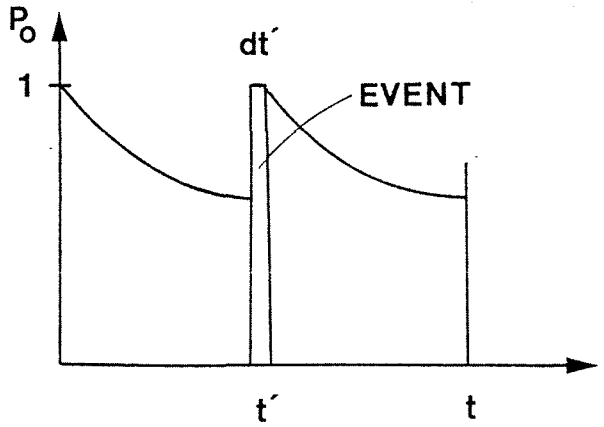

Fig. A1.2

P_0 is the probability of a non-observation of an event after a certain time. At t' an event occurs and P_0 starts from 1 again.

APPENDIX 2

About deadtimes

Varying deadtime for the observed events.

The title will become clear as the subject is developed.
What is the total deadtime of N events, each having a deadtime t_d, during a time τ? The events are randomly spread out over $-\infty < t < \infty$ with an average density of N/τ.

First, let $N/\tau = 2$. The average livetime-fraction with only one event in $[0,\tau]$, is $(\tau - t_d)/\tau = 1 - t_d/\tau$. Let $t_d/\tau \equiv x$. So the average livetime overlap fraction between two such single event intervals, will be $(1-x)^2$, and its duration $\tau(1-x)^2$ which is equal to the livetime overlap for A + B in Fig. A2.1. In the same way the average deadtime overlap will be τx^2, and

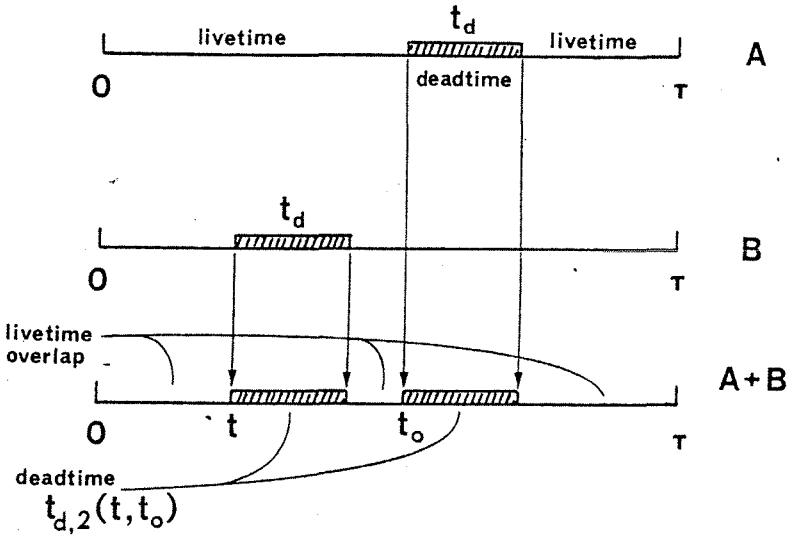

Fig. A2.1

Simple example of how the livetimes and deadtimes add when two events are incident on $[0,\tau]$. Notice that the resulting livetime (for A + B) = the livetime overlap, however the deadtime overlap is not the resulting deadtime, this overlap is defined by the average coincidence time between the two events.

hence the average deadtime, $2t_d - \tau x^2$, which is the total deadtime for A + B in Fig. A2.1. To calculate this, define $t_{d,2}(t,t_o)$ to be the deadtime of the two events at t and t_o in $[0,\tau]$. $\overline{t_{d,2}}$ is simply found by intergrating,

$$\overline{t_{d,2}} = \frac{1}{\tau}\int_0^{\tau} t_{d,2}(t,t_o)dt = 2t_d - \tau x^2$$

For a density of N/τ we will find the average livetime overlap to be,

$$\bar{L} = \tau(1-x)^N \qquad \text{(A2.1)}$$

and the average deadtime

$$\overline{t_{d,N}} = \tau - \bar{L} = \tau(1-(1-x)^N) \qquad \text{(A2.2a)}$$

In the following the bars indicating averages, are dropped. We may find the average deadtime directly. In general,

$$t_{d,N} = t_d + t_{d,N-1} - xt_{d,N-1} \qquad \text{(A2.2b)}$$

which simply says that the deadtime with a density N/τ, is equal to the sum of the deadtimes with densities $(N-1)/\tau$ and $1/\tau$, minus the overlap between these two deadtimes. Let us show that (A2.2b) implies (A2.2a).

$$t_{d,1} \equiv t_d = \tau x = \tau(1-(1-x))$$

$$t_{d,2} = t_{d,1} + t_{d,1} - xt_{d,1} = \tau(1-(1-x)^2)$$

$$t_{d,3} = t_{d,1} + t_{d,2} - xt_{d,2} = \tau(1-(1-x)^3)$$

by use of the recurrence formula (A2.2b). Assume that

$$t_{d,N} = t_{d,1} + t_{d,N-1} - xt_{d,N-1} = \tau(1-(1-x)^N)$$

then

$$\begin{aligned} t_{d,N+1} &= t_{d,1} + t_{d,N} - xt_{d,N} \\ &= \tau(x + (1-(1-x)^N) - x(1-(1-x)^N)) \\ &= \tau(1-(1-x)^N + x(1-x)^N) \\ &= \tau(1-(1-x)^{N+1}) \end{aligned}$$

So by induction we have found the correct expression for the average deadtime, $t_{d,N}$.

Since $L = \tau(1-x)^N$, the mean number of <u>observed</u> events will be,

$$N_o = N(1-x)^N \qquad \text{(A2.3)}$$

I shall comment on this conclusion. We know that all the N events are poisson distributed (see appendix 1), hence one may calculated the mean time distance between events. Knowing the total livetime overlap, one

may find the number of individual livetimes = number of events (if $N \gg 1$). This is apparant from Fig. A2.2. We shall calculate $\overline{l_n}$ in two ways.

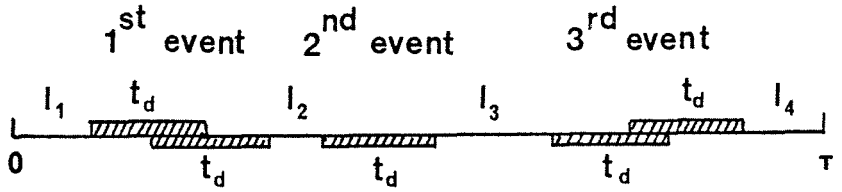

Fig. A2.2

The relation between individual livetimes and events is exemplified.

By definition of the mean value, $\overline{l_n} = L/N_0$.
Having <u>had</u> one event whatever its length, in the time development, what is the probability of a non-observation during a time t after the end of the event? It is shown in appendix 1 that this probability is given by,

$$P_0(t) = e^{-\bar{m}t} = \exp(-\frac{N}{\tau}t)$$

The mean length of having had no event, is τ/N (one must calculate, $(\int_0^\infty tP_0dt)/(\int_0^\infty P_0dt)$). Hence we have found, $\overline{l_n} = L/N_0 = \tau/N$, and making use of (A2.1); $N_0 = LN/\tau = N(1-x)^N$.

The average duration of each event will be

$$t_{d,R} = \frac{t_{d,N}}{N_0} = \frac{\tau(1-(1-x)^N)}{N(1-x)^N} = \frac{\tau}{N(1-x)^N} - \frac{\tau}{N} \qquad \text{(R for real)}$$

Now $(1-x)^N = \exp(N\ln(1-x)) \approx \exp(-Nx)$ since $x \ll 1$, inserting this in (A2.2) and (A2.3), we find,

$$t_{d,R} = \frac{\tau}{N}(e^{Nx}-1) = t_d \qquad \text{for } Nx \ll 1 \qquad \text{(A2.4)}$$

$$= \frac{\tau}{N}(Nx + \tfrac{1}{2}(Nx)^2) = \tau x(1 + \tfrac{1}{2}Nx)$$

$$= t_d(1 + \tfrac{1}{2}Nx) \text{ for } (Nx)^2 \ll 1 \qquad \text{(A2.5)}$$

We can also find the number of lost events,

$$N - N_0 = N - N(1-x)^N = N(1 - e^{-Nx}) \qquad \text{for } x \ll 1$$

$$= N(Nx - \tfrac{1}{2}(Nx)^2 + \cdots) \qquad \text{(A2.6)}$$

Notice that due to the exponential approximation of $(1-x)^N$, the number of observed events depends in this way on N,

$$N_o = Ne^{-Nx} \tag{A2.7}$$

hence, in the first approximation,

$$N = \frac{1 - \sqrt{1 - 4N_o x}}{2x} \tag{A2.8}$$

Structures in the eventrate (= some 'unrandomness').

How would an eventual structure in the eventrate influence N_o? In this case the intensity is a function of time, $I = I(t)$. With pulsed accelerators this is always the case. The observed number of events in a short time interval dt in $[0,\tau]$, during which I may be considered constant, can be written as,

$$dN_o = I_o(t)dt = I(t)dt\left(1 - \frac{t_d}{dt}\right)^{I(t)dt} = I(t)dt\exp[I(t)dt\ln(1 - \frac{t_d}{dt})]$$

in analogy with (A2.3). If, $t_d \ll dt$, that is, the individual deadtime t_d, should be much smaller than the typical periods of the I-variations, then,

$$dN_o = I(t)dt\exp[-I(t)t_d]$$

and if $I(t)t_d \ll 1$,

$$dN_o = I(t)(1 - I(t)t_d)dt \qquad \text{and,}$$

$$N_o = \int_0^\tau I(t)dt - t_d\int_0^\tau I^2(t)dt = N - t_d\int_0^\tau I^2(t)dt$$

$$= N\left(1 - \frac{t_d}{\tau}N\tau[\int_0^\tau I^2(t)dt]/N^2\right) = N(1 - NxD^{-1}) \tag{A2.9}$$

where,

$$D \equiv \frac{\left(\frac{1}{\tau}\int_0^\tau I(t)dt\right)^2}{\frac{1}{\tau}\int_0^\tau I^2(t)dt} = \frac{\bar{I}^2}{\overline{I^2}}$$

D is called the duty cycle. The fraction Nx is the normal unbiased reduction we get in the number of events due to the deadtime (assuming $(Nx)^2 \ll 1$), see (A2.6). However, this may increase with structure in the eventrate, how much is given by D. The reason for calling it the duty cycle, is that we

may consider this beam with varying intensity as a bursted one with constant intensity during a period $D\tau$, and zero intensity during the rest, $\tau(1-D)$.

Let us turn to the more general case when t_d is not necessarily much smaller than dt, the period of constant I. Assume that the losses due to deadtime only come from events with length t_d. The chances of one event (as defined in Fig. A2.2) being made up of 3 or more true events in such a way that the total event length exceeds $2t_d$, are so small that these contributions to N_{le} $(= N - N_o)$, may be disregarded. The event loss for t in [t,t+dt] can then be expressed as,

$$dN_{le} = I(t)dt \int_{t}^{t+t_d} I(t')dt'$$

Which may be understood in this way. I(t)dt is the actual number of events in [t,t+dt], obviously dN_{le} is proportional to this, and the integral from t to $t+t_d$ of I is equal to the number of lost events if there is exactly one event in [t,t+dt]. To find all N_{le} one should intergrate,

$$N_{le} = \int_0^{\tau} dN_{le} = \int_0^{\tau} I(t)dt \int_0^{t+t_d} I(t')dt' \qquad \text{(A2.10)}$$

To be able to go further with this one should make a Fourrier expansion of I(t) over τ,

$$I(t) = \sum_{n=-\infty}^{\infty} c_n e^{in\omega t} \qquad \text{where } \omega = 2\pi/\tau$$

This will not be done here. It would bear out that the main contribution to D comes from the effect already calculated $(= \bar{I}^2/\overline{I^2})$. Additional small effects which may be as well positive as negative, will appear if n, the frequency, is close to the frequency defined by τ/t_d. In particular, when $n \approx \frac{1}{2}\tau/t_d$, $n \approx \tau/t_d$ or $n \approx 2\tau/t_d$, will some effect be noticable. The more the factor of proportionality differs from 1, the more this special effect diminishes in importance. Notice that this whole argument assumes that the c_n's in question, contribute to I(t).

This situation of deadtimes is typical for updating registration. For example in MWPC's (multi wire proportional chambers), may a chamber wire be

retriggered long before the output pulse is finished. The chamber inherent deadtime is small compared to the pulse durations. Hence two real events may look like one. The same is true for scintillation counters where two pulses, close in time, will trigger both the PM and the discriminator twice (if the discriminator is updating). But since the second pulse triggers during the output cycle of the previous pulse, only one pulse leaves the discriminator. A scaler for ex., which is supposed to monitor the flux through the scintillator, therefore will count once instead of twice. The deadtime that we have calculated is the one which the scaler will see.

Now we shall look at the situation with fixed deadtimes per event, non-updating.

Fixed deadtime for the observed events

This simply means that the total deadtime is given by,

$$\tau_d = N_o t_d$$

where N_o is the number of observed events and t_d is the deadtime per event. If the events arrive randomly, how many events have been lost due to τ_d? $N_{le} = N - N_o$. Let τ be the the period during which the events arrive. Then,

$$N_{le} = N - N_o = N \frac{\tau_d}{\tau} = N \frac{N_o t_d}{\tau}$$

From this we find,

$$N_o = \frac{N}{1 + kN} \quad \text{and} \quad N = \frac{N_o}{1 - kN_o} \quad \text{where} \quad k = \frac{t_d}{\tau} \qquad \text{(A2.11)}$$

What happens in this case if the events no more arrive randomly? In analogy with the case considered above, we find the number of observed events in a small time interval dt, in which the event intensity I(t), is constant. Then,

$$dN_o = \frac{I(t)dt}{1 + kI(t)dt} \qquad \text{where } k = \frac{t_d}{dt}$$

hence if $I(t)t_d \ll 1$,

$$dN_o = I(t)\,(1 - I(t)t_d)dt$$

Integrating we again find,

$$N_o = N(1 - NxD^{-1}) \qquad \text{where } D = \bar{I}^2/\overline{I^2} \quad \text{and} \quad x = t_d/\tau \qquad \text{(A2.12)}$$

We have assumed that $I(t)t_d << 1$. This implies, $Nx = Nt_d/\tau = I(t)t_d << 1$. Therefore, if D^{-1} is not very different from 1, we may write (A2.12) as,

$$N_o = \frac{1}{1 + \frac{t_d}{\tau \cdot D} N} \qquad (A2.13)$$

Therefore τD may be considered as the effective period during which events arrive.

Calculation of the dutycycle parameter D in WA7.

I have calculated the parameters, D and τD, for all the data taking runs at -30 GeV/c incident beam momentum. The distributions for the parameters, are shown in Figs. A2.3.a and b. Here will be given a brief description of the method used.

As event signal is used the actual WA7 event (candidate) generated by the 'elastic' logic, see Fig. 5.3. An observed event, therefore, corresponds an interrupt. The deadtime imposed for each interrupt in principle is fixed (it may vary, but this is not due to updating). Solving in (A2.13) for D, remembering that $\tau_d = N_o t_d$, we find,

$$D = \frac{\tau_d}{\tau(1 - \frac{N_o}{N})} \qquad (A2.14)$$

The ratio N_o/N, is measured indirectly by means of the beamhodoscopes, which monitor the beam flux. Scalers which did the actual counting, were gated in two ways:

1) By the livetime 2 (see Fig. 5.3) which corresponds to the time during which the experiment was ready for a new event. This would be symbolized by the l_i - intervals in Fig. A2.2, had all the events been of equal length.

2) By the burstgate. Corresponds to τ in the notation above. The burstgate was considerably longer than the actual particle spill, $\tau \approx 2$ seconds and the spill, ≈ 1.3 seconds.

For a whole data taking run, let the number of beam monitor counts be C_L and C_B, when the beam hodoscope scalers are gated in the first and second way respectively. Since C_L/C_B represents the fraction of the incident beam particles for which the logic has been ready to accept an

event, we may set,

$$\frac{C_L}{C_B} = \frac{N_o}{N}$$

Also gated in the same ways, was a clock (giving time) which therefore measured τ and $\tau_L \equiv \tau - \tau_b$. Hence by means of the 4 accumulated scalers, C_L, C_B, $CLOCK_L$ and $CLOCK_B$, the results of which were recorded on tape, the WA7 dutycycle parameter was calculated,

$$D_{WA7} = \frac{1 - \frac{\tau_L}{\tau}}{1 - \frac{N_o}{N}} = \frac{1 - \frac{CLOCK_L}{CLOCK_B}}{1 - \frac{C_L}{C_B}}$$

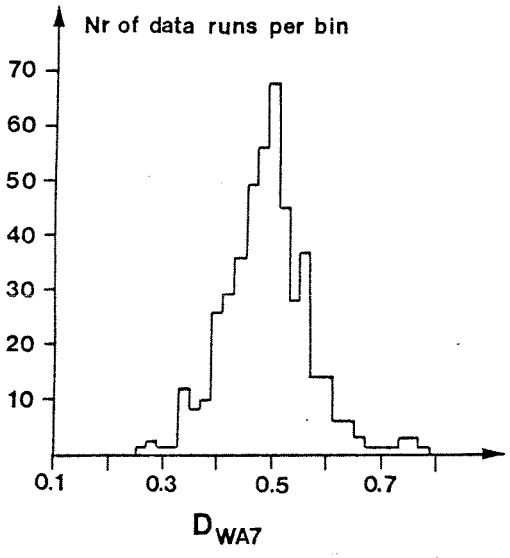

Fig. A2.3.a

The WA7 dutycycle parameter distribution, the binwidth is 0.02.

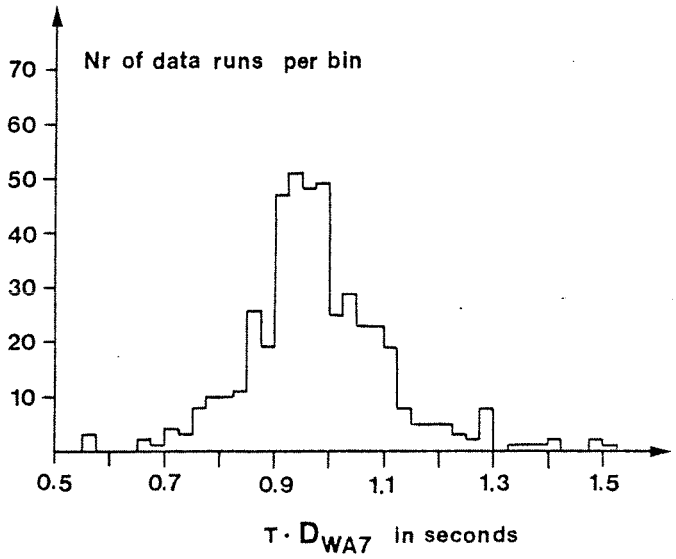

Fig. A2.3.b

The effective spill duration distribution. The binwidth is 0.025 seconds.

APPENDIX 3

Accidentals

This notion refers to accidental coincidences, mostly between scintillator signals which are treated in a decision making logic.

Given that one signal (1) arrives with a rate I_1, and has a mean width t_1, and that another signal (2) arrives with a rate I_2 and has a mean width t_2, what is then the accidental rate of (1)*(2)? The signal-(1) stream, timewise covers $t_1 I_1$ of [0,1]. For each (2)-signal, the probability of a coincidence is $(t_1 + t_2) I_1$. Hence the number of coincidences; $(t_1 + t_2) I_1 I_2$. This is correct only as long as $(t_1 I_1)^2$ and $(t_2 I_2)^2 \ll 1$, see appendix 2. It is also assumed that the timeoverlap between (1) and (2) which is sufficient for the coincidence unit to produce an output, is zero. Actually this minimum overlap t_m, ranges from 1 to 5 ns. Taking into account this effect one finds,

$$R_{12} = (t_1 + t_2 - 2t_m) I_1 I_2 \qquad \text{(A3.1)}$$

for the accidental coincidence rate. Assume for simplicity that these $2t_m$ are included either in t_1 or t_2. What is the mean width of such an accidental coincidence? By considering Fig. A3.1 one sees that, given such a coincidence, the mean duration of the time overlap is,

$$\overline{O(t_r)} = \left(\frac{t_2 - t_1 + (t_1 + t_2)}{2} t_1\right) \Big/ (t_1 + t_2) = \frac{t_1 t_2}{t_1 + t_2}$$

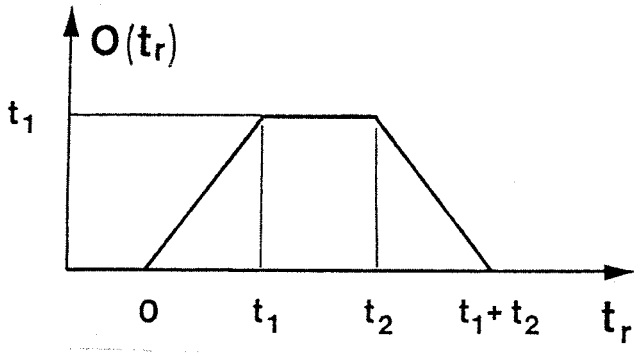

Fig. A3.1

$O(t_r)$ is the time overlap between signals (1) and (2) as a function of their relative position on the time scale. Notice that,

$$t_1 \leq t_2.$$

So one accidental coincidence rate may be considered as a single random rate with,

$$t_{12} = \frac{t_1 t_2}{t_1 + t_2} \quad \text{and} \quad R_{12} = (t_1 + t_2) I_1 I_2 \qquad \text{(A3.2)}$$

Therefore the accidental rate between three or more signals is easily calculated,

$$t_{123} = \frac{t_{12}\, t_3}{t_{12} + t_3} = \frac{t_1 t_2 t_3}{t_1 t_2 + t_1 t_3 + t_2 t_3}$$

and $$R_{123} = (t_{12} + t_3) I_{12} I_3 = (t_{12} + t_3) R_{12} I_3$$

$$= (t_1 t_2 + t_1 t_3 + t_2 t_3) I_1 I_2 I_3$$

by insertion of t_{12} and R_{12} from (A3.2).

APPENDIX 4

Calculating the 'rejection' of calorimeters.

First about 'rejection'. As we have seen in chapter 4B, a hadron hitting a calorimeter produces a shower which deposits some of its energy as light in scintillators. Let Q be the charge of the signal sent off by the scintillation counters and σ_Q, the r.m.s. deviation of the Q-distribution. Both σ_Q and Q_{mean} (the mean charge produced) are energy dependent,

$$Q_{mean} \sim E \tag{A4.1}$$

and

$$\sigma_{Q,R} \equiv \frac{\sigma_Q}{Q_{mean}} \sim E^{-\frac{1}{2}} \tag{A4.2}$$

Therefore, introducing a certain signal requirement, Q_{cut}, so as to discriminate between particles (hadrons) of different energies, one will accept more particles - a larger part of the distribution - the higher the energy. The 'rejection' is then defined as,

$$R(E) = \frac{\int_0^{Q_{cut}} I(Q,E)dQ}{\int_0^{\infty} I(Q,E)dQ} \tag{A4.3}$$

where I(Q,E) is the Q- or charge-distribution.

In the following I shall outline how the R(E) curves of Figs. A4.4.a and b were obtained. The data used are from ref. 10, chapter 4. The results to be presented are valid for sandwich calorimeters measuring the shower every 10 cm of iron. 100% shower containment is assumed in the calculations. To be able to use the rejection curves, the absolute energy calibration must be known, that is, one must know the coefficient in (A4.1) for the detector in question.

By fitting I(Q,E)-data points with poisson distributions, Barish et al. (ref. 10, chapt. 4) obtained σ_Q and Q_{mean}. These were then shown to follow nicely the energy dependencies expressed in (A4.1) and (A4.2). A detailed parameterization of $\sigma_{Q,R}$ and Q_{mean} will be given below. The resulting functions are inserted in I, hence also the Q-distribution is parameterized

for all values of (Q,E) or (Q,Q_{mean}), see (A4.6) and (A4.8). This allows to determine $R_{Q_{cut}}(E)$ as a continuous function of E and Q_{cut}.

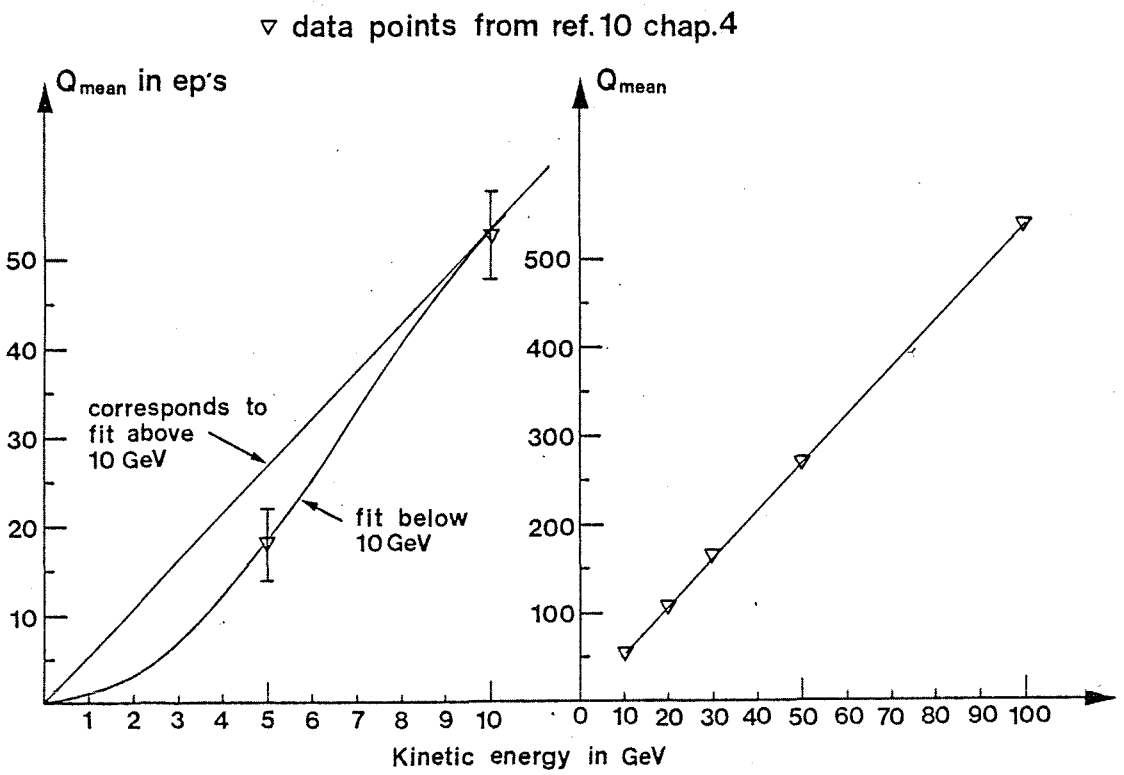

Fig. A4.1

Energy dependence of Q_{mean}, the mean signal produced by the calorimeter described in ref. 10, chapt. 4. The triangles represent their data points, the fully drawn curve, the fit used here.

Q_{mean} and σ_Q were fitted in the following way,

$$Q_{mean}(E) = e_{11}E + e_{12}E^2 \qquad 0 \leq E \leq 5 \text{ GeV}$$

$$Q_{mean}(E) = e_{21}E + e_{22}E^2 + e_{23}E^3 \qquad 5 \leq E \leq 10 \text{ GeV} \qquad \text{(A4.4)}$$

$$Q_{mean}(E) = e_{31}E \qquad E \geq 10 \text{ GeV}$$

where,

e_{11} = 0.22 ep/GeV, e_{12} = 0.684 ep/GeV^2, e_{21} = -1.49 ep/GeV
e_{22} = 1.37 ep/GeV^2, e_{23} = -0.0684 ep/GeV^3 and e_{31} = 5.35 ep/GeV.

E is given in GeV's and Q in ep's (for a definition of 1 ep, see chapter 4B). The non linear fit below 10 GeV was motivated by a small deviation from the straight line of the 5 GeV data point, see Fig. A4.1. Next to the

fitting of σ_Q. $\sigma_{Q,R}(E) \equiv \sigma_Q(E)/Q_{mean}$, the measured relative resolution may be represented by,

$$\sigma_{Q,R}(E) = e^{a_1+a_2\,y(x(E))} \qquad \text{(A4.5)}$$

where,

$$x(E) = b_1+b_2\,\ln E \quad (E \text{ in GeV})$$

and,

$$y(x) = \begin{cases} x_{11}+x_{12}x & 0 \le E \le 5 \text{ GeV} \\ x_{21}+x_{22}x+x_{23}x^2+x_{24}x^3 & 5 \le E \le 20 \text{ GeV} \\ x_{31}+x_{32}x & E \ge 20 \text{ GeV} \end{cases}$$

a_1=-4.605, a_2=0.2765
b_1=-5.79, b_2=3.597
x_{11}=13.2, x_{12}=-0.2137,
x_{21}=13.2, x_{22}=-0.1114,
x_{23}=-0.0428, x_{24}=6.16×10^{-4},
x_{31}=14.116, x_{32}=-0.4932

First the x-coefficients were obtained graphically from Fig. A4.2 (using the same linear scale along both axis), then the transformation to the $(\sigma_{Q,R},E)$-coordinate system was performed (by means of a_1, a_2, b_1 and b_2). Again the non-linear fit (on the log-log scale) between 5 and 20 GeV was motivated by the behaviour of the data in this energy range. However, the extrapolation is less certain for $\sigma_{Q,R}$ than for Q_{mean}. $Q_{mean}(E=0) = 0$, and there-

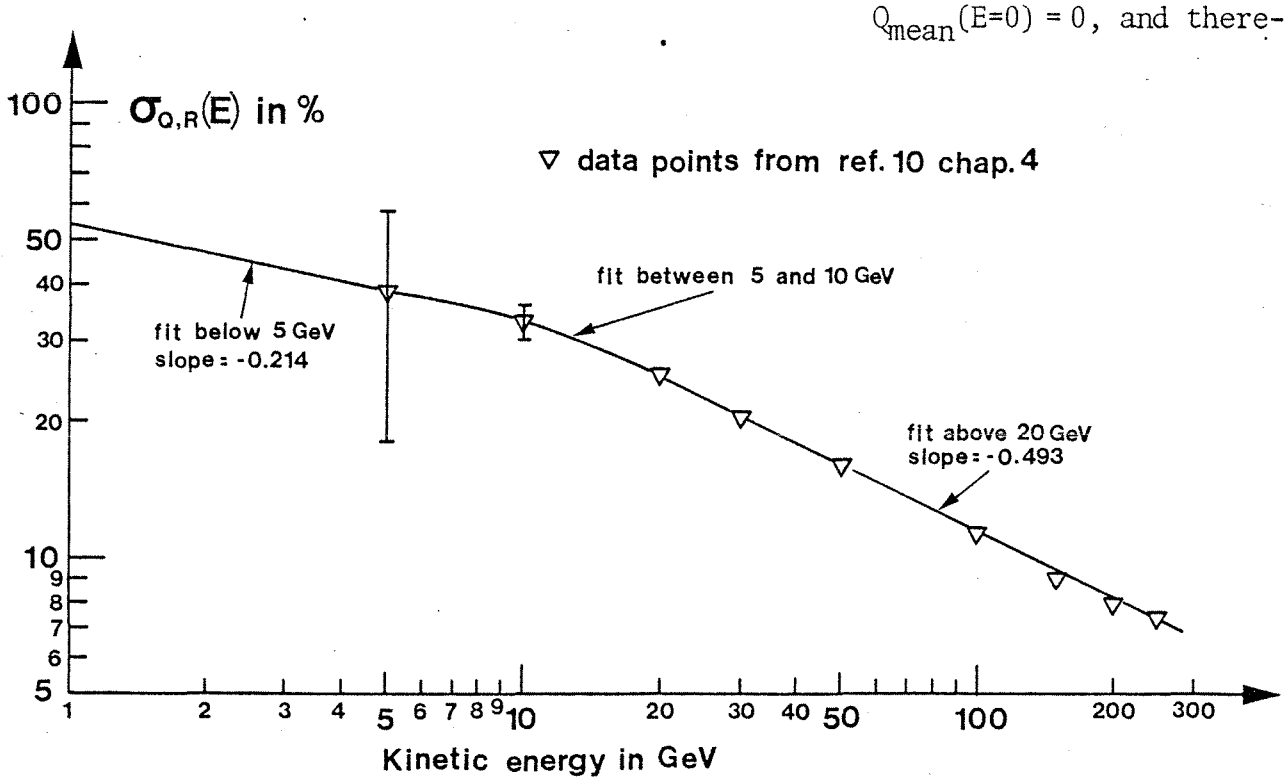

Fig. A4.2

Energy dependence of $\sigma_{Q,R}$, the relative signal- or energy-resolution. Again the data are measurements from ref. 10, chapt. 4. The graph shows the used fit. Slopes are given in units of 100%.

fore $Q_{mean}(E)$ is fitted rather well between 0 and 10 GeV. For $\sigma_{Q,R}$, a linear continuation was chosen (see Fig. A4.2), its gradient is equal to the mean gradient of $\sigma_{Q,R}$ between 5 and 20 GeV. This is more a reasonable guess. Therefore the calculations for energies less than 4 - 5 GeV should only be considered qualitatively. At such low energies the fluctuations are so big that the energy information most often is uninteresting*, however, knowledge of the resolution is useful for carrying out estimates like the ones performed here.

Notice that the straight line, $y(x) = x_{31} + x_{32}x$, corresponds to the familiar, $\sigma_{Q,R} \sim E^{-\frac{1}{2}}$. This relation reflects the statistical nature of hadron showers. It would be extremely difficult to calculate $\sigma_{Q,R}(E)$ directly, such a shower being a very complex phenomenum which involves all kinds of interactions (hadron - nuclei, hadron - hadron, lepton-interactions, annihilations, decays, etc.; both electromagnetic and strong forces play important roles) from some MeV up to the incident hadron energy. Therefore to estimate the shower fluctuations (not only for the total shower, but also in each point of the shower), one avoids the calculative problems by simulating showers with computers, see refs. 20 and 21, chapt. 4. The showers are generated randomly, however, in such a way that, 1), some criteria are fulfilled at each vertex (= interaction point), such as energy and momentum conservation and 2), cross sections involved (total, absorption and differential cross sections and branching ratios) are reproduced if the number of generated showers is sufficient to give significant statistics. For energies below 5 GeV, the multiplicities are low, also the hadron - nuclei cross sections are more energy dependent than at higher energies (ref. 22, chapt. 4) and production channels may be blocked because of too low energy, all these factors will influence the resolution and actually a continuation of the $E^{-\frac{1}{2}}$ behaviour below 5 GeV, would be surprising.

Having fitted $\sigma_{Q,R}$ and Q_{mean}, one can now obtain a continuous expression for I. In general,

$$I(n,\bar{n}) = \frac{e^{-\bar{n}}\bar{n}^n}{n!} \qquad (A4.6)$$

where $\bar{n}$ is the mean value of the I-distribution, and n is the variable,

---

* One can measure the momentum (or energy) with much higher precisions using magnets (the bending in a known magnetic field is directly related to the particle momentum).

n and $\bar{n}$ should be considered as continuous variables. The denominator is trivially continued in between integer values of n. n! may be replaced by the Γ - function, $n! = \Gamma(n+1)$, which is the standard mathematical continuation of the faculty function. There is no explicit analytical expression for Γ, but it can be approximated very well by the Stirling formula,

$$\Gamma(x) = x^x e^{-x} \frac{\sqrt{2\pi x}}{x}\left(1 + \frac{1}{12x} + \frac{1}{288x^2} + O(x^{-3})\right) \qquad (A4.7)$$

Q and Q_{mean} have to be scaled properly before being entered into $I(n,\bar{n})$. The r.m.s. deviation of I is given by, $\sigma_I = \sqrt{\bar{n}}$, and therefore $\sigma_{I,R} = \sigma_I/\bar{n} = \bar{n}^{-\frac{1}{2}}$. Let $\bar{n} = kQ_{mean}$, then the requirement,

$$\sigma_{I,R} = \sigma_{Q,R} \quad \text{fixes k:}$$

$$\sigma_{I,R} = (kQ_{mean})^{-\frac{1}{2}} = \sigma_{Q,R}$$

$$\Rightarrow \quad k = [\sigma_{Q,R}{}^2 \cdot Q_{mean}]^{-1}$$

therefore

$$\bar{n}(E) = \bar{n}(Q_{mean}) = \frac{1}{\sigma_{Q,R}{}^2} \quad \text{and} \quad n(E,Q) = \frac{Q}{\sigma_{Q,R}{}^2 \cdot Q_{mean}} \qquad (A4.8)$$

which inserted in (A4.6) yields the desired function I(Q,E). To calculate R(E) numerically is now only a question of fortran programming. The results are presented in Figs. A4.4.a and b. R(E) is shown for values of Q_{cut} ranging from 3 ep to 500 ep.

Notice that the cut becomes relatively sharper with increasing energy. Fixing Q_{cut}, then an overlap O_V, at a certain energy $\bar{E}$ which is such that $R_{Q_{cut}}(\bar{E}) = 0.50$, may be defined as,

$$O_V(\bar{E}) \equiv \frac{E(R=0.9) - E(R=0.1)}{\bar{E}} \qquad (A4.9)$$

O_V is the relative energy range that corresponds to going from 90% to 10% rejection. Defined this way the energy dependence of O_V is shown in Fig. A4.3. Actually there is a paradoxal increase in O_V as $\bar{E}$ increases up to 10 GeV. This is due to the fact that O_V not only depends on $\sigma_{Q,R}$, but also on how Q_{mean} develops. With the parameterization used below 10 GeV, the E-dependence is faster than linear (see (A4.4)); this more than compensates for the decrease in O_V which one would expect due to the

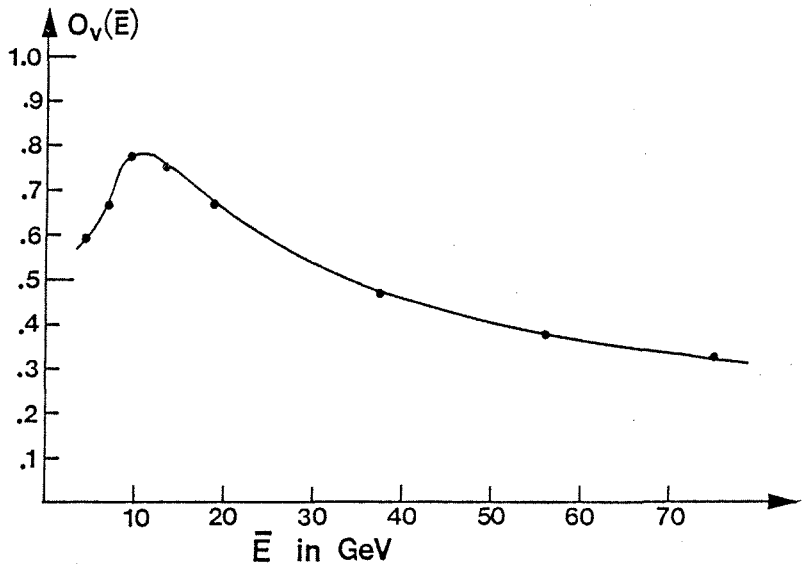

Fig. A4.3
Energy dependence of the overlap function O_V, defined in the text.

improved resolution at higher energies.

On the next page are shown the rejection curves for a full containment sandwich (iron/scintillator) calorimeter which is sampled every 10 cm.

Reduced containment rejection

As explained in chapter 4F, the WA7 forward arm calorimeter is being extended so that there will be 5 sampling planes. It would therefore be interesting to obtain the rejection, $^{R}Q_{cut}(E)$, for this somewhat reduced configuration (the 5 planes will occupy the 5 most upstream slots in the calorimeter).

As in the above case, to perform the calculations, $I_M(Q,E)$, the modified charge distribution, must be known. To find I_M, I shall assume that it may also be fitted by a poisson distribution which depends on $\sigma_{Q,R,M}$ and $Q_{mean,M}$ (the modified relative resolution and modified average calorimeter signal, respectively) in the same way as above, see (A4.8). This should be a rather good assumption; integrating the distributions of Fig. 4.10 appropriately, one obtains the containment fraction f(E), shown in Fig. A4.5, which simply tells how big a fraction of the total shower is sampled by the first 5 planes. It is seen that the maximum lost fraction at the very highest energies, is one third. Due to the relatively small signal lost at the back with this reduced calorimeter, it seems reasonable to assume that

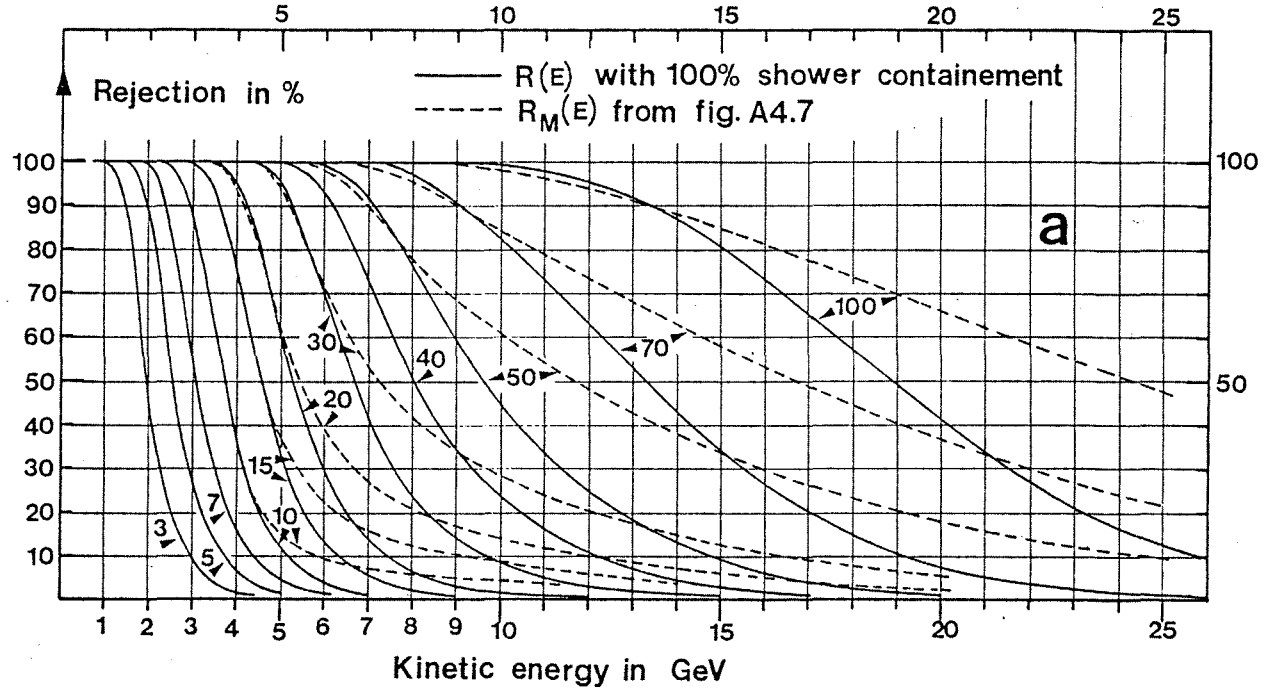

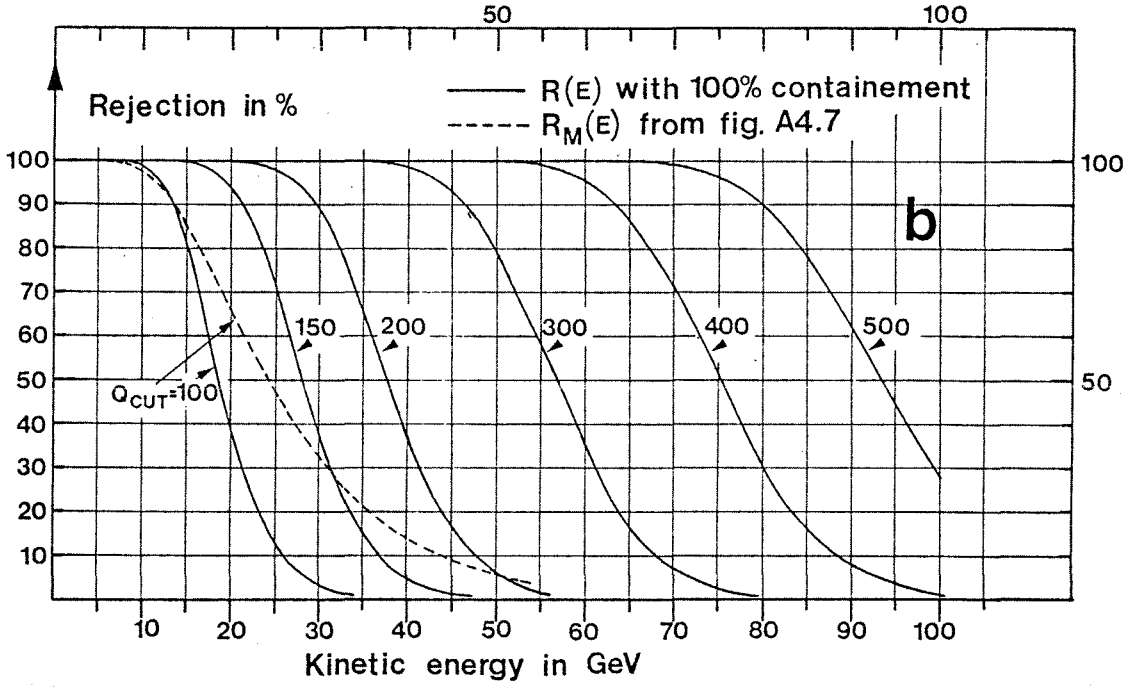

Figs. A4.4.a and b

Energy dependence of R, the fraction of the signal spectrum one would have cut away by imposing that the calorimeter signal should be above a certain threshold, Q_{cut}, which is given in units of ep. The calculation is described in the text. Also shown (as the dashed curves), the rejection one would have had with the reduced configuration (5 scintillator planes only), transferred from Fig. A4.7. Notice the very much longer tails of these curves, and also that the effect of R_M being less than R, becomes more pronounced with higher energy.

I_M is distributed according to (A4.6). The relation below defines f(E),

$$Q_{mean,M} = f(E) \cdot Q_{mean}(E) \qquad (A4.10)$$

The parameterization of f(E) is discussed later. While these results were based on data from ref. 10, chapt. 4, $\sigma_{Q,R,M}$ will be found from shower simulations performed by Sciulli and collobrators (ref. 11 chapt. 4). They calculated $\sigma_{Q,R}$ as a function of f(E), keeping E fixed. Their results are shown in Fig. A4.6; along the vertical axis, F, the resolution with 100% containement devided by the resolution one has with f containment and along the horizontal axis, the variable, 1 - f, which is the lost fraction. These shower simulation results should be ok; the computer program reproduces well existing data on longitudinal containment (that is, the lenght of iron needed to contain a certain fraction of the energy deposited by the shower), also this program predicts satisfactorily F as a function of the number of sampling planes (at 200 GeV, see the quoted reference). The fits to F(1-f,E) is done at the end of this section.

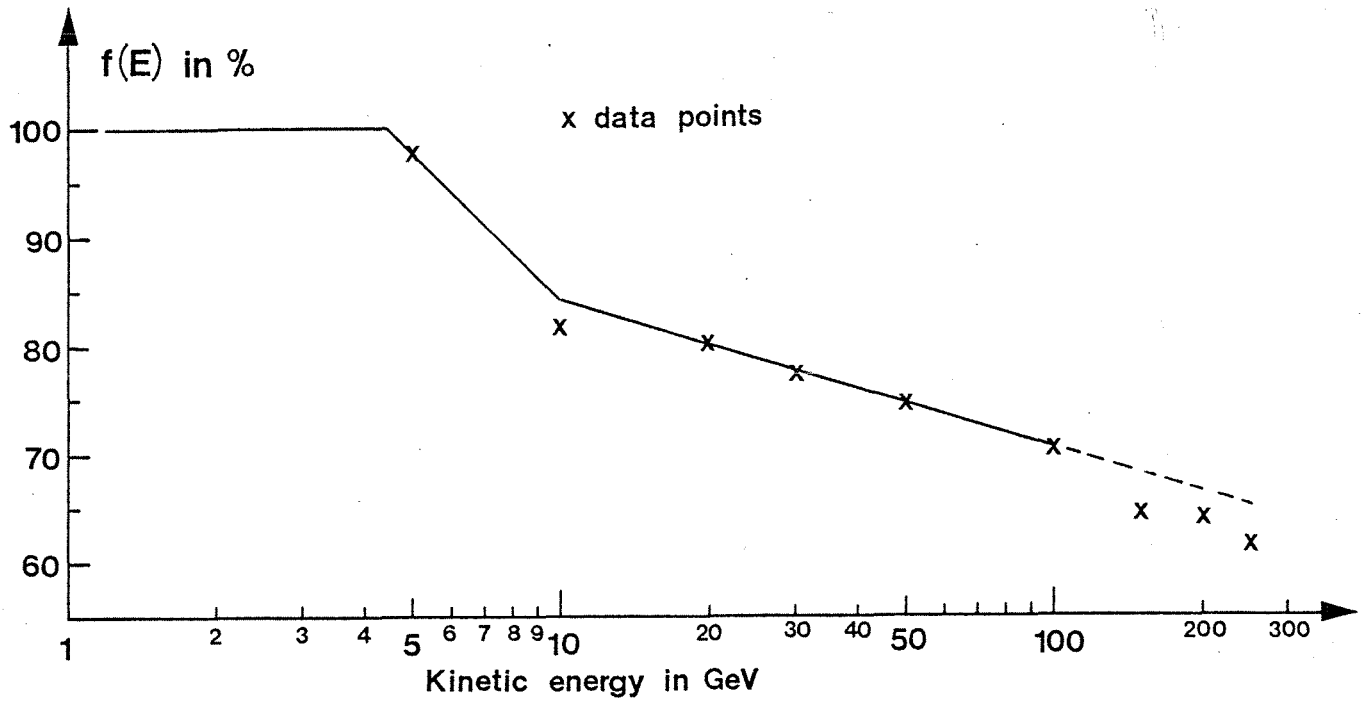

Fig. A4.5

Energy dependence of f, the fraction of the mean total signal (= Q_{mean}) which is sampled by the first 5 scintillator planes, see (A4.10). Crosses are data points, the three straight line sections, the fits used. Integration was only performed up to about 50 GeV, therefore a best fit to data points below 100 GeV was chosen.

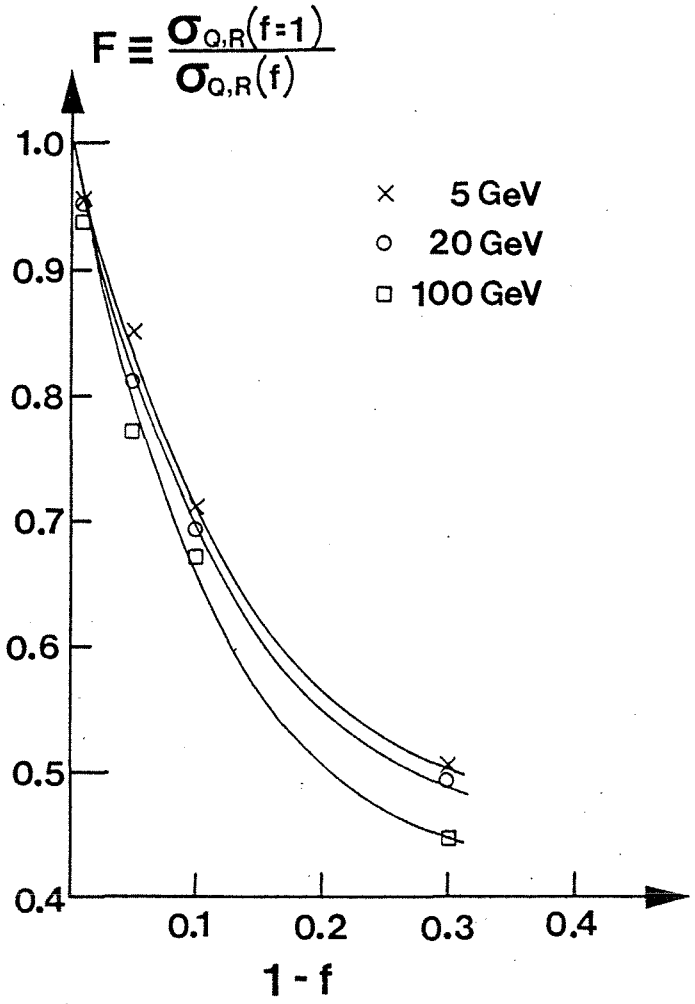

Fig. A4.6

×, ○ and □ points are taken from ref. 11 chapt. 4 and represent the calculated increase in the resolution due to an average non-containment of 1-f. Notice that,

1) the resolution is very sensitive to f, and
2) for fixed f, the resolution worsens with increasing energy. The fully drawn lines shows the fits used to calculate $R_M(E)$, i.e., the rejection when $f < 1$.

Since f is only a function of E, the relative resolution with reduced containment is,

$$\sigma_{Q,R,M}(E) = \frac{\sigma_{Q,R}(E)}{F(E)} \qquad (A4.11)$$

Inserting $Q_{mean,M}$ and $\sigma_{Q,R,M}$ (instead of Q_{mean} and $\sigma_{Q,R}$) in (A4.8), one obtains the modified charge distribution $I_M(Q,E)$. Integrating this function according to (A4.3), one finds $R_M(E)$, shown in Fig. A4.7. Q_{cut} ranges from 3 to 100 ep. For comparison, some of the $R_M(E)$ curves have also been plotted in Figs. A4.4.a and b. Obviously, for the same value of E and Q_{cut}, R_M should be bigger than R; this is generally seen to be the case.

However, as E increases and parts of the I(Q,E) distribution starts to lie above Q_{cut}, the opposite is observed, namely $R_M < R$. This could be explained by the incorrectness of assuming I_M to be poisson-distributed. When R_M and R starts to decrease, it is the large signals in the upper

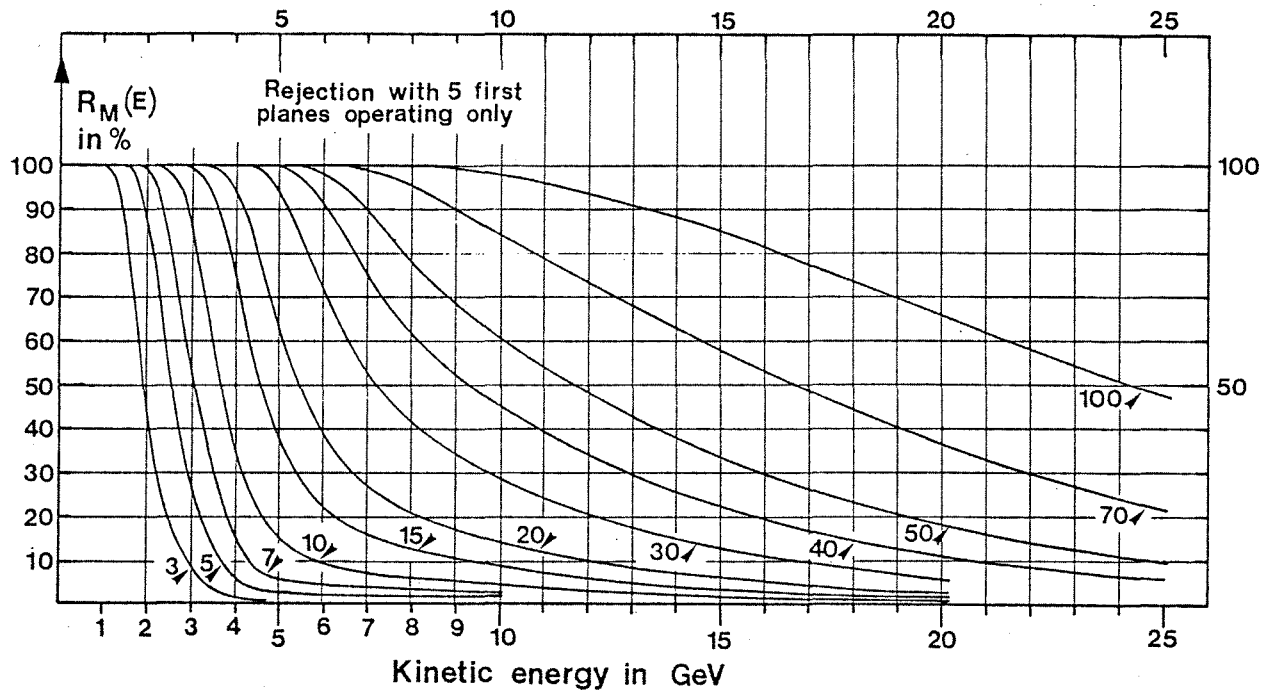

Fig. A4.7

The rejection R_M that a 5-plane calorimeter would introduce as a function of the incident hadron energy for various values of Q_{cut} between 3 and 100 ep. Notice that R_M approaches 0 much slower than R, meaning that Q_{cut} must be fixed lower, otherwise the rejection becomes inacceptable at the higher energies.

tail of the distribution which is responsible. Even if $Q_{mean,M} < Q_{mean}$, this sinks the upper tail of I_M less than what it is enhanced by $\sigma_{Q,R,M}$. That the poisson distribution gives a too big tail, is confirmed by remarking that the deviation effect becomes more pronounced with energy. This is to be expected since reducing the configuration of scintillator planes will more affect the big signals than the smaller ones. Remember that the center of gravity for a hadron shower is located at a thickness $\sim \ln(kE)$ of the stopping material, see ref. 12 chapt. 4. Hence, the higher the energy, the more important the 'non-poisson-distributed' fraction of the shower signal. But the agreement between R_M and R for the lower values of E, is fairly good. To do better, one would need more precise knowledge of $I_M(Q,E)$, preferably from direct measurements.

There is one important conclusion to be made. Comparing R and R_M at 10 GeV, we see that by imposing a 30 ep threshold, one would in the first

case cut away (loose) only 8% of the 10 GeV particles, in the second case this figure is almost 30%. To continue: If one accepts a 8% loss, then with a reduced configuration, one would have to lower Q_{cut} to 15 ep, and furthermore, a 15 ep cut with a full containment calorimeter, implies a loss of only 0.5%. These figures are rather surprising remembering that at 10 GeV one has $\approx 85\%$ containment. The reason is evident, considering Fig. A4.6 one sees that for 1-f = 0.15, the resolution nearly doubles compared with the resolution at 1 - f = 0. Therefore I_M extends to much lower values of Q than I.

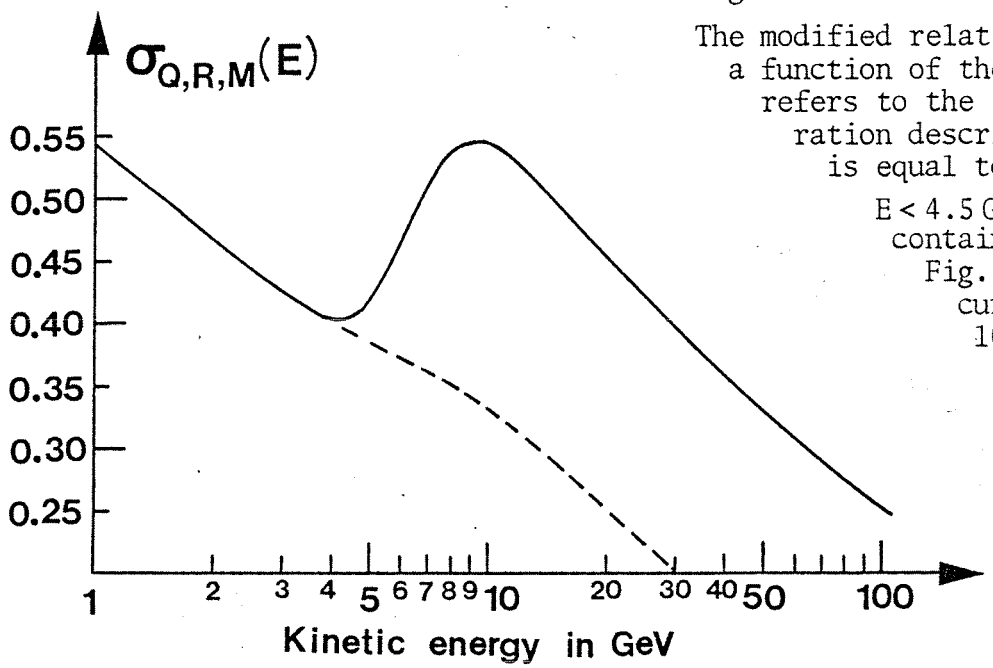

Fig. A4.8
The modified relative resolution as a function of the energy. 'Modified' refers to the 5-plane configuration described above. $\sigma_{Q,R,M}$ is equal to $\sigma_{Q,R}$ for E < 4.5 GeV, because here the containment is 100%, see Fig. A4.5. The dashed curve corresponds to 100% containment.

From (A4.11) and the fitting of F and f at the end of this appendix,

$$\sigma_{Q,R,M}(E) = \sigma_{Q,R}(E) \cdot [F(E)]^{-1}$$

$$= \sigma_{Q,R} \exp\left(a(E)\cdot[1-f(E)] + b(E)\cdot[1-f(E)]^2\right) \qquad \text{(A4.12)}$$

where $\sigma_{Q,R}$ is given by (A4.5), a(E) by (A.15.a), b(E) by (A4.15.b) and f(E) by (A4.13). The resulting $\sigma_{Q,R,M}$ is shown in Fig. A4.8. Notice that the resolution increases for $5 < E < 10$ GeV; there are two competing effects which yield $\sigma_{Q,R,M}$, the decreasing $\sigma_{Q,R}$ and the increasing t (= 1 - f). As we shall see, $a > 0$ and $b < 0$ for all E, and from Fig. A4.6

one sees that t increases with E. Therefore, for the lower values of E, the resolution will be dominated by the exponential term (reflecting the increase in non-containment). For the higher energies, the negative b will slow down the energy dependence of the exponent, hence $\sigma_{Q,R}$ again becomes the dominating. Remark also that the total variation of $\sigma_{Q,R,M}$ is relatively modest, corresponding to a factor 2 between 1 and 100 GeV, for $\sigma_{Q,R}$ this variation is a factor 5.

Fitting of f(E) and F(1-f,E).
f(E) is shown in Fig. A4.5, the abscissa being logarithmic in E. f is defined separately for three energy intervals,

$$f(E) = \begin{cases} 1 & 0 \le E \le 4.5\ \text{GeV} \\ f_{21}+f_{22}\,x_2(E) & 4.5 \le E \le 10\ \text{GeV} \\ f_{31}+f_{32}\,x_3(E) & 10 \le E \le 100\ \text{GeV} \end{cases} \qquad \text{(A4.13)}$$

where $x_i(E)=x_{i1}+x_{i2}\,\ln E$, E in GeV's. The constants are the following, $f_{21}=1.0$, $f_{22}=-0.0551$, $f_{31}=0.8425$, $f_{32}=-0.01528$, $x_{21}=-5.86$, $x_{22}=3.902$, $x_{31}=-8.98$ and $x_{32}=x_{22}$.

We have seen that F is a function of E and t, where $t \equiv 1-f$. First the t-dependence of F was fitted. This was done for several values of E, see Fig. A4.6. F was parameterized as,

$$F(t) = e^{-(at+bt^2)} \qquad \text{(A4.14)}$$

where (unfortunately) a and b are slowly varying functions of E,

$$a(x_a(E)) = \begin{cases} a_{11} & 0 \le E \le 5\ \text{GeV} \\ a_{21}+a_{22}(x_a(E))^2 & 5 \le E \le 100\ \text{GeV} \end{cases} \qquad \text{(A4.15.a)}$$

$$b(x_b(E)) = \begin{cases} b_{11} & 0 \le E \le 5\ \text{GeV} \\ b_{21}+b_{22}(x_b(E))^2 & 5 \le E \le 100\ \text{GeV} \end{cases} \qquad \text{(A4.15.b)}$$

where, $x_a(E)=x_{a1}+x_{a2}\,\ln E$ and $x_b(E)=x_{b1}+x_{b2}\,\ln E$ and the constants, $a_{11}=a_{21}=4$, $a_{22}=0.006575$, $b_{11}=b_{21}=-5.7$, $b_{22}=-0.012784$, $x_{a1}=x_{b1}=-6.28$ and $x_{a2}=x_{b2}=3.902$.

APPENDIX 5

Estimating the average current in a calorimeter PM with maximum beam energy (= 92 GeV).

This has been done by means of the LeCroy 3001 charge analycer, see the first part of chapter 4E. The L3001 can be started by three different kinds of pulses. 1), by an external gate 2), by an external trigger pulse (in which case the L3001 internally generates a gate, the length of which is set by the user) and 3), the L3001 is started by the pulse which is also input to the integrator, in this case the start is given when the level at the integrator input fluctuates sufficiently, the fluctuation threshold (range, -1 to -15 mV) as well as the width of the internally generated gate, are both set by the user. Triggering on the PM-signals with a -1 mV, we obtained the total spectrum of Fig. A5.1. The idea is then to extract the beam dependent part of this spectrum. As the measurements were done, we don't have an absolute time-calibration of these. However, the counting rates above different thresholds have been determined, these rates were normalized to the beam intensity, see Fig. 4.32. Therefore,

[continued next page]

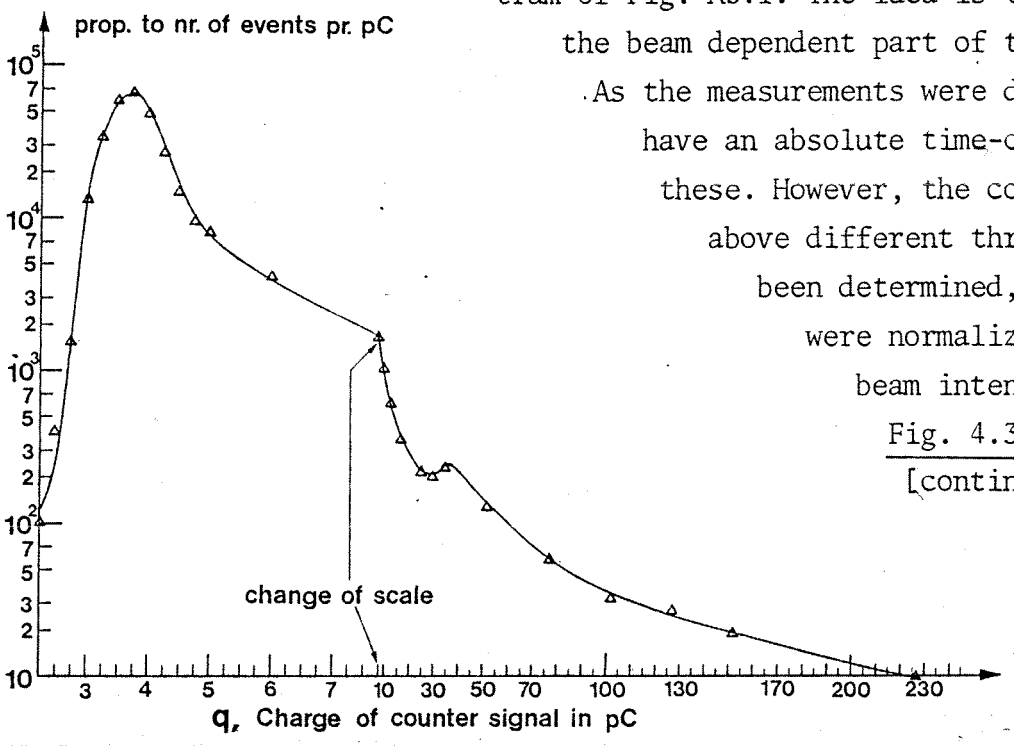

Fig. A5.1

Total spectrum of counter 18 in L1 (see chapt. 4A). The internal gatewidth was set to 100 ns and the fluctuation threshold to -1 mV. Along the x-axis is the charge of the signal in pC, along the y-axis, the number of events within a certain chargebin ($q_0 < q < q_0+\Delta q_0$). The spectrum was accumulated with beam, it therefore extends to high values for q. Contributions to the spectrum come from, 1), particle induced signals 2), PM-noise and 3), pickup noise. The big left peak corresponds to 2) and 3). The small peak at q = 34.5pC is caused by relativistic minimum ionizing particles. Notice the break in scale for q = 7.75pC. 0 pC is the position of the pedestal when a random 100 ns wide gate is applied to the L3001, PM high voltage off.

integrating the beam dependent spectrum above -30 mV (the cutoff sets in at 9.5 pC and is fully efficient at 6.5 pC, see Fig. 4.35), we could determine the normalization constant for Fig. A5.2.

Below is shown a blow up of the pedestal spectrum of Fig. A5.1, also shown is the equivalent spectrum obtained when triggering in between bursts

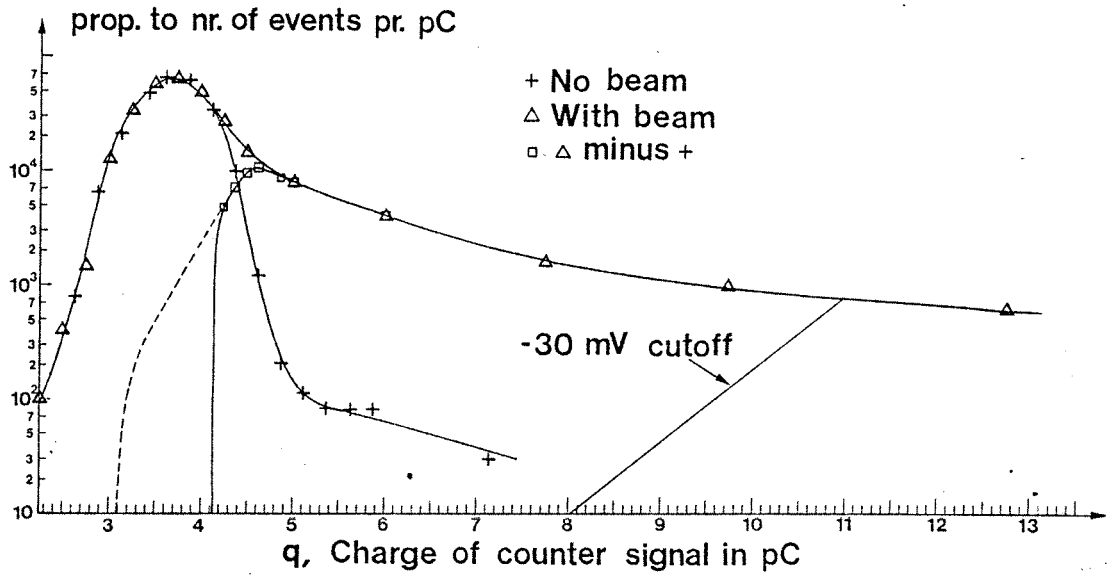

Fig. A5.2

Pedestal spectrum with beam (△ - points) and without (+ - points) for counter 18 in L1. The zero of the abscissa is fixed as explained in the text to Fig. A5.1. The difference between the two curves (□ - points) is defined as the beam induced signal. The number of entries above the -30 mV threshold is 45% of the total. Notice that the corresponding q-values quoted in the text (6.5 and 9.5 pC), seem to disagree with this figure; the -30 mV cutoff charges are here referred to the 'PM HV off' dc-level, while the quoted charges are referred to the 'PM HV on' dc-level (taken from Fig. 4.35), this explains the discrepancy. See the discussion later in the appendix about the significance of the different pedestals. In the same place will also be explained why the dashed curve might be a better continuation below 4.25 pC. The fully drawn curve has been used for the current calculation, however, either curve could be used; the intensity at the very lowest q-values doesn't affect the integrated current significantly, see (A5.2).

only. The curves are normalized in such a way that they have the same maximum. Besides, the difference curve (used for the current calculations) and the effect of the -30 mV cutoff are shown. Performing the intergration of the difference spectrum of Fig. A5.2, we obtained 161,850 for the total and 72,709 for the part above -30 mV (with the indicated normalization).

Notice that the counter 18 in L1 counts 512.7 per burst and per ionization chamber count (≡ icc/c) above -30 mV. This is running with a -92 GeV/c beam, the element 18 is located 40 cm inside the iron in the z-direction, and the center at 31 cm inside in the x-direction, the deflected beam passes 104 cm away from the iron in the x-direction, see Fig. 4.1. Assuming a burst duration of 1.3 second and a calibration of the ionization chamber equal to one count per 75,000 beam particles, with a beam of 10^7 burst^{-1}, the counting rate of counter 18 above -30 mV will be,

$$\frac{10^7 \cdot 512.7}{1.3 \cdot 75{,}000}\ s^{-1} = 5.26 \times 10^4\ s^{-1} \qquad (A5.1)$$

Therefore the normalization factor is $(5.26 \times 10^4)/72{,}709 = 0.723$. I.e., adjusting the vertical scale of Figs. A5.2 and A5.2 by a factor 0.723, one will obtain the absolute values per second with 10^7 per burst incident.

Let I_{diff} denote the normalized difference spectrum, then the average beam dependent current is found by calculating,

$$\int_{1.5}^{\infty} (q - 1.5)\ I_{diff}(q)\, dq = 2.98 \times 10^6\ pC\ s^{-1} = 2.98\ \mu A \qquad (A5.2)$$

One should start the integration in the channel which corresponds to the pedestal obtained when the PM HV (the photomultiplier high voltage) is <u>on</u>. This is due to the fact that the PM analog signal sits on top of a dc-level which is dependent on the PM HV, see Fig. 4.19. The shift in the pedestal position is 1.5 pC when the PM HV is switched on, whence the lower limit of the integral in (A5.2).

In the normal setup which we used for the calorimeter electronics (see Fig. 4.23), the anode signal is split twice in two. So the anode ac-current for counter 18 is $4 \times 2.98\ \mu A = 11.9\ \mu A$. Notice that this current depends both on the location of the counter (see Fig. 4.2) and on the PM HV.

The above measurements were done with a voltage so that, 1 ep = 20 pC. (the signal of one minimum ionizing particle). It is more intersting to find a parameterization that gives the current as a function of the beam intensity, I_b, the counter number, i, and the PM HV. To do this, three assumptions will be made,

1) The anode current increases linearly with I_b. This is a good assumption as long as the beam halo is unimportant.

2) The charge spectra for all counters are equal in shape. This is correct if every counter is calibrated in the same way and in addition the momentum spectrum of the calorimeter incident particles is x-independent. The validity of this last point will be discussed in a moment. However, since counter 18 is second closest to the beam, its charge spectrum will include more high momentum 'particles' than the other counters. Hence, basing the current evaluation on counter 18, will yield an upper limit for the currents in the other anodes (except for c.17).

3) The calibration is linear for all signals, adjusting the PM HV will affect the PM amplification factor in the same way for small as well as big light flashes on the PM photocathode. Normally this is a good assumption.

Using (A5.1) and (A5.2), we may find the anode current per count above -30 mV,

$$i_{ac} = \frac{4 \times 2.98 \times 10^6 \text{ pA}}{5.26 \times 10^4 \text{ count}} = 227 \frac{\text{pA}}{\text{count}}$$

To get the dependence on the beam intensity, let, $f_i \equiv [N_i(I_B)]/I_B$, where $N_i(I_B) \equiv$ the counting rate of counter i per burst (above -30 mV). According to assumption 1), f_i does not depend on I_B. Notice that it does depend on the beam momentum, but for all our measurement this was constant at -92 GeV/c. The anode current for element i can now be calculated,

$$I_{ac,i} \leq f_i \frac{I_B}{1.3} \times 227 \text{ pA} = f_i I_B \times 175 \text{ pA} \qquad (A5.3)$$

where I_B must be given in 'ionization chamber counts' if f_i is taken directly from Fig. 4.32. The inequality signe is due to the remark made in assumption 2).

Actually Fig. 4.32 displays indirectly this variation in the mean signal and hence also in the current, for some counters in L1. From this, one may deduce the curves of Fig. A5.3 which give a good idea about the shape of the different charge spectra. Along the abscissa, the pulseheight ph (in -mV), along the ordinate, the counting rate density normalized to

counter 18, R(i,ph), defined in the text below Fig. A5.3. Notice first the peak which is a feature of the 5 curves. It may be attributed to the difficulty in using the ionization chamber measured beam flux as the common reference for the counting rates. Since an important fraction of the particles traversing the calorimeter scintillation counters are halo muons whose intensity only to some extent depends on the beam, a clear one-to-one correspondance between the scintillator and ionization chamber counts, does not exist. Hence the halo flux may fluctuate without this being monitored by the ionization chamber. It is supposed that this has actually happened to the data in Fig. A5.3. This is possible because $f_{18}(ph)$ (along the ordinate in Fig. 4.32), was not measured at the same time as $f_{17}(ph)$, $f_{21}(ph)$, $f_{25}(ph)$, $f_{29}(ph)$ and $f_{32}(ph)$. The peak position

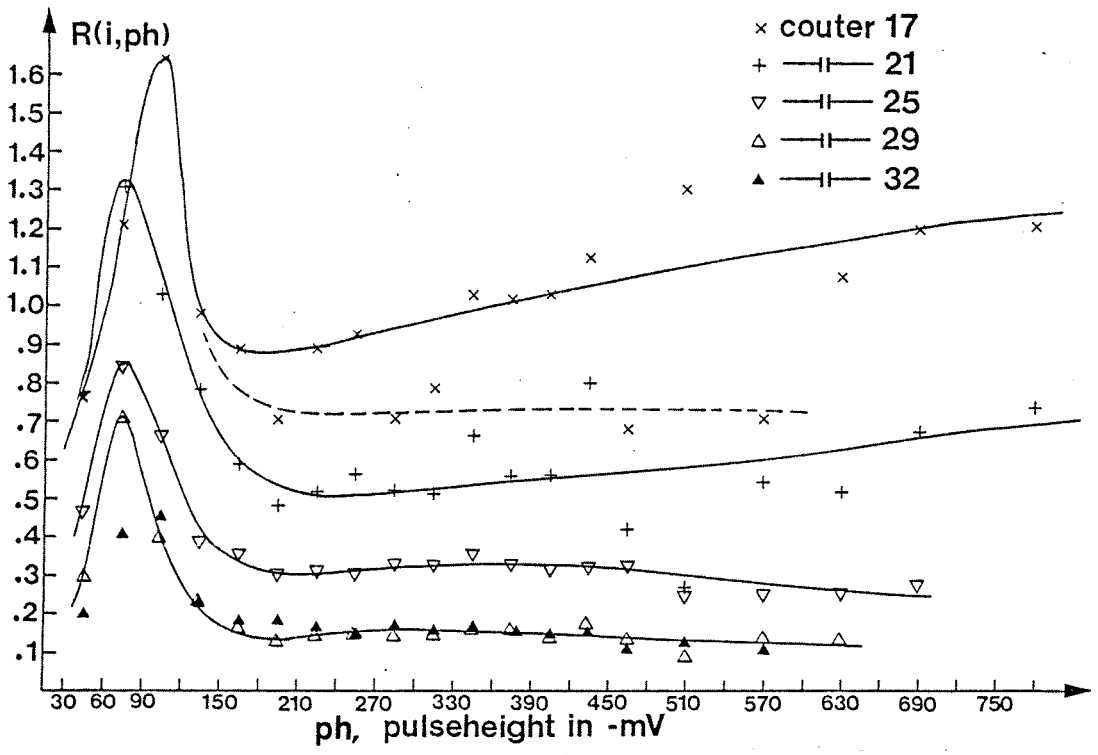

Fig. A5.3

Counting rate densities normalized to counter 18, as a function of the pulse-height for various counters. If CR is short for counting rate, $R(i,ph) \equiv [CR(i,ph_1 < ph < ph_2)]/[CR(18,ph_1 < ph < ph_2)]$. Both nominator and denominator are normalized to the beam intensity. The beam momentum = -92 GeV/c. For all data points, $ph=(ph_1+ph_2)/2$, for most, $\Delta ph \equiv ph_2 - ph_1 = 30$ mV, otherwise, $\Delta ph = 60$ mV or 120 mV. R(i,ph) decreases with increasing i, corresponding to counters further away from the beam.

on the ph-axis agrees well with the known calibration of minimum ionizing signals, i.e., 1 such signal (= 1 ep) = 20 pC or 75 mV (see Fig. 4.35). Halo muons are minimum ionizing and the explanation of the peak seems plausible. Considering Fig. A5.3, notice that flat curves corresponds to 'same shape of the signal spectrum as that from counter 18'. There are two curves for counter 17, the dashed one corresponds to bad data points; the beam was unstable while these rates were recorded. Up to 400 mV, this is clearly seen to affect counters closest to the beam the most (as it also should). The big fluctuations above 400 mV up to 600 mV for the two innermost counters, were caused by simultanuous collimator adjustments, above 600 mV the conditions were again stable.

If the peak is disregarded as due to normalization problems, we see that the relative responses of counters 17 and 21 increase by respectively 1.5 and 1.3 when ph goes from 0 → 750 mV. From Fig. 4.32 it is seen that this ph-range contains respectively 93 and 97% of the PM-signals from the two counters. The relative responses of counters 25, 29 and 32 are flat. The mean of the relative responses are given by, $\overline{R(i=17)} \approx 1.0$, $\overline{R(i=21)} \approx 0.55$, $\overline{R(i=25)} \approx 0.30$, $\overline{R(i=29)} \approx 0.14$ and $\overline{R(i=32)} \approx 0.15$. To conclude it is therefore correct in a first approximation to say that the shape of the charge spectra does not depend on i, and hence we may drop the inequality signe in (A5.3) and write,

$$I_{ac,i} = f_i \, I_B \times 175 \text{ pA} \qquad \text{(A5.4)}$$

It is simple to introduce indirectly the PM HV in this expression. When this voltage is set, it is adjusted until the most probable signal from a minimum ionizing particle, has got a desired charge, q_{max}. Hence, $q_{max} = q_{max}(\text{PM HV})$. The data in Fig. 4.32 as well as equation (A5.4), are based on $q_{max} = 20$ pC (notice that $q_{max} = 1$ ep). Therefore,

$$I_{ac,i}(q_{max}, I_B) = f_i \, I_B \, \frac{175}{20} \, q_{max} = 8.72 \, q_{max} \, f_i \, I_B \quad \text{(in pA)} \qquad \text{(A5.5)}$$

As an example: With 10^8 per burst incident, $q_{max} = 20$ pC, $i = 17$ (closest to the beam) and hence $f_{17} = 532.9$ c/icc (from Fig. 4.32) one finds,

$$I_{ac,17} = 8.72 \times 20 \times \frac{10^8}{75 \times 10^3} \times 532.9 \text{ pA} = 124 \, \mu\text{A}$$

Pedestals

I shall turn to the question of pedestals referred to in the A5.2 figure text. Fixing these pedestals is necessary in order to obtain the zero reference for both the ac-current and the dc-current. Three pedestals have been used. In all three cases is the anode branched through a fan in-out to the charge input of the L3001 analycer as shown in Fig. 4.17, common also is the gatewidth which is 100 ns. The positions of the pedestals on the charge axis, in pC, are shown below. Referring to the

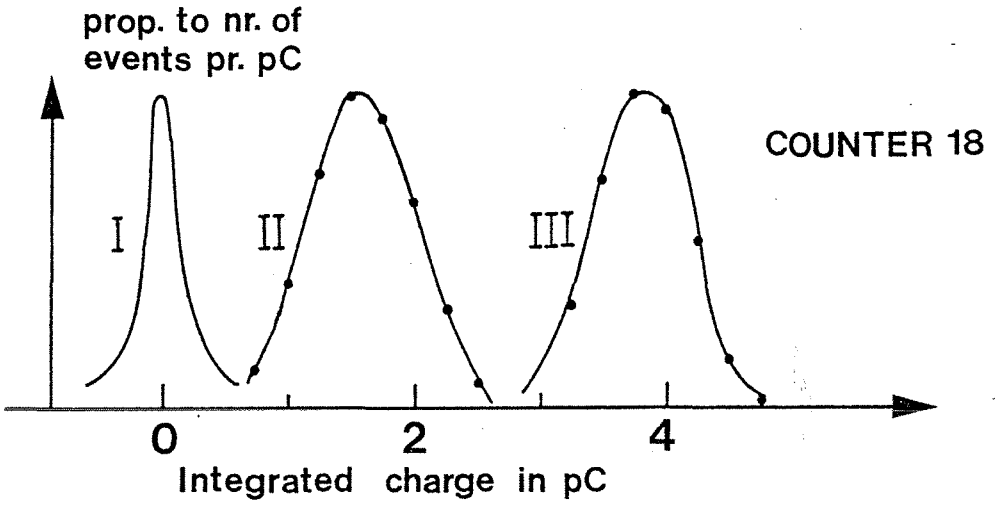

Fig. A5.4

Relative positions of pedestals. I corresponds to zero dc-current on the PM anode, II corresponds to zero ac-current on the anode and III corresponds to noise on the line. Notice that this last has a very little contribution from the PM itself, otherwise the pedestal would have been asymmetric.

numeration in the figure, the pedestals were measured in the following ways,

I Triggering each single charge measurement uncorrelated of what is on the charge input (of the L3001). Leaving the PM HV off.

II Triggering in the same way as above. However, the PM HV is on. Implies that 1 ep = 20 pC.

III Triggering directly on the pulses at the charge input when these fluctuates more than -1 mV. The PM HV naturally is on.

Since the difference in experimental conditions between I and II is only

a question of the PM HV, the observed Δq between peaks I and II can only be due to the contribution of the PM dc-level to the general level at the charge input. This amounts to 1.5 pC per 100 ns, or a current of 15 μA. Since this is a dc-level (= -0.015 mA multiplied by the load, in our case with NIM logic the load is 50 Ω, hence the dc-level is -0.75 mV), the same change in level would have been observed at the line to CAMAC and to the 50 Ω termination resistor (cf.. Fig. 4.23). Therefore the resulting anodic dc-current is $I_{dc,18} = 3 \times 15\,\mu A$, which is typical for the PM's on our L1/L2-counters. To obtain the total current through the anode, we added the ac and dc-currents. With the most severe conditions; choosing the counter closest to the beam and having high incident intensity, the total current may be as much as 124 μA + 45 μA = 169 μA. Here the first current is taken from above, it depends on intensity and energy of the beam, on the counter number and the high voltage setting; the second current depends only on the counter number and the high voltage.

One interesting remark can be made. Notice that the peak is situated at 1.5 pC while data from Fig. A5.2 tell that the beam related signals start at about 4.25 pC. Now, for counter 18 we measured the FWHM (with 1 ep = 20 pC) of the distribution produced by minimum ionizing particles, FWHM = 15 pC and therefore $f \equiv FWHM/q_{max} = 15/20 = 0.75$. Using formula (4.7) for the average number of photoelectrons produced at the cathode, we find n = 10.8 photoelectrons, each of which produce a charge of, $(20 + \delta)/10.8$ pC = 1.85 pC.* In light of this the very fast rise of the difference curve in Fig A5.2 reflects the onset of the photomultiplier efficiency. The extension below 4.25 pC cannot be determined from our data, cf. again Fig. A5.2. With 1 photoelectron giving in the mean 1.85 pC, one would expect this onset to start a bit lower than what the fully drawn curve indicates. There should be some efficiency for one photoelectron, that is at 3.35 pC, therefore the dashed curve may be a more reasonable extension. Anyway it is clear that the important rise in the efficiency takes place between 3.35 and 5.2 pC corresponding to one and two photoelectrons.

Peak III is not really used for anything, however, it shows that there is a lot of noise on the line. This noise looks periodic on an oscilloscope

* δ represents the difference in charge between the position of q_{mean} and q_{max}, for these considerations (with as many as 10.8 photoelectrons) δ may be disregarded.

and is of rather low frequency(< 1MHz). The difference between peaks II and III is explained by the fact that there must be a -1 mV fluctuation for the L3001 to trigger (when accumulating pedestals III). This corresponds to an enhancement of roughly $[0.001(V) \times 10^{12}]/[50(\Omega) \times 10^{7}(s^{-1})]pC =$ 2 pC in the charge observed (cf. Fig. A5.4). Notice that while pedestals II and III are of equal width, I is a lot narrower. This seems to indicate that the noise is related to the PM power supply, the oscillations become less important when it is swithed off.

The detailed behaviour of the pedestal positions have been studied to some extent. In Fig. A5.5 are displayed curves corresponding to the pedestal I (▽ - points) and pedestal II (• - points) positions for different gatewidths, Δt. The ∘ - points represent the difference between the other two curves. Notice that for Δt > 70 ns, it seems correct

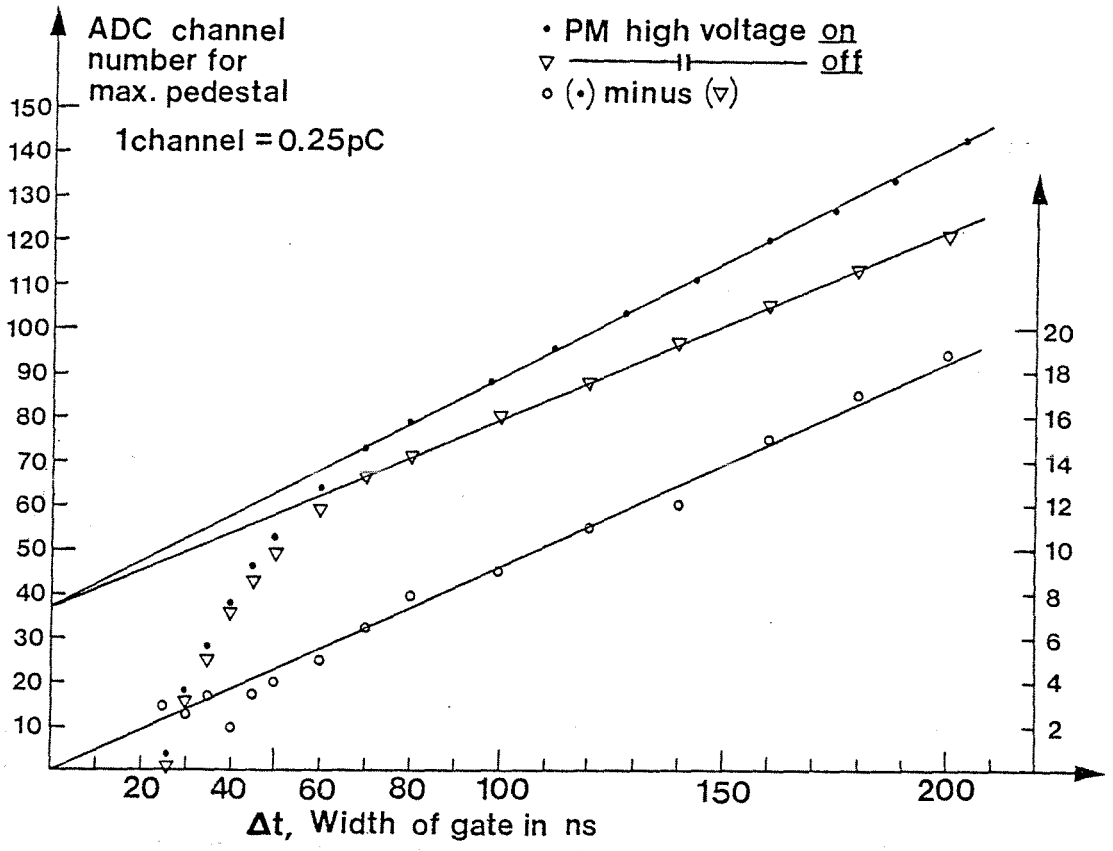

Fig. A5.5

Development of pedestal positions for counter 20 as a function of the applied gatewidth, Δt. The zero of the left ordinate axis is arbitrary, but constant throughout all measurements. On the contrary, the zero of the right ordinate is as shown, it displays in units of 0.25 pC (= 1 channel), the difference between the two curves.

that the L3001 integrates a dc-level, the peak position increases linearly with Δt. However, below 70 ns a non linear effect sets in which clearly comes from the L3001 itself (letting the charge input simply be a 50 Ω resistor yields pedestal positions slightly below the curve represented by ▽-points). Concerning the difference curve, observe first that •- and ▽-points extrapolate linearly very well to the same point (channel 37) on the y-axis. Therefore the difference, which represents the contribution of the PM, is proportional to Δt, which it also should be. The irregularities at lower Δt are due to the very small charges measured (< 1 pC), the resolution of the L3001 is 0.25 pC. Noticing that at Δt = 100 ns, the PM-contribution represents 9 channels = 9/4 pC = 2.25 pC, we may calculate the overall dc-current on the anode of counter 20,

$$I_{dc,20} = 3 \times \frac{2.25\ pC}{10^{-7}\ s} = 67.5\ \mu A$$

where the factor 3 is again due to the splitting in 3 of the anode output, one to a 50 Ω termination resistor, another to the L3001 and the third to the CAMAC ADC. Confere Fig. 4.23, observe that fast anode pulses are split twice in two before they arrive either in the logic or in an ADC, hence the factor 4 in (A5.3). The same is not true for the anodic dc-current, it sees 3 resistors of 50 Ω in parallel to earth.